

Design and Validation of a Decentralized Biomass Torrefaction System

by
Kevin S. Kung

A.B., Physics, Princeton University (2008)
M.Phil., Physics, University of Cambridge (2009)
S.M., Biological Engineering, MIT (2013)

Submitted to the Department of Biological Engineering
in partial fulfillment of the requirements for the degree of

Doctor of Philosophy
at the
Massachusetts Institute of Technology

May 2017 [31 May 2017]

© Massachusetts Institute of Technology 2017. All rights reserved.

Author: **Signature redacted**
.....
Department of Biological Engineering
May 26, 2017

Certified by: **Signature redacted**
.....
✓ Ahmed F. Ghoniem
Ronald C. Crane (1972) Professor
Thesis Supervisor

Accepted by: **Signature redacted**
.....
Mark Bathe
Chair, Graduate Program





77 Massachusetts Avenue
Cambridge, MA 02139
<http://libraries.mit.edu/ask>

DISCLAIMER NOTICE

Due to the condition of the original material, there are unavoidable flaws in this reproduction. We have made every effort possible to provide you with the best copy available.

Thank you.

The images contained in this document are of the best quality available.

Design and Validation of a Decentralized Biomass Torrefaction System

by
Kevin S. Kung

Submitted to the Department of Biological Engineering
on May 26, 2017 in partial fulfillment of the
requirements for the degree of
Doctor of Philosophy in the Field of Biofuels and Renewable Energy

Abstract

To date, there has been limited usage of biomass and agricultural residues in rural areas as a form of renewable energy, mainly due to the expensive costs involved in collecting and transporting raw biomass. A decentralized biomass torrefaction system has the potential to upgrade the quality and transportability of distributed biomass residues *in situ*, thereby creating additional localized economic values and mitigating the environmental consequences associated with open burning of the excess biomass residues. Nonetheless, most existing biomass torrefaction systems so far have been designed for large-scale, centralized deployment, and are unsuitable to be scaled down in decentralized applications due to their high level of sophistication and capital cost.

We propose a biomass torrefaction system based on the concept of torrefaction in a low-oxygen environment. By eliminating the stringent requirements of an inert torrefaction environment, we demonstrated that we can greatly simplify the reactor design and derive a laboratory-scale system that is also scalable. We proceeded to build and validate this torrefaction system with respect to different operating conditions and types of biomass. Using a quantitative definition for torrefaction severity, we were also able to relate the various fuel user requirements in real life back to the fundamental reactor operations. By

quantifying in detail the overall energy performance, pressure requirements, and transient timescales, we also demonstrated how such a reactor system can be operated at scale, as well as the various design improvements that can further boost the performance of a scaled-up system. Therefore, this work builds the foundation towards the development of a low-cost, small-scale, and portable torrefaction system that can potentially be widely deployed in rural areas.

Thesis Committee:

Ahmed F. Ghoniem

Ronald C. Crane (1972) Professor of Mechanical Engineering, MIT

Alexander H. Slocum

Pappalardo Professor of Mechanical Engineering

Robert J. Stoner

Director, MIT Tata Center for Technology and Design

Scott R. Manalis

Andrew and Erna Viterbi Professor of Biological Engineering

Acknowledgements

On many levels, this PhD thesis passes beyond just an intellectual journey into a spiritual one, and involves a host of people who have helped me and rooted for me during my time at MIT. The list below is my best attempt at digging through years of fading memories, and is, sadly, by no means comprehensive, but rather just a screenshot.

Coming from a physics background, many people had some difficulty relating why I wanted to move into engineering for graduate studies. I would like to thank the MIT Department of Biological Engineering for offering me a chance to study and make use of all the resources at this institute, and in particular, Professor Douglas Lauffenburger, for being flexible and letting me defer my graduate studies for one year while I study abroad. I would also like to acknowledge the members of BE Class of 2009—Rebecca Adams, John Casey Jr., Issac Chaim, Seymour De Picciotto, Jing Ge, Melissa Hanson, Kara Huang, Watthanachi Jumpathong, Aaron Meyer, Deepak Mishra, Shengyong Ng, Nirmala Paudel, Miriam Sefta, Josephine Shaw, Adrian Slusarczyk, and Carrie Thompson—for supporting each other and studying together during the first year in the BE curriculum. Occasionally, especially during my latter years, often with a pang of panic, I am reminded that I am the last one in the Class of 2009 still remaining in the program, but I have no regrets whatsoever with the somewhat extended detour that I took and all the rewards that I have reaped as a result.

At my time at MIT, I was first exposed to engineering and design in the context of resource-constrained considerations through my volunteer work with the MIT Engineers Without Borders (EWB). I would like to acknowledge my MIT-EWB colleagues Helen D’Couto, Marisa Simmons, Rebecca Gianotti, Gajan Sivandran, Stephen Pennybaker, Rebecca Heywood, Grace Teo, Chris Arsenault, Michael Zanchi, as well as the local Engeye team (John Kalule and Joseph). Dr. Alison Hynd was instrumental in supporting this project through a MIT Public Service Center fellowship and providing weekly feedback.

My exposure in engineering and design was further broadened through my engagement with the D-Lab curriculum. I went to Ghana with Amy Smith, Kofi Taha, Mette Andersen, Raghu Mahajan, Mary Xu, Anita Lin, Elaina Present, Kellie Courtney, and Catherine Johnson. Also thanks to Pastor George Fuachie, Timothy Kyiu, Asante Johnson, Crossman Hormenoo, Master Stone and their communities in Kumasi, Swami Magazine, and New Longoro, for being such generous hosts and allowing me to learn. Following the D-Lab: Development class, I learned more about design with Nathan Cooke, Gwyn Jones, and Jack Whipple, and it was a pleasure to work with the Coriolis Centrifuge team, Daisy Chang, Kwami Williams, Melvin Salinas, and Roberto Melendez. Finally, I took the Development Ventures class with Joost Bensen, and met wonderful colleagues who worked with me in developing the first development venture concept: Maria Davydenko, Ali Kamil, Mohit Kansal, David Lee, Rishi Trivedi, Coralie Vergez, and Nicole Yap.

It was in the Global Health Delivery Lab that I first encountered the seedling of the biomass torrefaction concept. This experience was made possible by Anjali Sastry, as well as my fellow student-consultants Alexandra Geertz, Sydney Atkins, and Nirav Patel. More

importantly, our local host in Carolina for Kibera opened the doors of their community to me, thanks to Hillary Omala, Ben Haggai, Jeffrey Okoro, Moses Ojwang, Erick Omondi, Erick Owour, Judy Mien, Norbert Aluku, Medina Abakar, Botul Sebit, the Jitunze Youth Group, as well as the Kibera Waste Recyclers.

As I developed the initial organic waste conversion concept further, it was Laura Sampath who was instrumental in helping me formulate this into a team and a project with a self-sustaining and self-growing prospect. It was during the Trash Talk at the IDEAS Global Challenge that Libby McDonald introduced me to Amy Banzaert and Kendra Leith, and gave me sharper project definition. Alison Hynd from the MIT Public Service Center, together with Laura Sampath from the former MIT International Development Initiative, Saida Benhayoune from the new D-Lab Scale-Ups program, and the Legatum Center provided the seed funding to help me explore this project more in depth. In addition to the formerly mentioned partners from Carolina for Kibera, I also had the pleasure of working with Will Ruddick, Jack Menya, Kenfield Griffith, Kenneth Owade, Dickson Kamau, Dr. Kamau Gachigi, and all the households and charcoal vendors we interviewed. This work forms the early section of the Takachar blog (takachar.blogspot.com). Thanks also to the following MIT students for being a part of this early journey: Jacob Young, Marie Burkland, Sophie Ni, Ala'a Siam, Yannan Zheng, Ya Lin, Vincent Liu, Yafei Han, Lyndsy Muri, Daisy Chang, and Viveka Mishra. *Asanteni sana!*

At this point, as I made a somewhat scary transition in my research focus from cancer research to renewable energy, several of my colleagues and mentors played a key role in supporting me and being flexible. This included Sandy Klemm, Ya Lin, Monica Wolf, Miaoqing Fang, Christoph Engert, Professors Terry Orlando, Douglas Lauffenburger, Scott Manalis, Forrest White, Alexander van Oudenaarden, and Carlo Ratti.

It was during a haphazardly arranged meeting with Prof. Alexander Slocum that the idea of doing a PhD thesis in biowaste conversion entered my mind. Dr. Robert Stoner and Prof. Sanjay Sarma instigated the possibility of carrying out such a project under the formative MIT-Tata Center, and introduced me to Prof. Ahmed Ghoniem, who, when I was about to give up on this pursuit, encouraged me to stay optimistic, and ultimately became my thesis advisor.

Having found support in the MIT-Tata Center, I traveled for the first time to India with Randy Kirchain, Rich Roth, Angi Acocella, Emmanuel Lim, Rachel Perlman, Caroline Howe, Devin Currie, and Jeremy Gregory. I am grateful to my local hosts in Hyderabad (Dr. Reddy and his colleagues at the WALAMTARI), Bangalore (Kamal Raj, Siddarth Kumar, Kuldeep Dantewadia, Almitra Patel, Mohini Acharya, Omer Kaiser), Pune (Dr. Anand Karve and Dr. Priyadarshini Karve), Chennai (Prof. Vinu and Deepak Ojha), Islampur (Shantilal Jakite, Mukund Deogaonkar, and Arkajit Mandal), Patna (Col. Baljit Singh and Manoj Sinha), Faisabad (Ambarish Singh), Delhi (Siddhartha Bountra), and Coimbatore/Ooty (Balram Warriar, Mr. Aditya, and Mr. Annamalai). Thanks to the extremely competent staff at the MIT-Tata Center and the Tata Trusts—Wendy Duan, Jazy Ma, Darayes Shaw, Dickie Daruwalla, and Alamin Nomanbhoy—for organizing our trip amidst our somewhat chaotic

schedules. And thank you, of course, Sir Ratan Tata, for your personal support of this project and all Tata projects. धन्यवाद!

I would like to thank all the students that have tolerated my mentoring over the past few years and that have contributed in different ways to this project. This includes a master's student (Megan O'Brien), two S.B. thesis students (K.K. Wopat and Jonathan Rea), as well as a handful of UROPs (Meredith Barr, Ali Daher, Dheekshita Kumar, Tamanna Urmi, Abu Saleh, Jennifer Otiono, Gal Zeidman, Nikita Kodali, Marie Moudio, Neil Aggarwal, Aaron Gonzalez, and Tim Manganello).

I would like to thank my colleagues in the Reacting Gas Dynamics group (including Addison Stark, Richard Bates, George Dimitrakopoulos, Akhilesh Bakshi, Xiaoyu Wu, Ashwin Raghavan, Nadim Chakroun, Lorraine Rabb, Christos Altantzis, Gaurav Kewlani, Ray Speth, Cristina Botero, and Rajesh Sridhar), the Precision Engineering Research Group (including Dr. Nevan Hanumara, Sandy Campbell, and Kevin Simon), the MIT Energy Initiative (including Randy Field and Navid Seifkar), Hobby Shop (Hayami Arakawa and Ken Stone), as well as my laboratory neighbors in NW14 as well as colleagues from the Environmental Health and Safety (EHS) for bearing with dusty and often foul-smelling experiments (Jim Doughty, Matt Orosz, Karen Cote, Dan Herrick, and Matt Fulton). Of course, thank you, Dean Maria Zuber, for letting us use the empty lab room in NW14, without which the instrumentation would have been much more difficult to set up.

I would like to thank my collaborators at IIT-Bombay (Professor Sanjay Mahajani, Dr. Sonal Thengane, Ankita Gupta, and Ramesh Naidu) for assisting with the elemental analysis of the fuel samples, as well as at D-Lab (Dr. Dan Sweeney) for lending me the emission and cookstove measurement equipment and set-up. Thank you, Jack Whipple, also for helping me weld the secondary oxidation device at moment's notice.

I would like to thank my family for their unconditional support, as well as Florina Feng, with whom I have had the honor of being a life partner, both in the up times and the down times. 謝謝你們的支持以及諒解!

I would like to thank the funding sources that made this research possible. This included the Dolores Zohrab Liebmann Fellowship for supporting my tuition and a large part of my stipend for three years, the Legatum Fellowship for supporting my stipend for the first two years, as well as the MIT-Tata Fellowship for supporting all the remaining expenses, including my trips to India, the laboratory supplies, as well as all the capital equipment.

Last of all, thank you, Dr. Santosh Shanbhogue, for being a critical scientific mentor in my project. Thank you also once again, Dr. Robert Stoner, Professors Scott Manalis, Alex Slocum, and Ahmed Ghoniem for being on my thesis committee and being part of my journey for the past few years. You continuously challenged me to reach new heights, to question my own assumptions as well as yours, and to achieve what had seemed to me four years ago only achievable by some form of miracle or magic. Thank you, in other words, for believing in me and helping me achieve my dream.

Table of Contents

CHAPTER 1 CASE FOR DECENTRALIZED TORREFACTION	13
1.1 FATE OF UNUSED BIOMASS ENERGY AND ITS ENVIRONMENTAL IMPACTS	13
1.2 BIOMASS TORREFACTION AND ITS FUNCTIONAL EFFECTS	19
1.3 OVERVIEW OF TORREFACTION REACTOR DESIGNS.....	21
1.3.1 <i>MOVING BED.....</i>	22
1.3.2 <i>FLUIDIZED BED.....</i>	23
1.3.3 <i>ROTARY DRUM</i>	24
1.3.4 <i>SCREW CONVEYOR</i>	25
1.3.5 <i>MICROWAVE</i>	26
1.4 NEED FOR A SMALL-SCALE, DECENTRALIZED TORREFACTION REACTOR DESIGN.....	27
CHAPTER 2 A LOW-OXYGEN TORREFACTION REACTOR DESIGN.....	33
2.1 TORREFACTION IN A LOW-OXYGEN ENVIRONMENT.....	33
2.2 PROPOSED REACTOR DESIGN CONCEPT	37
2.3 COARSE-GRAINED MODEL.....	38
2.3.1 <i>MODELING DESCRIPTION</i>	39
2.3.2 <i>ANALYSIS OF HEAT TRANSFER PATHWAYS.....</i>	43
2.3.3 <i>IMPLICATIONS FOR REACTOR SIZING</i>	44
2.4 FINE-GRAINED MODEL	45
2.4.1 <i>KINETICS AND THERMOCHEMISTRY SUBMODEL.....</i>	46
2.4.2 <i>GOVERNING EQUATIONS.....</i>	47
2.4.3 <i>PARTICLE SHRINKAGE.....</i>	48
2.4.4 <i>IMPLEMENTATION AND VALIDATION</i>	49
2.4.5 <i>RESULTS</i>	49
2.5 DETAILED REACTOR DESIGN.....	51
2.5.1 <i>BIOMASS FEED COMPONENT.....</i>	53
2.5.2 <i>UPPER GAS SAMPLING PORT COMPONENT.....</i>	53
2.5.3 <i>MOVING BED COMPONENT</i>	55
2.5.4 <i>LOWER GAS SAMPLING PORT COMPONENT</i>	55
2.5.5 <i>OXIDATIVE ZONE COMPONENT</i>	56
2.5.6 <i>CHAR-COOLING SEGMENT</i>	57
2.5.7 <i>MOTOR DRIVE</i>	58

2.6	SUMMARY AND PERSPECTIVES	59
------------	---------------------------------------	-----------

CHAPTER 3 VALIDATION OF A SCALABLE BIOMASS TORREFACTION REACTOR AND ITS PERFORMANCE METRICS..... 61

3.1	NEED FOR A SCALABLE TORREFACTION TEST REACTOR.....	62
3.2	EXPERIMENTAL SET-UP AND DESIGN	63
<i>3.2.1</i>	<i>CONTROL OF SOLID RESIDENCE TIME.....</i>	<i>63</i>
<i>3.2.2</i>	<i>CONTROL OF TORREFACTION SEVERITY.....</i>	<i>65</i>
3.3	READOUT PROTOCOLS.....	67
<i>3.3.1</i>	<i>SOLID MASS FLOW</i>	<i>68</i>
<i>3.3.2</i>	<i>PROXIMATE ANALYSIS</i>	<i>68</i>
<i>3.3.3</i>	<i>ULTIMATE ANALYSIS.....</i>	<i>69</i>
<i>3.3.4</i>	<i>HIGHER HEATING VALUE.....</i>	<i>69</i>
3.4	VALIDATION OF STABLE OPERATING CONDITIONS.....	70
3.5	REACTOR PERFORMANCE ANALYSIS.....	76
<i>3.5.1</i>	<i>ENERGY DENSIFICATION</i>	<i>76</i>
<i>3.5.2</i>	<i>SOLID MASS YIELD</i>	<i>77</i>
<i>3.5.3</i>	<i>SOLID ENERGY YIELD</i>	<i>78</i>
<i>3.5.4</i>	<i>SOLID PROXIMATE ANALYSIS</i>	<i>79</i>
<i>3.5.5</i>	<i>SOLID ELEMENTAL ANALYSIS</i>	<i>80</i>
<i>3.5.6</i>	<i>VOLATILE ELEMENTAL ANALYSIS.....</i>	<i>81</i>
<i>3.5.7</i>	<i>NATURE OF PRIMARY OXIDATION.....</i>	<i>85</i>
<i>3.5.8</i>	<i>COMPOSITION OF REACTOR EXHAUST.....</i>	<i>86</i>
3.6	CHARACTERIZATION OF UNCERTAINTIES.....	89
<i>3.6.1</i>	<i>INTRINSIC UNCERTAINTIES.....</i>	<i>90</i>
<i>3.6.2</i>	<i>EXTRINSIC UNCERTAINTIES</i>	<i>90</i>
3.7	COMPARISON OF PERFORMANCE METRICS WITH EXISTING LAB-SCALE REACTORS.....	93
3.8	GENERAL APPROACH FOR RAPID REACTOR VALIDATION AND SCALING.....	98

CHAPTER 4 A DESIGN-ORIENTED INDEX OF TORREFACTION.....101

4.1	THE NEED FOR AN INDEX OF TORREFACTION	101
4.2	DEFINITION OF THE INDEX OF TORREFACTION.....	103
4.3	A MOTIVATING DESIGN CASE STUDY USING THE INDEX OF TORREFACTION	104
4.4	VARIOUS FUNCTIONAL MAPPINGS TO THE INDEX OF TORREFACTION	106

4.4.1	<i>PROXIMATE ANALYSIS</i>	107
4.4.2	<i>ELEMENTAL (ULTIMATE) ANALYSIS</i>	108
4.4.3	<i>FUEL GRINDABILITY</i>	109
4.4.4	<i>SELECTED COOKING CHARACTERISTICS</i>	118
4.5	GENERAL APPROACH FOR RAPID REACTOR VALIDATION AND SCALING	126

CHAPTER 5 ANALYSIS AND MITIGATION OF ENERGY LOSS MECHANISMS IN A TORREFACTION REACTOR.....129

5.1	NEED FOR AN ENERGY-BASED METHOD FOR REACTOR IMPROVEMENT	130
5.2	TOTAL BIOMASS ENERGY FLUXES FROM THE REACTOR SYSTEM	131
5.3	CHARACTERIZING AND MITIGATION LOSSES FROM REACTOR SIDE WALLS	132
5.3.1	<i>MEASUREMENT METHODOLOGY</i>	133
5.3.2	<i>RESULTS AND DISCUSSION</i>	135
5.3.3	<i>SCALING THE SIDE WALL THERMAL LOSS</i>	136
5.3.4	<i>OPTIMIZATION OF THERMAL INSULATION</i>	137
5.4	CHARACTERIZING AND MITIGATING LOSSES FROM THE CHAR-COOLING SEGMENT ..	141
5.4.1	<i>MEASUREMENT METHODOLOGY</i>	141
5.4.2	<i>RESULTS AND DISCUSSION</i>	143
5.4.3	<i>PROPOSED AIR-PREHEATING MECHANISM AND VALIDATION STRATEGY</i>	144
5.4.4	<i>AIR-PREHEATING VALIDATION RESULTS</i>	148
5.5	CHARACTERIZING AND MITIGATION LOSSES AND EMISSIONS FROM THE EXHAUST ..	153
5.5.1	<i>MEASURING THE SENSIBLE ENTHALPY LOSS</i>	154
5.5.2	<i>MEASURING THE CHEMICAL ENTHALPY AVAILABILITY</i>	154
5.5.3	<i>EMISSION PROFILES AND COMPLETENESS OF SECONDARY COMBUSTION</i>	160
5.5.4	<i>CHARACTERIZATION OF UNCERTAINTY RANGES</i>	165
5.5.5	<i>DISCUSSION ON ENERGY LOSSES IN THE EXHAUST STREAM</i>	167
5.6	SUMMARY AND PERSPECTIVES FOR IMPROVEMENT	169

CHAPTER 6 BULK HYDRODYNAMIC CHARACTERISTICS IN A BIOMASS MOVING BED AND THEIR EFFECTS ON SCALING

6.1	IMPORTANCE OF HYDRODYNAMIC DATA IN BIOMASS MOVING BED	171
6.2	EXPERIMENTAL SET-UP	173
6.3	VALIDATION OF DARCY'S LAW IN BIOMASS MOVING BED	177
6.4	COMPARISON WITH EXISTING PERMEABILITY CORRELATIONS	179
6.5	SCALING PRESSURE REQUIREMENTS IN TORREFACTION REACTOR	181

6.6	DISCUSSION	189
CHAPTER 7 CHARACTERIZATION OF TRANSITION TIMESCALES IN SCALING BIOMASS		
	REACTOR OPERATIONS.....	193
7.1	TRANSIENT RESPONSE OF THE REACTOR SYSTEM	193
7.2	ANALYSIS OF REACTOR THERMAL MASS	194
7.3	STARTING A REACTOR FROM COLD STATE.....	197
7.4	TWO METHODS FOR SHUTTING DOWN THE REACTOR	206
<i>7.4.1</i>	<i>KEEPING THE REACTOR WARM</i>	<i>207</i>
<i>7.4.2</i>	<i>COOLING THE REACTOR QUICKLY</i>	<i>209</i>
<i>7.4.3</i>	<i>PERSPECTIVES IN COOLING THE REACTOR.....</i>	<i>214</i>
7.5	TRANSITIONING BETWEEN TWO REACTION CONDITIONS.....	215
7.6	DISCUSSION	217
CHAPTER 8 PERSPECTIVES AND FUTURE WORK		219
BIBLIOGRAPHY.....		226

Chapter 1 Case for Decentralized Torrefaction

Biomass—such as post-harvest agricultural residues—represents a vast untapped value for energy and other applications. However, most of the world’s biomass resources are located in remote distributed locations, which make the logistics of conversion and utilization expensive. In this Chapter, the goal is to present a case for decentralized biomass torrefaction as a strategy to locally densify and process the excess biomass resources, so that they can be stored longer in solid form and more easily consumed locally and/or transported and processed. A review of the existing biomass torrefaction technologies reveals that they tend to be too large-scale and complex to be compatible with decentralized biomass torrefaction. We therefore define the functional requirements for enabling the design of such a system, and propose a simplified but scalable low-oxygen moving bed reactor design concept that we will study and quantify further for the rest of this thesis.

1.1 Fate of Unused Biomass Energy and Its Environmental Impacts

Biomass, as loosely defined, consists of organic materials produced by the photosynthetic activities of plants. These can include trees, grass, agricultural products, and their residues. The term lignocellulosic biomass gives the term more specificity, by referring to the three main constituent components of biomass: cellulose, hemicellulose, and lignin. Indeed, many studies in the literature have assumed that the diverse types of biomass can all be broken down into different combinations of cellulose, hemicellulose, and lignin (Pérez *et al.*, 2002; Yang *et al.*, 2006). Because biomass is very diverse, as summarized in Table 1, in the remainder of this Chapter, in order to motivate the discussion and design goals, we will be focusing only on a specific sub-type of biomass: agricultural residues, especially those agricultural residues in India. However, the work done in this thesis is applicable to all types of biomass throughout the world, including those that are non-agricultural in origin.

Table 1 – Classification of different types of biomass, and examples of each (adopted from Nhuchhen *et al.*, 2014). Our discussion will be primarily on agricultural residues.

Class	Type	Examples
Forestry	Dedicated forestry	Short rotation plantations (willow, eucalyptus, etc.)
	Forestry products	Wood blocks and chips
Agriculture	Crops and residues	Oil seeds, sugar crops, starch crops, straws, pruning
	Livestock	Wet and dry manure
Industry		Sawdust, paper industry waste
Others	Garden waste	Pruning and grasses
	Contaminated	Municipal solid waste, sewage sludge, demolition wood

Many people are interested in biomass because of its potential as a mostly renewable energy resource: the plant matter can be converted into carbon dioxide and water, releasing energy in the process, whether through rapid oxidation such as combustion or gasification, or through slower biological conversion such as anaerobic digestion or aerobic composting. While biomass can be converted into other valuable uses, such as fertilizer, animal mulch, and even structural materials, in this thesis, we focus specifically on the energy potential of biomass.

What are some examples of common agricultural residues, and what are their respective energy potentials? This figure is notoriously difficult to obtain on a macroscopic level, but studies such as Lal (2005) have begun to help shed light into this worldwide potential. As summarized in Table 2, most of the world’s agricultural residues can be broken down into four families: cereals (e.g. barley, corn, millet), legumes (e.g. beans, chickpeas, groundnut), oil crops (e.g. linseed, sesame, sunflower), and sugar crop (e.g. sugar beet, sugarcane, potatoes). Altogether, Lal (2005) estimates that the total crop residue is about 3.8 billion tons/year. In terms of energy equivalent, this is about 69.9 exajoules (10^{18} J), or about 60 quads—which is sufficient to satisfy the primary energy demand of 13.5% of the world.

Table 2 – Worldwide biomass potential as an energy resource in 2001 (Lal, 2005).

Crop family	Worldwide crop production	Worldwide crop residue
Cereals	2.1 billion tons/year	2.8 billion tons/year
Legumes	305 million tons/year	305 million tons/year
Oil crops	79 million tons/year	108 million tons/year
Sugar crop	677 million tons/year	170 million tons/year

While the worldwide biomass potential is enormous, different geographical regions have different types of biomass and different energy needs. Thus, a broad discussion without geographical specificity is likely going to bewilder rather than to aid the development of the main goals of this thesis. To be more specific, we start by examining the case of biomass utilization in India, while keeping in mind that this specific case is also generalizable to many other regions and contexts in the world.

Done in a similar spirit as Lal (2005), a more recent study by Hiloidhari *et al.* (2014) examines the bioenergy potential from biomass in India. Figure 1(a) illustrates the residues from the different crop types found in different Indian states, as well as their contribution to the overall energy potential. Figure 1(b) represents this information on a map, normalized by the population. We observe that there is a significant geographical disparity: this surplus biomass energy potential is greatest in the western states such as Gujarat and Maharashtra (> 10,000 MJ/year per capita) while it is the least in the eastern and northern states such as Mizoram, Bihar, and Jharkhand (< 1,000 MJ/year per capita). Altogether, Hiloidhari *et al.* estimated that the total surplus biomass provides an equivalent of 4.15 exajoules of energy per year, or 132 GW of energy availability in the country.

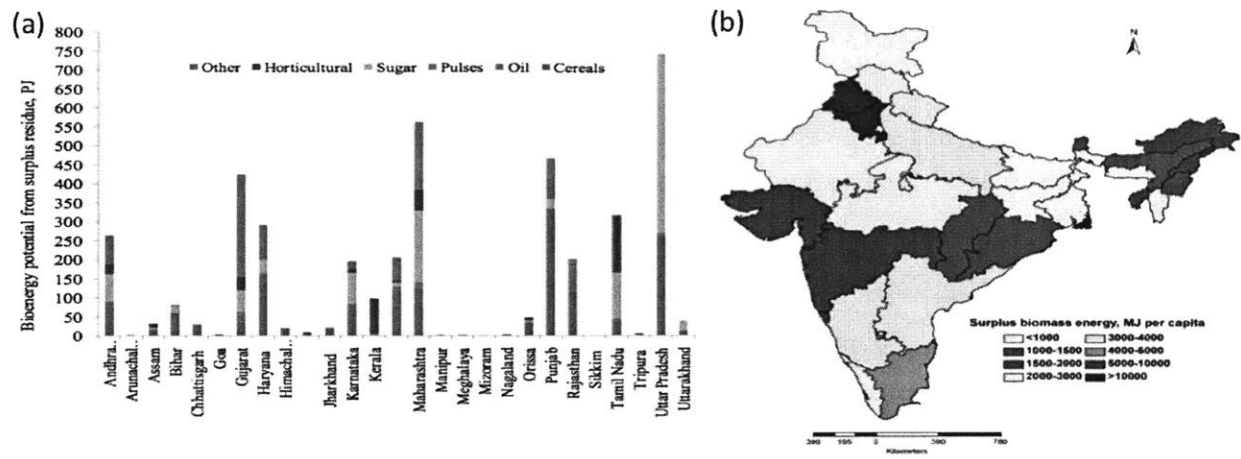


Figure 1 - Energy potential of surplus biomass in India, from Hiloidhari *et al.* (2014). (a) Breakdown of the energy potential from different crop types by different states in India. (b) Map of the surplus biomass energy per capita in different states.

Table 3 – Breakdown of the capacities of biomass-related energy generation in India (MNRE, 2016) as of March 31, 2016.

Sector	Capacity
On-grid power (combustion, gasification, bagasse cogeneration)	4,831.11 MW
On-grid waste to power	115.08 MW
Off-grid biomass (non-bagasse) cogeneration	651.91 MW
Off-grid biomass gasifiers (rural)	18.15 MW
Off-grid biomass gasifiers (industrial)	164.24 MW
Off-grid waste to energy (power, heat)	160.16 MW
Total installed capacity	5,941 MW
Total surplus biomass energy potential (Hiloidhari <i>et al.</i>, 2014)	132,000 MW

Yet when we see a breakdown of the biomass energy utilization in India, we note a stark discrepancy: currently, only 5.94 GW, or 4.5% of the total surplus biomass energy potential, is being utilized as energy, as listed in Table 3. This then begs the question: What happened to the remaining 95% of the surplus biomass energy potential? To say that most of the remaining biomass is being used for other non-energy purposes such as fertilizer

(compost) or animal mulch is hardly accurate, as Hiloidhari *et al.* in their biomass energy estimation already considered and subtracted these other competing uses from the overall biomass energy availability. While the current literature is lacking on a detailed accounting for the fate of the remaining 95% of the energy potential, we can make some educated guesses based on what is often observed in the field, often based on specific types of biomass and its fate.

One of the most well studied cases of the fate of agricultural residues is that of post-harvest rice stubbles in the Punjab State in India. Anyone who has traveled to rural parts of India during October and November may be familiar with sights of open biomass burning in the field (Figure 2a). It is estimated that the Punjab State produces about 17 million tons of rice stubble every year, and of that, more than 90% is being burned in the open (Milham *et al.*, 2014). As seen in a satellite image (Figure 2b) taken by NASA, this burning releases tremendous amounts of atmospheric aerosols. These aerosols can travel thousands of kilometers, and is considered a major contributor to urban smog in places like Delhi (Subramanian, 2016). Therefore, the negative public health effects of aerosol inhalation (van der Werf *et al.*, 2006; Pandey *et al.*, 2005) extend beyond just the local regions where the open burning occurs, to large metropolitan areas with millions of people. Furthermore, these atmospheric aerosols have historically contributed to a significant uncertainty in modeling climate change (Andreae *et al.*, 2005; Ramanathan *et al.*, 2007; and Sharma *et al.*, 2010). A more recent modeling study (Jacobson, 2014) suggests that open biomass burning can contribute up to 18% of global anthropogenic CO₂ emissions.

While it is not within the scope of this work to try to track down the fate of the different types of surplus biomass in India or in the world, it suffices to say that (a) a significant portion of the energy potential from the surplus biomass is not currently being utilized, and (b) some of the surplus biomass is being burned in the open, which is not only a waste of resources and energy, but also contributes to air pollution, negative public health outcomes, and global climate change. The next question is: What are some common factors that prevent this surplus biomass energy from being harnessed?

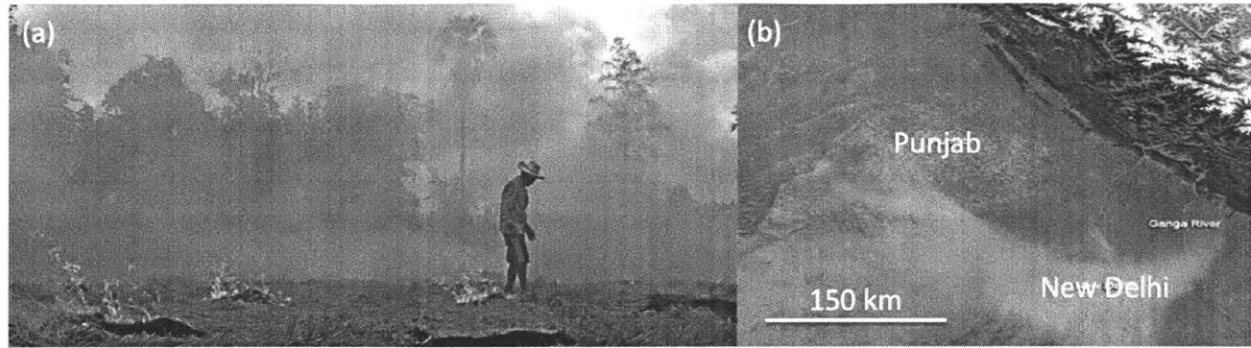


Figure 2 - Evidence of biomass burning. (a) Burning of stubbles in a rice field in the Punjab State of India (Martin, 2014). (b) A NASA satellite image showing the macro-scale particulate plumes associated with biomass burning in Punjab, India (NASA, 2015).

While the use of biomass energy is highly context-dependent, a survey of the existing literature reveals some outstanding difficulties in harnessing this biomass energy in rural areas. Most types of agricultural biomass residues do not present themselves in a form that cannot be easily manipulated. For example, due to the high moisture content, and low mass and energy density in its native state, biomass is often very costly to transport and process without some preprocessing step, such as baling or pelleting, that improves the density and other transportation-related characteristics (Hess *et al.*, 2007; and Eranki *et al.*, 2011). In some cases, it may make sense to set up a biomass energy supply chain in the vicinity of an industrial cluster with an intensive energy demand (for example, Chattopadhyay *et al.*, 2016). On the other hand, in many cases, the location of energy availability and the location of energy demand are frequently not contiguous (Lin *et al.*, 2016). In such cases, significant amount of energy and cost can be expensed in bringing the agricultural residue from one location to another, and this therefore limits the territory around a biomass energy plant where biomass collection and transportation are feasible (Survilo and Beryozkina, 2016). As an example, an interview that the author carried out with the Biomass Power Association revealed that for many biomass power plants, the cost of collecting and transporting the biomass feedstock can comprise 90% of the operating costs. This often limits the feasible transportation to a radius of less than 30 kilometers from the plant (Cleaves *et al.*, 2015).

Due to these logistical challenges in a centralized biomass processing facility, recent studies have shown increasing interest in a decentralized mode of biomass utilization. Lamers *et al.* (2015), for example, propose a network of decentralized biomass depots to make biofuel production and utilization more economical. While such concepts are commendable, their actual implementation is still questionable. One reason is that the majority of biomass processing and utilization technologies are, by and large, designed to be large-scale and centralized. While decentralized and off-grid biomass technologies, such as some small-scale gasifier or combustor designs (< 100 kW), have existed for many years (Dong *et al.*, 2009; and Arena *et al.*, 2010), they mainly produce combustible gases, heat or power, and herein lies a central problem: these forms of energy are either not readily storable, or have a high cost of energy storage. Consider the fact that in rural, decentralized areas, surplus biomass is not available constantly, but often is only available during one or at most two peak seasons immediately after harvest, and the fact that this biomass has a limited lifetime (before the land needs to be cleared, or before the biomass starts to decompose, for example), then we can see that it becomes a significant challenge to not just to harness this seasonal energy supply, but also to *store* it in a decentralized and cost-effective manner so that it can be used in off-seasons where surplus biomass residues are not readily available. The question then becomes as follows: In decentralized biomass processing, if gases, heat, or power do not provide an easily storable form of energy, can we identify technologies or processes to store this energy instead in a non-reactive solid form without requiring specialized storage containers?

1.2 Biomass Torrefaction and Its Functional Effects

Our interest in biomass torrefaction arises as a potential answer to the question posed at the end of the previous section. Biomass torrefaction is a pretreatment process whereby lignocellulosic biomass such as agricultural residue is subject to an elevated temperature of typically between 200-320°C for a timescale of minutes to hours. Under such conditions, the biomass undergoes chemical changes in the form of devolatilization, whereby the low-energy molecules such as water, carbon dioxide, carbon monoxide, and organic acids leave

the biomass in the form of volatile gases rich in hydrogen and oxygen. Because these low-energy molecules carry mass away to a greater extent than they carry away energy, what remains in the torrefied solid becomes more energy dense (both on mass basis and on volumetric basis) and more carbon-rich. This results in a visual change of color in the appearance of the biomass (Figure 3).

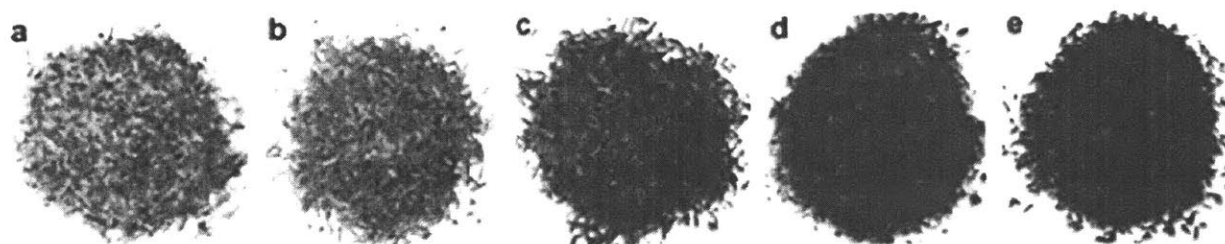


Figure 3 - Visual appearance of pine shavings as they are increasingly torrefied from (a) to (e) (O'Brien, 2016).

As a result of this energy densification, the cost of transporting torrefied biomass is reduced on an energy basis, as the same truckload of torrefied fuel now contains more energy compared to the original case of raw biomass fuel. Furthermore, torrefied biomass has been shown to be more hydrophobic, which means that it is resistant to moisture attack and does not tend to degrade over time (Acharya and Dutta, 2015). Therefore, torrefied biomass can be stored as a stable fuel for a much longer period of time compared to its raw biomass counterpart. Table 4 lists some of the functional changes to the biomass fuel as it becomes torrefied.

Table 4 – Changes in the functional characteristics of biomass fuel upon torrefaction.

Criterion	Raw biomass	Torrefied biomass
Bulk density	200-250 kg m ⁻³	550-850 kg m ⁻³
Mass energy density	9-15 MJ kg ⁻¹	19-25 MJ kg ⁻¹
Volumetric energy density	2-3 GJ m ⁻³	15-19 GJ m ⁻³
Energy transportation cost	~\$0.020 GJ ⁻¹ km ⁻¹	~\$0.016 GJ ⁻¹ km ⁻¹
Native moisture content	10-50% (hydrophilic)	1-5% (hydrophobic)
Storage shelf-life	Weeks (biodegradation)	Months

As can be seen in Table 4, the various challenges in decentralized biomass processing can be directly addressed by torrefaction. In addition, there are other features of biomass torrefaction such as decreased energy requirement for grinding the torrefied biomass into smaller pieces (Li, 2015); while they do not directly improve transportability and storage, they do confer advantage to the subsequent solid fuel processing, because many solid fuel boilers—especially of fluidized bed design—require that the incoming fuel feedstock be pulverized.

Finally, the volatile gases released by the biomass feedstock during the torrefaction process contain energy and can be combusted. Therefore, this heat can, in theory, be harnessed to supply the heat source to the torrefaction reactor itself, without requiring external energy. This *autothermal* nature of biomass torrefaction under certain conditions is a key to a scalable biomass torrefaction process.

1.3 Overview of Torrefaction Reactor Designs

Given these functional changes that can be effected on the biomass upon torrefaction, we come to the conclusion that torrefaction is a promising preprocessing step in order to overcome the aforementioned challenges with using surplus biomass in rural areas. In this section, we explore some of the existing torrefaction technologies. In the following section, we explain why they have been ineffective so far in addressing the utilization of agricultural residues.

The basic functional requirement of a torrefaction reactor is that (a) it needs to heat the biomass up to a certain target temperature range, and (b) it needs to convey biomass continuously. In this section, we discuss several common types of reactor design that can satisfy the criteria above. While our list below is not exhaustive, it represents the most common varieties in existence.

1.3.1 Moving Bed

A vertically oriented reactor where a packed bed of biomass migrates downwards, driven by gravity. Towards the bottom of the reactor, the temperature steadily increases as the biomass travels downwards. At the base of the reactor, a mechanism (e.g. screw auger) continuously removes torrefied biomass from the reactor. The temperature gradient can be set up by the injection of hot gases directly into the bottom of the moving bed, and the hot gases then flow upwards (counter-flow) through the moving bed. The temperature gradient can also be set up by the conduction of heat into the moving bed from the exterior in an indirect fashion. One example of a moving bed reactor (Figure 4) is the Torspyd™ design by Thermya (France), and then validated in modeling by Ratte *et al.* (2011).

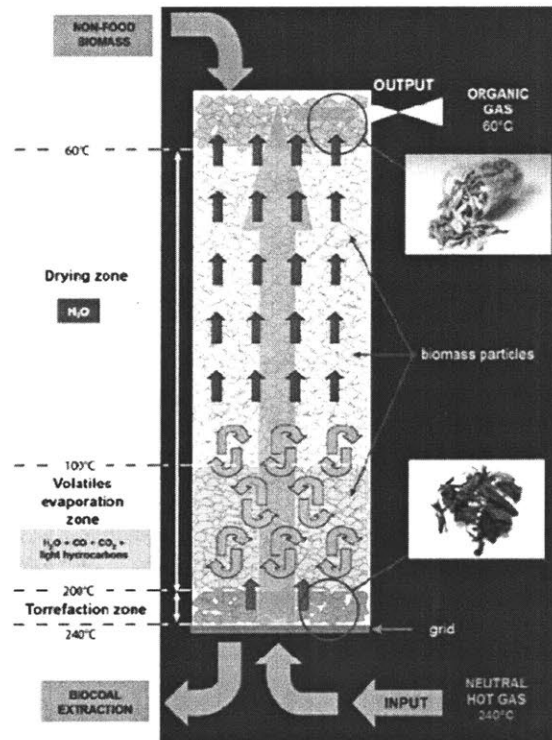


Figure 4 - The Torspyd™ column, an example of a moving bed torrefaction reactor design (Ratte *et al.*, 2011)

The advantage of a moving bed reactor is that it is possible to completely fill the reactor volume with biomass (unlike some other designs to be discussed below). Therefore, for a given production capacity, the reactor volume can be reduced by a factor of at least 3,

which translates to a smaller capital cost. The main disadvantage is that the moving bed reactor is often prone to inhomogeneity in the heat transfer process, as the biomass is typically not stirred. This inhomogeneity is especially pronounced when an indirect heating method (e.g. heat conduction from the side or bottom walls) is involved.

1.3.2 Fluidized Bed

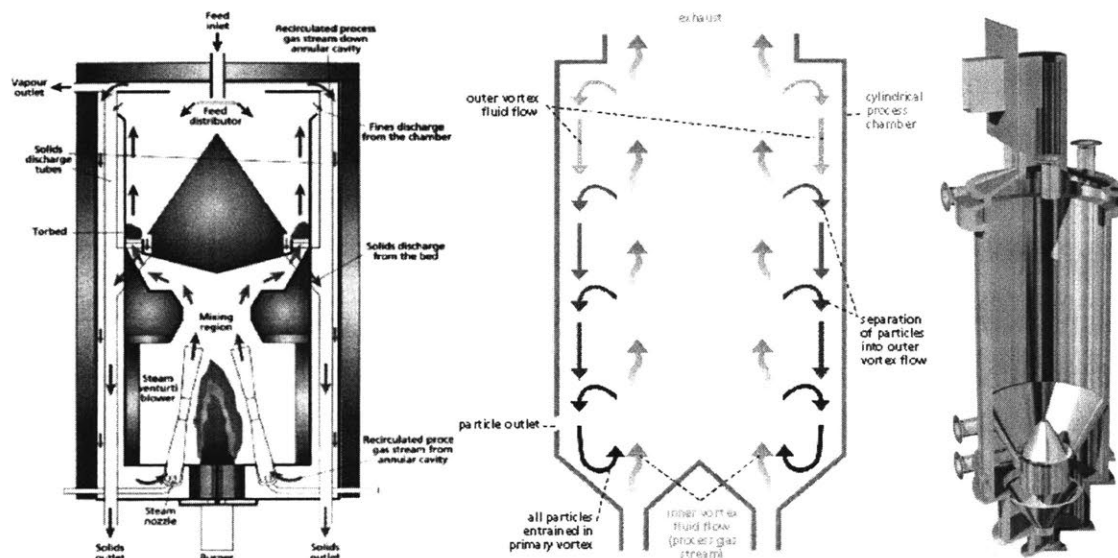


Figure 5 – Different view of Torbed, a modified fluidized bed torrefaction reactor design (Eseyin *et al.*, 2015; TorfTech, 2017).

Like the moving bed reactor design, there is also a packed bed of solid biomass of very small particle sizes, but the difference is that the packed bed is also filled with a heat carrier solid (e.g. sand) with a high specific heat capacity. However, in this case, hot gases are injected directly into the packed bed at a much higher velocity—often around $50\text{--}80\text{ m s}^{-1}$ (Koppejan *et al.*, 2012)—than in the moving bed design, such that the solid particles (both biomass and the carrier solid) will be carried by the gases and move about vigorously, almost like a fluid—hence the name fluidized bed (9). Because of the extensive gas-solid mixing, heat conduction from the hot gases to the solid particles is rapid and homogeneous. However, it becomes difficult to separate the biomass particles from the heat carrier solid particles. Laboratory-scale experiments have also reported a significant amount of losses in the torrefied fines (10). One example of a fluidized bed reactor is the Torbed design (by

Topell in the Netherlands) (Figure 5), in which due to the high rate of heat transfer, the average residence time of biomass inside the reactor is only about 80 seconds, therefore resulting in a small reactor size for a given production capacity (Koppejan *et al.*, 2012).

1.3.3 Rotary Drum

The reactor consists of a slightly downward inclining cylinder that rotates. Biomass enters into the higher end of the cylinder, and as the cylinder rotates, the biomass also tumbles (Figure 6). Due to this tumbling motion, the typical biomass particle alternates in its contact with the hotter reactor wall and the gas inside the reactor, resulting in a relatively good mixing and homogeneous heating. However, the volatiles released inside the rotary drum typically needs to be combusted elsewhere and then redirected back to the outside of the reactor, necessitating an indirect mode of heating through the wall of the rotary drum, and this therefore imposes some heat transfer limitations. Another major limitation is that, in order to support the solid tumbling motion, the maximum fill volume of the reactor is limited to about 30% (Barr *et al.* 1989; and Boateng and Barr, 1996). This means that for a given rated production capacity, the volume of the reactor will be at least 3 times bigger than, for example, a completely filled moving bed reactor, thereby resulting in a higher capital cost. On the other hand, one benefit of a rotary drum design is that it is a relatively proven technology with other applications such as biomass drying and pyrolysis (for example, Benanti *et al.*, 2011), as well as chemical looping (Zhao *et al.*, 2012; and Zhao *et al.*, 2014). Therefore, quite a few companies have developed torrefaction technologies based on the rotary drum design—using either existing rotary drum suppliers or developing custom-designed parts—including Atmosclear (Switzerland), Bio Energy Development North (Sweden), Earth Care Products (USA), Renergy (the Netherlands), and Torr-Coal (the Netherlands). Recent studies, such as one by Bates and Ghoniem (2014), have also considered the coupled phenomenon of torrefaction thermochemistry and heat transfer within thermally thick biomass particles, especially in the fluidized bed setting, as a function of input particle size and moisture content.

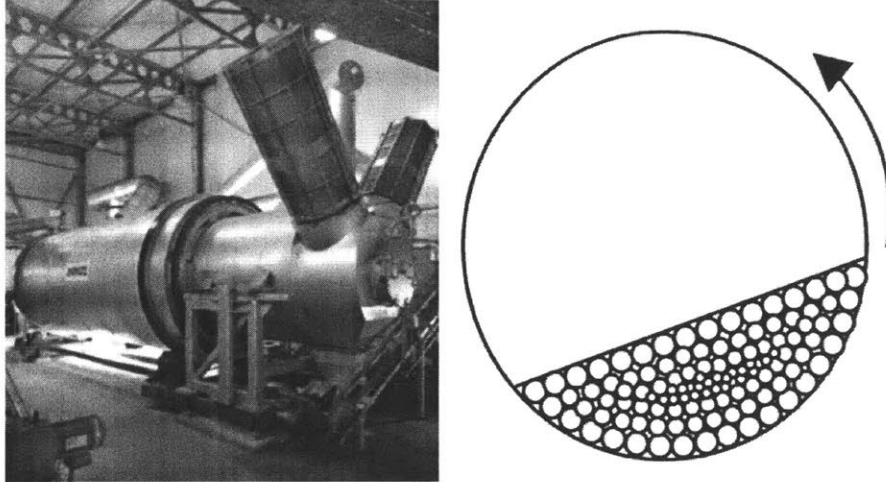


Figure 6 – Photograph (Thamer, 2013) and cross-sectional schematic visualization (Li *et al.*, 2002) of a rotary drum reactor.

1.3.4 Screw Conveyor

This is typically a horizontally or vertically oriented reactor, with one or more screw augers that rotate in order to continuously convey biomass through the system. The hot gases are often provided to the outside of the reactor or within the hollow shaft of a screw, and the heat is indirectly transferred to the biomass. The heat transfer, however, is somewhat better than the rotary drum, as in addition to the heated outer wall, the screw itself can also be heated, thereby providing a larger surface area for more effective heat exchange. Like the rotary drum, in order to work properly, the screw conveyor cannot be completely filled. Therefore, for a given biomass processing capacity, the reactor volume must be significantly larger. Like the rotary kiln, the screw conveyor is also a relatively proven technology, with various existing torrefaction designs such as BTG (the Netherlands) (Figure 7a), Foxcoal (the Netherlands), and Biolake (the Netherlands). Furthermore, the author and his colleagues, in an earlier iteration of the torrefaction reactor design, also built and experimented with a small-scale vertically oriented screw conveyor. The learning from this operation, as well as a subsequent proposed improved design involving a horizontal screw conveyor design, are documented in O'Brien (2016) (Figure 7b).

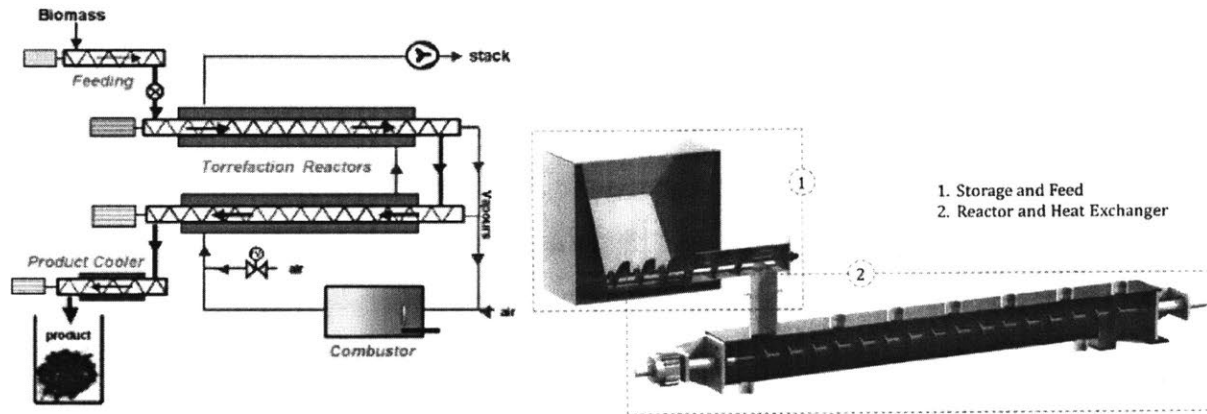


Figure 7 – Two examples of screw conveyor torrefaction reactor designs. (a) The BTG system (BTG, 2017), and (b) a system proposed by O'Brien (2016).

1.3.5 Microwave

The microwave reactor uses radiation energy to heat up the biomass, allowing it to reach torrefaction conditions. Several laboratory-scale experiments have been carried out (Wang *et al.*, 2012; and Satpathy *et al.*, 2014) (Figure 8a); however, limited work so far has been done to scale the design up (Shang, 2012). A few examples of commercial pilots include Rotawave (UK), CanBiocoal (UK), Airex (Canada), and Torrefaction Systems (USA). While heating from microwave can be rapid and uniform (Ren *et al.*, 2012), which can reduce the solid residence time and reduce the reactor size for a given solid throughput (Huang *et al.*, 2012), this is shown to cause drastic intra-particle temperature and torrefaction inhomogeneity in thermally thick biomass particles (Dhungana *et al.*, 2012) (Figure 8b). Another major disadvantage of using a microwave reactor is that the radiation energy required is most easily generated by electricity, and is otherwise very difficult to convert from either heat or the chemical energy contained in the volatile gases released from the torrefaction process. The complexity associated with generating microwave radiation also means that there is often a high capital cost and operational expenses associated with an at-scale design.

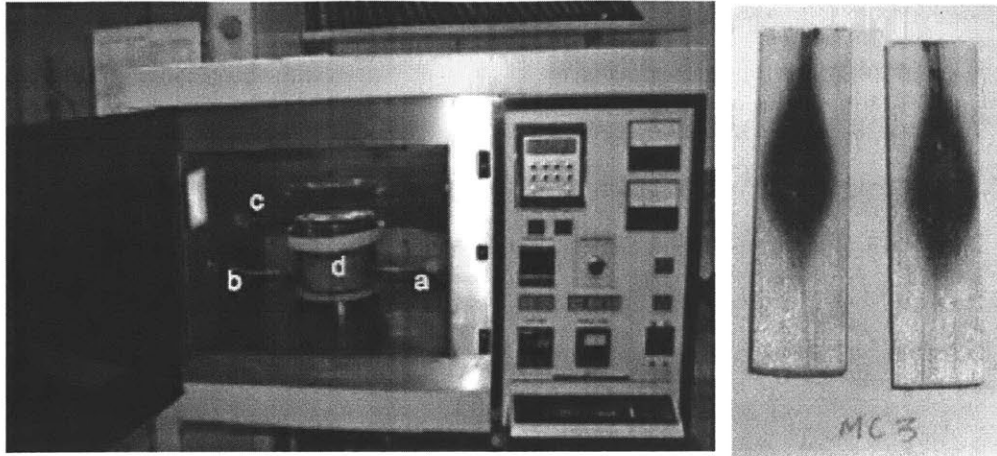


Figure 8 – Microwave torrefaction. (a) An example of a microwave torrefaction reactor set-up (Satpathy *et al.*, 2014). (b) Microwave torrefaction can result in severe intra-particle inhomogeneity for thermally thick particles (Dhungana *et al.*, 2012).

1.4 Need for a Small-Scale, Decentralized Torrefaction Reactor Design

As summarized in Section 1.3, there exists various torrefaction reactor designs, in different stages of commercialization. While the list is not exhaustive, it does encompass the most common types of biomass reactors. The advantages and disadvantages of the different designs are summarized in Table 5.

Table 5 – A summary of the advantages and disadvantages of the different torrefaction reactor designs.

Reactor type	Advantages	Disadvantages
Moving bed	High degree of filling	Heat transfer inhomogeneity
Fluidized bed	High heat transfer, uniform	Separation of biomass from solid heat carrier particles; fines losses
Rotary drum	Proven	Low degree of filling, heat transfer limitation
Screw conveyor	Low cost, proven	Low degree of filling, heat transfer limitation
Microwave	Homogeneous and rapid heating rate	High capital cost and sophistication; intra-particle inhomogeneity

Table 5 summarizes the representative commercial designs of the torrefaction reactor as well as their designed full-scale capacity, and we begin to see a potential problem. That is, most of these existing torrefaction reactors have been designed with a large-scale operation in mind (between 1-33 tons/hour) for the operating context of primarily Europe and North America, often in the vicinity of a large biomass producer such as a lumber mill or an agricultural processing mill. Can any of these existing technologies be feasibly scaled down and applied to the rural, decentralized context, in order to overcome the issues of biomass transportability and storability discussed earlier in Section 1.2?

In order to understand the scale requirements of decentralized biomass torrefaction, let us consider a potential use case in rural India. While there is a wide distribution in the sizes, the typical farm size in South Asia is around 1.3 hectares and decreasing (Lowder *et al.*, 2016). While the yield of agricultural residues per hectare is also highly dependent upon the soil conditions, rainfall, fertilizer applied, and so forth, we have assumed that a representative value is 2.25 tons/hectare (Laurin and Chamberland, 1981) upon harvest. This means that a representative farm in rural India may have about 3 tons of post-agricultural residues to be processed, and these farms are spread geographically amongst a large rural region. If, as discussed in Section 1.2, transporting the raw, unprocessed agricultural residues to a centralized processing facility is to be avoided due to the high logistical costs, then the only option for a decentralized biomass processing system is to be portable, moving from farm to farm and conducting the biomass upgrading on-site. Assuming that a rural community operates one or a few of these biomass torrefaction reactors, and that the different farms/regions—which harvest on slightly different dates—are also visited by the reactor on different days, then we conclude that a decentralized torrefaction reactor not only has to be small-scale, portable, low-cost, and low-maintenance in a resource-constrained setting, but it also must have a biomass processing capacity of around a few tons per day.

Table 6 – Design production capacities of different torrefaction technologies (Thrän *et al.*, 2016)

Torrefaction Technology	Design	Production Capacity
Torr-Coal (the Netherlands)	Rotary drum	4,500 kg h ⁻¹
BioEndev (Sweden)	Screw conveyor	2,100 kg h ⁻¹
Solvay (USA)	Screw conveyor	33,300 kg h ⁻¹
Topell (the Netherlands)	Fluidized bed	8,000 kg h ⁻¹
River Basin Energy (USA)	Fluidized bed	6,000 kg h ⁻¹
ECN (NL) / Andritz (Denmark)	Moving bed	1,000 kg h ⁻¹
Thermya/Areva (France)	Moving bed	2,500 kg h ⁻¹

As we examine Table 6, we see that most the current commercial torrefaction reactor designs have a scale mismatch by at least a factor of 10. However, can any of these existing reactor designs be scaled down and be applied in a decentralized manner? If so, what would be the resultant capital installation cost? Data for the capital installation costs of the existing commercial technologies, especially for a hypothetical scaled-down reactor design, are notoriously difficult to obtain. Instead, we sought the reactor techno-economic analysis literature for the approximate scaling law for capital expenditure associated with biomass reactors:

$$\text{Cost}_{\text{size 2}} = \text{Cost}_{\text{size 1}} \times \left(\frac{\text{Size 2}}{\text{Size 1}} \right)^{\text{scale factor}},$$

where the scale factor has been empirically determined to be around 0.6-0.8 (Jenkins, 1997; Flynn and Searcy, 2009; Bain and Overend, 2002; and Flynn *et al.*, 2003) in biomass reactor applications, including torrefaction (Svanberg *et al.*, 2013). We therefore adopted a scale factor of 0.7 for our approximation. We further assume that the size of the reactor is directly proportional to the biomass processing capacity of the reactor. Based on the capital cost estimates for torrefaction reactor systems given by Pirraglia *et al.* (2013) and existing commercial data, we concluded that a hypothetical scaled-down torrefaction reactor at 5 tons/day would cost between \$96,000 and \$320,000. How does this cost compare with the affordability in rural areas? To obtain an order-of-magnitude estimate of the latter, we first

assume that a rural village in India contains a population on the order of 1000 people (Singh *et al.*, 2006), with a median income of about US\$630/year (Times of India, 2016). This yields an approximated total GDP of about \$1 million/year in a typical Indian rural village. A reactor unit with a capital cost of around 15-50% of the entire village's annual GDP is clearly out of the price range. Why do the existing biomass torrefaction reactor designs cost so much?

Upon analyzing the common designs for existing torrefaction reactors (for example, Figure 4 through Figure 7), our hypothesis as follows: the current torrefaction reactors are capital-intensive because they incorporate many sophisticated features to boost their performance. Consider the case of harnessing energy from the volatile gases. Most of the existing technologies collect the volatile gases, cool them, scrub moisture from the mixture, inject with air in an external burner, and then recycle the hot post-combustion gas back to heat the torrefaction reaction at a specified temperature. As the volatile gases tend to be low in energy density and difficult to burn completely, this multi-step process upgrades the quality of the volatile gases and better controls the overall energy efficiency. While these cleaning/upgrading components do not add significantly to the cost of a large-scale torrefaction reactor while conferring energy benefits as described above, they can pose as a major barrier for scaling down existing torrefaction reactor designs. In a scaled-down torrefaction reactor design for decentralized deployment, is it possible to sacrifice some of the performance characteristics of a large-scale torrefaction process in order to exchange for a more simplified design with a more affordable capital installation cost?

The natural follow-up question becomes as follows: What is an affordable capital installation cost? To get an order-of-magnitude estimate of this figure, we use two distinct approaches. First, we note that typically, a village-based production utilizing biomass torrefaction may also require other peripheral hardware equipment for the post-processing of this fuel locally—such as grinding and pelleting—into suitable fuel. Based on the author's personal experience managing a solid fuel company in Kenya, such peripheral hardware typically costs several thousand U.S. dollars, such that the village-based conversion unit may cost about \$10,000-20,000 to set up. Given this price range, an

affordable torrefaction unit should also fit comfortably within this budget range. Second, we note that a 5 tons/day processing of biomass would yield between 1-3 tons/day of torrefied fuel, depending on the moisture content as well as the torrefaction severity. Based on the author's experience in Kenya and India, comparable solid fuels in the market typically fetch \$200-600/ton in price. Assuming a medium production of 2 tons/day of torrefied fuel, and assuming a medium price of \$400/ton, this implies that a torrefaction reactor can generate about \$800/day of revenue for the operator. Assuming that the local village has two harvest seasons, each lasting about 60 days, and that the torrefaction reactor is fully operational during these seasons. This implies that in one year of reactor operation, the revenue is about \$100,000. Crudely assuming a 20% gross margin, we see that the gross profit is around \$20,000/year. In order for the torrefaction conversion to be an interesting business proposition to a local entrepreneur or investor, the return on investment of 1-2 years is reasonable. This implies that the capital expenditure of the entire torrefaction system cannot be more than about \$10,000-30,000. Therefore, we see that the two distinct methods of capital expenditure estimation yields a similar upper limit on the capital cost of a decentralized torrefaction reactor system to be on the order of \$10,000. This represents roughly a one-tenth reduction in the capital expenditure of the sized-down versions of the current commercial torrefaction reactors.

While in this thesis, it is premature to put an exact final system cost just based on the work of a laboratory-scale prototype, the number above does give us a motivating design constraint. Therefore, in this thesis, can we come up with a significant design simplification and demonstrate its performance functionality—and therefore potential subsequent capital expenditure saving—in scaling such a torrefaction reactor designed for decentralized deployment?

This question becomes the central theme for the remainder of this thesis, and as we will demonstrate, an affirmative answer will be the major contribution of this thesis to the current state of the art. In Chapter 2, we consider torrefaction in a low-oxygen environment, and describe a scalable laboratory-scale moving bed reactor design that is more simplified in comparison with the reactor designs we have seen above. In 0, we

validate the operation and key performance metrics of this reactor under various torrefaction reaction conditions and types of input biomass feedstock. In 0, we utilize the performance maps obtained in 0 to devise a simplified and design-oriented approach to select the torrefaction reactor condition based on the index of torrefaction, and show how to operate the reactor in order to satisfy different end user requirements on energy density, fixed carbon content, stove temperature, grindability, and even combustion emissions profile. This also serves to verify that the various biomass improvements associated with the classical inert torrefaction still exists in our low-oxygen torrefaction reactor. In 0, we consider various energy loss mechanisms in the current laboratory-scale reactor, and arrive at a science-based approach to improve the design of a scaled-up version through optimal insulation, air pre-heating, and secondary oxidation of uncombusted volatiles in the reactor exhaust stream. In Chapter 6, we consider what it takes to inject a specified flow rate of air into the reactor in order maintain a low-oxygen environment by characterizing the hydrodynamic characteristics of the biomass moving bed, and using a combination of the natural stack effect and, in some cases, forced air. Finally, in 6.1, we consider what it takes to start the reactor from a cold state, to stop the reactor, and to transit the reactor from one operating condition to another. Therefore, the collection of studies in this thesis will serve as a quantitative basis for scaling up a low-cost, portable, and small-scale torrefaction reactor unit suitable for decentralized torrefaction in rural areas.

Chapter 2 A Low-Oxygen Torrefaction Reactor Design

Most existing torrefaction reactor designs are complex and capital-intensive because they often impose strictly inert conditions that guarantee a high reactor performance in a large-scale biomass throughput. In contrast, our interest in a decentralized torrefaction reactor lies in simplifying the reactor, reducing its complexity and costs such that it can be feasibly deployed in a rural setting. In this section, we explore the concept of a low-oxygen torrefaction environment, and describe how we can take advantage of this concept to significantly simplify the reactor design via a moving bed reactor. We then developed a coarse-grained model description of the moving bed based on length scales and heat transfer approximations, and demonstrated that the primary heat transfer mechanism in the moving bed is through the gaseous phase alone. Then we built upon this to implement a fine-grained model description of the biomass moving bed in order to validate our design concept and to derive base case operating conditions. We demonstrated that the moving bed reactor designed using reasonable length scales and operating conditions can indeed satisfy the requirements of torrefaction. Finally, we use the learning above to derive and describe a more detailed design that will be implemented and validated subsequently.

2.1 Torrefaction in a Low-Oxygen Environment

In the previous Chapter, we hypothesized that one main reason why current torrefaction reactor designs are unsuitable for deployment in a rural, decentralized setting is that they are designed for high performance with many sophisticated parts. The main question that we pose is whether we can reduce the capital installation cost by simplifying the reactor design.

Svanberg *et al.* (2013), in characterizing the capital cost of current commercial-scale torrefaction reactors, noted that almost all current torrefaction reactor designs enforce a near-inert condition inside the biomass reactor, and this is one main reason why the capital cost has remained high. This study further commented that if this inert requirement can be

lifted, then both the capital cost and operational cost associated with the reactor operation can be reduced. Indeed, the classical wisdom for torrefaction is that the absence of oxygen (for example, by immersing the system in unreactive gases such as nitrogen or carbon dioxide) is desired because the presence of oxygen under torrefaction conditions can rapidly oxidize the feedstock, decreasing the mass and energy yield. In order to burn the volatiles released from the torrefaction process and harness that energy, oxygen-containing air is carefully injected into a separate external combustor, such that the biomass itself never sees the oxidizing environment.

In the search of a simplified torrefaction reactor design for decentralized deployment, this low-oxygen torrefaction appears to be an attractive option, because it can simplify the reactor design in a few ways. With the injection of a limited amount of oxygen directly into the biomass reactor, some (if not all) of the volatile gases released from the biomass torrefaction process can be combusted *in situ*, releasing heat directly to the biomass bed, which then sustains the torrefaction reaction. This means that it is no longer necessary to design an external combustor to burn the volatile gases separately. This also means that the volatile gases can be directly generated and burned in the torrefaction zone without needing to be first co-mingled and diluted by the steam generated from the drying process (for example, in the Torspyd™ column). This then also makes the volatile gas cleaning/scrubbing step redundant. But does the torrefaction environment (200-320°C) provide for sufficiently high temperature to actually oxidize the volatiles? To answer this question, we researched on the ignition temperature of different types of biomass (Table 7). Ignition typically occurs when the volatiles released by the biomass start oxidizing. As can be seen, the ignition temperatures of these types of biomass lie within the realm of torrefaction temperature. This is good news for us, as it means that assuming that we can bring the biomass to the torrefaction condition, then the presence of oxygen can cause the volatiles to spontaneously ignite, and the heat released from this oxidation can then heat the incoming biomass to the torrefaction condition, resulting in a self-sustaining, autothermal process. The other data point to note is that the ignition temperature of charcoal is higher, at 350°C. This is also good news for us, as one potential concern for conducting torrefaction in the presence of oxygen is that oxygen, instead of attacking the

volatile gases, can directly attack the fixed carbon in the torrefied biomass, resulting in decreased mass and energy yield in the product. The fact that charcoal only ignites at a higher temperature suggests that the kinetics of the undesirable char oxidation reaction proceeds more slowly compared to the kinetics of the volatile oxidation reaction. Therefore, our hypothesis is that, as long as we keep to the torrefaction condition (which is less than 350°C), we should not observe excessive char oxidation.

Table 7 – Ignition temperature for different types of biomass (Jones *et al.*, 2015).

Feedstock	Onset of combustion*
Olive cake	183°C
Mesquite	233°C
Sunflower husk	225°C
Miscanthus	223°C
Pine	236°C
Red berry juniper	230°C
Charcoal	350°C

*Defined as the temperature where the solid mass loss rate exceeds 1% min⁻¹ on thermogravimetric measurement under oxidative conditions.

While low-oxygen torrefaction may sound attractive in principle, is there any experimental evidence that it can work? Does it have any untoward effects on the performance of the reactor, and if so, how much? It is only in recent years, that laboratory-scale studies have begun studying torrefaction in a low-oxygen environment. One of the first intentional studies was carried out by Wang *et al.* (2013), who set up a batch fluidized bed reactor to compare the torrefied sawdust under (a) inert nitrogen sweep gas, and (b) 3-6% oxygen. The study found that the low-oxygen environment produced torrefied outputs of similar density, higher heating value, and energy yield. While there is a slight decrease in the performance of moisture absorption (hydrophobicity) and hardness under low-oxygen environment compared to the inert environment, this decrease, according to the study, was

negligible. Therefore, the study concluded that torrefaction under a low-oxygen environment is also feasible.

A follow-up study by Chen *et al.* (2013) characterized the torrefaction performance (e.g. solid and energy yield) when the biomass is heated by nitrogen or air at different superficial velocities. By using air (which is 20% oxygen), this study is even more aggressive in imposing an oxidative environment to the torrefaction process. The study noted that while in inert nitrogen, varying the superficial velocity of the carrier gas does not affect the yield of the torrefied solid output, in contrast, in the case of a fully oxidative environment, not surprisingly, increasing the superficial velocity decreases the yield, but only up to a certain air velocity threshold, beyond which the solid yield stays constant. The study therefore concludes that while by sweeping the biomass with nitrogen, the devolatilization is limited by heat and mass transfer, in contrast, by sweeping the biomass with heated air of increasing flow rate, initially, the additional heat from the oxidation at the surface of the biomass causes increased internal heat and mass transfer (Figure 9), resulting in a lower mass yield. Then, when the air sweep velocity is large enough, the surface oxidation no longer intensifies, but rather the devolatilization process is once again limited by internal heat and mass transfer. The study therefore concludes that under the fully oxidative torrefaction environment, both the solid yield and the energy yield of the torrefied output decrease.

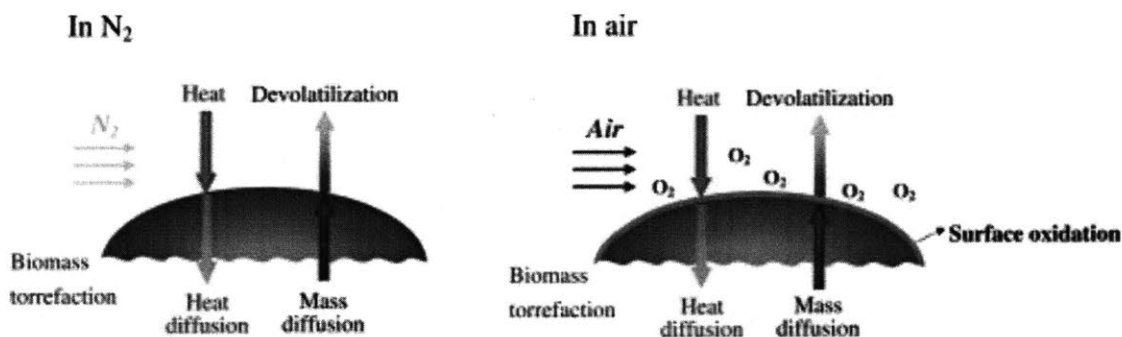


Figure 9 – Comparison between torrefaction under an inert (nitrogen) environment and under a fully oxidative (air) environment (Chen *et al.*, 2013).

Therefore, what we know is that, while torrefaction under low-oxygen environment incurs negligible penalty on the performance metrics of the torrefied output, when the environment becomes increasingly oxidative, there is also an increasingly severe penalty. While a sensible low-oxygen torrefaction reactor design has no reason to go to the fully oxidative environment, it does need sufficient oxygen to oxidize the volatile gases and provide sufficient heat to sustain the reaction autothermally. Thus, our expected reactor performance is likely in-between the two extremes described above. While the penalty in the mass or energy yield of torrefied product under oxidative environment is not a desirable outcome, as long as we characterize it carefully and avoid unnecessary additional losses, it may still be a worthwhile trade-off in consideration of the economic and environmental benefits of having a low-cost and simplified torrefaction reactor design that can actually be implemented in a decentralized manner in rural areas where current large-scale, more sophisticated torrefaction reactors are unable to do so.

2.2 Proposed Reactor Design Concept

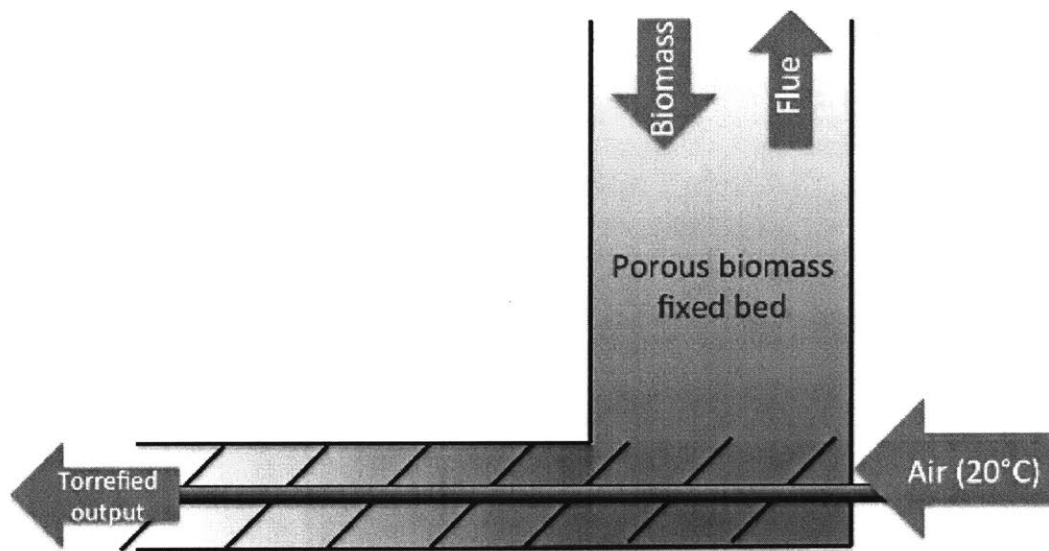


Figure 10 – Schematic of a low-oxygen moving bed torrefaction reactor design.

In incorporating the low-oxygen torrefaction into a scalable reactor design, we first revisit Section 1.3 in selecting a suitable reactor design. In consideration of the high level of design complexity, we excluded microwave and fluidized bed reactors from consideration. In

consideration of the low capital cost requirement, we also ruled out the screw conveyor and rotary drum designs, both of which have a low filling ratio and thus a large reactor volume requirement for a given biomass processing capacity. This leaves us with a moving bed design. A schematic of the design is shown in Figure 10.

In this design, biomass is continuously fed from the top into a porous biomass moving bed. At the bottom, a turning auger continuously removes the biomass from the moving bed, allowing the incoming biomass column to migrate downwards by gravity. Air (at room temperature) is introduced near the bottom of the reactor, resulting in a low-oxygen environment that supports torrefaction at the bottom of the moving bed. As the reacting air, volatiles, and flue gas mixture travels upwards through the moving bed in a counter-flow manner, it cools and is exhausted from the top of the reactor. Therefore, while the biomass is traveling downwards, it is also being heated until it reaches torrefaction temperature at the bottom of the moving bed. To the side of the moving bed, there is an extension with a length of the auger conveying biomass away from the moving bed. This length serves two functions. Firstly, as the biomass at the bottom of the moving bed is hot, it needs to be cooled before emerging from the reactor, or else there may be a spontaneous combustion. Therefore, the primary function of the auger extension is to cool the hot, torrefied biomass. Therefore, this section is also referred to as the “char-cooling segment”. Secondly, the auger flights and the inner diameter of the char-cooling segment form quite a tight fit, such that it prevents the injected air, volatiles, and post-combustion flue gas mixture from escaping sideways with the cooling char, but rather directs almost all of it upwards through the moving bed. In order for this to happen, the pressure drop for the gas across the char-cooling segment should be higher than that for the gas across the moving bed. This means that for the preliminary design, the char-cooling segment should be at least longer than the height of the moving bed.

2.3 Coarse-Grained Model

Before we finalize a design based on the concept described in Figure 10, it is prudent to conduct an initial sizing of the reactor in order to gain a coarse-grained understanding of the behaviors of the reactor.

2.3.1 Modeling Description

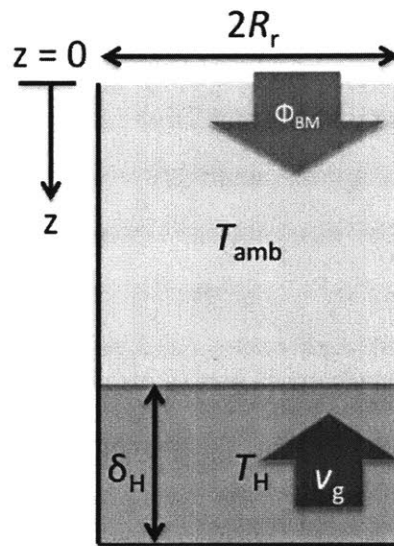


Figure 11 – Lump-sum zonal representation of the biomass bed reactor. The model consists of a “hot zone” of torrefaction homogeneous at temperature T_H and axial thickness δ_H , as well as a “cold zone” at ambient temperature T_{amb} . Biomass flows down with a mass flux of Φ_{BM} (gray arrow); hot gases move up with a superficial velocity of v_g (red arrow). The z axis (axial direction) is also defined from the top.

We first develop a very simplified lump-sum model description of the moving bed reactor as illustrated in Figure 11. We consider only axial heat transfer, and ignore any radial variations (assume perfect insulation surrounding the reactor side walls). We further simplify the case by treating the torrefaction as two zones only: a lower “hot zone” where torrefaction takes place, homogeneously at an elevated temperature T_H , as well as an upper “cold zone” at ambient temperature T_{amb} . We ask no questions regarding how T_H is achieved: we assume that there exists an oxidative environment where this temperature can be achieved and sustained via the mechanism described in Section 2.2. The solid biomass, of mass flow rate \dot{m}_{BM} , flows downwards the reactor of radius R_r with an axial

mass flux of $\Phi_{\text{BM}} = \dot{m}_{\text{BM}}/\pi R_r^2 [\text{kg s}^{-1} \text{m}^{-2}]$. On the other hand, gases flow upwards with a superficial velocity v_g . Here, in a boring-looking two-zone model of the reactor, the only parameter of interest is the axial thickness δ_{H} of the hot zone. This parameter is of interest because given a specific desired solid residence time τ_{res} in the hot zone, we need to adjust the biomass downward axial velocity v_{BM} such that the following is satisfied:

$$v_{\text{BM}} \sim \frac{\delta_{\text{H}}}{\tau_{\text{res}}}.$$

If we assume that the biomass moving bed has an effective axial thermal conductivity coefficient of k_r , and if we ignore any thermochemistry for now, then we can write the steady-state governing axial (z) heat equation as:

$$\frac{d}{dz} (\Phi_{\text{BM}} c_{\text{p},s} T) = \frac{d}{dz} \left(k_r \frac{dT}{dz} \right).$$

By doing a dimensional analysis, we can relate the quantity to δ_{H} various biomass and reactor operating parameters as:

$$\delta_{\text{H}} \sim \frac{k_r}{c_{\text{p},\text{BM}} \Phi_{\text{BM}}}.$$

The question now is: How do we describe the thermal characteristics of the biomass moving bed in terms of k_r ? To do so, we first note that the moving bed itself actually consists of two inhomogeneous phases: a solid phase (biomass) and a gas phase (a mixture of air, volatile gases, and post-combustion flue gases). The two phases conduct heat differently in the axial direction, and the two phases can also exchange heat with each other. We will consider each phase separately.

Solid bulk thermal conductivity. The actual heat transfer coefficient k_{rs} in the solid phase is a complex interplay of (i) heat conduction within a single biomass particle, (ii) biomass particle-to-particle contact conduction, (iii) particle-to-particle radiation via the porous void, and so forth. In simplifying these effects, we searched for the closest possible lump-sum description in the biomass gasification literature, and utilized the empirical correlations given by Hobbs (1992). The results are summarized in Table 8.

Table 8 – Correlations for bulk homogeneous phase conduction characteristics in a biomass moving bed (Hobbs, 1992).

Characteristics	Source	Correlation
Gas bulk conductivity	Froment & Bischoff, 1979	$k_{rg} = k_g \left(\epsilon \left(1 + \frac{d_p h_{rv}}{k_g} \right) + \frac{0.14(\text{Pr})(\text{Re})}{1 + 46(d_p/D_{\text{react}})^2} \right)$
Solid bulk conductivity	Froment & Bischoff, 1979	$k_{rs} = k_g(1 - \epsilon) / \left((1/\phi + h_{rs}d_p/k_s)^{-1} + 2/(3\kappa) \right)$
Gas conductivity	Di Blasi & Branca, 2013	$k_g = 4.8 \times 10^{-4} T_g^{0.716}$
Solid conductivity	Di Blasi & Branca, 2013	$k_s = 0.0013 + 0.005(T_s/1000) + 0.63(T_s/1000)^2$
Void-to-void radiation coefficient	Froment & Bischoff, 1979	$h_{rv} = 2.27 \times 10^{-7} T_g^3 / \left(1 + \frac{\epsilon}{2(1-\epsilon)} \frac{1-\epsilon'}{\epsilon'} \right)$
Solid radiation coefficient	Froment & Bischoff, 1979	$h_{rs} = 2.27 \times 10^{-7} T_s^3 \epsilon' / (2 - \epsilon')$
Packing parameter	Kunii & Smith, 1960	$\phi = \phi_2, \epsilon < 0.260$ $= \phi_1, \epsilon > 0.476$ $= \phi_2 + (\phi_1 - \phi_2) \frac{\epsilon - 0.260}{0.476 - 0.260}, 0.260 \leq \epsilon \leq 0.476$
Loose packing parameter	Kunii & Smith, 1960	$\phi_1 = \frac{0.3525((\kappa-1)/\kappa)^2}{\ln(\kappa-0.5431(\kappa-1))-0.4569(\kappa-1)/\kappa} - \frac{2}{3\kappa}$
Dense packing parameter	Kunii & Smith, 1960	$\phi_2 = \frac{0.07217((\kappa-1)/\kappa)^2}{\ln(\kappa-0.9250(\kappa-1))-0.07498(\kappa-1)/\kappa} - \frac{2}{3\kappa}$
Conductivity ratio		$\kappa = k_s/k_g$

Gas bulk thermal conductivity. Similar to the solid effective bulk thermal conductivity k_{rs} , the gas effective bulk thermal conductivity k_{rg} describes the homogeneous heat transfer within the gaseous phase inside the biomass moving bed, via a combination of conduction, convection, and radiation. Once again, we utilized the gasifier correlations from Hobbs (1992), listed in Table 8.

Solid-gas heat transfer. In the biomass moving bed, the solid and the surrounding gas can exist at different temperatures (T_s and T_g , respectively), and there may be heat transfer between the two phases of the form $Q_{sg} = h_{sg}A_{sg}(T_s - T_g)$, where h_{sg} is the solid-gas heat transfer coefficient with the units of $W m^{-2} K^{-1}$, and A_{sg} is the total area of exposure between the solid and the gas phases. Considerable characterization of this heat transfer coefficient has been carried out in biomass moving bed and fluidized beds by authors such as Chilton and Colburn (1934), Gamson *et al.* (1943), and De Acetis (1960). Ultimately, we used the amended correlation proposed by Gupta and Thodos (1963), which has been experimentally confirmed with beds of spheres, and has been widely used in other biomass moving bed gasifier models (45; Di Blasi, 2004; Radulovic *et al.*, 1995):

$$h_{sg} = \frac{2.06c_{p,g}\rho_g v_g}{\varepsilon} (Re)^{-0.575} (Pr)^{-2/3},$$

where $c_{p,g}$, ρ_g , and v_g are the specific heat capacity, mass density, and superficial axial velocity of the gas phase, respectively. In the equation above, Re and Pr are the Reynolds and Prandtl numbers associated with the superficial flow of the gaseous phase, respectively. Once knowing h_{sg} , the volumetric heat flow rate q_{sg} (in units of $W m^{-3}$) from the solid to the gas phase is given as follows:

$$q_{sg} = \frac{6(1 - \varepsilon)\gamma}{d_p} h_{sg}(T_s - T_g),$$

where γ is an adjustable factor proposed by Hobbs *et al.* (1992) to account for unsteady heat transfer effects (Hobbs *et al.*, 1990; Hobbs *et al.*, 1993), and was generalized by Dzhaphyev *et al.* (1986), Lowry (1963), Cho and Joseph (1981), Di Blasi (2000), and Ghani *et al.* (1996) to account for other factors—such as chemical reactivity within the bed—in order to better fit the experimental data. The magnitude of this adjustable factor ranges from 0.02 to 1 in these previous studies. Because there have been no studies so far in the low-temperature torrefaction regime, we do not know *a priori* the magnitude of γ . For now, we assume that it is 0.2.

2.3.2 Analysis of Heat Transfer Pathways

Having described the various types of heat transfer mechanisms above, we are now poised to answer the following questions: Which of these is the rate-limiting step in the heat transfer process? Which steps of heat transfer occur so rapidly that we can approximate them as almost instantaneous? In order to answer this question, we employ the analogous electrical circuit analysis (Figure 12a). By analogy, if we think of the temperature difference between the bottom and top of the moving bed $T_H - T_{amb}$ as the potential difference (voltage), the volumetric heat transfer rate q [$W\ m^{-3}$] as the electric current, then the resistivity term R associated with each heat transfer mechanism in this system can be written as labeled in Figure 12a (in units of $m^3\ K\ W^{-1}$). The smaller this resistivity value is, the more rapidly the heat flow occurs given a temperature difference (i.e. less resistance in that pathway). The “circuit” splits into two parallel “wires”, one representing the solid-phase bulk heat transfer and the other representing the gas-phase bulk heat transfer. Linking the solid and gas phases is the gas-to-solid heat transfer.

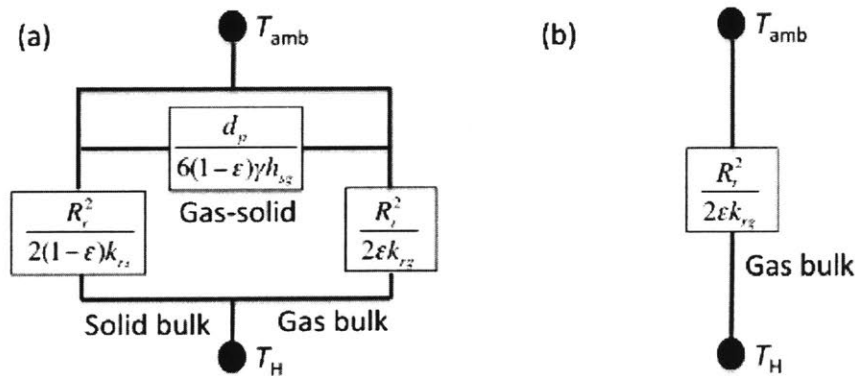


Figure 12 – Circuit representation for heat flow through the biomass moving bed. (a) Full representation, and (b) a simplified representation showing only the rate-limiting step in the bulk gaseous phase.

Table 9 shows the typical ranges of values of the different heat transfer resistivities with the regime of our interest. We first note that the gas-to-solid heat transfer resistivity is very small compared to all the other terms. In fact, the resistivity against heat flow between the solid and gas phases is so small that we can approximate it as roughly zero (i.e. “short

circuit”). This means that the solid and the gas phases assume very similar temperature (“potential”) throughout the moving bed, as heat can exchange freely between the two phases. Next, we compare the solid and gas bulk heat transfer resistivities. We found that the ratio of the solid bulk heat transfer resistivity to the gas bulk heat transfer resistivity is always less than 0.1, when the characteristic particle diameter d_p is larger than ~ 1 cm. When this condition is satisfied, it implies that most of the heat flow within the bulk of the reactor occurs through the gas phase, with very little going into the solid phase. Therefore, we can simplify the electrical circuit diagram further by assuming that the solid bulk heat transfer path is an “open circuit” with infinite resistivity. With these simplifications in mind, our heat flow circuit simplifies to that in Figure 12b. In this case, we see that the bulk thermal conductivity coefficient k_r that we wanted to find earlier is nothing more than the effective gas bulk heat transfer coefficient k_{rg} , which typically has a value of 1-10 W m⁻¹ K⁻¹ in our regime of interest.

Table 9 - Typical ranges of values of the different heat transfer resistivities across the biomass moving bed.

Type of resistivity	Typical value range
Solid bulk heat transfer	1-100 m ³ K W ⁻¹
Gas bulk heat transfer	0.01-10 m ³ K W ⁻¹
Gas-to-solid heat transfer	0.0005-0.008 m ³ K W ⁻¹

2.3.3 Implications for Reactor Sizing

What does this mean in terms of the thickness of the “hot zone” as well as the mass flux / solid velocity through the moving bed? Let us, for the sake of reality, assume that the full-scale reactor, rated to process about 5 tons/day of biomass, has a diameter no larger than 2.5 m. This implies that the solid mass flux through the system is in the range of 0.01 kg m⁻² s⁻¹, or a downward axial velocity of around 2 cm min⁻¹. This yields a hot zone thickness δ_H on the order of 20 cm, and a solid residence time τ_{res} on the order of 10 min. Therefore, we can see that it is possible to design a moving bed torrefaction reactor that can realistically

satisfy the typical torrefaction requirements. This also means that for a laboratory-scale reactor design whose diameter does not exceed 10 cm, this represents a factor of 1/625 from the full-scale reactor, with a typical biomass processing capacity of around 1 kg h⁻¹.

2.4 Fine-Grained Model

In the prior section, we used coarse-grained scaling arguments to conduct an initial sizing of the moving bed biomass torrefaction reactor concept, and to verify that it meets the torrefaction requirements. In this section, building on this scaling argument, we propose a fine-grained steady-state axial model of the moving bed in an effort to understand in greater detail the interplay between thermochemistry and heat transfer before embarking on a specific reactor design. The main design parameters to this fine-grained model are: solid mass flux Φ_{BM} (which takes into account the reactor radius), and the reactor height H_r . Our goal here is to fine-tune the reactor sizing parameters such that the design goals related to target treatment temperature, duration, and additional constraints can be satisfied. For these reasons, we treat the target treatment temperature and solid residence time in this study as two output parameters, which depend on the reactor sizing input parameters.

The main input parameters to model include: solid mass flux (on a dry basis) Φ_{BM} , height of the reactor H_r , bulk solid density of the moving bed ρ_s , bulk void fraction in the moving bed ε , incoming biomass moisture content expressed as a mass fraction of the dry biomass Y_{MT} , and the characteristic biomass particle size d_p . We have assumed, in our base case, that $Y_{MT} = 0.11$, $\varepsilon = 0.6$, and $\rho_s = 30 \text{ kg m}^{-3}$.

2.4.1 Kinetics and Thermochemistry Submodel

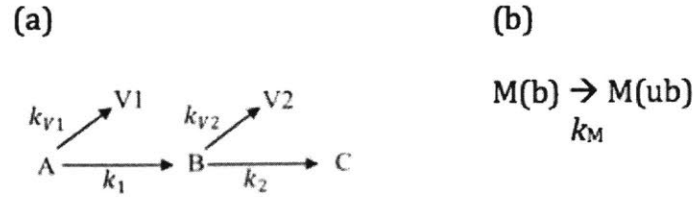
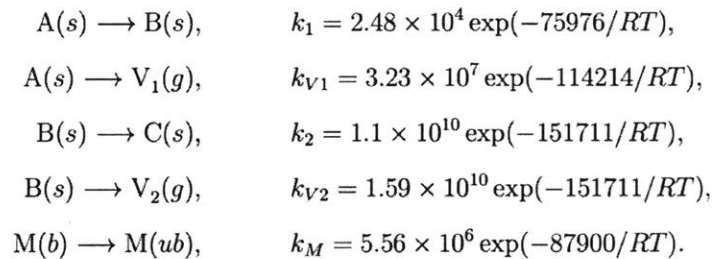


Figure 13 - A simplified kinetics model for torrefaction and drying. (a) A kinetic description of the solid devolatilization kinetics during biomass torrefaction, as proposed by Bates and Ghoniem (2012). (b) A one-step simplified model describing drying kinetics in biomass, as adopted from Peters and Bruch (2003).

In order to describe the solid devolatilization process, we utilized the kinetic model proposed by Bates and Ghoniem (2012), developed for the case of willow (Figure 13a). In this model, the solid-phase devolatilization following a two-step process. First, the raw biomass (A) can either decompose into volatile gas (V1) or become solid intermediate (B). Then, the solid intermediate (B) becomes either volatile gas (V2) or char (C). Each of these reactions are assumed to be first-order Arrhenius in nature. In addition, for the drying of biomass, we utilized a simplified model proposed by Peters and Bruch (2003), where water bound to the biomass (M(b)) in the solid phase becomes unbound (M(ub)) in the gas phase as a first-order Arrhenius-type process (Figure 13b). This gives us the following rate equations:



In a subsequent paper, Bates and Ghoniem (2013) derived the enthalpy H_i associated with each i th reactant or product at temperature T . Therefore, the overall volumetric enthalpy change due to the chemical reaction is given as $\sum_i r_i H_i$, where r_i is the volumetric creation rate of the i th species [$\text{kg m}^{-3} \text{s}^{-1}$].

2.4.2 Governing Equations

We have the following variables to solve: the gas/solid axial temperature profile $T(z)$ within the biomass moving bed, the mass flux Φ_i of each of the 3 gas species (volatile group 1, volatile group 2, and unbound moisture) and of each of the 4 solid species (raw biomass, solid intermediate, char, and bound moisture), as well as the elemental analysis of the solid phase (Y_j) consisting of 5 components—carbon, hydrogen, oxygen, nitrogen, and ash. This gives us 13 unknowns. The 13 steady-state equations are correspondingly listed as follows:

- Seven mass conservation equations of the solid and gas phases in the moving bed (for each of the 4 solid species and 3 gas species):

$$\frac{d\Phi_i}{dz} = r_i,$$

where Φ_i is the mass flux through the reactor cross-section of the i th species, and r_i is the volumetric creation rate [$\text{kg s}^{-1} \text{m}^{-3}$] of the i th species and is calculated in the coupled chemical kinetics/thermochemistry submodel. Note that, as done in other similar studies on biomass moving bed (2, 3, 6), we have assumed that diffusion of the gas species is negligible compared to convection. It is understood that the mass flux of the dry solid through the reactor is $\Phi_s = \Phi_A + \Phi_B + \Phi_C$, while the mass flux of the gas, $\Phi_g = \Phi_{V1} + \Phi_{V2} + \Phi_{M(\text{ub})}$.

- Five mass balance equations for the j th elemental analysis component (carbon, hydrogen, oxygen, nitrogen, and ash) in the solid phase:

$$\frac{d}{dz}(\Phi_s Y_j) = \sum_i r_i Y_{ij},$$

where Y_j is the mass fraction of the j th elemental component, and Y_{ij} is the mass fraction of the j th elemental component in the i th species.

- One energy balance equation:

$$\sum_i \frac{d}{dz}(\Phi_i c_{p,i} T) = \frac{d}{dz} \left(k_r \frac{dT}{dz} \right) - \sum_i r_i H_i$$

where the first term on the right-hand side describes the effective heat conduction through the moving bed in the axial direction, and the second term describes the heat of reaction (computed in the chemical kinetics/thermochemistry submodel). The summation terms are summed over all 7 solid and gas species in the biomass fixed bed.

The initial and boundary conditions are set as follows:

$$\begin{aligned}\Phi_A(z = 0) &= \Phi_{BM} \\ \Phi_{M(b)}(z = 0) &= \frac{Y_{MT} \Phi_{BM}}{1 - Y_{MT}} \\ \Phi_i(z = 0) &= 0, i \notin \{A, M(b)\} \\ Y_j(z = 0) &= \text{Ult}(j) \\ T(z = 0) &= T_{amb} \\ T(z = H_r) &= T_H,\end{aligned}$$

where $\text{Ult}(j)$ is the elemental mass fraction of the j th element through the elemental (ultimate) analysis of the original raw biomass.

2.4.3 Particle Shrinkage

As the biomass is thermochemically treated, it is expected that the shrinkage of the biomass particles will affect the bulk bed porosity and therefore the heat transfer characteristics. Indeed, previous studies have accounted for this shrinkage in the gasification/combustion regime (Goh *et al.*, 2001; and Cooper and Hallett, 2000), or in the pyrolysis regime (Bellais *et al.*, 2003; Villiermaux *et al.*, 1986; and Larfeldt *et al.*, 2000). However, it is questionable how well these models apply to the low-temperature torrefaction regime—and as far as we are aware, no studies so far have proposed a shrinkage model in the torrefaction regime of interest, and all that is available right now are sparse experimental data. For example, Bergman (2005) reported little torrefaction-induced biomass shrinkage. Likewise, Basu *et al.* (2013) and Kennedy (1965) experimentally measured the shrinkage to be around 3-9%, in comparison with 22-40% in the pyrolysis regime (Davidsson and Pettersson, 2002).

For the sake of simplicity, we have modeled the solid-phase shrinkage in the same manner as described in the works of Anca-Couce *et al.* (2012, 2013) and others (Bellais *et al.*, 2003; and Davidsson and Pettersson, 2002) by defining some shrinkage factor f_s which modifies the characteristic particle size d_p with respect to its initial size d_p^0 , up to a maximum possible shrinkage as characterized in Basu *et al.* (2013):

$$d_p = f_s d_p^0,$$

$$f_s = 1 - (0.00395T - 2.62 \times 10^{-6}T^2 - 1)(1 - \Phi_A/\Phi_A^0)^2.$$

2.4.4 Implementation and Validation

The mathematical model was implemented in MATLAB using a standard stiff solver (ode15s) with the shooting method. As there have been no experimental studies done with our design so far, in order to validate the model, we compared the obtained results with a limiting case of bone-dry, non-reactive case where an analytical solution can be derived. The model was found to match the analytical solution for various input parameters in this case.

2.4.5 Results

For the simulation, we utilized the operating conditions identified in the previous section, where the dry biomass flux $\Phi_{BM} = 0.0024 \text{ kg s}^{-1} \text{ m}^{-2}$ and reactor height $H_r = 36 \text{ cm}$. Figure 14a plots the axial temperature profile within the biomass moving bed, starting with a position of $z = 0$ from the top of the reactor. As we can see, the temperature increases quite smoothly, reaching a solid exit temperature of 300°C . In Figure 14b, we can observe the chemical changes in the solid biomass phase by a decrease in oxygen and increase in carbon. This change is also corroborated in Figure 14c, where the mass fractions of torrefied (B) and char (C) components increase while that of the raw biomass (A) component decreases. Finally, in Figure 14d, we also see a change in the composition of the locally released volatile phase: in the upper part of the biomass moving bed, the volatiles being released are rich in moisture, signifying the drying process. Lower down in the reactor, the non-moisture volatile groups (V1 and V2) become dominant as torrefaction takes place.

One note is that for the large part of the reactor, there is not much change in the biomass solid phase except for drying. It is only in the bottommost 10 cm do we see significant changes in the composition. This makes sense, as for most part of the moving bed, the temperature is rising but is always below 200°C . The onset of torrefaction typically occurs above 200°C , which is around 25 cm from the top of the reactor. Nonetheless, this does not

mean that the upper part of the reactor becomes unnecessary. In fact, having the drying occur higher up in the reactor in a zone slightly separate from the devolatilization process has advantages to the reactor performance: the combustible volatile gases released in the oxidation zone will be less diluted by the inert steam released from drying. Therefore, we expect that this zonal separation will also help improve the performance of the reactor.

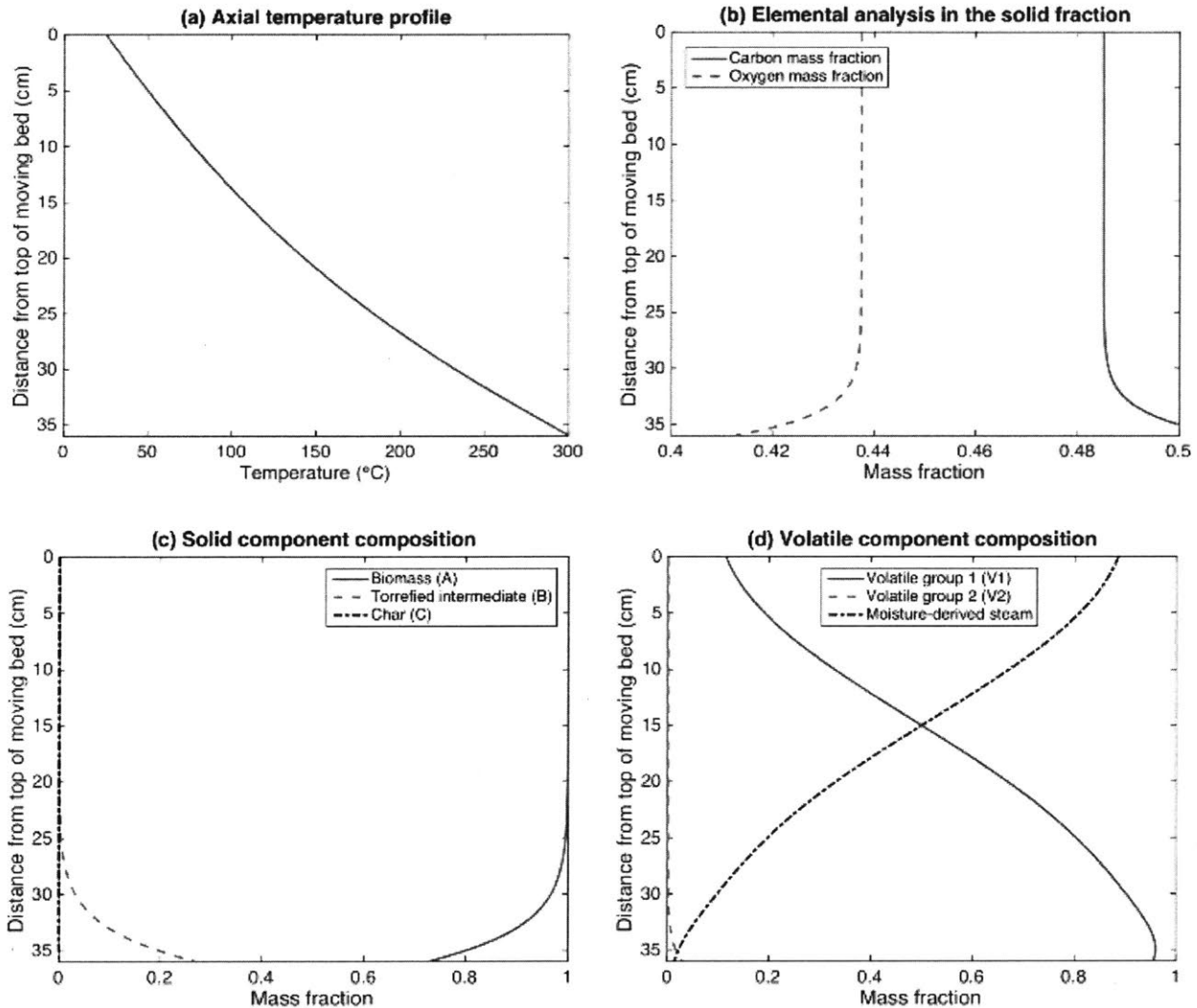


Figure 14 - Axial profiles of (a) temperature, (b) elemental analysis of the solid, (c) component composition of the solid, and (d) component composition of the locally released volatiles in the biomass torrefaction moving bed model.

In this section, we built a fine-grained model that describes the thermochemistry and heat transfer within the biomass moving bed reactor during biomass torrefaction. Using the base-case operating scenario derived using the coarse-grained model, we are able to obtain a better understanding about the various changes that take place both in the solid and the gaseous phases within the moving bed reactor. We learned that most of the devolatilization occurs within the bottommost 10 cm of the reactor, and that there are advantages in the zonal separation between drying and devolatilization.

While much more can be learned from this model, we choose not to use it too much beyond the purpose of initial validation of our concept. One reason is that the model, given the various built-in assumptions and uncertainties, is at best only a pale imitation of the actual reactor. As an example, the model makes no description or design-relevant predictions whatsoever about the complex interplay between heat and mass transfer within the oxidative torrefaction zone, except by assuming that it can be achieved at a target temperature T_H . Soon we will be building and validating an actual device, so there is no point in spending too much time dwelling on the particulars of this imperfect model when we actually have the ability to take real measurements.

2.5 Detailed Reactor Design

Based on the preliminary validation and science-based understanding about the moving bed reactor design using the coarse-grained and then the fine-grained models implemented above, we are now ready to embark on a detailed design in the laboratory scale. Because our laboratory-scale reactor is designed as a scientific instrument for careful testing and measurement under various operating conditions, we add a few more features to it that would be unnecessary in the final scaled-up version. These features satisfy the following:

- A temperature profile within the reactor must be carefully taken.
- The reactor, for initial experimental validation and also for reason of safety (in case an oxidation experiment gets out of hand), must have the ability to operate switch to the inert (N_2) conditions from the oxidative condition on demand.

- The reactor, for potential measurements in the future, must have gas-sampling ports built into the side of the reactor, in addition to the exhaust exit at the top.

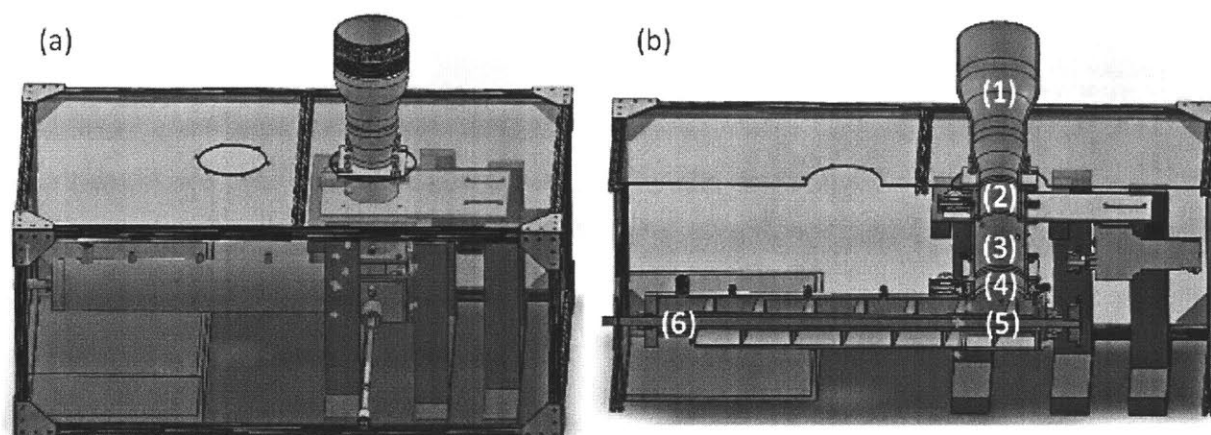


Figure 15 - SolidWorks rendering of the reactor assembly (a), and (b) in a cutaway view from the same angle. The various parts making up the assembly are labeled as: (1) biomass feed, (2) upper gas sampling port, (3) moving bed reactor, (4) low gas sampling port, (5) oxidative zone, and (6) char-cooling segment. The entire assembly is surrounded by a Plexiglas enclosure that is connected to an exhaust vent to ensure safety while operating indoors in a laboratory setting.

An overview of the reactor assembly is shown in Figure 15. For safety measure of testing indoors, the entire system is enclosed within a hood constructed of Plexiglas and 80/20, and the hood is vented via an exhaust with a measured flow rate of 200 standard $\text{ft}^3 \text{min}^{-1}$. The reactor system comprises of several components, labeled numerically in Figure 15b. Essentially, biomass enters into the biomass feed region (1), where the exhaust gas from the torrefaction reaction also escapes. Then, the biomass moves downwards in the moving bed that is contiguous in components (2) through (5). There are two gas sampling ports, one upper (2) and one lower (4), from which, if we wish, the gas from the reactor can be sampled or vented. Then the biomass enters the oxidative “hot zone” (5) where a limited amount of air is injected and where low-oxygen torrefaction occurs. Finally, the torrefied biomass is conveyed away from this hot zone via a char-cooling segment (6). In the subsections below, we will discuss the design and implementation of each of these components in greater detail.

2.5.1 Biomass Feed Component

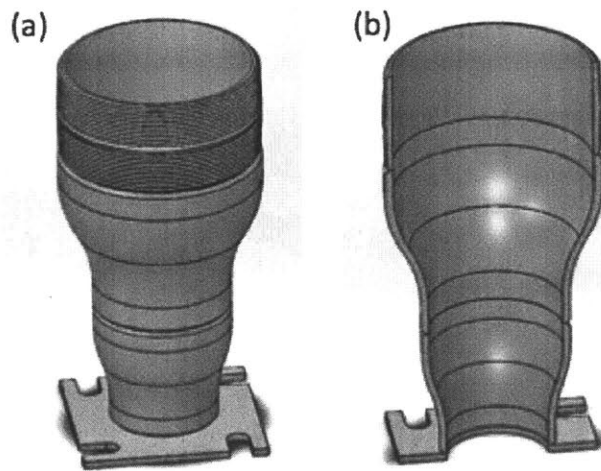


Figure 16 - (a) SolidWorks rendering and (b) cutaway view of the biomass feed component.

The biomass feed consists of a wide outlet that is 6 inches (15.24 cm) in diameter to make manual feeding of biomass easy. In the case of escaping exhaust gas, the widening opening also allows the gas to slow down in vertical velocity, so that it does not overwhelm the exhaust system and spill into the rest of the lab. Then the inner diameter gradually reduces to 3 inches (7.62 cm) (Figure 16). This reduction was done by welding various existing NPT components together: a standard 6-NPT steel pipe nipple (McMaster-Carr 44615K138), a standard butt-weld 304 stainless steel straight 6-by-4 NPT reducer (McMaster-Carr 45605K786), and a standard butt-weld 304 stainless steel straight 4-by-3 NPT reducer (McMaster-Carr 45605K783). The feed was then welded to a 304 stainless steel flange component that has been cut on a waterjet. This flange enables the different components in the assembly to be bolted together.

2.5.2 Upper Gas Sampling Port Component

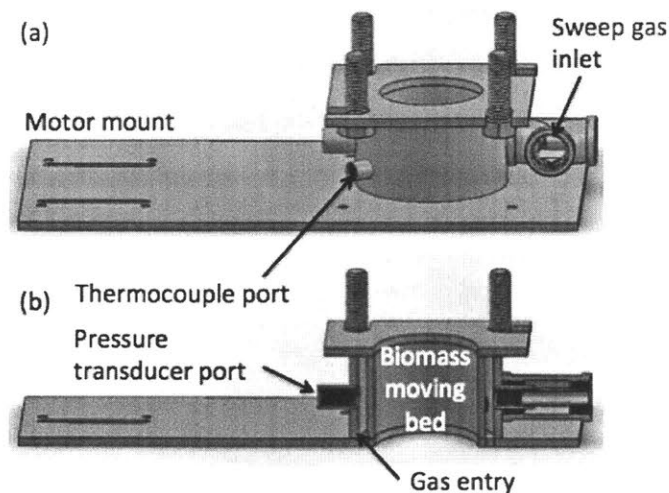


Figure 17 - (a) SolidWorks rendering and (b) cutaway view of the upper gas sampling port component, which also includes an extension for the motor mount.

Immediately beneath the biomass feed component lies the upper gas sampling port component (Figure 17). Here, the biomass travels downwards along the inner moving bed, which comprises of a 2.5-inch (6.35-cm) segment of a standard 304 stainless steel, 3-NPT welded pipe (McMaster-Carr 1947K79). Then, concentrically surrounding the 3-NPT pipe is a larger standard 304 stainless steel, 4-NPT welded pipe of the same segment length (McMaster-Carr 7750K199). Between the 3-NPT and 4-NPT pipe is a jacket that opens to the biomass moving bed at the bottom via a series of small slits. The jacket also communicates to the exterior via a welded standard $\frac{3}{4}$ -NPT tee (McMaster-Carr 44605K155), and serves as the gas sampling port. The third end of the tee serves as an inlet for sweep gas, in case we feel the need either to dilute the reactor gas with inert nitrogen, or to combust this gas by mixing it with air. Also welded to the exterior side of the 4-NPT pipe segment are a few female couplings of 1/8-NPT and 1/4-NPT sizes (McMaster-Carr 46685K261 and 46685K262 respectively). These ports are designed for insertion of thermocouples (via a male compression tube to NPT fittings) and of pressure transducers (via barbed hose to NPT fittings), and are sealed with NPT caps when they are not in use. Therefore, they do not openly communicate with the exterior. Finally, the top of the upper gas sampling port component is welded to a flange connection that is identical to the one at the bottom of the biomass feed component so that the two components can be bolted to

each other (with some compressible gasket material in-between). The bottom of the upper gas sampling port component, on the other hand, is welded to a large rectangular ¼-inch-thick 304 stainless steel sheet that is also cut on a waterjet. This sheet (a) serves as the lower flange to connect to the component below, and (b) as labeled in Figure 17, provides for a place to mount the motor that drives the auger at the bottom of the reactor assembly.

2.5.3 Moving Bed Component

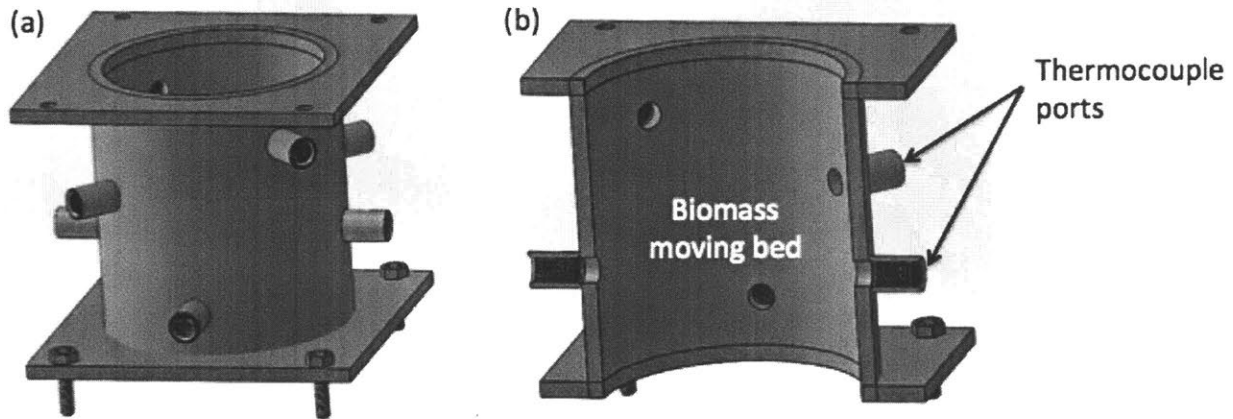


Figure 18 - (a) SolidWorks rendering and (b) cutaway view of the moving bed reactor.

Immediately beneath the upper gas sampling port component is the moving bed reactor component (Figure 18). The inner side of this component is made from a 5-inch-long (12.7 cm) segment of the same 304 stainless steel, 3-NPT welded pipe (McMaster-Carr 1947K79). Therefore, the inner biomass moving bed is contiguous with that in the upper gas sampling port component above, as well as with that in the lower gas sampling port component below. Eight female couplings of 1/8-NPT size (McMaster-Carr 46685K261) are welded to the exterior of the 3-NPT pipe to serve as thermocouple ports. Both the top and the bottom of this component is welded to a stainless steel flange that has been cut using a waterjet, in order to provide tight connection with the components above and below.

2.5.4 Lower Gas Sampling Port Component

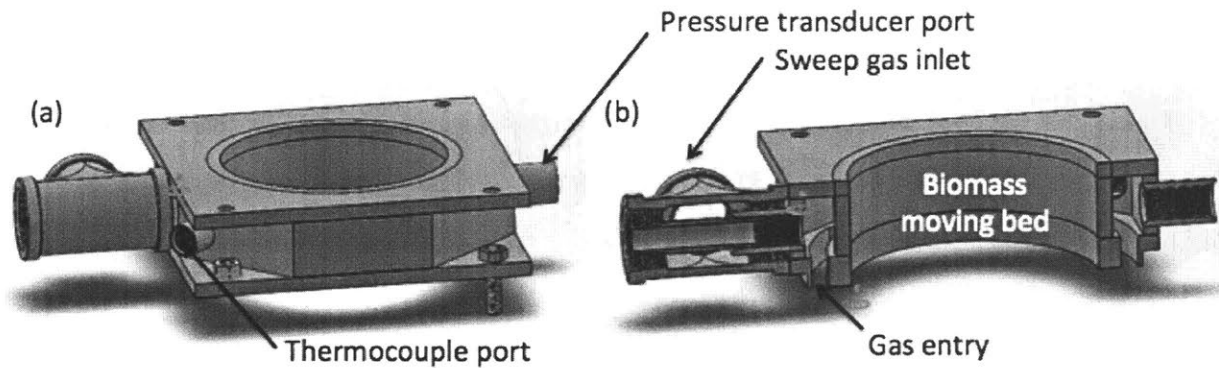


Figure 19 - (a) SolidWorks rendering and (b) cutaway view of the lower gas sampling port component.

Mirroring the upper gas sampling port component, this component also consists of an inner 3-NPT pipe that makes up the biomass moving bed, as well as a concentric surrounding 4-NPT pipe that forms the outer wall of the gas jacket (Figure 19). The gas jacket communicates to the biomass moving bed via several thin slits at the bottom, and a 3/4-NPT tee communicates the gas jacket to the outside, with the same sweep gas inlet feature included, as previously described for the upper gas sampling port. This component, like the upper gas sampling port component, also has welded female NPT couplings that provide places for the pressure transducer and thermocouples to enter.

2.5.5 Oxidative Zone Component

Beneath the lower gas sampling port component lies the rectangular box that houses the auger and constitutes the oxidative hot zone (Figure 20). As the biomass travels through the inside of the lower gas sampling port and falls into this oxidative hot zone, it has been heated sufficiently hot such that torrefaction reaction can take place. There are two primary air inlets, located opposite from each other, in the form of a pair of welded standard 1-NPT female couplings (McMaster-Carr 4513K650), where air (with or without preheating) from a compressed source can be connected via a compression tube to NPT fitting. There are also four thermocouple ports at different locations, consisting of welded standard 1/8-NPT female couplings (McMaster-Carr 4513K261). The left side of the oxidative zone opens to the char-cooling segment, and the right side of this component

comprises of a wall with an opening for the shaft of the auger to go through, an O-ring to provide an airtight seal, as well as a flange-mounted ball bearing (McMaster-Carr 6665K33) that helps position the auger shaft axially and allows it to rotate. The left, right, and upper faces of the component have bolt holes to secure the component to its adjacent neighbors. Finally, the incoming air is injected at the same level as the auger flights, whose shape also helps disperse the air throughout the biomass moving bed. For safety measure, there is an option to switch the air stream with an inert stream.

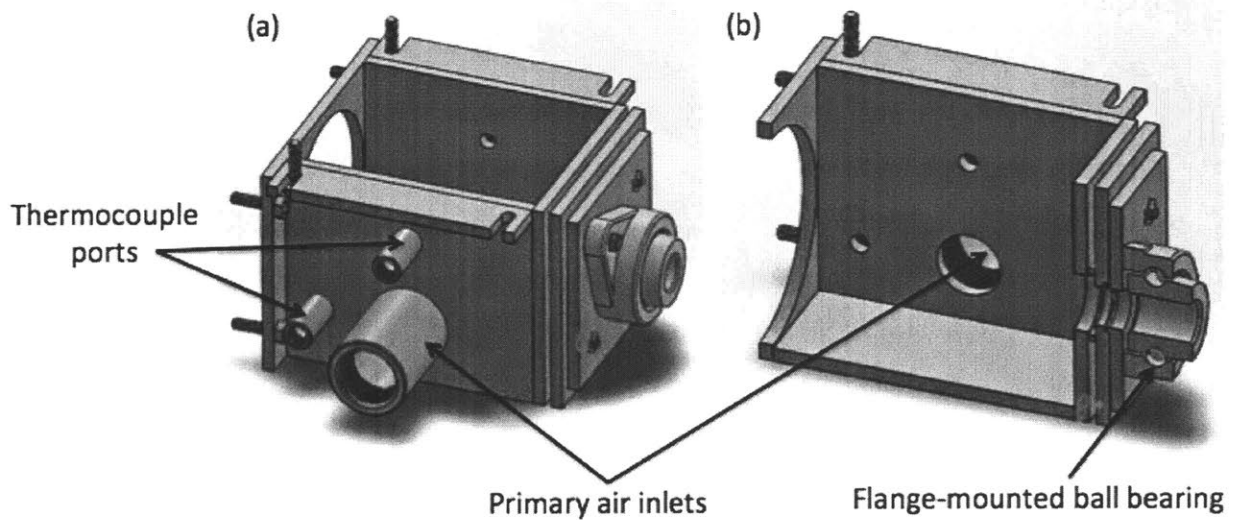


Figure 20 - (a) SolidWorks rendering and (b) cutaway view of the oxidative zone.

2.5.6 Char-Cooling Segment

After the biomass passes through the oxidative zone, it is carried by the auger into the char-cooling segment (Figure 21). As described previously, this segment is designed to ensure adequate cooling of the hot torrefied biomass, such as when it emerges from the reactor, it does not risk spontaneously catching fire. The auger is housed within a 2-foot-long (61 cm) piece of standard 4-NPT steel pipe (McMaster-Carr 7750K199). The right-hand auger flights have a diameter of 4 inches (10.16 cm), and the auger component is supplied by Tanaka Power Equipment. The auger sizing calculations and torque requirements, as well as some modifications that we made to the auger in order to make it compatible with biomass torrefaction, are described earlier in O'Brien (2016). At the left end of the char-cooling segment, a square opening, cut into the NPT pipe 3 inches by 3 inches (7.62 cm),

allows the cooled torrefied product to exit the reactor assembly. The char-cooling segment is capped at the left end, and a clamping two-piece shaft collar (McMaster-Carr 6436K16) maintains the axial position of the auger in conjunction with the flange-mounted ball bearing described earlier on the right-side wall of the oxidative zone.

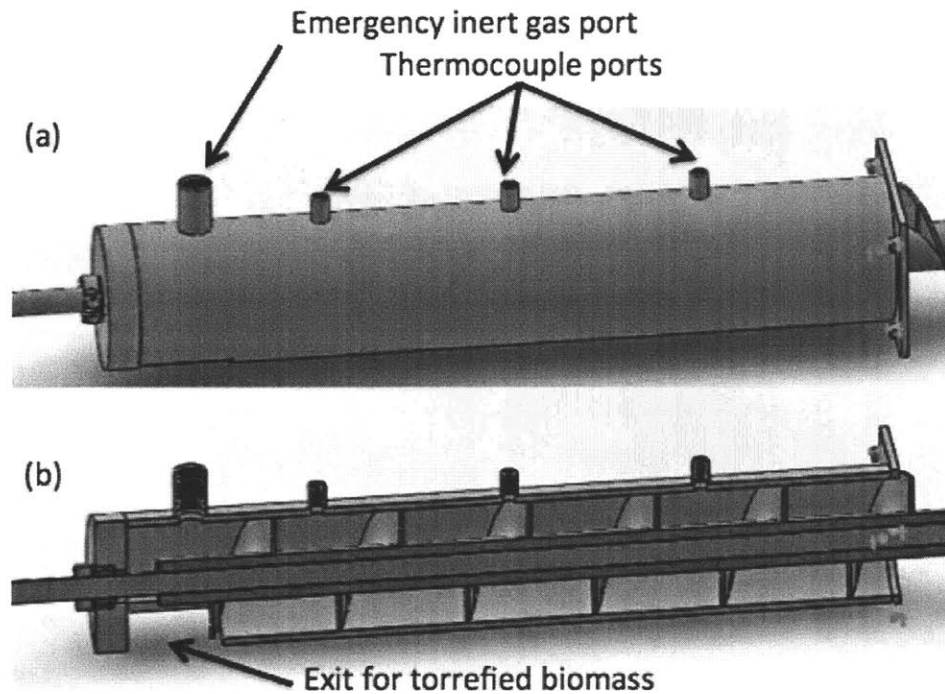


Figure 21 – (a) SolidWorks rendering and (b) cutaway view of the char-cooling segment.

2.5.7 Motor Drive

Finally, as shown in Figure 22, in order to provide sufficient torque to turn the biomass-filled auger on a continuous basis, a Bison 336 Series 37 Watt permanent magnet 90V/130V DV motor was mounted below the motor mount on the lower face of the upper gas port component. The motor's 5/8-inch pitch, 10-teeth, 5/8-inch bore motor sprocket (McMaster-Carr 6280K871) is connected via the #50 chain to a 5/8-inch pitch, 20-teeth, 5/8-inch bore sprocket that is connected via a square key to the auger shaft (McMaster-Carr 6280K808). The DC motor speed is adjustable via an Iron Horse silicon controlled rectifier 180 VDC drive.

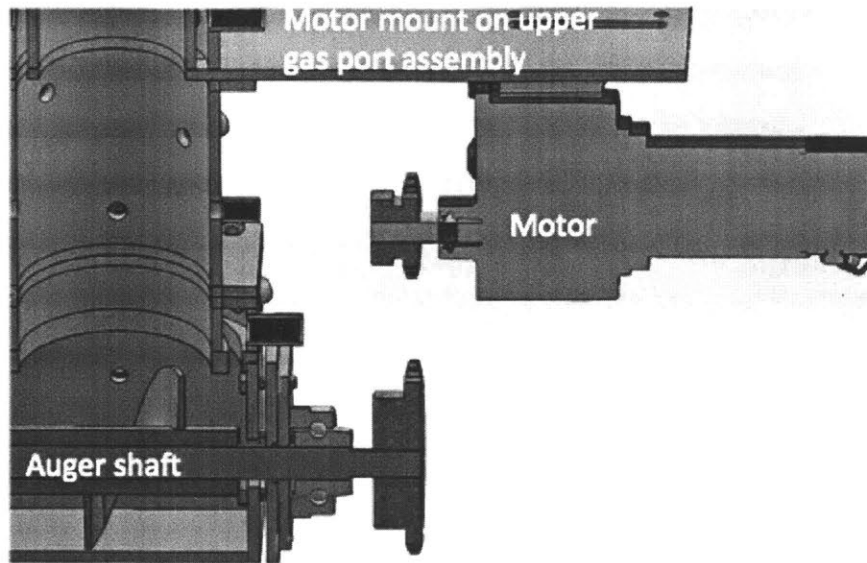


Figure 22 - SolidWorks rendering of the motor drive. Not shown is the #50 chain connecting the motor sprocket to the auger shaft sprocket.

2.6 Summary and Perspectives

In this section, in seeking a more simplified and low-cost biomass torrefaction reactor design deployable in a decentralized setting, we considered the concept of biomass torrefaction under a low-oxygen environment. We explored the existing literature as well as the possible underlying mechanisms and trade-offs in low-oxygen torrefaction in comparison with the classical inert torrefaction, and arrived at a moving bed torrefaction reactor design concept. We subsequently developed a coarse-grained model to describe the heat transfer and length scales within the reactor, and learned that the primary heat transfer mechanism within the moving bed occurs through the gaseous phase. We then derived a fine-grained model description coupling the chemistry, heat transfer, and mass transfer effects, and showed that under the base case reactor sizing and input parameters, we can design the reactor to satisfy the requirements for biomass torrefaction. Finally, we close by describing a detailed reactor design, which we implemented and will be validating in 0.

Chapter 3 Validation of a Scalable Biomass

Torrefaction Reactor and Its Performance Metrics

A decentralized torrefaction system has the potential to create additional economic value and mitigate environmental consequences from burning the excess biomass residues located in rural areas. Nonetheless, to date, there lacks realistic experimental set-ups that can easily predict and inform the performance of such a torrefaction reactor at scale under different reaction conditions and types of feedstock, and thus much of the commercial development is still being done at best as guesswork. In this paper, we validate and characterize the performance of a lab-scale torrefaction test reactor, with respect to three types of biomass: pine shavings, hay, and rice husks. We found that the reactor performance depends drastically on the type of feedstock, but in each case we identified a set of operating conditions where the reactor was able to sustain a stable and continuous torrefaction reaction of different degrees of severity for several hours. For each operating condition, we characterized the product yield, energy yield, and energy densification and show key differences with existing literature data obtained from artificial inert conditions—in general, torrefaction under a low-oxygen environment results in an over-torrefaction and reduced solid mass and energy yield under a given torrefaction temperature and residence time. By using mass closure and elemental analysis, we further calculated the elemental composition in the volatile mixture, and demonstrated that the reactor operates almost always on the air-rich side with respect to the available combustible volatiles. These performance metrics can be used to predict the necessary torrefaction reactor conditions at scale. Our reactor is therefore a manifestation of a more general phenomenological framework and methodology whereby biomass processing reactors can be validated in a realistic, low-cost, and rapid setting under a broad set of biomass feedstock types and reaction conditions before significant capital is expended to scale up a reactor design.

3.1 Need for a Scalable Torrefaction Test Reactor

Most biomass residues do not present themselves in useful or desirable forms in the field: they can be too loose, bulky, and wet to transport, process, and utilize. Therefore, torrefaction as a means to densify and improve the characteristics of biomass residues has received significant interest, both academically and commercially. Academically, many researchers have set out to validate, on a lab scale, potential torrefaction reactor designs that include fluidized beds (Bergman *et al.*, 2004; Li *et al.*, 2012), fixed/moving beds (Branca *et al.*, 2014; Couhert *et al.*, 2009), rotary kilns (Nhuchhen *et al.*, 2016; Repellin *et al.*, 2010), and microwave ovens (Gronnow *et al.*, 2012; Ren *et al.*, 2012). Most of these lab-scale torrefaction reactor set-ups, however, are unrepresentative of the scaled-up reactor designs in the following ways: (a) they are often batch reactors and therefore do not accurately portray the continuous feedstock flow nature of the scaled-up commercial reactors; (b) they rely on artificial heat sources such as electric heating coils, rather than employing more energetically realistic methods such as the heat from combusting the volatiles released from the torrefaction reaction; (c) they only test a limited range of biomass—often pellets and woody biomass—and do not propose how their reactor can generalize to a wider range of biomass types. On the other hand, current commercial-scale torrefaction reactors of different designs are often being developed without the useful input of realistic lab-scale prototypes due to the weaknesses described above, and therefore can be prone to validation failure and unforeseen problems after huge capital expenses in setting up these plants. We therefore see a gap between the existing lab-scale torrefaction prototypes in properly informing the scale-up of such reactors.

In this study, we propose and validate a laboratory-scale torrefaction test reactor that we believe is a more realistic and scalable portrayal of a fixed-bed reactor design. We validate how such a reactor can operate under various conditions for biomass types with diverse characteristics (pine shavings, hay, and rice husks), and quantify the reactor performance (product yield, energy yield, energy densification ratio, chemical composition, and the nature of *in-situ* volatile oxidation) under different operating conditions. We also demonstrate the difference between the performance metrics obtained from our test

reactor versus those interpolated from the existing literature data. This test reactor therefore is a manifestation of a more phenomenological and generalizable experimental framework and methodology that we have developed for the rapid validation and scaling of biomass processing reactors from lab scale to commercial scale.

3.2 Experimental Set-Up and Design

In order to validate and control experimental conditions, the test reactor needs to be able to control two dominant independent variables: solid-phase residence time, and the reactor temperature. We first describe how we use the solid fixed-bed reactor flow to control the solid residence time. We then describe how we can modulate the amount of air entering into the reactor in proportion to the amount of biomass, which in turn controls the torrefaction severity.

(a) Cross-section rendering in SolidWorks (b) Actual test reactor with an operator

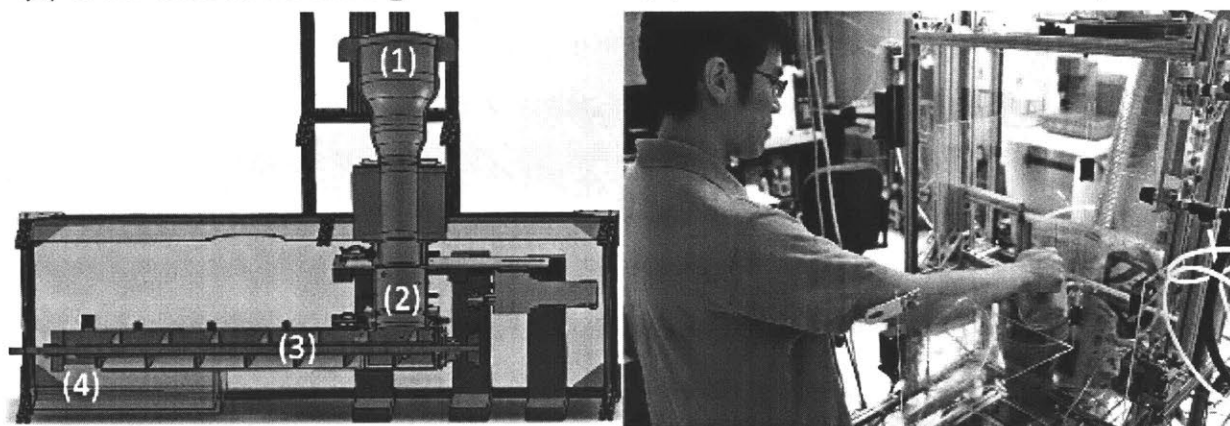


Figure 23 - A lab-scale biomass torrefaction reactor was designed and built. (a) Cross-section rendering of the reactor design in SolidWorks, with biomass feeding inlet (1), fixed-bed reactor zone (2), screw auger (3), and torrefied product outlet (4) labeled; (b) actual test reactor assembly in operation with an operator (Miller, 2016).

3.2.1 Control of Solid Residence Time

A lab-scale, continuous-flow biomass torrefaction reactor design for a feedstock capacity of about 1 kg/h and a cross-sectional diameter of 4 inches, as described previously in Section

2.5, was implemented and tested in this study. This test reactor utilizes a fixed-bed reactor concept (labeled in Figure 23a), with a screw auger at the bottom to continuously remove torrefied biomass. The screw auger was sized to be 2 feet in length in order to allow sufficient time for the heated, torrefied biomass to cool off before it exits from the reactor outlet. The screw auger is connected to a motor drive with an adjustable turning rate, so that we are able to control how quickly the screw auger turns, and therefore, the solid-phase residence time inside the reactor for the torrefaction reaction.

In order to calculate the solid residence time, the density ρ_{BM} and input mass flow rate \dot{m}_{BM} of biomass were measured for each type of biomass and auger turning speed. Then given the radius R_r and height H_r of the fixed-bed reactor, the effective residence time τ_{res} of biomass is given by:

$$\tau_{res} = \frac{\rho_{BM}\pi R_r^2 H_r}{\dot{m}_{BM}}$$

Given our specific lab-scale reactor dimensions (diameter = 4 inches, depth of torrefaction zone ~ 10 cm), in Table 10, we provide the typical ranges of possible input feeding rates for our lab-scale reactor given the normal ranges of torrefaction residence times.

Table 10 - Typical ranges of possible input feeding rates in our lab-scale reactor for different solid residence times. The possible ranges of feeding rates depend significantly on the type of biomass.

Residence time	5 min	20 min	40 min
Pine shavings / hay	0.58 kg/h	0.15 kg/h	0.073 kg/h
Rice husk	2.0 kg/h	0.51 kg/h	0.26 kg/h

We can therefore see that for our lab-scale reactor, by fixing the torrefaction residence time, our biomass feeding rate is generally on the order of 0.1-2 kg/h. While this is sufficient for lab-scale tests for biomass samples in small quantities, in real life, a commercial torrefaction reactor capable of processing about 500 kg/h of biomass will need to be scaled up from our lab-scale design by a factor of 250-5,000.

3.2.2 Control of Torrefaction Severity

At a given solid residence time (i.e. feeding rate), in order to control the torrefaction severity, we need to introduce air in different proportions to the solid feeding rate. As shown in Figure 24, in order to achieve this, we introduced two air flow inlets near the base of the fixed bed reactor. These inlets are connected to a compressed air cylinder (Airgas AI D300). A mass flow controller (Omega Engineering FMA-5528A) was used to adjust the input air flow rate, with an adjustable flow rate range between 0.1 to 50.0 standard L/min.

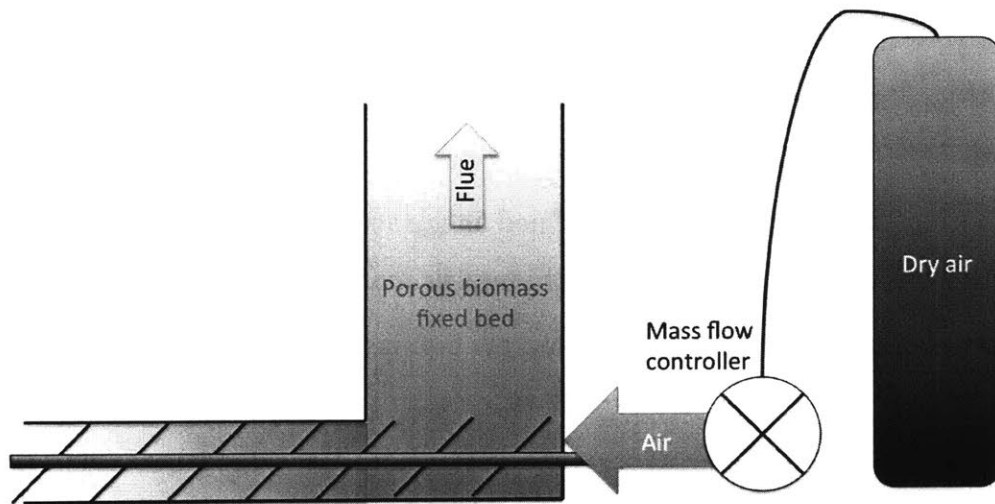
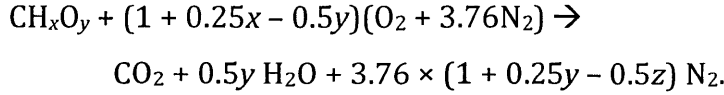


Figure 24 - We utilized adjustable air flow inlets to control torrefaction severity. As shown in the schematic, the air is injected at the bottom of the reactor and its flow rate is controlled via a mass flow controller.

Because different types of biomass under different reaction conditions have different bulk densities and therefore volumetric flow rate, for the purpose of conducting a controlled and scalable experiment, we introduce a dimensionless quantity called the *normalized air/fuel ratio*, or σ . This quantity represents the proportion of air mass flow rate to biomass mass flow rate, and is defined via the following steps:

- (1) For a specific type of biomass, determine its elemental analysis of the form CH_xO_y as well as moisture mass fraction Y_M and ash content Y_{ash} .
- (2) Assuming stoichiometric oxidation of this type of biomass, then the fully balanced chemical equation will be:



(3) Therefore, based on the chemical equation above, at stoichiometry, and with the molecular weights of carbon, hydrogen, and oxygen atoms are given by MW_C , MW_H , and MW_O , respectively, then the mass flow rate $\dot{m}_{ox,stoic}$ [kg/s] of air that is required to fully oxidize \dot{m}_{BM} [kg/s] of biomass (as received, on a wet basis) is given by:

$$(\text{AF})_{\text{stoic}} \equiv \frac{\dot{m}_{ox,stoic}}{\dot{m}_{BM}} = \frac{(2 + x/2 - y)(MW_O + 3.76MW_N)}{(1 + Y_M + Y_{ash})(MW_C + MW_Hx + MW_Oy)}$$

where $(\text{AF})_{\text{stoic}}$ is the stoichiometric ratio (mass) of air to biomass to enable complete oxidation.

(4) The *normalized air/fuel ratio* σ is defined as the actual mass flow rate of air \dot{m}_{ac} output from the air inlets to the stoichiometric mass flow rate of air, \dot{m}_{ox} , as determined previously, to enable complete biomass combustion:

$$\sigma \equiv \dot{m}_{ac}/\dot{m}_{ox}.$$

Therefore, if we have stoichiometric oxidation of biomass, we expect $\sigma = 1$. In the regime of low-oxygen biomass torrefaction, we expect $\sigma < 1$. As we will show later, for the different types of biomass, general values of σ range between 0.2 to 0.5, with increasing value corresponding to increasing torrefaction severity. For those readers who are familiar with combustion engineering, they may note that the concept of σ is akin to the inverse of the *equivalence ratio*. However, in this paper, in order to avoid terminology confusion, we deliberately avoided the term equivalence ratio, which is reserved normally for premixed homogeneous air/fuel combustion.

It is clear that in order to calculate the normalized air/fuel ratio, we need to know the elemental composition of the three types of biomass that we test. We experimentally obtained the elemental compositions of the raw biomass that we used (pine shavings, hay, and rice husks) by using a CHON analyzer available at Professor Sanjay Mahajani's group at Indian Institute of Technology-Bombay. The moisture and ash contents for the raw biomass were obtained experimentally using a thermogravimetric analyzer (TA Instruments Q50).

These values are listed in Table 11. Alongside these values, we also listed values reported in the literature. As can be seen, for pine shavings the values are extremely close, but for hay and rice husks there are discrepancies of a few percentage points. However, these variations are not large, so we ended up using the values that we experimentally obtained ourselves. Based on the elemental analysis data in Table 11, we derived the following mass ratios of air to biomass for stoichiometric combustion, listed in Table 12.

Table 11 - Elemental compositions of three types of raw biomass by mass fraction, as determined experimentally (“exp.”) by us, and comparing to values in the literature (“lit.”).

Biomass type	Carbon		Hydrogen		Oxygen		Source
	Exp.	Lit.	Exp.	Lit.	Exp.	Lit.	
Pine shavings	49.6%	49.5%	5.7%	5.9%	44.8%	44.7%	Crombie <i>et al.</i> , 2013
Hay	43.7%	45.7%	4.4%	5.7%	51.3%	37.9%	Riechel <i>et al.</i> , 2010
Rice husks	37.6%	41.4%	3.9%	5.6%	58.3%	53.1%	Crombie <i>et al.</i> , 2013

Table 12 - The approximated chemical formula, moisture content, ash content, and stoichiometric air/ratio of different types of biomass.

Biomass type	Formula	Moisture content	Ash content	Stoichiometric air/fuel ratio
Pine shavings	$C_{4.13}H_{5.61}O_{2.80}$	6.3%	1.6%	5.26
Hay	$C_{3.65}H_{4.32}O_{3.21}$	4.4%	5.1%	3.94
Rice husks	$C_{3.14}H_{3.86}O_{3.64}$	7.2%	17.0%	2.53

3.3 Readout Protocols

In order to measure the performance of the reactor unit, we monitored a few specialized quantities: solid mass flow, solid proximate analysis, and solid ultimate (elemental) analysis. In this section, we briefly describe the protocols we used to measure these readouts.

3.3.1 Solid Mass Flow

The input solid mass flow rate [kg s^{-1}] is measured by weighing a bucket of the raw biomass every 5-10 minutes as an operator manually feeds a certain amount of biomass into the reactor manually. The output solid mass flow rate is measured by weighing a bucket placed at the reactor outlet to continuously collect the torrefied biomass that falls out, again once every 5-10 minutes or so. Dividing the mass change by the time elapsed gives an estimated solid mass flow.

3.3.2 Proximate Analysis

Proximate analysis, as described in ASTM D-3175, measures the mass fractions of moisture, fixed carbon, volatile matter, and ash components in a given biomass sample. In particular, the volatile matter component is the portion of combustible biomass that departs the solid fraction under non-oxidative thermochemical conditions (defined by ASTM as heating the biomass sample to 950°C within 30 minutes and maintaining the sample at that temperature for 7 minutes under inert conditions such as nitrogen). The remaining part of the solid consists of fixed carbon and ash. In order to distinguish the two, we then subject the residues to an oxidative environment (air) at an elevated temperature of $600\text{-}750^{\circ}\text{C}$ so that all the fixed carbon becomes oxidized into gaseous carbon dioxide and steam. What remains after this reaction consists of ash.

We have available a thermogravimetry analyzer (TA Instruments Q50), which consists of a EGA furnace as well as a mass balance to keep track of the mass loss in the torrefied sample when the sample is heated to different temperatures. This can be used to understand the fixed carbon, volatile matter, and ash components of the system. This procedure, known as proximate analysis, was performed as per ASTM-D3175 standards. Figure 25 shows the TGA analyzer that we employed (a), as well as a sample temperature (b) and mass loss traces (c) in time associated with a proximate analysis on the TGA. The mass loss measurements of the various solid components are denoted by m_A , m_B , m_C , and m_D .

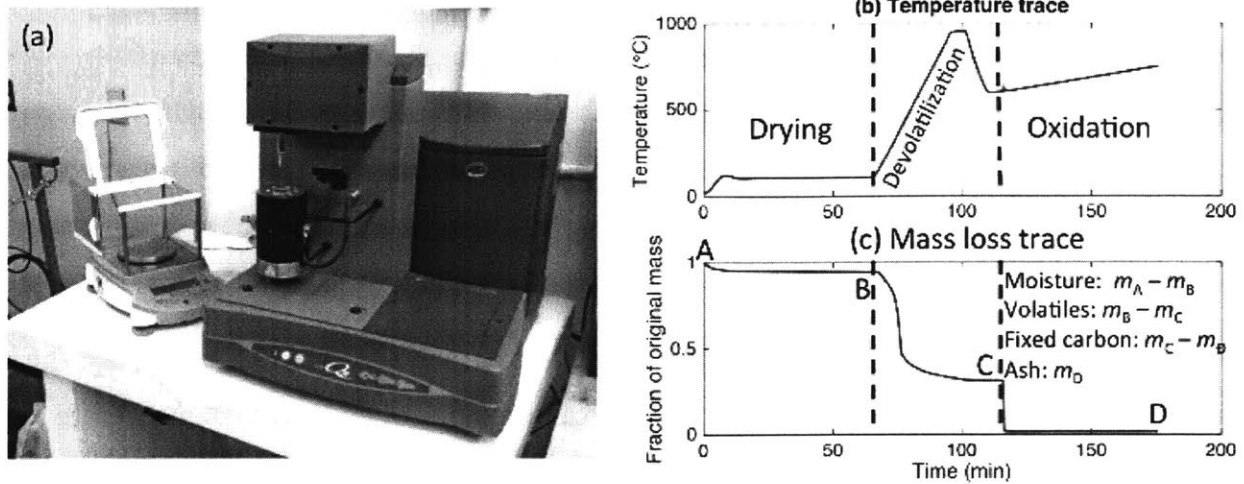


Figure 25 - (a) The thermogravimetric analysis set-up (TA Q50) used to perform proximate analysis on various biomass and torrefied biomass samples. A sample trace of temperature (b) and mass loss curves (c) in time for a torrefied pine shavings sample on the TGA as per the ASTM D-3175 protocol.

3.3.3 Ultimate Analysis

Elemental analysis—also known as ultimate analysis—breaks down the biomass or torrefied biomass sample into the mass fractions of its elemental components: mostly carbon, hydrogen, oxygen, and nitrogen (CHON), as per ASTM-D5373-16 protocol. By keeping track of the number of different atoms coming in and going out of the reactor, we can infer the reaction chemistry as well as the chemical composition of the outgoing volatile gases. The elemental analysis was carried out using a CHON analyzer (Thermo Finnigan Flash EA 1112) at Professor Sanjay Mahajani's group in Indian Institute of Technology-Bombay.

3.3.4 Higher Heating Value

The higher heating value (HHV) [J kg^{-1}] of a fuel sample is defined as the energy that can be harvested if we combust a certain amount of the fuel sample and cool the post-combustion flue gas down to the standard condition (including the latent heat of condensation of water vapor and other vapors). In order to measure the higher heating values of the raw biomass and torrefied biomass samples, we first ground the prospective samples to small particles

of sizes inferior to 0.5 mm. Then we compressed these particles into pellets using a manual ¼"-diameter-by-1" pelleting press (Parr Instrument 2810 series), and then analyzed using a calorimeter (Parr Instrument Model 6200 isoperibol).

3.4 Validation of Stable Operating Conditions

Once we have defined the independent parameters above (solid residence time τ_{res} and the normalized air/fuel ratio σ), we can select a few combinations of (τ_{res}, σ) to demonstrate that the torrefaction reactor can indeed operate continuously and stably.

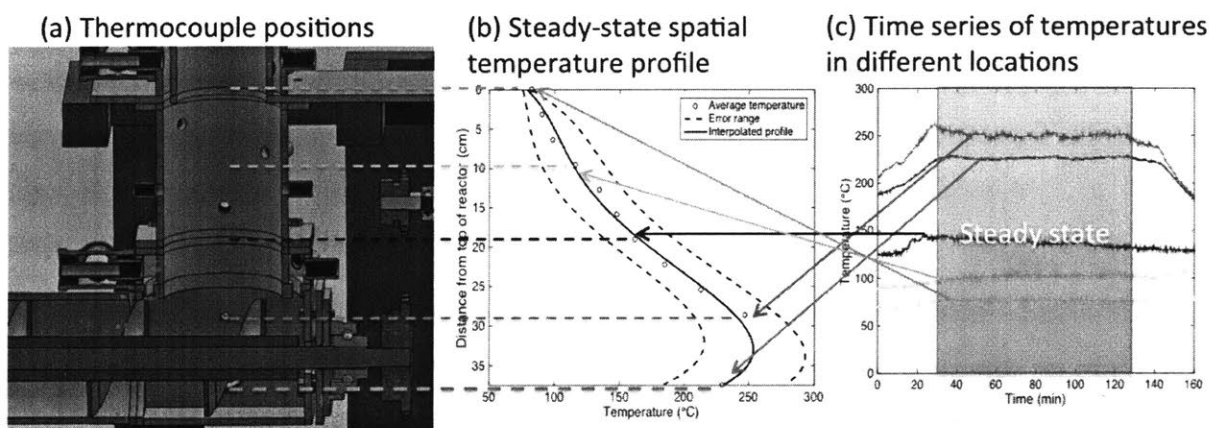


Figure 26 - Sample steady-state temperature validation for the torrefaction reactor operating on pine shavings, with the following reaction conditions $\tau_{res} = 11$ min, $\sigma = 0.19$. (a) Throughout the axial length of the reactor, various thermocouples are placed about 1 inch apart to measure the temperature at each point in the biomass fixed bed. (b) A steady-state axial temperature profile is achieved. (c) Sample time-series traces of select thermocouples located in different axial locations along the reactor (corresponding to different colors), illustrating that the reactor is capable of sustaining a steady-state temperature profile under continuous feeding conditions for at least 100 minutes.

In order to monitor the reactor operation, we inserted 10 thermocouple points, in approximately 1 inch spacing, axially throughout the length of the reactor (Figure 26a). As a sample proof of steady-state operation, we flowed air into the reactor at the normalized

air/fuel ratio of $\sigma = 0.18$, and the screw auger turning rate was adjusted such as the solid residence time $\tau_{\text{res}} = 11$ min. We then ignited some initial pine shavings at the bottom of the reactor, and continuously fed pine shavings into the reactor such that the level of pine shavings at the top was maintained. After some initial start-up period, where the entire reactor assembly and the fixed bed were heated up, a steady-state condition was reached at each axial location (Figure 26c), and we demonstrated that the steady-state condition could be sustained for at least 100 minutes before turning the reactor off by quenching the torrefaction reaction with inert nitrogen in place of air. The mean steady-state temperature readouts at different axial locations were compiled into an axial temperature profile of the reactor (Figure 26b).

We note that the fixed bed temperature increases axially towards the bottom of the reactor, and reaches a maximum near the middle of the screw auger area, where the air inlets are also located. This temperature profile further suggests that the biomass fixed bed in this specific experiment can be broken down into the following zones:

- (1) Drying zone: For the first 5 cm from the top of the reactor, the temperature of the fixed bed is less than 100°C, and therefore drying occurs.
- (2) Heating zone: From about 5 cm to 25 cm from the top of the reactor, the temperature of the fixed bed is between 100-200°C. At this point, the input biomass is practically dry, but no torrefaction reaction has taken place yet.
- (3) Torrefaction zone: In the bottommost 15 cm of the reactor, the temperature of the fixed bed stays above 200°C but below 300°C, where torrefaction is defined to occur under a low-oxygen environment.

This zonal separation of drying and torrefaction is consistent with the temperature profile predicted earlier by our coarse-grained analysis in Section 2.4.5. This separation is also advantageous as it automatically separates the combustible volatile gases from the non-combustible steam, thereby achieving a higher combustion efficiency and flammability.

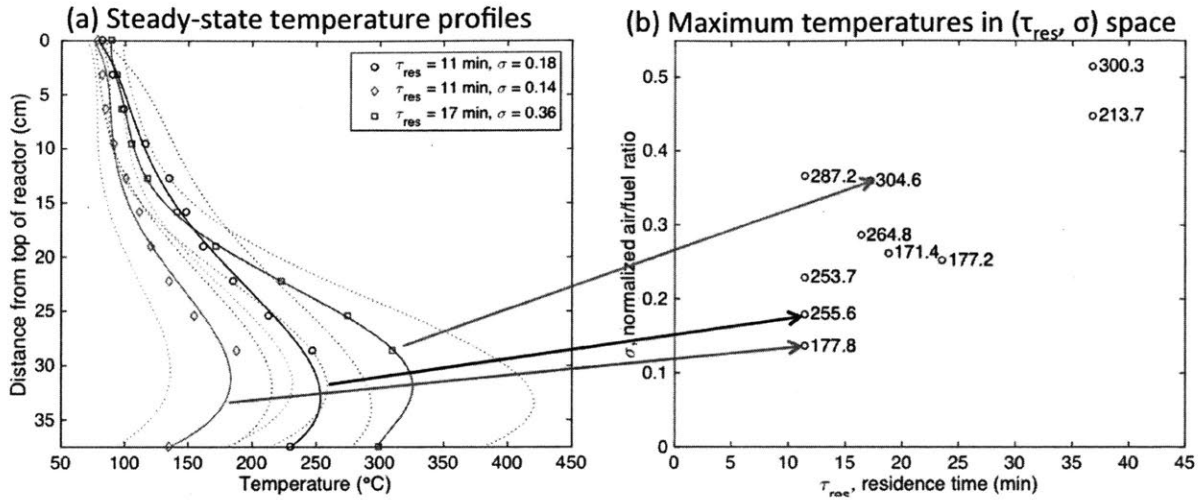


Figure 27 - (a) Steady-state temperature profiles were achieved for pine shavings for the torrefaction reactor under various operating conditions: ($\tau_{res} = 11$ min, $\sigma = 0.18$) in black, ($\tau_{res} = 11$ min, $\sigma = 0.14$) in red, and ($\tau_{res} = 17$ min, $\sigma = 0.36$) in blue. Note that increasing σ (torrefaction severity) also increases the maximum temperature in the fixed bed. (b) A plot of the maximum fixed bed temperatures under different (τ_{res}, σ) combinations for pine shavings. As we move towards the top-right (increasing torrefaction severity) of the plot, we also notice that the maximum reactor temperature increases.

We have demonstrated a stable reactor steady state for one reactor operating condition for pine shavings. The next question that we address is: Can we show steady states for other reactor conditions? We operated the reactor under two additional conditions ($\tau_{res} = 11$ min, $\sigma = 0.18$), and ($\tau_{res} = 17$ min, $\sigma = 0.36$). Figure 27a shows that each of these conditions has resulted in stable steady-state temperature profiles. Notably, as we increase the torrefaction severity by introducing more air, we observe a higher maximum temperature, as expected.

Finally, we convert Figure 27b in the τ_{res} - σ phase space into an interpolated color plot for the maximum temperature for pine shavings in Figure 28a. Each colored point in the plot represents a real experimental point, while the color gradient from 180°C to 300°C represents a linear interpolation of the maximum steady-state reactor temperatures under

other possible (τ_{res} , σ) combinations based on the real experiments. We can repeat the same process for hay (Figure 28b) and rice husk (Figure 28c).

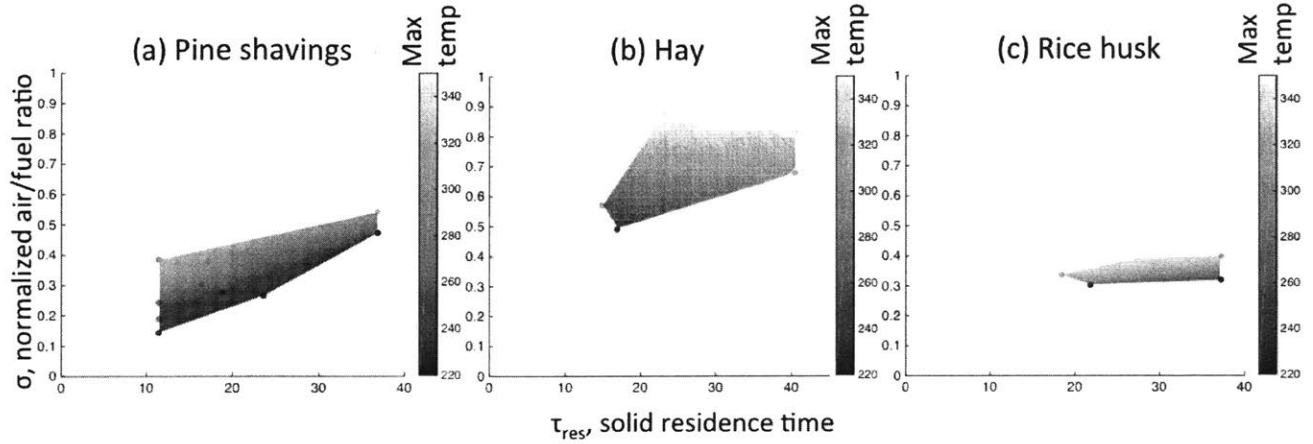


Figure 28 – The color map of maximum reactor temperature under different reactor operating conditions, in its original scale. Linearly interpolated maximum steady-state reactor temperatures under different operating conditions, with the solid residence time τ_{res} plotted on the x axis and the normalized air/fuel ratio σ plotted on the y axis, for three types of biomass: pine shavings (a), hay (b), and rice husks (c). Each color dot in the τ_{res} - σ space represents a real experimental data point, while the intervening color gradient swathes represent linear interpolations based on the actual experimental readouts.

One important point to note here is that different types of biomass have very different regimes of operation. In the case of rice husks, for example, due to the high density of the biomass, for each given value of normalized air/fuel ratio σ and for each given residence time, a much higher volumetric flow of air is needed in the reactor to make the reaction go. This means that before σ becomes very large, we have already reached the maximum safe air flow rate for indoor experimentation. This explains why the polygon delineating rice husks in Figure 28c is highly compressed in the vertical direction, where the range of σ tested lies only between 0.3 and 0.4. We found that hay, on the other hand, is qualitatively difficult to light and sustain a reaction: it is notorious for flaming out unpredictably. Thus, we have only been able to obtain a sustained reaction at a comparatively higher air flow at about $\sigma = 0.5$ - 0.8 . While in plotting Figure 28, we attempted to keep all three biomass types

on the same scale on both the x and y axis, it quickly becomes apparent that doing so will not lead to very meaningful interpretation, especially for the case of rice husks. Therefore, in Figure 29, we re-plotted Figure 28 with the x and y axes in different scales, such that we can more clearly see the trends. From this point onwards, all the color maps illustrating the different reactor performance metrics in the τ_{res} - σ space will be plotted in the rescaled version to enable better visual interpretation. Therefore, we conclude that different types of biomass behave quite differently in our lab-scale torrefaction reactor, and therefore it is necessary to carefully test each new type of biomass in order to determine the reactor's corresponding regime of operation.

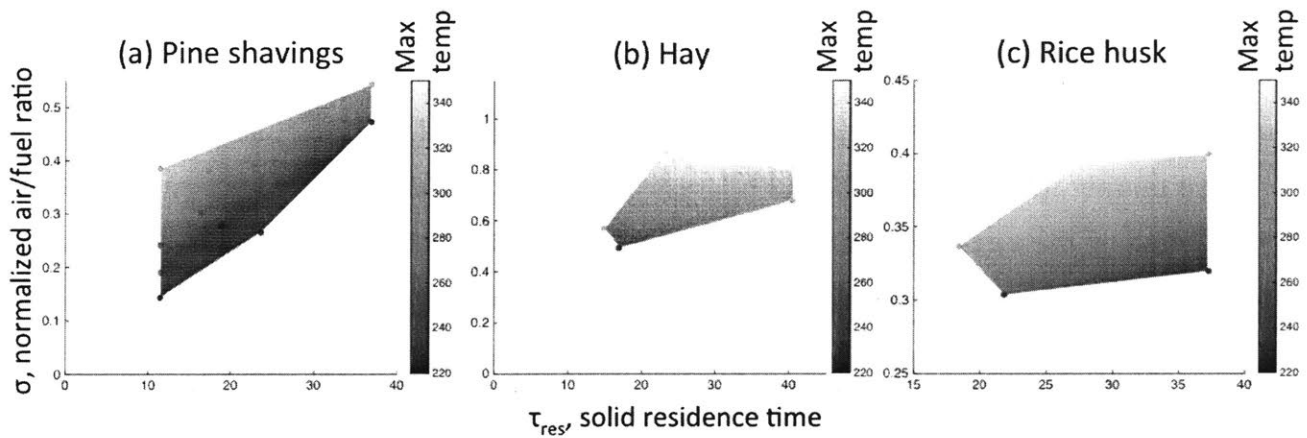


Figure 29 – Rescaled color map of temperature in different reactor conditions. Linearly interpolated maximum steady-state reactor temperatures under different operating conditions, with the solid residence time τ_{res} plotted on the x axis and the normalized air/fuel ratio σ plotted on the y axis, for three types of biomass: pine shavings (a), hay (b), and rice husks (c). Each color dot in the τ_{res} - σ space represents a real experimental data point, while the intervening color gradient swathes represent linear interpolations based on the actual experimental readouts.

We also note that in Figure 29, the interpolated temperatures are bounded in polygons. The left and right edges are typically limited by the maximum and minimum possible solid feeding rates given our lab-scale screw auger set-up. The upper edge of the polygon is frequently limited by the amount of suction that the indoor exhaust hood can provide

(typically measured at about 100-200 ft³/min): a higher σ beyond the polygon typically generates too much exhaust to be safely removed from the indoor laboratory space. Finally, the bottom edge is interesting for reactor scaling, as it is limited by the autothermal boundary: we have in general done experiments at a lower σ values than given by this bottom edge, but have found them unable to stably sustain a torrefaction reaction, and often result in reactor flame-out after initial ignition, without ever reaching a non-room-temperature steady-state temperature profile. Indeed, our observation is that as the operating conditions approach this autothermal boundary, the torrefaction reactor generally becomes less stable.

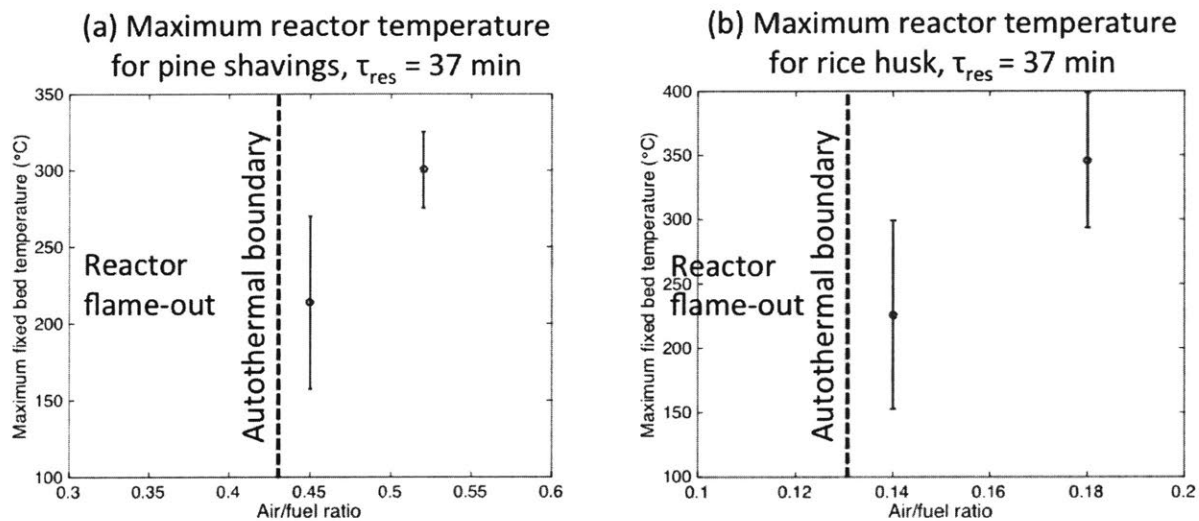


Figure 30 - The reactor becomes less stable near the autothermal boundary. By fixing the solid residence time, as we reduce the normalized air/fuel ratio towards the autothermal boundary for both the cases of pine shavings (a) and rice husks (b), we note that the variations in maximum reactor temperatures also increase, as seen by the widened error bars.

Qualitatively, we have noticed that operating near the autothermal boundary, the reactor tends to “flame out” frequently and need an external spike to return to the steady-state condition. Figure 30 quantifies this stability in greater detail: as we approach the autothermal boundary, the maximum reactor temperature decreases to about 200-250°C, which also corresponds to the normal onset autoignition temperatures of these types of

biomass as quantified by other studies (e.g. Jones *et al.*, 2015). Furthermore, as we approach the autothermal boundary, the variation in the temperature profile (denoted by the error bar) also increases, suggesting a less stable reactor prone to flaming out.

3.5 Reactor Performance Analysis

In order for the lab-scale reactor to be useful in scaling up the torrefaction reactor design, we need to define performance metrics that can be measured and optimized under different design constraints and/or requirements. In this Section, we explore a few quantifiable results under different reaction conditions: energy densification ratio, solid mass yield, solid energy yield, solid proximate analysis, solid elemental composition, and volatile elemental composition.

3.5.1 Energy Densification

One fundamental manifestation of biomass torrefaction, as discussed earlier in Section 1.2, is energy densification. We expect torrefied biomass to have a higher HHV value compared to raw (untorrefied) biomass.

Figure 31 illustrates what we call the *energy densification ratio*—defined as the ratio of higher-heating value (HHV) of torrefied biomass to the HHV of raw biomass (dry basis)—for a wider range of reactor operating conditions for all three types of biomass, plotted in the $\tau_{\text{res}}-\sigma$ phase space. As expected, we observe an increase in the index of torrefaction in response to increasing solid residence time and/or normalized air/fuel ratio (more severe torrefaction conditions). As we will see later in 0, this energy densification ratio is nothing more than what we will define as the index of torrefaction, which we will in turn use to quantify torrefaction severity and relate to other end-user design requirements. Therefore, the results in Figure 31 will be crucial in the design selection process, as we will explain later.

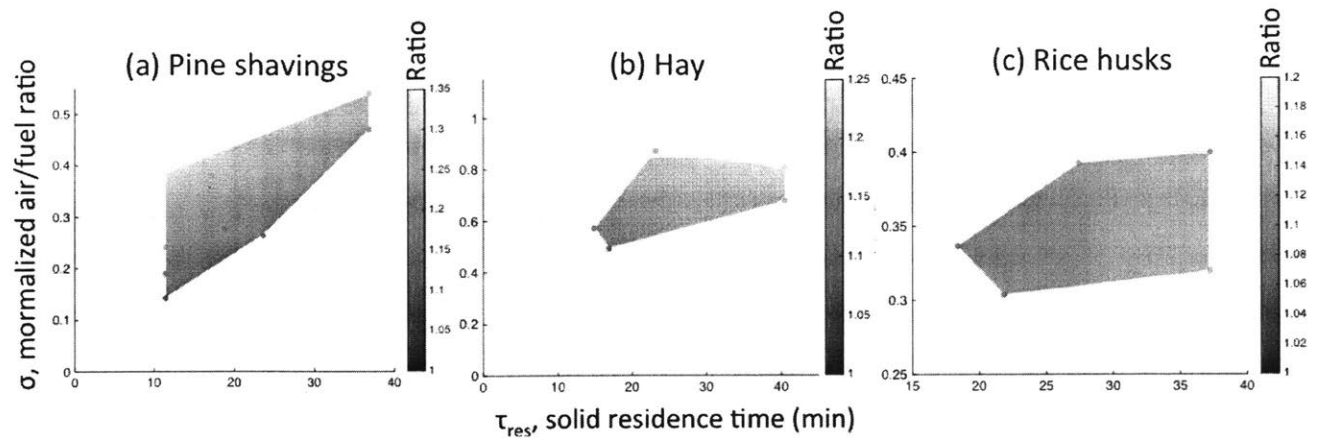


Figure 31 – The ratio of higher-heating value (HHV) of torrefied biomass to the HHV of raw biomass (dry basis)—also known as the energy densification ratio—under different reactor operating conditions (τ_{res} , σ) for three types of biomass: pine shavings (a), hay (b), and rice husk (c). Index of torrefaction increases with increasing τ_{res} and/or σ

3.5.2 Solid Mass Yield

Next, we evaluate another important performance metric: output solid mass yield, defined as the ratio of the mass flow rate of the torrefied output to the mass flow rate of the input biomass feedstock. Figure 32 illustrates this solid mass yield interpolated for different operating conditions for the three types of biomass utilized in this study. As can be observed, in general, the solid mass yield decreases with increasing torrefaction severity, from about 75% near the autothermal boundary to less than 25% under very severe torrefaction conditions. This trend is expected as a larger part of the original biomass is converted into volatile gases at a higher torrefaction temperature (due to faster solid devolatilization kinetics).

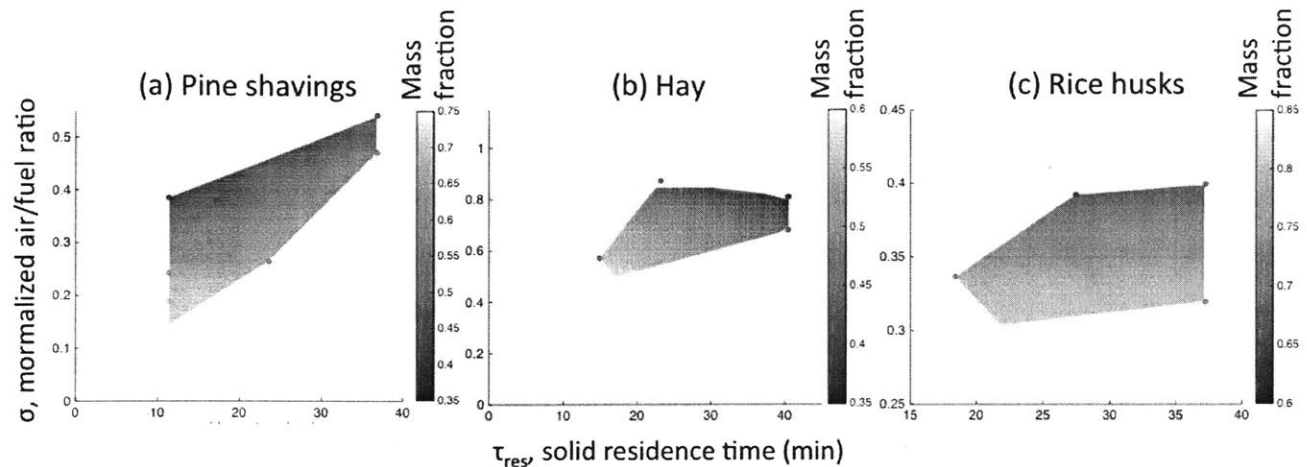


Figure 32 - Mass yield of output torrefied product under different reactor operating conditions (τ_{res} , σ) for three types of biomass: pine shavings (a), hay (b), and rice husk (c). The solid mass yield decreases with increasing τ_{res} and/or σ .

We can already observe that there is a trade-off between the index of torrefaction and the solid product mass yield as we increase the torrefaction severity and/or solid residence time: while a higher index of torrefaction signals that the original biomass has become much more energy dense (per mass unit of output), we are at the same time losing product mass. In order to appreciate how strongly these two competing forces play out, we define another performance metric: solid energy yield, to be quantified in the next Section.

3.5.3 Solid Energy Yield

The solid energy yield is defined as the fraction of the energy contained in the original raw biomass that is still retained in the solid phase after the torrefaction treatment. We do not have a good experimental apparatus to directly measure the energy input and output from the reactor, but we note that the solid product energy yield can be calculated as the product between the solid product mass yield and the index of torrefaction:

$$\text{Solid product energy yield} = \text{Solid product mass yield} \times \text{Index of torrefaction.}$$

Figure 33 shows the result of this calculation for different reactor operating conditions for the three different types of biomass. We observe that as torrefaction severity increases, the

reduction in the solid product mass yield outweighs any increase in the energy densification (index of torrefaction), such that there is a net reduction in the solid product energy yield. For pine shavings and hay, this energy yield ranges from about 80% near the autothermal boundary to less than 50% under severe torrefaction conditions. In the case of rice husk, over a much narrower range of normalized air/fuel ratio, the overall solid product energy yield decreases from about 80% to 70%.

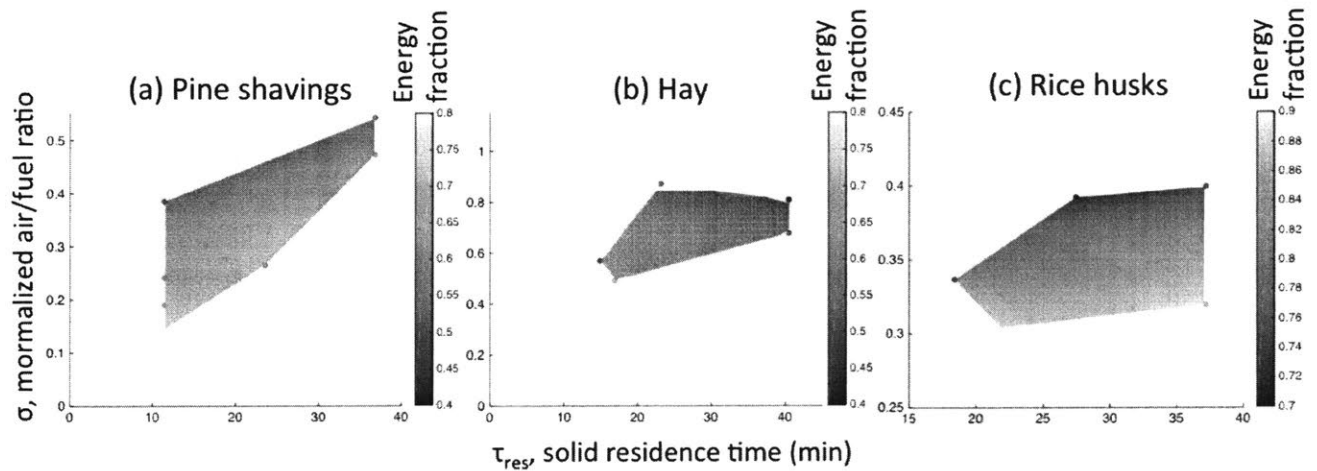


Figure 33 - Energy yield of output torrefied product under different reactor operating conditions (τ_{res} , σ) for three types of biomass: pine shavings (a), hay (b), and rice husk (c). The solid mass yield decreases with increasing τ_{res} and/or σ .

3.5.4 Solid Proximate Analysis

Next, we examined the underlying changes in the chemical component of the biomass. Figure 34, which shows the results from the proximate analysis on the different torrefied outputs, indicates that as the torrefaction severity increases (increasing normalized air/fuel ratio, the mass fraction of fixed carbon in the remaining torrefied biomass increases, while that of volatile matter decreases. This agrees with our understanding of torrefaction, which drives out the volatile matter from the raw biomass, resulting in a product that contains less volatiles and more fixed carbon.

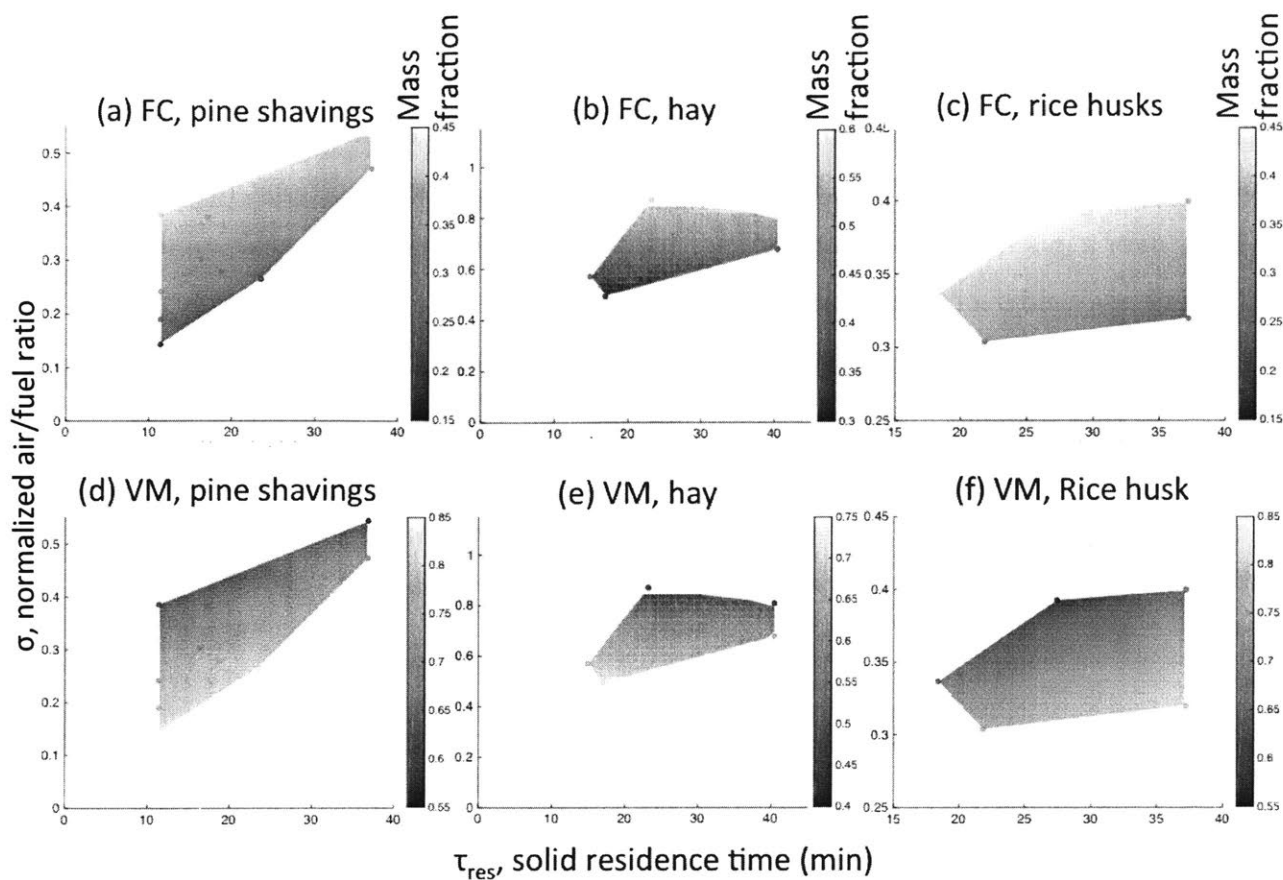


Figure 34 – Proximate analysis on the torrefied biomass samples under different reaction conditions for pine shavings (a: fixed carbon; d: volatile matter), hay (b: fixed carbon; e: volatile matter), and rice husks (c: fixed carbon; f: volatile matter).

3.5.5 Solid Elemental Analysis

Next, we examined the elemental composition of the torrefied output, and how such composition was altered by the different torrefaction conditions. As can be seen in Figure 35, for the torrefied output from all types of biomass, the elemental carbon mass fraction increases with increasing torrefaction severity. On the other hand, both elemental oxygen and hydrogen decreases as torrefaction becomes more severe. This makes sense, as torrefaction is well known to drive out the low-energy molecules (rich in hydrogen and oxygen) and preserve the carbon in the torrefied biomass.

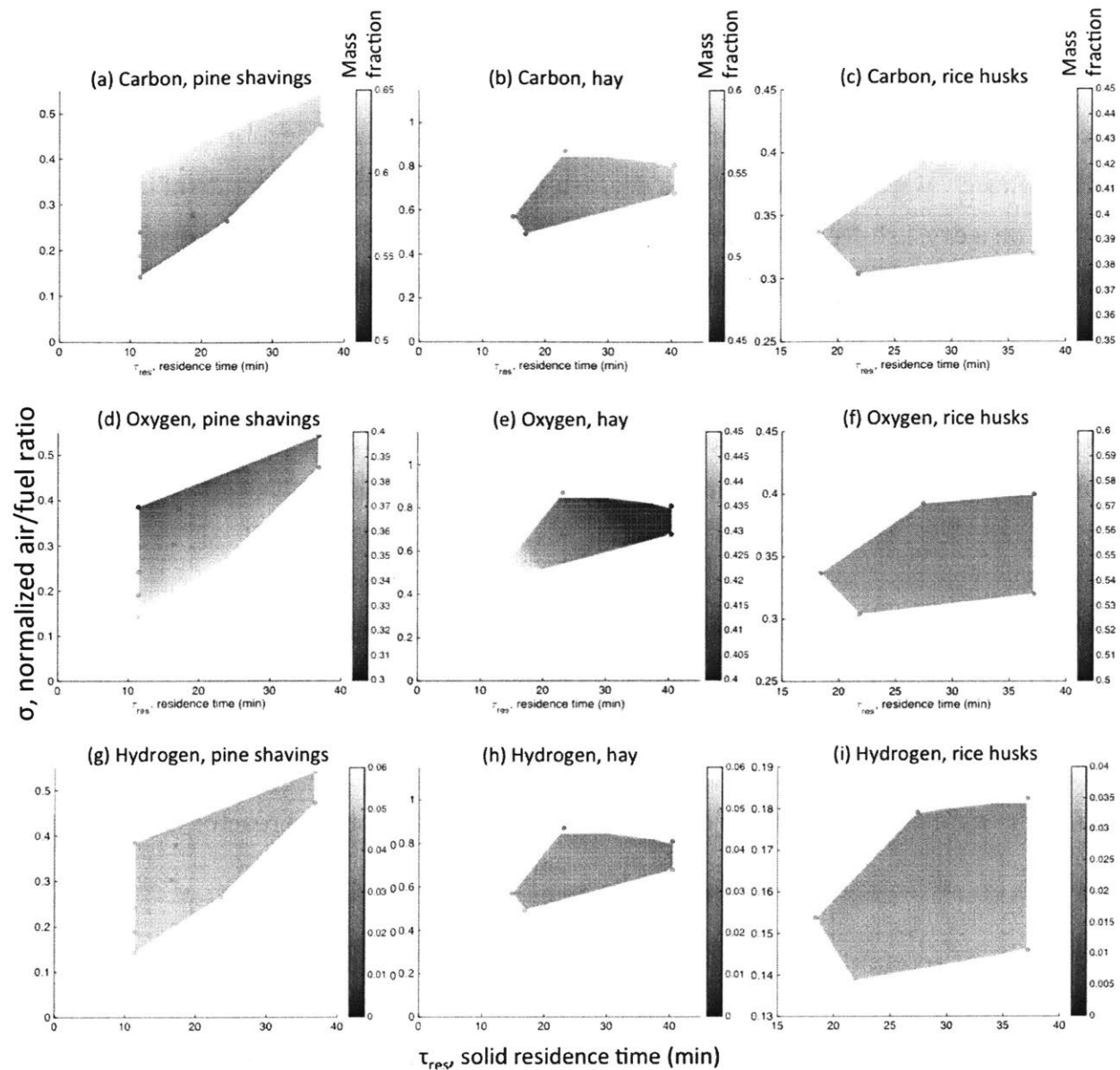


Figure 35 – Ultimate (elemental) analysis on the torrefied biomass samples under different reaction conditions for pine shavings (a: carbon, d: oxygen, g: hydrogen), hay (b: carbon, e: oxygen, h: hydrogen), and rice husks (c: carbon, f: oxygen, i: hydrogen).

3.5.6 Volatile Elemental Analysis

While we do not have an experimental means of measuring the composition of the gaseous exhaust stream, we can estimate the mixture's chemical composition in general terms based on the solid-phase elemental analyses and based on mass closure.

For a given torrefaction experiment, consider the initial input biomass with mass flow rate of \dot{m}_{BM} , a moisture content of Y_{M} , and ash content of Y_{ash} , with ash and moisture contents determined using the method of proximate analysis as described in Section 3.3.2, and with both of whose values are reported on a dry, ash-free basis. Then the flow rate of incoming biomass on a dry, ash-free (DAF) basis is given by $\dot{m}_{\text{BM}}/(1 + Y_{\text{M}} + Y_{\text{ash}})$. We assume that while the moisture component in the input biomass can devolatilize, the ash component is always inert and will stay within the solid torrefied output. Let us also consider the elemental composition (also on a dry, ash-free basis) of the raw input biomass as (Y_{C} , Y_{H} , and Y_{O}) in terms of carbon, hydrogen, and oxygen atoms respectively. This means that the total mass flow rate of carbon atoms $\dot{m}_{\text{C,BM}}$ going into the reactor is given by

$$\dot{m}_{\text{C,BM}} = \frac{\dot{m}_{\text{BM}} Y_{\text{C}}}{1 + Y_{\text{M}} + Y_{\text{ash}}}$$

By the same reason, the total mass flow rate of hydrogen atoms $\dot{m}_{\text{H,BM}}$ going into the reactor (does not include the hydrogen in the biomass moisture) is given by

$$\dot{m}_{\text{H,BM}} = \frac{\dot{m}_{\text{BM}} Y_{\text{H}}}{1 + Y_{\text{M}} + Y_{\text{ash}}}$$

Finally, the total mass flow rate of oxygen atoms $\dot{m}_{\text{O,BM}}$ going into the reactor is given by

$$\dot{m}_{\text{O,BM}} = \frac{\dot{m}_{\text{BM}} Y_{\text{O}}}{1 + Y_{\text{M}} + Y_{\text{ash}}}$$

once again not accounting for the oxygen contained in the biomass moisture.

On the other hand, with the mass flow rate of the output torrefied biomass measured as \dot{m}_{char} , we can then also write the outgoing flow rate $\dot{m}_{i,\text{char}}$ of the i th element of carbon, hydrogen, and oxygen atoms in the torrefied output product as:

$$\dot{m}_{i,\text{char}} = \frac{Y_i}{1 + Y_{\text{ash}}^*} \dot{m}_{\text{char}}$$

where Y_i is the i th component (carbon, hydrogen, oxygen) in the ultimate (elemental) analysis of the torrefied output, and Y_{ash}^* is the newly measured ash content in the torrefied output.

Now, let us turn our attention to the *volatile* component—this consists of the total volatile mixture (excluding moisture from the biomass drying process) that is emitted from the biomass as it travels through the reactor due to torrefaction. Because this volatile mixture is instantaneously mixed with incoming air and oxidized, even if we had analytical chemistry equipment at our disposal, this chemical information would be extremely difficult to measure. While experimentally determining its chemical composition is beyond the scope of this Chapter, based on the mass closure on the individual elements (carbon, hydrogen, oxygen, and nitrogen) from prior results from the solid-phase ultimate (elemental) analysis, we can nonetheless write the lump-sum mass flow rates of the carbon, hydrogen, and oxygen atoms in the volatile species ($\dot{m}_{C,\text{vol}}$, $\dot{m}_{H,\text{vol}}$, and $\dot{m}_{O,\text{vol}}$) as:

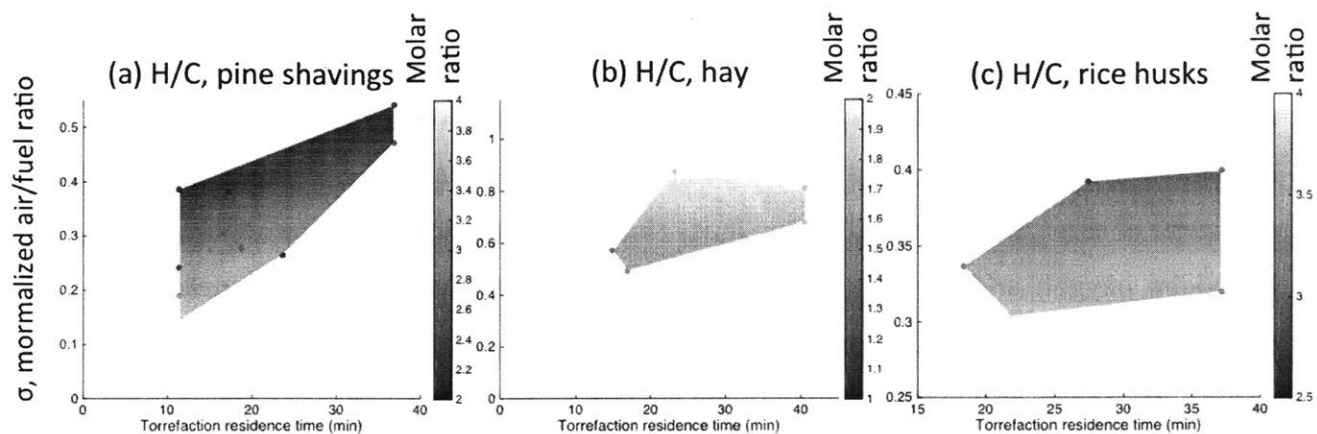
$$\begin{aligned}\dot{m}_{C,\text{vol}} &= \dot{m}_{C,\text{BM}} - \dot{m}_{C,\text{char}}, \\ \dot{m}_{H,\text{vol}} &= \dot{m}_{H,\text{BM}} - \dot{m}_{H,\text{char}}, \\ \dot{m}_{O,\text{vol}} &= \dot{m}_{O,\text{BM}} - \dot{m}_{O,\text{char}}.\end{aligned}$$

This implies that the elemental composition of the volatile species, in the lump-sum molar form CH_xO_y , can be computed as follows:

$$\begin{aligned}x &= \frac{\dot{m}_{H,\text{vol}} \text{MW}_C}{\dot{m}_{C,\text{vol}} \text{MW}_H}, \\ y &= \frac{\dot{m}_{O,\text{vol}} \text{MW}_C}{\dot{m}_{C,\text{vol}} \text{MW}_O}.\end{aligned}$$

In other words, x denotes the molar ratio of hydrogen atoms to carbon atoms in the unknown component of the reactor exhaust, and y denotes the molar ratio of oxygen atoms to carbon atoms. Judging from Figure 36, we can see that different types of biomass exhibit different chemistries. While for pine shavings and rice husks, increasing torrefaction severity leads to an increased H/C molar ratio, the opposite appears to be true for hay. On the other hand, all three types of biomass uniformly exhibit increasing molar O/C ratio with decreasing torrefaction severity, suggesting that under mild torrefaction, the volatile mixture is likely more “oxidized” and, therefore, lower in calorific value. Furthermore, there is a large range of H/C and O/C ratios for the different types of biomass. For example, while for pine shavings, the O/C molar ratio is in the range of 1-2, in the case of rice husks, this range is between 1 and 1.5, suggesting that for pine shavings, the volatile component comes more “oxidized”, and therefore potentially, has lower calorific value when further oxidized.

H/C molar ratio in the volatile component



O/C molar ratio in the volatile component

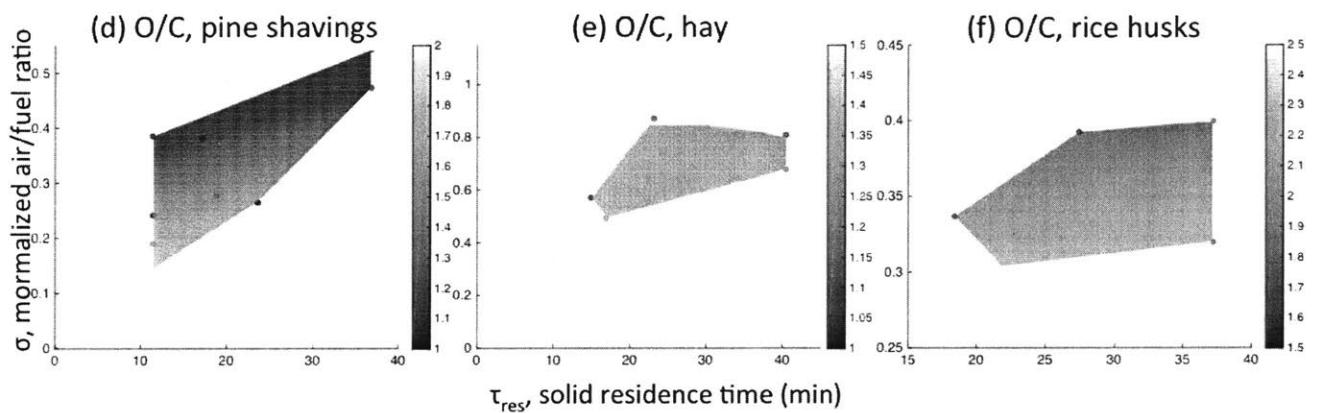


Figure 36 – Estimated elemental composition of the volatile component emitted from the biomass torrefaction process (excluding drying-associated moisture). (a-c) Estimated molar ratio of hydrogen to carbon under different reaction conditions for pine shavings (a), hay (b), and rice husks (c); and (d-f) estimated molar ratio of oxygen to carbon under different reaction conditions for pine shavings (d), hay (e), and rice husks (f).

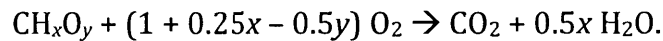
As a sanity check, we compared these elemental compositions with those reported in the literature. Bates and Ghoniem (2012), for example, in devising a devolatilization kinetics description of willow torrefaction, reported that the volatiles can be approximated as two lump-sum mixture of species, one (V1) dominant at low torrefaction severity and the other one (V2) at high torrefaction severity. From their study, the elemental formula for V1 is

$\text{CH}_{4.7}\text{O}_{3.1}$, while that for V2 is $\text{CH}_{3.0}\text{O}_{1.15}$. We therefore see that the values for the H/C and O/C molar ratios that we calculated in our reactor performance are generally consistent with what is expected in torrefaction, and that with the exception of hay, the H/C and O/C ratios exhibit the same trend (decreasing value) as a function of increasing torrefaction severity, signifying volatile molecules at an increasingly higher energy state.

It will also be crucial to understand how much chemical energy is contained in the volatile species, in order to understand how the torrefaction reaction can be made autothermal. We save a more detailed discussion (and experimental characterization) for later in Section 5.5.2.

3.5.7 Nature of Primary Oxidation

While we do not know the individual species, we can also devise a clever method to try to evaluate the nature of the oxidation reaction occurs in a low-temperature environment within the reactor. By considering the volatile species of the general form CH_xO_y as determined in the previous Section, we can then balance the chemical equation for idealized complete oxidation as:



This means for each kilogram of volatile of the form CH_xO_y , the mass [kg] of oxygen needed to fully oxidize the volatile $\dot{m}_{\text{O,stoic}}$ is given by:

$$\dot{m}_{\text{O,stoic}} \equiv \frac{\text{MW}_{\text{O}}}{\text{MW}_{\text{CH}_x\text{O}_y}} \left(\frac{\dot{m}_{\text{BM}}}{1 + Y_{\text{M}}} - \dot{m}_{\text{char}} \right) (2 + 0.5x - y).$$

At the same time, in reality, we have a constant supply of primary air coming into the reactor, which contributes to a mass flow rate of oxygen atoms $\dot{m}_{\text{O,air}}$ as follows:

$$\dot{m}_{\text{O,air}} = \frac{\text{MW}_{\text{O}_2}}{4.76\text{MW}_{\text{air}}} (\text{AF})_{\text{stoic}} \sigma \dot{m}_{\text{BM}},$$

where $(\text{AF})_{\text{stoic}}$ is defined as the mass ratio of the amount of air to the amount of biomass (as received) to enable stoichiometric oxidation, as discussed previously in Section 3.2.2. Putting this together, we can define an *ersatz* air-to-volatile equivalence ratio σ_{AV} as

$$\sigma_{\text{AV}} \equiv \dot{m}_{\text{O,air}} / \dot{m}_{\text{O,stoic}}.$$

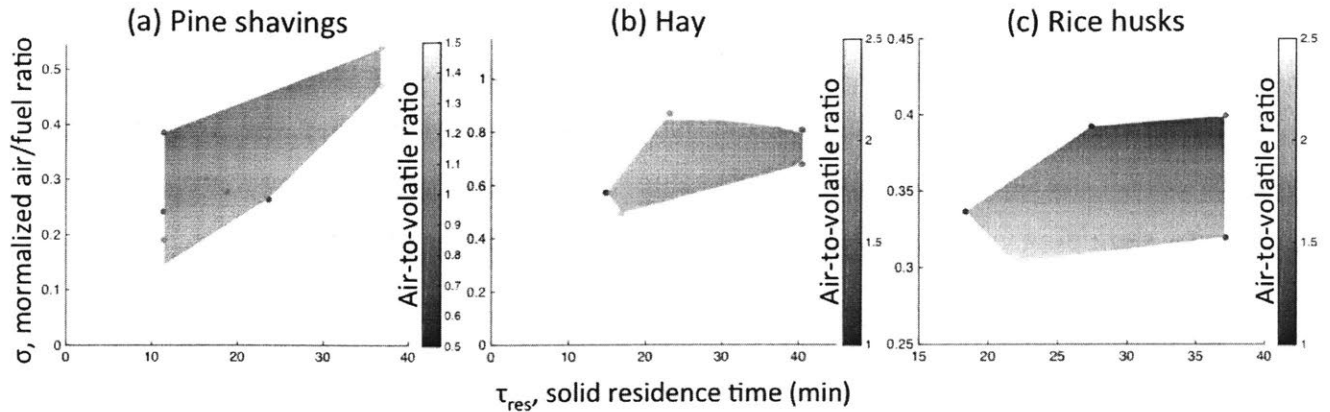


Figure 37 – Primary air-to-volatile equivalence ratio under different reaction conditions for pine shavings (a), hay (b), and rice husks (c).

As shown in Figure 37, the torrefaction reactor operates almost always in the air-rich side ($\sigma_{AV} > 1$) with respect to the oxidizable volatile mixture, except for very severe torrefaction where the devolatilization process may be so vigorous that the volatile flow rate overwhelms the air supply, resulting in incomplete combustion. This suggests that in almost all reaction conditions, there is an excess of air in the reactor exhaust as well.

3.5.8 Composition of Reactor Exhaust

By mass closure, we can then define the total mass flow rate of the exhaust gas from the reactor \dot{m}_{exh} as

$$\dot{m}_{\text{exh}} = (1 + (AF)_{\text{stoic}}\sigma)\dot{m}_{\text{BM}} - \dot{m}_{\text{char}}$$

Dividing this quantity by the cross-sectional area of the reactor gives us a scalable quantity that relates to the mass flux of the reactor exhaust. We plot this quantity in Figure 38, and note that the reactor exhaust mass flux increases with increasing torrefaction severity (more outgassing as well as primary air influx) as well as a shorter residence time (higher solid flux through the reactor, and therefore a higher matching gas flux as well).

This exhaust constitutes a mixture of *known* and *unknown* species. The known species consist of: (a) the nitrogen gas—assumed to be unreactive—that is introduced with primary air into the reactor and accompanies the reactor exhaust still as nitrogen gas, and (b) steam that is derived from drying of biomass (not associated with any additional steam

contribution from the torrefaction reaction). The unknown species consist of: (a) any unreacted or partially reacted torrefaction volatile gas mixture, (b) post-combustion products such as CO₂ and H₂O in unknown proportion, as well as (c) any unreacted oxygen.

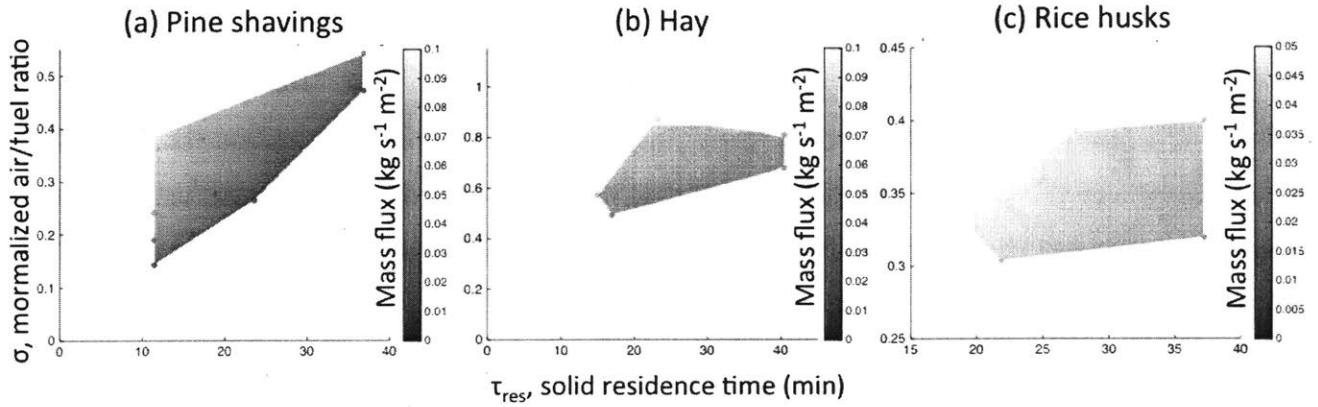


Figure 38 – Estimated reactor exhaust mass flux [$\text{kg s}^{-1} \text{m}^{-2}$] under different reaction conditions for pine shavings (a), hay (b), and rice husks (c), as determined by mass closure.

While a detailed characterization of all chemical species is beyond the scope of this study, we will characterize the mass fractions of the two known species in the exhaust mixture as an example. Unreacted nitrogen is the easy one, as its mass flow rate $\dot{m}_{\text{N,air}}$ can be calculated from knowing how much air we are letting into the reactor:

$$\dot{m}_{\text{N,air}} = \frac{3.76 \text{MW}_{\text{N}_2}}{4.76 \text{MW}_{\text{air}}} (\text{AF})_{\text{stoic}} \sigma \dot{m}_{\text{BM}}$$

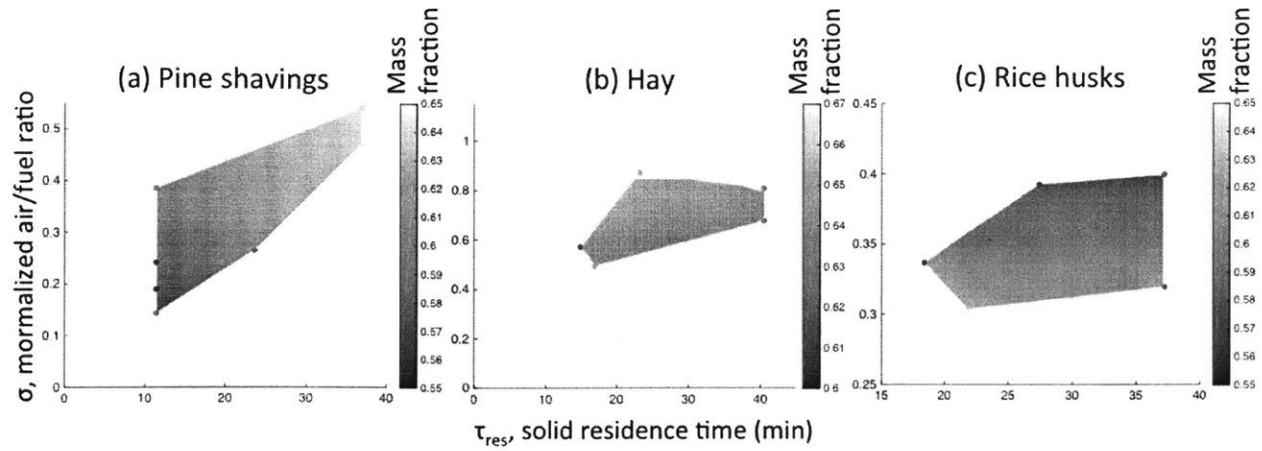
Hence, we can calculate the mass fraction of nitrogen in the reactor exhaust as:

$$Y_{\text{N}_2} = \dot{m}_{\text{N,air}} / \dot{m}_{\text{exh}}$$

Likewise, the mass fraction of the steam from biomass moisture in the drying process is:

$$Y_{\text{moisture}} = \frac{Y_M}{1 + Y_M + Y_{\text{ash}}} \frac{\dot{m}_{\text{BM}}}{\dot{m}_{\text{exh}}}$$

N₂ mass fraction in reactor exhaust



Moisture mass fraction in reactor exhaust

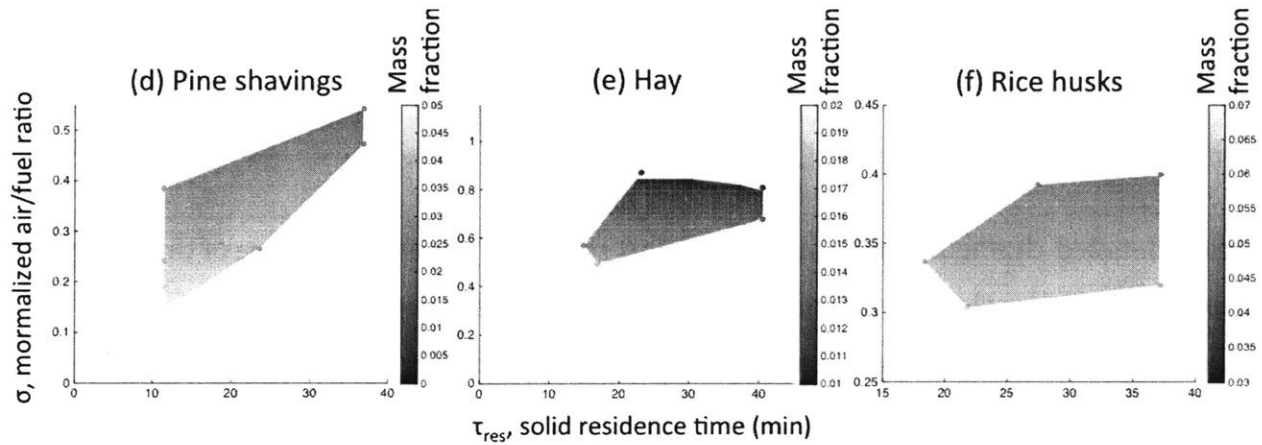


Figure 39 – Estimated chemical composition of known species in the reactor exhaust. (a-c) Estimated nitrogen mass fraction analysis in the reactor exhaust under different reaction conditions for pine shavings (a), hay (b), and rice husks (c); and (d-f) estimated moisture mass fraction associated with biomass drying in the reactor exhaust for pine shavings (d), hay (e), and rice husks (f).

The mass fractions of these two “known” species are plotted in Figure 39 for nitrogen (Panels a-c) and for the moisture derived from biomass drying (Panels d-f). For nitrogen mass fraction, consider that normal air has about 77% of N₂ by mass. The fact that it is lowered to about 55-65% by mass in the reactor exhaust implies dilution by volatile gases and moisture. We note that the dilution of N₂ fraction is most significant in the mild

torrefaction regime for all types of biomass. One possible explanation is that the increase in the mass flow of air to support a more severe torrefaction process is more than the increase in the mass flow of the volatiles being emitted from the biomass. This makes sense from the perspective that an increasing torrefaction severity increases the overall calorific value of the volatile gases from the biomass, such that the volatile mixture shifts away from being abundant in inert and low-energy species (such as H_2O , CO_2 , CO , etc. that is more oxygen-rich and less carbon-rich) that do not require much more additional oxygen to combust to completion, to being more abundant in high-energy species (such as organic acids and methanol that is more carbon-rich and less oxygen-rich) that require much more oxygen (and hence air) to combust to completion (Bates and Ghoniem, 2012). This increasing air-volatile stoichiometric combustion ratio as the torrefaction reaction increases in severity likely accounts for the higher requirement in air, and hence, smaller dilution of N_2 in the reactor exhaust.

Panels (d-f) of Figure 39 tell a similar story with respect to the moisture escaping from the biomass drying process. Its mass fraction is most significant in the mild torrefaction regime, due to that there is not much volatile gases to begin. As the torrefaction increases in severity, the increasing flow rate of volatile gases implies that the moisture fraction becomes further diluted.

3.6 Characterization of Uncertainties

In the previous section, we quantified various performance metrics—including the mass and energy yields, the energy densification ratio, as well as the proximate and elemental analyses—under various solid residence times and normalized air/fuel ratios. However, how confident are we about the reactor performance? In order to answer this question, we undertake an error analysis of the various measurement inputs and outputs. First, we divide the uncertainty ranges into two categories: intrinsic and extrinsic. Intrinsic uncertainties are those directly associated with the instrument readout. Extrinsic uncertainties are those associated with the variability in the reactor process and operations.

3.6.1 Intrinsic Uncertainties

The first type of uncertainty comes from the inherent instrument readout errors. For example, if a mass flow controller indicates that the flow rate is 3.0 L min^{-1} , how confident are we that the actual value is indeed 3.0 L min^{-1} , rather than 2.9 L min^{-1} or 2.5 L min^{-1} ? Table 13 lists the various instruments that we used in the process of reactor validation, as well as their advertised intrinsic uncertainty ranges.

Table 13 – Summary of various instruments used in the reactor performance characterization and their intrinsic uncertainty ranges in the readout signals.

Quantity	Instrument	Uncertainty range
Mass flow, primary air	Omega FMA5528A	Max of $\pm 1.5\%$ and $\pm 0.1 \text{ L/m}$
Temperature	Omega	Max of $\pm 0.4\%$ and $\pm 1.1 \text{ K}$
Solid mass (in/out)	Dr. Meter ES-PS01	Max of $\pm 1\%$ and $\pm 5 \text{ g}$
Proximate analysis	TA Instruments Q50	Max of $\pm 0.01\%$ and $\pm 0.1 \mu\text{g}$
Elemental analysis	FlashEA 1112	$\pm 2.0\%$
Solid higher heating value	Parr Instruments 6200	Max of $\pm 3\%$ and $\pm 0.5 \text{ MJ kg}^{-1}$

3.6.2 Extrinsic Uncertainties

Next, there are also operation-related uncertainties on top of the instrumental uncertainties. These are related to considerations such as that the current laboratory-scale reactor is an imperfect replica of an ultimate continuous-process in the scaled-up version. These uncertainties, specifically, describe the observed variations in repeated data measurements *while assuming* that the measurement instrument values are completely accurate. As an example, instead of metering the biomass feed precisely using an elaborate hopper system, for the purpose of laboratory-scale validation, the feeding had been manual, timed at regular intervals of 1-2 minutes each in order to keep the top of the biomass moving bed at a certain level. Once every 20-30 minutes during the steady state

reactor operation, we would measure the weight loss in the raw biomass feedstock, as well as the weight gain in the collected torrefied biomass on the readout from a digital balance (Dr. Meter ES-PS01), which has a known instrument uncertainty range of $\pm 1\%$ (or ± 5 grams, whichever is greater). *Even if we ignore this instrument uncertainty range, and assume that the weight measurement readout is absolutely accurate (with 0% uncertainty), nonetheless each time we repeat the weight measurement at different time points in the course of the steady-state torrefaction reactor experiment, we note in Table 14 that there are some variations in the mass in- and out-flow rates that we recorded. In this case, this variation is not related to the accuracy of the instrument, but rather to the inhomogeneity in the laboratory-scale reactor operation, and should be characterized as an uncertainty range accordingly, as we will calculate below.*

Table 14 – Sample uncertainty calculation for solid mass flow rates and mass yields

Biomass in	Torrefied biomass out	Calculated solid mass yield
900 g/h	570 g/h	63%
840 g/h	410 g/h	49%
470 g/h	410 g/h	88%
830 g/h	550 g/h	66%
860 g/h	350 g/h	41%
880 g/h	370 g/h	42%
690 g/h	440 g/h	64%
1030 g/h	550 g/h	53%
1110 g/h	420 g/h	38%

To calculate an uncertainty range from the data in Table 14, we first start by computing the mean input biomass flow rate, which is 850 g/h in this case, with a standard deviation of ± 190 g/h. Assuming a Gaussian distribution of the measurement values, and given 9 sample sizes, this gives us a 95% confidence interval of $\pm 190 \text{ g/h} / \sqrt{9} \times 1.95 = \pm 120 \text{ g/h}$, or $\pm 14\%$ of the mean. Likewise, we can calculate that the mean output torrefied biomass mass flow rate is 450 g/h, with a standard deviation of ± 80 g/h and a 95% confidence interval of

±50 g/h, or ±11% of the mean. The ratio of the output flow rate to the input flow rate—which defines the solid mass yield—has a mean value of 56%, with a standard deviation of ±16% and a 95% confidence interval of ±10%, or ±18% of the mean.

We can similarly compute the operated-related uncertainties associated with other variables (such as temperature and emissions) using the same replication method as above. These uncertainty ranges are summarized in Table 15.

Table 15 – Summary of the uncertainty ranges associated with reactor operation with respect to various relevant variables.

Quantity	Uncertainty range (% of the mean)
Input biomass mass flow rate	±14%
Output torrefied biomass mass flow rate	±11%
Solid residence time	±14%
Solid mass yield	±18%
Solid higher heating value	±3%
Energy densification ratio	±12%
Solid energy yield	±31%
Proximate analysis, volatile matter	±0.5%
Proximate analysis, fixed carbon	±14%
Proximate analysis, ash	±19%
Proximate analysis, moisture	±34%
Elemental analysis, carbon	±1.0%
Elemental analysis, oxygen	±1.2%
Elemental analysis, hydrogen	±0.1%

We note that in general, the extrinsic uncertainty ranges are much larger than the corresponding intrinsic uncertainty ranges, which suggests that there is a high degree of variability in our laboratory-scale torrefaction process. For example, while the TGA measures mass very accurately to a level of ±0.01%, the moisture content as determined by

proximate analysis indicates a 34% uncertainty with respect to the mean value. This can be explained by the fact that moisture in the sample can vary greatly depending on the prevalent atmospheric conditions, as the samples are stored in ambient air.

There are various quantities—such as the normalized air/fuel ratio—that have negligible extrinsic uncertainty ranges. The reason in this case is because once the mass flow meter is set to a specific value, this value is unaffected by the fluctuations in the biomass torrefaction process. Therefore, the overall uncertainty range normalized air/fuel ratio is only limited to the intrinsic uncertainty of the instrument.

We can use the classical error propagation technique to infer overall uncertainty ranges. As an illustration, the energy densification ratio is the division of two higher heating values, each having an extrinsic uncertainty range of $\pm 3\%$ as well as an intrinsic uncertainty range of $\pm 3\%$. Dividing two values means that their relative uncertainty ranges are summed, resulting in a final uncertainty range of $\pm 12\%$. On the other hand, the solid energy yield is calculated by multiplying the solid mass yield (extrinsic uncertainty of $\pm 18\%$ and intrinsic uncertainty of $\pm 1\%$) by the energy densification ratio ($\pm 12\%$). Because both of these values carry large relative uncertainty ranges, the relative uncertainty range for the solid energy yield is even greater ($\pm 31\%$). Therefore, all inferred/calculated values that are not directly measured from experiments tend to carry higher uncertainty ranges. We can undertake similar calculations for the uncertainty ranges of other quantities (such as the predicted mass fractions of various species in the exhaust) not listed in Table 15.

In general, we can see that all of the performance metrics carry an uncertainty range of less than 34% of the mean, which is reasonable given the highly heterogeneous nature of the biomass torrefaction process.

3.7 Comparison of Performance Metrics with Existing Lab-Scale Reactors

This study is not complete without a comparison of the performance metrics of our lab-scale torrefaction reactor with those of other similar lab-scale reactors in the literature. As

mentioned previously, many of these existing lab-scale torrefaction reactors often operate in artificial conditions (e.g. perfectly inert N₂ environment, with externally supplied heat source). Therefore, an important goal of this study is to identify and quantify the extent of any differences in the reactor performance metrics under different operating conditions between existing studies and our study.

Due to the paucity of available data for hay and rice husk, in this section we focus on pine feedstock, which is of a better-studied woody type in the literature. From the literature, we have recovered the index of torrefaction, mass yield, and energy yield data from two main studies. The first by McNamee *et al.* (2016) examines the torrefaction of North American pine in a horizontal tube furnace that has a constant flow of nitrogen. The second by Grigante and Antolini (2014) curates the torrefaction data of Italian spruce pine in a vertical fixed-bed reactor that has a constant flow of electrically preheated nitrogen. A compilation of the experimental data points from these two studies is given in Table 16.

Table 16 - Compilation of pine torrefaction data points from the literature utilized for comparison with our experimental data.

Temperature	Residence time	Mass yield	Index of torrefaction	Energy yield	Source
250°C	30 min	90.7%	1.01	91.3%	McNamee <i>et al.</i> (2016)
270°C	30 min	85.0%	1.05	89.2%	McNamee <i>et al.</i> (2016)
270°C	60 min	76.7%	1.09	83.8%	McNamee <i>et al.</i> (2016)
290°C	30 min	72.2%	1.16	84.0%	McNamee <i>et al.</i> (2016)
265°C	49 min	89.3%	1.07	95.9%	Grigante & Antolini (2014)
280°C	20 min	89.4%	1.08	96.2%	Grigante & Antolini (2014)
295°C	30 min	80.2%	1.12	90.1%	Grigante & Antolini (2014)
310°C	17 min	79.1%	1.12	88.5%	Grigante & Antolini (2014)
310°C	36 min	69.0%	1.16	80.1%	Grigante & Antolini (2014)

Unlike our study, both McNamee *et al.* and Grigiante & Antolini use the reactor temperature rather than the normalized air/fuel ratio as one of the independent variables, because in their reactors—both of which operate under inert conditions (N_2)—the use of air intake to modulate the reactor temperature is not a meaningful concept in informing the reactor operating condition and design. In Figure 40, we plot the indices of torrefaction in the temperature-residence time phase space, for our lab-scale reactor (a) and for the two comparative studies (b). In the color scale bar, blue dots indicate low indices of torrefaction and yellow dots signify high indices of torrefaction.

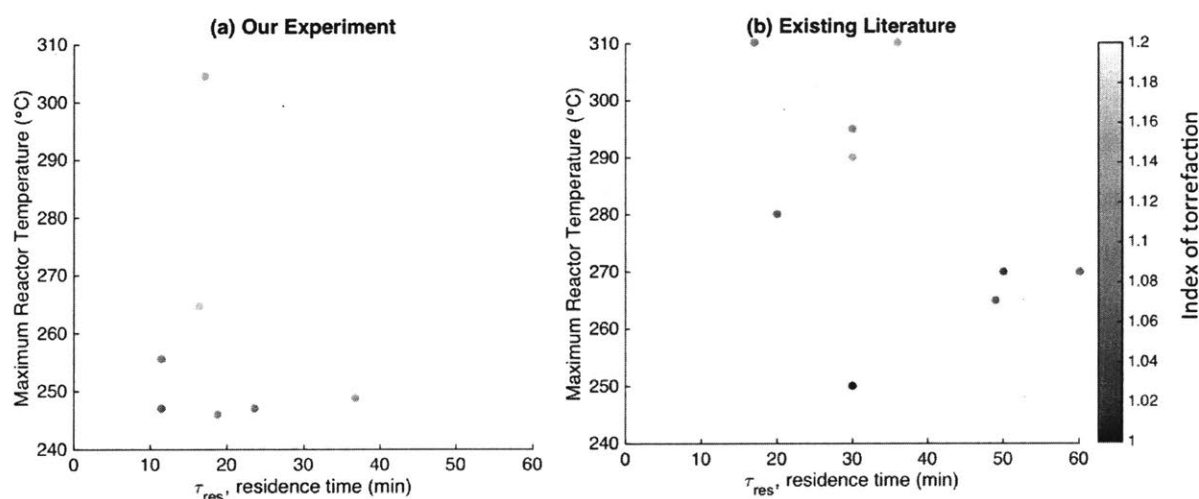


Figure 40 – Comparison of indices of torrefaction under different maximum reactor temperatures and residence times for our lab-scale reactor (a) and for data compiled from the existing literature (b) for pine shavings. Blue dots reflect low indices of torrefaction and yellow dots reflect high indices of torrefaction.

In both our lab-scale reactor and the existing literature, there is a dominant dependence of the index of torrefaction on the maximum reactor temperature (which, in our reactor design, is related to the normalized air/fuel ratio). There is a much weaker dependence of the index of torrefaction on the solid residence time in both cases. However, in our experiment, the indices of torrefaction for similar temperature-residence time combinations appear to be consistently higher than those obtained in the literature.

Because the colored dots are relatively difficult to visualize and compare, we interpolate and re-plot Figure 40 over the range of torrefaction conditions of interest in Figure 41, and from the color gradients, the differences described above are much more easily visualized.

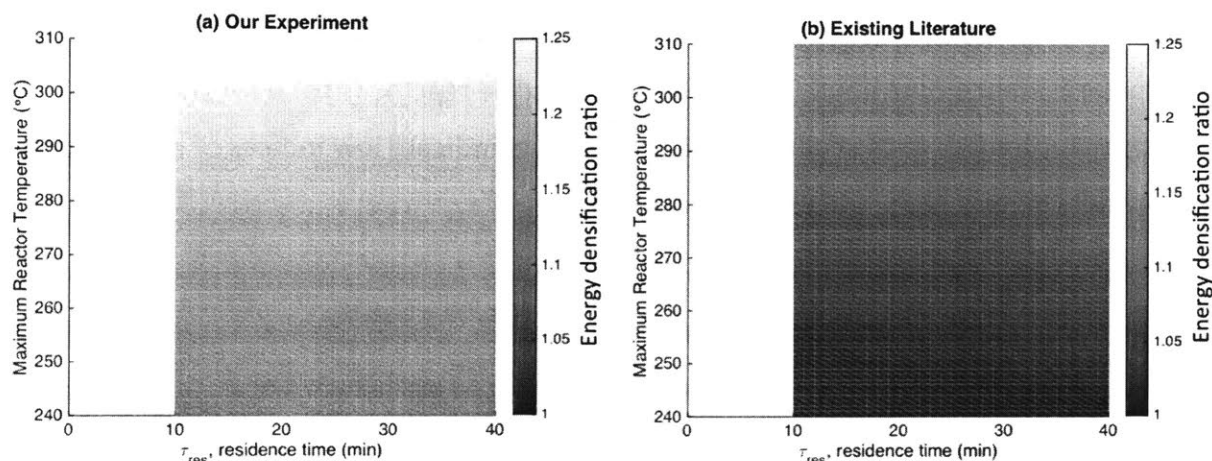


Figure 41 – Comparison of indices of torrefaction under different maximum reactor temperatures and residence times for our lab-scale reactor (a) and for data compiled from the existing literature (b) for pine shavings, interpolated from Figure 40 over a range of torrefaction conditions of interest.

To explore this difference more quantitatively, we interpolated the indices of torrefaction over the entire temperature-residence time phase space for both cases, and took the ratio of the indices of torrefaction for our reactor set-up in comparison to the existing literature data (Figure 42a). Here, as consistent with our observations in Figure 40, the interpolated indices of torrefaction in our lab-scale reactor are about 10-20% higher compared to the existing literature interpolation at a given temperature-residence time condition. This effect is most pronounced in the low-temperature, short-residence-time regime.

In the same vein, we can compare the solid mass yields in Figure 42b by their ratios, and note that our test reactor produces about 30-50% less solid mass yield compared to the existing literature. The combined effect of increased index of torrefaction and decreased solid mass yield is captured in Figure 42c, which shows a general 20-40% decrease in the solid mass yield in our test reactor compared to the existing literature.

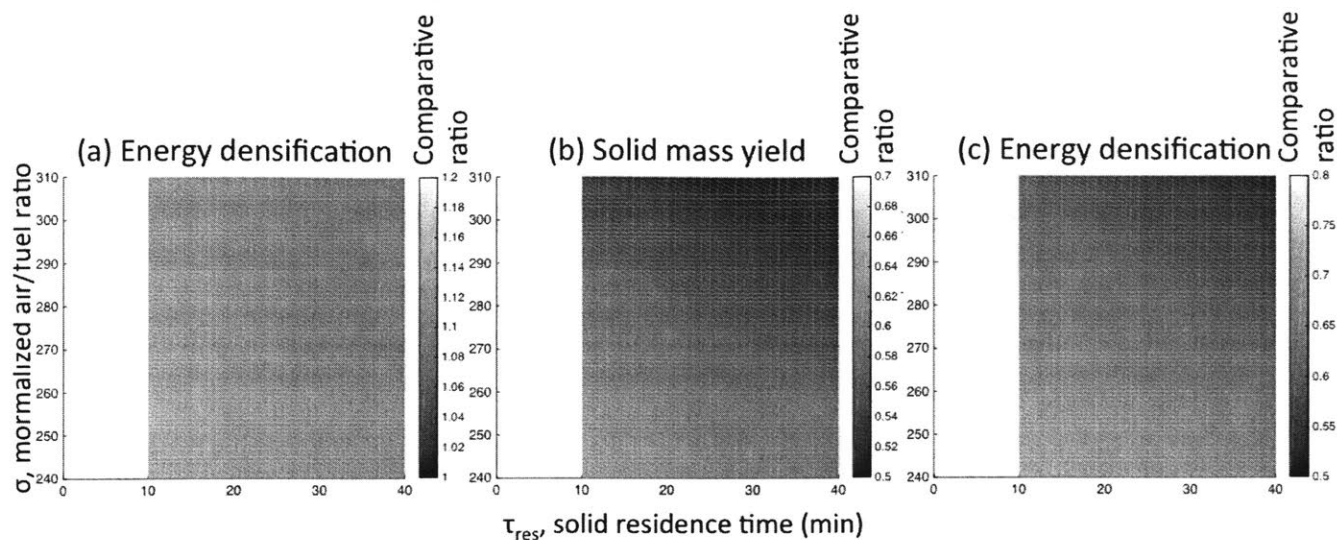


Figure 42 - Our low-air lab-scale reactor shows differences in key performance metrics compared to existing literature data under inert conditions. On the phase space of solid residence time (x axis) and maximum reactor temperature (y axis), we plot the interpolated ratios between our reactor set-up and existing literature data for index of torrefaction (a), solid mass yield (b), and solid energy yield (c).

As noted previous in the literature reviewed in Section 2.1, laboratory experiments have shown that torrefaction in the presence of oxygen, depending on the oxygen level, can result in negligible to significant reduction in performance in terms of mass and energy yields. In light of these earlier works, one logical explanation for these differences is that in our reactor, the introduction of non-inert, low-air environment into the reactor causes the *in-situ* combustion of volatile gases, and this creates hot spots that can locally over-torrefy the biomass, leading to a higher index of torrefaction and lower solid mass and energy yields. However, another explanation for these differences is that fact that our reactor design no longer operates in an idealized, highly controlled environment that was established in earlier works in torrefaction. The fact that we do not employ a controlled external heat source, and that we operate a continuous process as would be done in a real-life setting, imply that our reactor may operate in a less controlled environment, with higher degree of thermal inhomogeneity as well as heat losses, both of which may also lead to over-torrefaction in some regions and, as a result, decreased overall yields in mass and energy. This difference is one non-inert effect that may be expected of a realistic scaled-up

reactor design that our lab-scale reactor can capture with greater accuracy and realism in comparison with the traditional inert lab-scale set-ups.

3.8 General Approach for Rapid Reactor Validation and Scaling

In this study, we begin with the premise that many current lab-scale experimental set-ups are artificial representations of eventual scaled-up torrefaction reactor designs, given completely inert conditions, externally heat source, a narrow range of biomass types tested, and batch-wise process. While these set-ups are invaluable in providing the basic scientific understanding of torrefaction under a highly controlled condition with a minimum set of variables, they may not always capture the more complicated reality that can better inform a scalable reactor design.

We describe a lab-scale torrefaction reactor that we believe captures more realistic and phenomenological elements for scaling up, including a continuously fed fixed bed, a low-air (rather than inert) environment, and a broader selection of characteristically different biomass types (pine shavings, hay, and rice husks). We proceed to validate the stable and steady state operation of this lab-scale reactor under a variety of conditions, and define a scalable operating phase space consisting of residence time and normalized air/fuel ratio. We quantify key reactor performance metrics, such as the index of torrefaction (energy densification ratio), solid mass yield, solid energy yield, solid and volatile chemical composition, as well as the nature of *in situ* oxidation reaction. Furthermore, we compare these performance metrics to similar data from the existing literature, and show some key differences in that our lab-scale reactor results in generally higher index of torrefaction and lower mass and energy yields. The results we present, therefore, form a more realistic basis for scaling up a fixed-bed torrefaction reactor based on our current lab-scale design.

Moreover, we should note that the design and scaling methodology proposed in this study is not limited only to biomass torrefaction in a fixed-bed design, but also has wider applicability to other reactor designs not explored in this study. This approach is also

applicable to other processes involving heterogeneous and complex processes or factors, such as biomass pyrolysis and gasification, where a more phenomenological approach illustrated by our lab-scale reactor may have strength over other more controlled experimental approaches for the purpose of reactor scaling.

While this study makes science-based conjectures about how a scaled-up reactor may behave by observing a lab-scale counterpart, ultimately, its aim is directed not to understand and validate the myriad of underlying chemical or thermodynamic processes in mechanistic detail, but rather to encapsulate these underlying processes as reduced-order correlations that can inform reactor scaling in a rapid and easy way. However, even if a higher-fidelity description of the underlying processes is desired, a lab-scale reactor design like ours is still useful in that it serves as an initial, low-cost step towards more fine-grained diagnostics and measurements: for example, by identifying strong and weak dependencies of the overall reactor performance, our lab-scale reactor can inform which variables and relationships are more important than others for these subsequent fine-grained studies to then focus on, and thus precious resources can be saved by this more directed approach.

Finally, our lab-scale reactor is useful to the extent that it can more accurately inform scaling up the reactor, but this claim itself is to some extent still an untested hypothesis. The subsequent design and realization of a scaled-up reactor and its quantification will serve as the ultimate verification or falsification of our general phenomenological approach.

Chapter 4 A Design-Oriented Index of Torrefaction

Biomass torrefaction is a useful process because the input biomass feedstock, through a thermochemical treatment, becomes an improved fuel in terms of energy density, fixed carbon content, grindability, and so forth. While these various improvements are well known, to date, there is little effort in establishing a design methodology to systematically relate target improvements in these characteristics back to the extent of torrefaction. This missing gap is essential in better selecting the optimal torrefaction reaction conditions and designing more effective torrefaction reactors at scale. In this paper, we define an index of torrefaction based on the extent of energy densification of the output fuel, and show that this index is useful in that it has a functional mapping relationship with the various characteristic improvements mentioned above. We showed that the design conditions are highly dependent on the type of biomass feedstock, and the index of torrefaction is able to inform us which type is suitable or not. We also showed that while the index of torrefaction has a monotonic relationship with the higher heating value of the direct output of torrefaction, once such output has been briquetted into solid fuel and tested for cooking purposes, the useful fuel energy density and power output have a much more complex relationship with the index of torrefaction. The index of torrefaction therefore serves as a crucial and practical framework for understanding how various fuel characteristics that the various end users desire can be linked to the actual operating conditions of a torrefaction reactor in a simple and rapid manner.

4.1 The Need for an Index of Torrefaction

Biomass torrefaction has recently received significant interest because it improves the characteristics of the output fuel, making it easier to use, cheaper to transport, and less challenging to grind/process, and more hydrophobic. Table 17 lists some of the fuel improvements that some sample end users care about as design requirements.

Table 17 - Sample design requirements for the torrefaction process

User	Torrefaction requirements
Restaurant cook in India	I want a minimum heating value of 22 MJ/kg.
Pig iron industry in Brazil	Fixed carbon content must be more than 56%.
Industrial boiler operator	Boiler temperature should be maintained above 750°C.
Kenyan housewife	I want the water to be brought to boil in 20 minutes.

We note that different users place different priorities over the different improvements. Even though most of these improvements are often causally linked to the thermochemical changes that occur within biomass during torrefaction, yet somewhat surprisingly, many of these improvements are not well quantified, nor is it an easy task to understand how these various improvements relate to how the torrefaction reactor should be operated. We define these physical/chemical changes to the output fuel as “secondary characteristics”, named so because they arise due to the primary effect of torrefaction.

Most studies in the existing literature approach this from the temperature-residence time perspective: for each type of biomass, the temperature and residence time are varied one at a time to report secondary characteristics such as the heating value (HHV) of the torrefied fuel (Arias *et al.*, 2008), the fixed carbon content, or the specific grinding energy. This two-dimensional approach is akin to the temperature-air/fuel ratio phase space that we utilized in Chapter 3 in order to characterize the performance metrics (solid mass yield, energy densification ratio, and solid energy yield) of the torrefaction reactor. However, we contend that this two-dimensional approach is extremely time- and labor-intensive: there are a multitude of different secondary characteristics, and each time that a new secondary characteristic requirement arises, it becomes necessary to re-run the torrefaction reactor under the various conditions all over again in order to quantify and map out such a secondary characteristic on the temperature-residence time map. Our alternative hypothesis is that instead of the two-dimensional map, torrefaction can be characterized by a one-dimensional variable known as the index of torrefaction, which (a) quantifies the severity of the torrefaction process under various temperature and residence time

conditions and (b) can be determined solely by characterizing the selection of output solid fuels from the reactor, without necessitating re-running the reactor all over again. In order to satisfy the conditions above, mathematically speaking, there must exist a functional relationship between the different secondary characteristics of torrefaction and the index of torrefaction: in other words, for each value of the index of torrefaction, there is uniquely one mapped value for each of the desired secondary characteristics.

4.2 Definition of the Index of Torrefaction

The approach we take for defining and utilizing the index of torrefaction is an empirical one: let us select a definition for the index of torrefaction, and experimentally establish whether or not it is true that a wide selection secondary characteristics are indeed a function of such an index.

To define such an index, we draw upon the inspiration of Basu *et al.* (2017), which defined an index of torrefaction solely based on the ratio of energy densification of the output fuel to that of a reference torrefaction condition at 300°C and a residence time of 60 minutes. We modified and simplified their definition by establishing the index of torrefaction I_{torr} as the ratio of the higher-heating value of the output torrefied fuel to the higher-heating value of raw biomass:

$$I_{\text{torr}} \equiv \frac{\text{HHV}_{\text{torrefied}}}{\text{HHV}_{\text{raw}}}.$$

From the formula above, we see that any form of energy densification means that $I_{\text{torr}} > 1$. Table 18 lists some typical values of index of torrefaction for various types of biomass subject to a certain torrefaction condition at 300°C and 30 minutes; the HHV values in this case were experimentally measured using a calorimeter as described in Section 3.3.4.

Table 18 - Typical values for index of torrefaction for various types of biomass after being treated at 300°C for 30 minutes.

Feedstock	HHV _{raw}	HHV _{torrefied}	Index of torrefaction
Pine shavings	20.51 MJ/kg	23.87 MJ/kg	1.16
Hay	17.42 MJ/kg	21.10 MJ/kg	1.21
Rice husks	15.82 MJ/kg	17.36 MJ/kg	1.10

It should be remarked that the different types of biomass, when subject to the same torrefaction condition, may exhibit different degrees of energy densification, and hence, different values of index of torrefaction. It should be further remarked that the index of torrefaction that we defined above is actually equivalent to the energy densification ratio, which we defined as a key performance metric for the laboratory-scale in 0. This makes it easy for us later on to make design choices based on the index of torrefaction by simply referring to the color heat maps that we produced previously.

4.3 A Motivating Design Case Study Using the Index of Torrefaction

We begin by verifying that one important “secondary characteristic”, the energy content of the solid fuel, indeed has a one-to-one functional mapping to the index of torrefaction. We then walk through a design case involving the energy content requirement for the fuel and illustrate the utility of the index of torrefaction in the design process.

The solid fuel energy content is often determined by the higher heating value (HHV) of the torrefied fuel. In this case, by tautology from the definition of the index of torrefaction, there is indeed a one-to-one mapping: the HHV of the torrefied fuel is nothing more than the index of torrefaction multiplied by the HHV of the raw biomass.

Now suppose that an end user for the solid fuel requires that the fuel have a higher heating value of at least 21.25 MJ/kg. What does this mean for the torrefaction requirement of the different biomass input feedstock types? Based on the values in Table 18, we note that in order to reach 21.25 MJ/kg, this requires pine shavings be torrefied at $I_{\text{torr}} \geq 1.04$. As shown in Figure 43a, which replicates the color heat map of the energy densification ratio determined from 0, all reactor operating conditions above the autothermal boundary can satisfy this HHV requirement. On the other hand, for hay, an output HHV of 21.25 MJ/kg requires that $I_{\text{torr}} \geq 1.22$. According to Figure 43b, we must run the torrefaction reactor under very severe torrefaction conditions (in the upper-right quadrant) in order to satisfy this requirement. Finally, for rice husk, the corresponding index of torrefaction is $I_{\text{torr}} \geq 1.34$. This means that within the mapped torrefaction regime of interest in Figure 43c, it is not possible to satisfy this requirement, as the maximum energy densification ratio (i.e. index of torrefaction) is around 1.15 only.

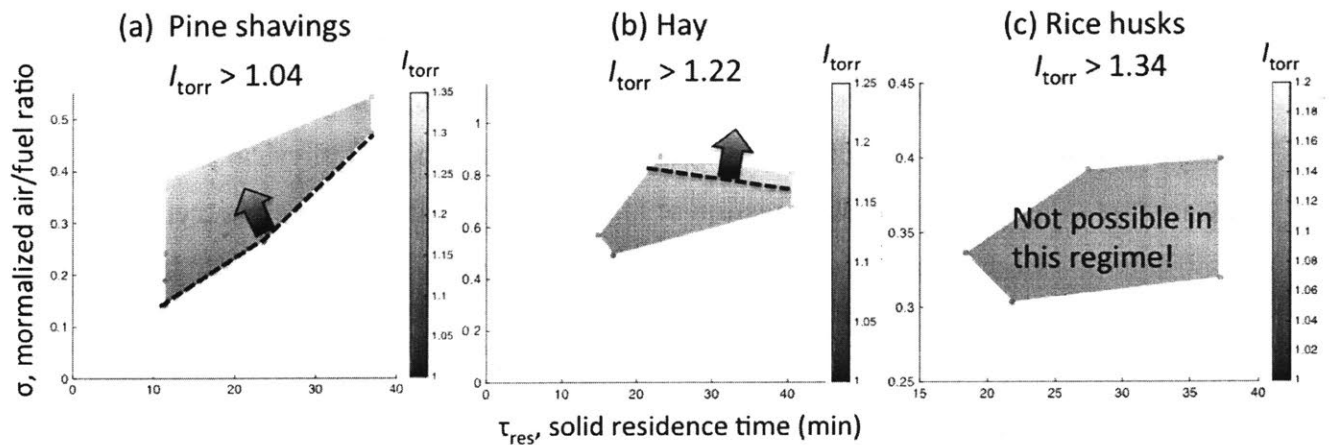


Figure 43 - An illustration of using the index of torrefaction to select for the torrefaction reactor operating condition for three different types of biomass feedstock. Note that depending on the biomass feedstock, we obtain very different design outcomes.

The intuition for our conclusion with respect to rice husk is as follows: rice husk, due to its high ash content, has a low HHV value (below 16 MJ/kg) in its raw form to start with. As it is torrefied, the relative ash mass fraction increases, which further dilutes the energy

density of the usable fuel. With the amount of ash inherent in rice husk, it is just very difficult to torrefy it severely enough to achieve 21.25 MJ/kg in energy density.

From the sample design case above involving the HHV requirement of the torrefied output, we can immediately see the utility of the index of torrefaction: not only can it be used as a tool to narrow down the reactor operating condition of interest without re-running multitude of torrefaction experiments, but it can also be further used to determine which type of biomass is better suited than others for achieving this specific design requirement.

The functional mapping between torrefied HHV and the index of torrefaction, as described above, is tautological. However, the *functional mapping* between other “secondary characteristics” with the index of torrefaction defined above is actually an unverified hypothesis: different combinations of torrefaction temperature and solid residence time may give the same torrefied HHV (and hence index of torrefaction), but these conditions are not guaranteed to give rise to the same proximate analysis, ultimate analysis, grindability, and cooking characteristics, because different temperature and time combinations may give rise to different changes to the chemical and physical properties of the torrefied solid. Therefore, the question of functional mapping that we are trying to establish in this study is actually non-trivial, and if successfully established, will be a powerful design selection tool indeed.

4.4 Various Functional Mappings to the Index of Torrefaction

In the previous section, we utilized HHV of the torrefied output as a motivating example for using the index of torrefaction for our reactor design process. In this section, we demonstrate that a wide selection of “secondary characteristics” related to the output torrefied fuel indeed forms a one-to-one functional mapping with the index of torrefaction, and that these mappings can be equally useful for informing reactor design selection.

4.4.1 Proximate Analysis

Conducting proximate analysis and measuring its readouts—namely fixed carbon, volatile matter, moisture, and ash—have been described previously in Section 3.3.2. For some industrial users of solid fuel—such as those in the pig iron industry—it is important to maintain a minimum fixed carbon content within the solid fuel, due to the high temperature requirements.

To establish a functional relationship between fixed carbon content and index of torrefaction for different biomass types, we need to experimentally measure the fixed carbon content of the different biomass and torrefied biomass samples. Figure 44 shows the experimentally determined correlations between the index of torrefaction and fixed carbon content (a) and volatile matter (b) for pine shavings (blue), hay (red), and rice husk (black), which we experimentally determined using the protocol described previously in Section 3.3.2. As can be observed, a one-to-one mapping generally exists. In order to verify that this functional mapping between fixed carbon and index of torrefaction is valid for a wider range of biomass, we sought the existing torrefaction literature and extracted the data on fixed carbon content and HHV values for other types of biomass under various torrefaction conditions. We transformed the HHV data into our defined index of torrefaction. As shown in Figure 44, for eucalyptus wood (cyan) from Arias *et al.*, (2008) and for willow (magenta), wheat (green), and canary grass (yellow) from Bridgeman *et al.*, (2008), we observe a similar monotonic relationship. This demonstrates that for a variety of different biomass types, we are able to establish a functional mapping between the fixed carbon content and the index of torrefaction.

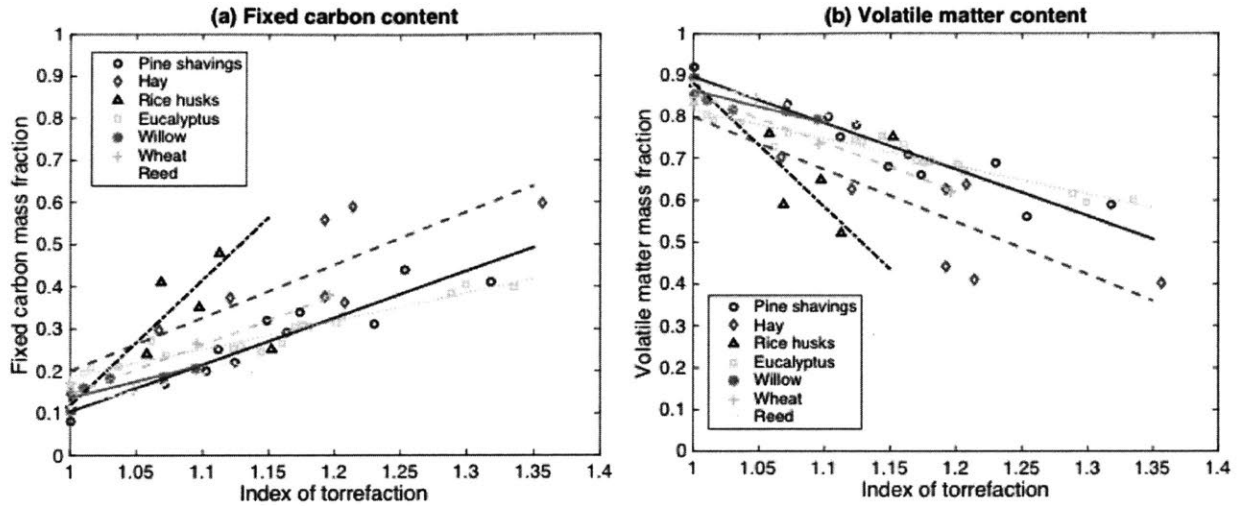


Figure 44 - A correlation map between the index of torrefaction and (a) fixed carbon content and (b) volatile matter of the torrefied output, for pine shavings (blue), hay (red), and rice husk (black), eucalyptus wood (cyan), willow (magenta), wheat (green), and reed (yellow). The eucalyptus data come from Arias *et al.* (2008), and the willow, wheat, and reed data come from Bridgeman *et al.* (2008).

4.4.2 Elemental (Ultimate) Analysis

Elemental (ultimate) analysis, as defined previous in Section 3.3.3, is useful in cases where the torrefied solid is not being burned as a solid fuel, but rather being buried underground as inert biochar. The carbon elemental composition, for example, gives a quantitative estimate of the amount of CO₂ equivalent being sequestered by the biochar (Parikh, 2017). If there is a carbon sequestration target, for example, a functional mapping of the carbon mass fraction to the index of torrefaction will directly inform the reactor operating conditions.

We performed an analysis on all our torrefied samples using the technique described in Section 3.3.3, analyzed the pine shaving, hay, and rice husk outputs from our torrefaction reactor. Furthermore, we also gathered the elemental analysis data for eucalyptus wood torrefaction from Arias *et al.* (2008). The results are plotted in Figure 45.

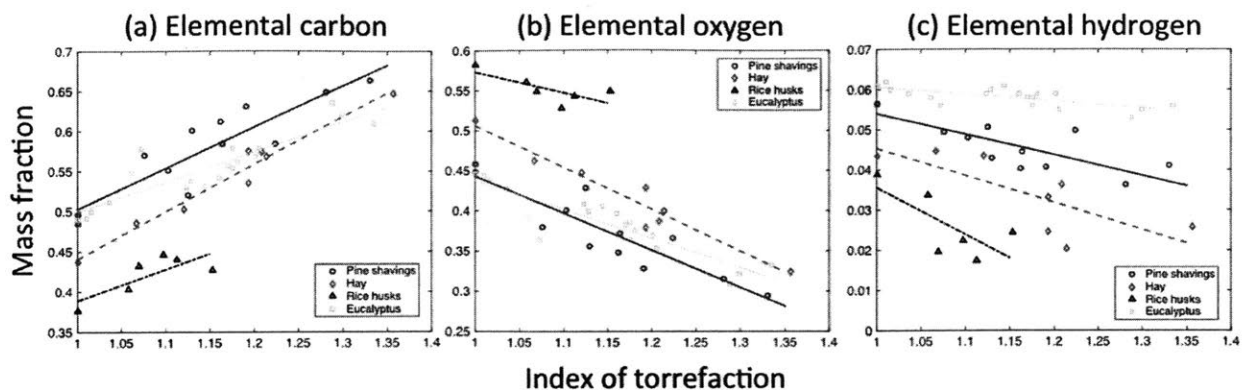


Figure 45 – Correlation plots between the elemental components—carbon (a), oxygen (b), and hydrogen (c)—in torrefied biomass and the index of torrefaction, for pine shavings (blue), hay (red), rice husks (black), and eucalyptus wood (cyan). We generally see that increasing torrefaction severity results in increased elemental carbon, as well as decreased elemental oxygen and hydrogen. Data for eucalyptus wood were obtained from Arias *et al.* (2008).

As can be seen in Figure 45a, as the index of torrefaction increases, the mass fraction of carbon increases for all four types of biomass analyzed. This is not surprising, as the chemical effect of torrefaction is to drive out low-energy molecules (often rich in oxygen) while making the torrefied residue more carbon-rich. This explanation is confirmed when we can contrast the result for oxygen in Panel b and hydrogen in Panel c. We see that both of these elemental components decrease in mass fraction as a response to increased torrefaction severity.

4.4.3 Fuel Grindability

It is well known that one of the key benefits of torrefaction is that it improves the grindability of solid fuel—that is, the ease with which the solid fuel can be pulverized (Bridgeman *et al.*, 2010; and Khalsa *et al.*, 2016). For many boiler and co-generation applications, especially for fluidized bed reactors, it is required that the solid fuel be pulverized and entrained before it can be utilized. Under such cases, an end user may impose grindability-related design criteria on the torrefied output.

There are two main ways to quantify “grindability” in the literature. In the first type of measurement, a certain known amount of grinding energy is delivered to the biomass or torrefied fuel in a batch process, and the resultant particle distribution characterized (such as done in Repellin *et al.*, 2010). In the second type of measurement, a continuous grinder is implemented that measures the grinding power delivered as a given flow rate of biomass or torrefied fuel passes through the grinder (Govin *et al.*, 2010; and Phanphanich and Mani, 2011). In this study, we implemented both grinding measurement methods, and showed how the quantified grindability in either case is affected by the index of torrefaction in the sample case of torrefied rice husks as well as pine shavings

Because of the intensive nature of the grinding experiment, we only performed the experiment on six biomass or torrefied biomass samples, as summarized in Table 19. As can be observed, we selected a lightly torrefied condition ($I_{\text{torr}} = 1.11$ for pine shavings and for rice husks) and a heavily torrefied condition ($I_{\text{torr}} = 1.16$ for pine shavings and $I_{\text{torr}} = 1.15$ for rice husks), and compared this against a negative control, which is raw biomass as received ($I_{\text{torr}} = 1.00$).

Table 19 - Biomass samples utilized in the solid fuel grindability studies.

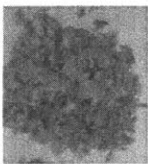
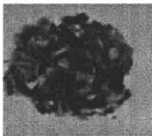
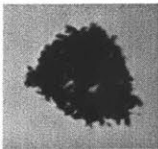

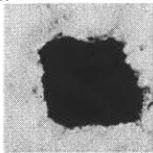
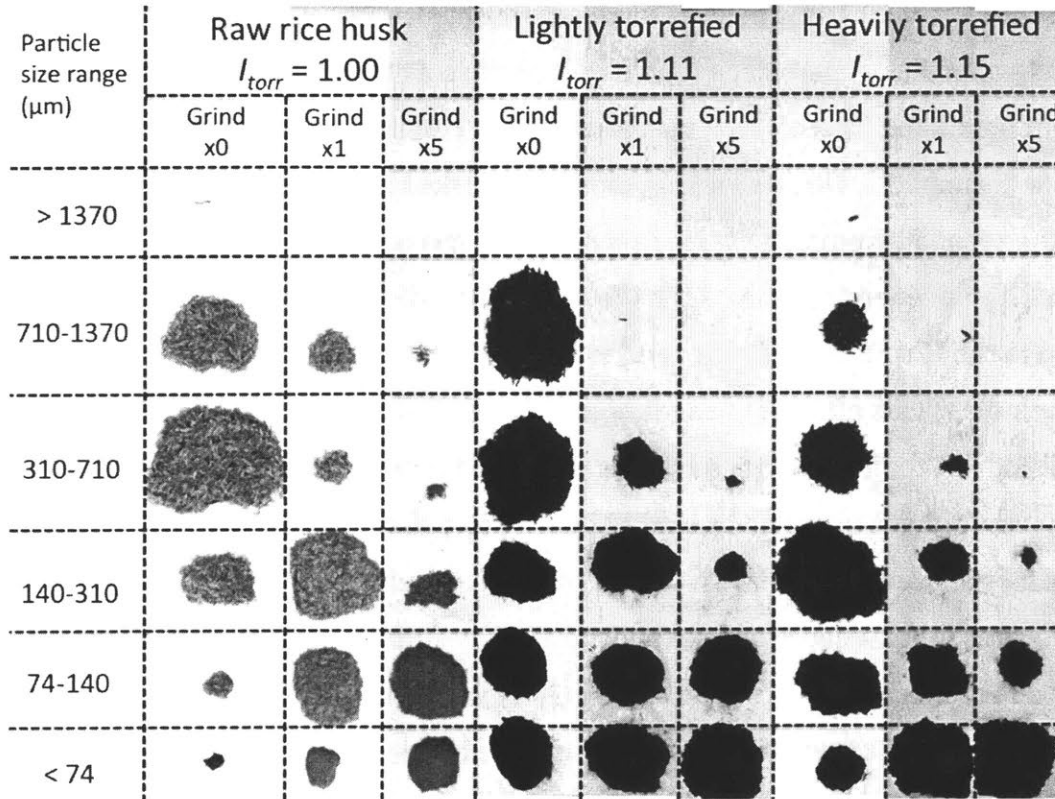
Feedstock type	Raw biomass	Lightly torrefied	Heavily torrefied
Pine shavings	As received $I_{\text{torr}} = 1.00$ 	Air/fuel ratio = 0.18 Res. time = 11 min $I_{\text{torr}} = 1.11$ 	Air/fuel ratio = 0.26 Res. time = 19 min $I_{\text{torr}} = 1.16$ 
Rice husk	As received $I_{\text{torr}} = 1.00$	Air/fuel ratio = 0.15 Res. time = 27 min $I_{\text{torr}} = 1.11$ 	Air/fuel ratio = 0.18 Res. time = 37 min $I_{\text{torr}} = 1.15$ 

Table 20 - Visualization of the distribution of particle sizes (each column represents the particles that lie between a specific range of sizes) under different experimental grinding conditions (no grinding, or “Grind x0”; 0.1 MJ/kg of grinding energy delivered, or “Grind x1”; and 0.5 MJ/kg of grinding energy delivered, or “Grind x5”) with respect to different rice husk samples torrefied to different extents (raw untoorrefied rice husks, or $I_{\text{torr}} = 1.00$; mildly torrefied rice husks, or $I_{\text{torr}} = 1.11$; and heavily torrefied rice husks, or $I_{\text{torr}} = 1.15$).



In order to conduct the first type of grinding experiment (batch-wise grinding, delivering a specific amount of energy and measuring the particle distribution), we utilized a coffee grinder (KRUPS F203), connected to a power consumption plug load logger (HOBO UX120). After loading about 100 g of biomass or torrefied biomass sample into the grinder, we performed three experimental conditions: (a) “Grind x0” condition: unprocessed, or 0 J kg⁻¹ of grinding energy applied, (b) “Grind x1” condition: 0.1 MJ kg⁻¹ of grinding energy applied, and (c) “Grind x5” condition: 0.5 MJ kg⁻¹ of grinding energy applied. After each experiment, we removed the ground samples, and then processed them through a series of wire mesh

sieves (McMaster-Carr) in increasingly small opening sizes of 1370 μm , 710 μm , 310 μm , 140 μm , and 74 μm .

Table 20 shows the outcome from sieving the products from the different experiments. Each column represents one experiment (“Grind x0”, “Grind x1”, or “Grind x5”) with respect to differently torrefied rice husks (raw rice husk with $I_{\text{torr}} = 1.00$, lightly torrefied rice husk with $I_{\text{torr}} = 1.11$, and heavily torrefied rice husk with $I_{\text{torr}} = 1.15$). Each row represents a specific particle size range based on passing through different levels of sieves of different hole sizes. Therefore, if we read the first column (raw rice husks, without grinding or “Grind x0”), we can see that most rice husks have a native size of 0.3-1.3 mm. Then, in the second column, the same raw rice husk has been ground in the coffee grinder with 0.1 MJ kg^{-1} of energy (“Grind x1”). We see that the distribution of the particles, compared to the “Grind x0” column, tend to shift towards smaller sizes as a result of the effect of grinding. This effect is even more pronounced as we deliver even more grinding energy “Grind x5” to the raw rice husks, as visualized in the third column. We can do the same analysis for light torrefied as well as heavily torrefied rice husks. What we notice are two trends. Firstly, even in the native form (without grinding, “Grind x0”), the distribution of particle sizes in torrefied biomass tends to already shift towards the smaller sizes, probably due to mechanical attrition during transport through the reactor as well as handling, as torrefied biomass is known to be more brittle. This effect is more pronounced in the heavily torrefied regime ($I_{\text{torr}} = 1.15$). The second trend to remark is that if we compare the “Grind x1” and “Grind x5” columns for the three samples, we can see that for each given grinding energy delivered to the samples, torrefaction results in a shift of particle size distribution to smaller sizes. As an illustration, in the “Grind x5” scenario, while the raw biomass has some residual particles between the sizes 710-1370 microns, this is completely absent in the case of lightly torrefied ($I_{\text{torr}} = 1.11$) rice husks, where the largest observed particle sizes are between 310-710 microns. Then, in comparison, in the heavily torrefied rice husks ($I_{\text{torr}} = 1.15$), we find that this 310-to-710-micron subpopulation is almost absent. In the meanwhile, more and more fraction of the particles ends up passing through the 74-micron sieves as the torrefaction severity is increased. Therefore, even by qualitative visual inspection, we can make the following conclusions: (a)

at a given amount of grinding energy imparted into solid fuel output, increasing the index of torrefaction improves the grindability because torrefaction results in a distribution smaller particle sizes, and (b) under increasing index of torrefaction conditions, the particles become more brittle, such that they tend to break into smaller pieces naturally, without the intervention of mechanical grinding.

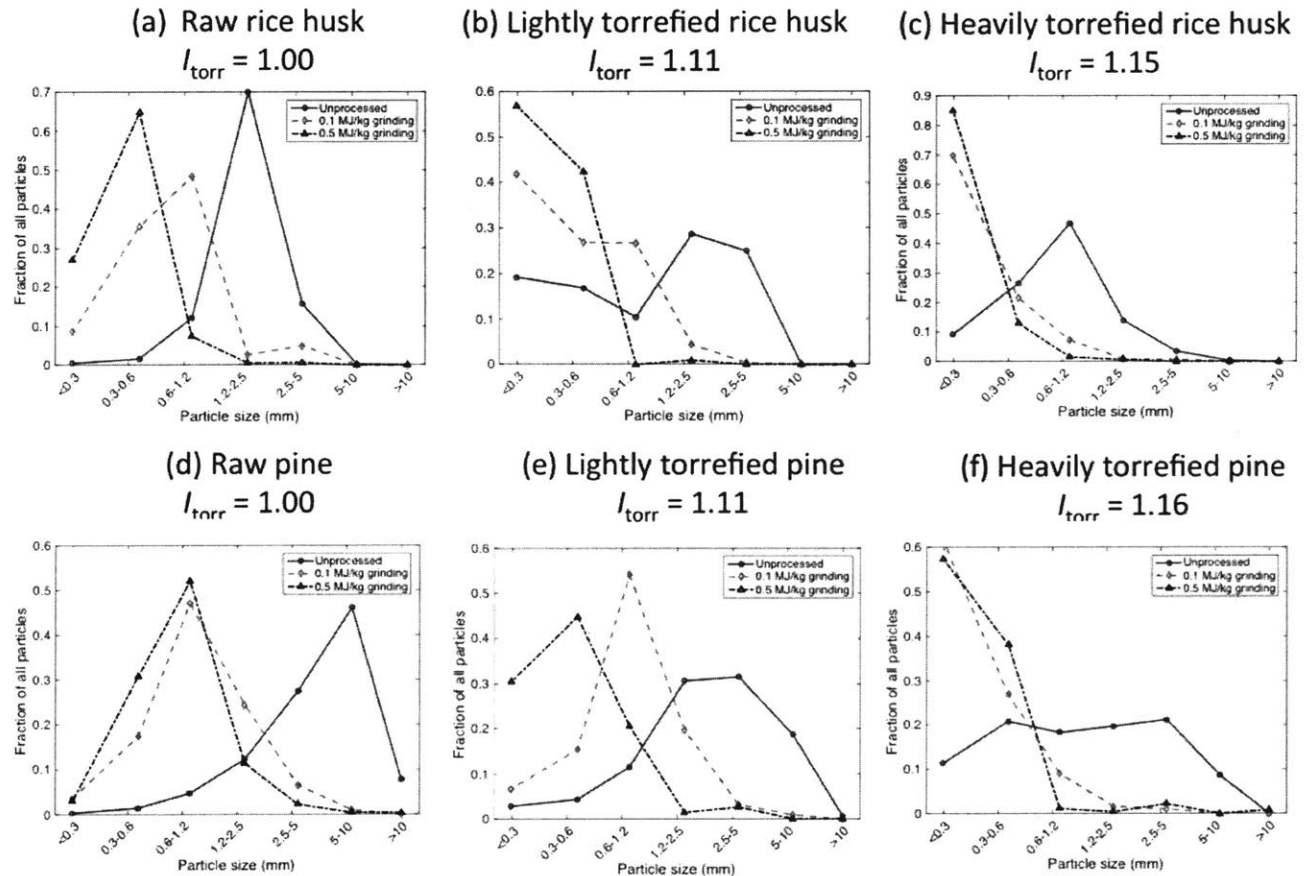


Figure 46 - Mass distribution of biomass/torrefied biomass samples imparted with no grinding energy (blue), 0.1 MJ/kg of grinding energy (red), and 0.5 MJ/kg of grinding energy (black). The samples are: (a) raw rice husk ($I_{\text{torr}} = 1.00$), (b) lightly torrefied rice husk ($I_{\text{torr}} = 1.11$), (c) heavily torrefied rice husk ($I_{\text{torr}} = 1.16$), (d) raw pine shavings ($I_{\text{torr}} = 1.00$), (e) lightly torrefied pine shavings ($I_{\text{torr}} = 1.11$), and (f) heavily torrefied pine ($I_{\text{torr}} = 1.16$). As grinding energy is increased, the mass distributions tend towards the smaller particle sizes.

Upon the implementation of grinding, we observe a further reduction in the particle sizes in all cases (red curves with 0.1 MJ/kg grinding energy, and black curves with 0.5 MJ/kg grinding energy). In particular, as we increase the index of torrefaction, we see a more significant shift of the mass distribution curve to the left (smaller particle sizes), thereby signifying the efficacy of torrefaction in improving biomass grindability.

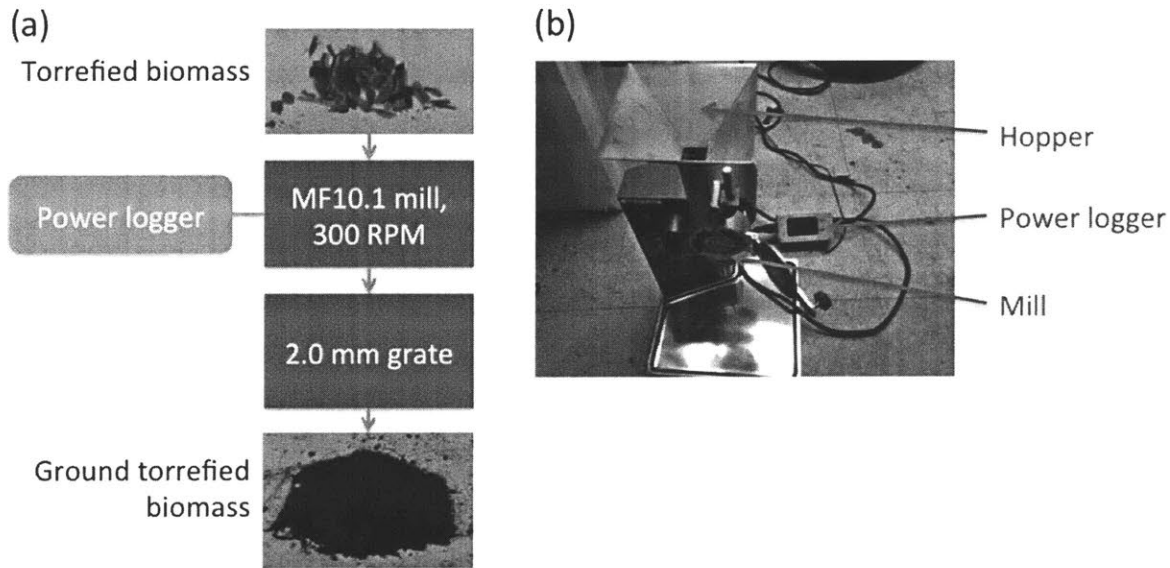


Figure 47 - Experimental set-up for quantifying the specific grinding energy of torrefied biomass samples.

While seeing the reduction in the particle sizes as distributions under different grinding conditions is an intuitive way to understand how torrefaction severity affects fuel grindability, we can do better in terms of putting a number on this grindability. In order to do so, we consider and implement the second way that grindability measurement can be implemented through a continuous grinding process. For our experimental purpose, we obtained an IKA MF 10.1 mill that we connected to a HOBO UX120 plug load logger. A 2.0 mm grate was placed at the bottom of the mill, such that only particles that have been ground to a size inferior to the grate opening can pass through and be collected. By measuring the power output supplied to the grinder, as well as the mass flow rate of the biomass or torrefied biomass sample through the grinder, we can arrive at a quantity that most existing literature calls the *specific grinding energy*. This is the unit energy required to

comminute a solid fuel sample into particles inferior to a certain target size. At a given measured flow rate of biomass input feeding, we measured the power consumption during the grinding process. Dividing the power consumption by the feeding mass rate gives us the specific grinding energy [J kg^{-1}]. Figure 47 shows a schematic as well as a photograph of the experimental set-up that we deployed.

Sample power logging time series

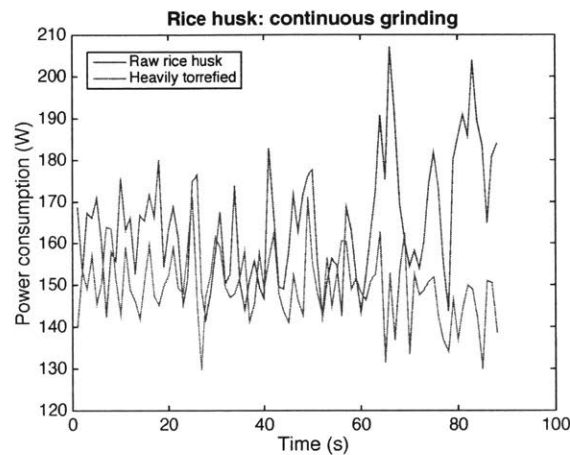


Figure 48 - Sample plug load power logging series (reflecting the power that the continuously operated grinder draws) as a function of time, for processing raw rice husks ($I_{\text{torr}} = 1.00$) and heavily torrefied rice husks ($I_{\text{torr}} = 1.15$). We notice that for the heavily torrefied rice husks, less grinding power on average is required, signifying improved grindability.

To understand how this works, in Figure 48, we plot the sample time series of the readout from the plug load power datalogger, which quantifies the amount of electric power that the grinding mill draws at a given point in time in order to process the given (raw/torrefied) rice husk sample on a continuous basis. From comparing the power requirements for raw rice husks ($I_{\text{torr}} = 1.00$, blue trace) to severely torrefied rice husks ($I_{\text{torr}} = 1.15$, red trace), we notice a reduction in the average grinding power requirement, which shows improved grindability with increasing torrefaction severity. In order to obtain the specific grinding energy, we integrate this power curve over time it takes to process

500 grams of the sample, in order to obtain some energy quantity [J]. Dividing by 500 grams, we thereby obtain a measure for the specific grinding energy.

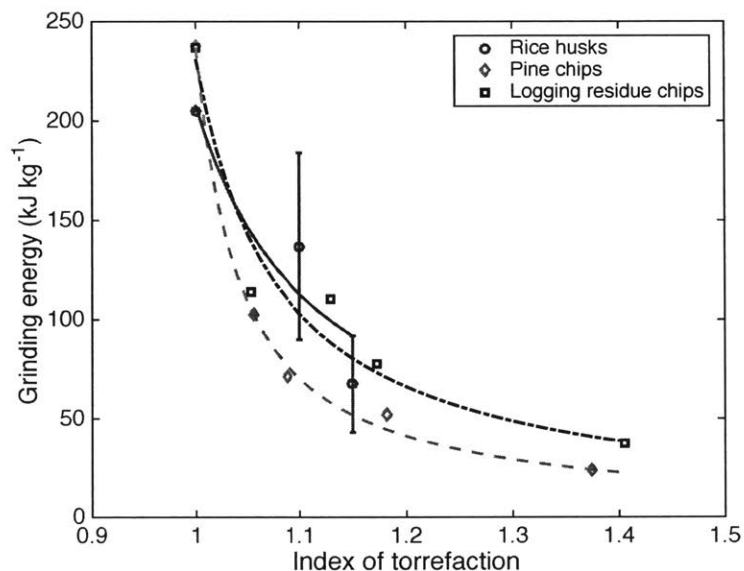


Figure 49 - Relationship between specific grinding energy and index of torrefaction for rice husks (blue), pine chips (red), and logging residue chips (black). The relationships generally follow that of a rational function of the form $a / (1 - bI_{\text{torr}})$. The rice husk data were obtained experimentally; the data for pine chips and logging residue chips were obtained from Phanphanich and Mani (2011).

Figure 49 shows that for rice husks (blue), the specific grinding energy decreases as the torrefaction becomes more severe. To supplement our experimental data on rice husks with a wider range of biomass, we also took data from the literature (Phanphanich and Mani, 2011) for pine chips and logging residual chips, which were also plotted in Figure 49. In general, we found that the specific grinding energy (SGE) decreases drastically as the biomass is increasingly torrefied, and that the SGE and the index of torrefaction (I_{torr}) can be fitted to a rational function of the form:

$$\text{SGE} = \frac{a}{1 - bI_{\text{torr}}},$$

where a and b are fit parameters. These parameters were determined via cftool fitting in MATLAB, and are given in Table 21.

Table 21 – Best fit of the specific grinding energy as a function of the index of torrefaction to a rational function of the form $a / (1 - bI_{\text{torr}})$.

Biomass type	Best fit value for a	Best fit value for b
Rice husks	24.73*	0.8808*
Pine chips	9.96 ± 1.95	0.958 ± 0.0093
Logging residue chips	18.54 ± 12.49	0.9198 ± 0.0641

* Number of data points for rice husks was too small (3) to determine a reliable confidence interval for the fitting parameters.

Furthermore, what we characterized that other prior studies have not done so, is that the maximum solid output flow rate in a continuous grinding set-up is also dependent on the index of torrefaction. Typically, the rate at which comminuted solids emerge from the grinder is limited by how quickly the mill can reduce the incoming solid feed. We found that, as Figure 50 demonstrates, as the index of torrefaction increases, the maximum output mass flow rate that is achievable under our grinding experimental setup also increases. Therefore, we learned that, in addition to the reduction in the grinding energy (as other studies have shown already), a new benefit of torrefaction is that it can increase the processing capacity of the grinder, which is also expected to reduce the operating costs for comminuting torrefied biomass feedstock.

In this section, we explored the concept that torrefaction improves grindability, and demonstrated how we can put quantitative relationship between grindability and index of torrefaction by implementing two experimental methods to quantify grindability. This is useful for the grinding process, as the grinding requirements can now be incorporated into the reactor operation process via the index of torrefaction.

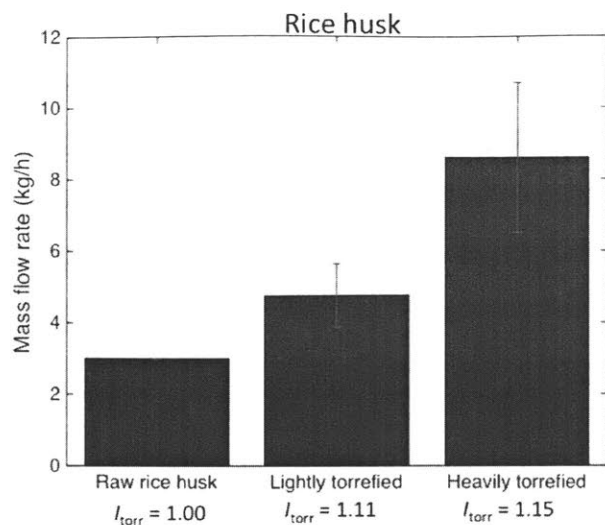


Figure 50 - The maximum possible grinding output flow rate improves as the index of torrefaction increases, which is an additional, less documented benefit of torrefaction on product grindability.

4.4.4 Selected Cooking Characteristics

One very common application of torrefaction is the upgrading of biomass into solid cooking fuel. One commonly held belief is that torrefaction makes raw biomass more charcoal-like when used for cooking. However, this belief is largely untested and unquantified. In this section, we demonstrate that the index of torrefaction can also be used as a vehicle to quantitatively elucidate these improvements of torrefied biomass as a cooking fuel. In order to quantify cooking performance, we must first define a formulation of cooking fuel from torrefied biomass, as well as a standardized cooking experiment that we can perform with respect to different torrefaction outputs. As shown in the flow diagram in Figure 51, torrefied biomass is first comminuted, using the same grinding set-up as described in the previous section, into small powder inferior to 2 mm.

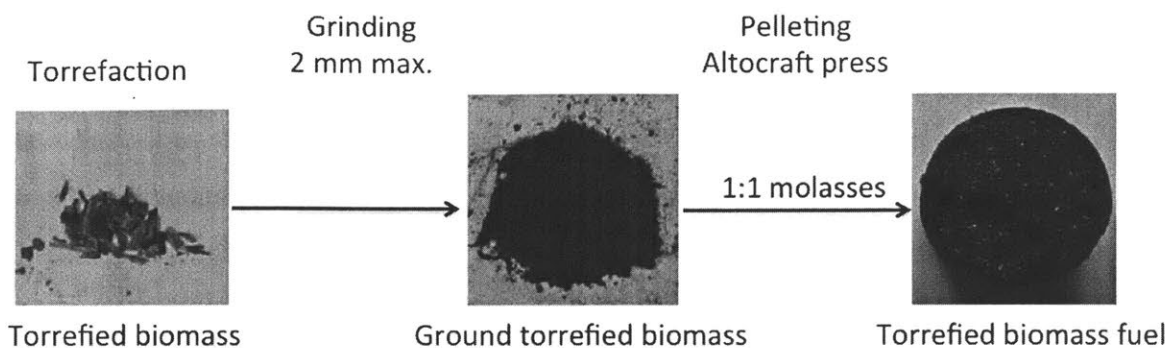


Figure 51 - Torrefied biomass is first ground to 2 mm size and then mixed 1:1 with molasses (a sticky binder) to form into solid fuel.

Then, once we have the pulverized torrefied biomass, we need to form (“bind”) it into usable form of solid fuel. There are many types of “binders” available, such as paper pulp, wheat flour mixture (Demirbaş and Şahin, 1998), molasses (Biesa *et al.*, 2003; Chin and Siddiqui, 2000; and Benk and Coban, 2011), sawdust (Taulbee *et al.*, 2009; Sivakumar *et al.*, 2012; and Rajaseenivasan *et al.*, 2016), cow dung (Emerhi, 2011; and Jain *et al.*, 2015), acid-denatured biomass (Zhang *et al.*, 2001; Cheng *et al.*, 2008), and even natural innate binders in the raw biomass itself (Kaliyan and Morey, 2010). Other meta-studies have furthermore compared the performance characteristics of the resultant fuel briquettes—such as mechanical strength and calorific value—under different binder mixtures and ratios in seeking an optimum (Richards, 1990; Rubio *et al.*, 1999; and Shyamalee *et al.*, 2015). In our study, we are not interested in necessarily optimizing the binder selection or ratios with respect to differently torrefied biomass, but rather in consistently defining a binding protocol so that the test results from the different torrefaction outcomes can be comparable. We therefore selected molasses as the binder as the binding agent is easily accessible and does not require extensive processing or pre-treatment. The binder to biomass ratio was gradually increased until we have briquettes that are stable and do not easily crumble into small pieces. The binder-to-fuel powder ratio that we used was 1:1 by mass. No water was added in the process.

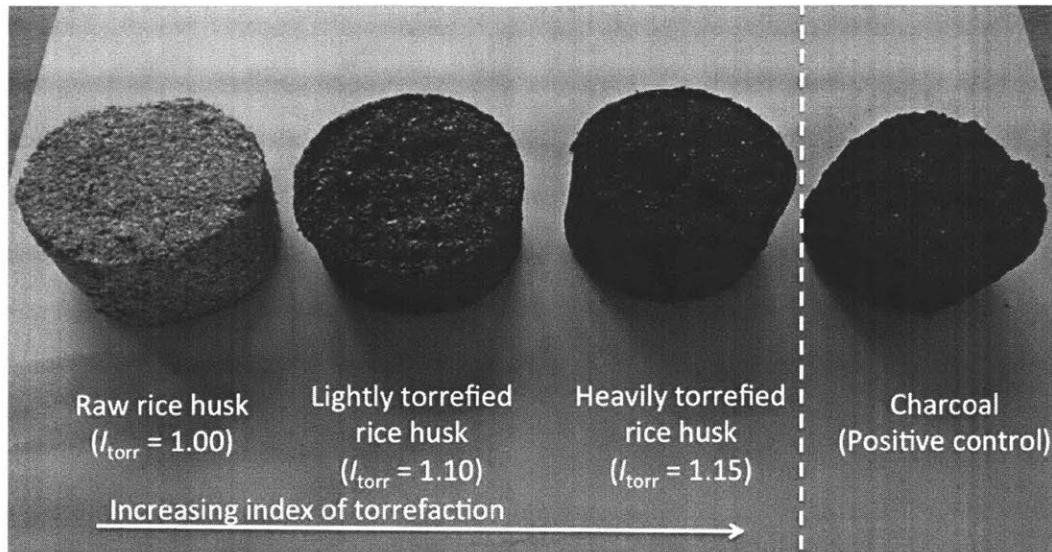


Figure 52 - Samples of rice husk briquettes under different torrefaction conditions that we used for cooking tests. From left to right: raw rice husk briquettes ($I_{\text{torr}} = 1.00$), lightly torrefied rice husk briquettes ($I_{\text{torr}} = 1.11$), heavily torrefied rice husk briquettes ($I_{\text{torr}} = 1.15$), and commercial charcoal briquettes as a positive control.

Figure 52 shows four sample fuel briquettes manufactured using the technique described above, consisting of raw rice husk briquettes ($I_{\text{torr}} = 1.00$, as a negative control), lightly torrefied rice husk briquettes ($I_{\text{torr}} = 1.11$), and heavily torrefied rice husk briquettes ($I_{\text{torr}} = 1.15$). As we see visually, as the index of torrefaction increases, the color of the briquettes also turn darker brown into black. For comparison purpose as a positive control, we also purchased commercial-grade charcoal, pulverized it, and then reconstituted the fuel briquettes using the same technique above.

After the fuel formation protocol is defined, the next step is to define the standard cooking experiment that we will utilize to quantify the relationship between the index of torrefaction and the cooking characteristics. There are many cookstoves that are designed for combustion of solid fuel, some unimproved (for example, Roden *et al.*, 2006, McCracken and Smith, 1998, and Jetter and Kariher, 2009), and some improved (for example, Armendáriz-Amez *et al.*, 2010, Mercado *et al.*, 2011, and Singh *et al.*, 2012). For the purpose of defining a standard protocol, we selected a charcoal-burning stove—called a *jiko*—that is

commonly used for domestic cooking in Kenya. Once again, our primary goal here is not to optimize the cooking performance *per se*, but rather, to demonstrate that for a specifically and realistically defined cooking practice, we can relate changes in the fuel performance to the index of torrefaction. Therefore, we will not spend too much time considering what stove design or cooking procedure to use, other than just specifying one as a standard. Figure 53a displays a typical Kenyan *jiko* cook stove.

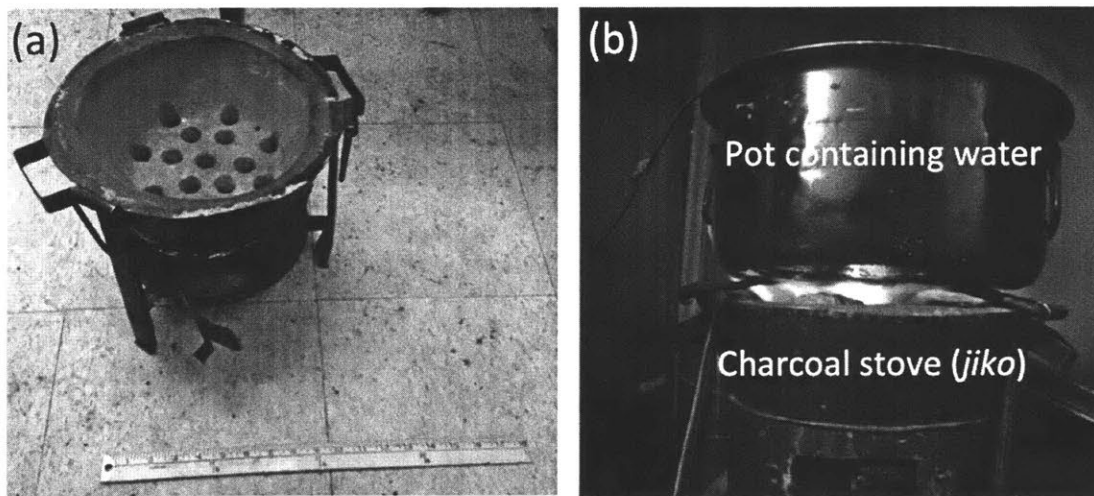


Figure 53 – Cook stove performance experimental set-up. (a) A Kenyan charcoal-burning cook stove called *jiko* was used in our cook stove experiments relating the index of torrefaction to certain cooking characteristics. (b) An experimental set-up consisting of the *jiko* and a pot of boiling water (3 liters).

To set up an experiment (protocol described in detail in Banzaert, 2013), about 400 grams of the solid fuel briquettes of a given type is loaded into the stove. A fire lighter was placed at the center of the briquettes to start the fire. A metal pot containing 3 liters of water at room temperature was placed onto the lit stove. The experimental set-up consists of a mass balance on which the stove, the fuel, and a pot of water are placed. The mass balance logs the weight loss of the cooking experiment in real time. The stove was covered with minimal evaporation taking place, such as the majority of this mass loss can be attributed to the fuel mass loss. We also placed a thermocouple inside the pot of water, as well as inside the cook stove, in order to log the temperature in real time. A photograph of the experimental set-up showing the torrefied fuel briquettes heating a pot of water is shown in Figure 53b.

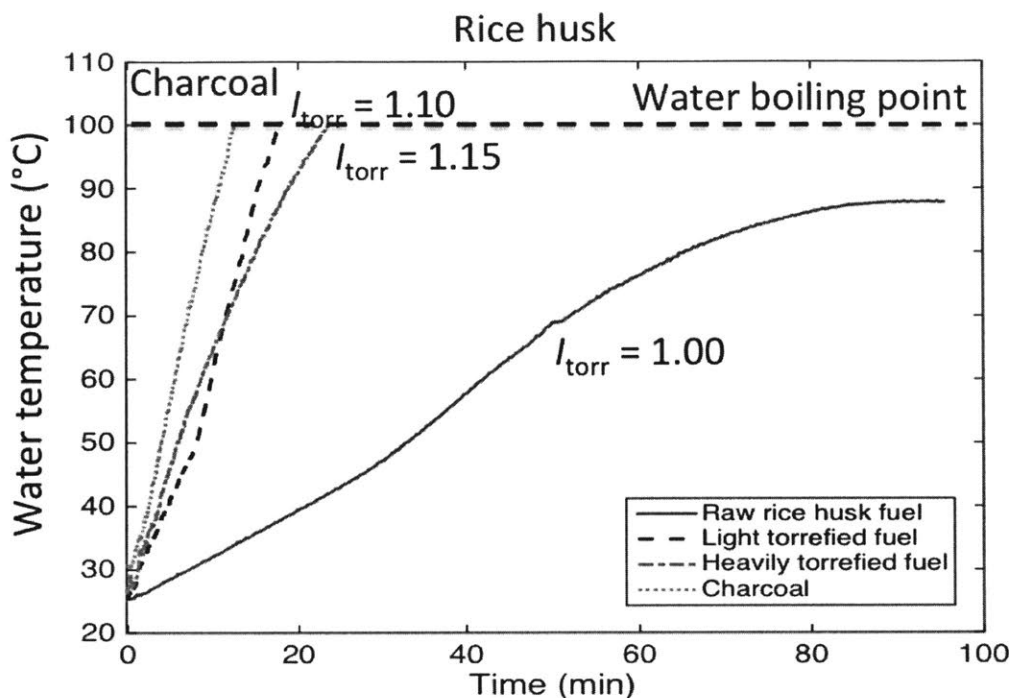


Figure 54 - Time trace of temperature inside a pot of water being heated on a cook stove using different types of fuel (blue curve: raw rice husk briquettes with $I_{\text{torr}} = 1.00$; black dashed curve: lightly torrefied rice husk briquettes with $I_{\text{torr}} = 1.11$; red dash-dotted curve: heavily torrefied rice husk briquettes with $I_{\text{torr}} = 1.15$; and purple curve: charcoal briquettes as a positive control).

Figure 54 summarizes the time trace of the water temperature in the pot using different types of biomass/torrefied fuel briquettes. We see that the fuel briquettes made from raw rice husks (blue curve) is actually insufficient to bring the pot of water to a boil even after 90 minutes. In contrast, both mild torrefaction ($I_{\text{torr}} = 1.11$, black dashed curve) and heavy torrefaction ($I_{\text{torr}} = 1.15$, red curve) dramatically improves the cooking experience by (a) successfully bringing water to a boil, and by (b) completing this heating in at a much faster rate of less than 20 minutes, in a way that is comparable to charcoal briquettes (purple curve). Hence, we can see that torrefaction has dramatic benefits in upgrading the characteristics of the cooking fuel, such that it is actually usable in the actual cooking scenario.

In order to quantify the observations in Figure 54 more rigorously, we defined a quantity called the *useful power output* P_u as heat flow from combusting the fuel briquettes that actually contributes to the heating of the water (e.g. instead of heating up the stove, or being lost to the surrounding environment). Essentially, the useful power output quantifies how rapidly things can be cooked with a given fuel type:

$$P_u \equiv \frac{m_{\text{water}}c_{\text{water}}(T_{\text{end}} - T_{\text{start}})}{t_{\text{end}} - t_{\text{start}}},$$

where the subscript “start” denotes the water temperature and time at the starting point of the cooking experiment, and “end” denotes the water temperature and time at the end point of the cooking experiment, respectively. The useful power outputs for the different fuel types are plotted in Figure 55a, and a discussion of the results will follow.

In the meanwhile, an additional quantity to define and consider is the *useful energy density*, or ρ_E . We felt the need to define this quantity, because even if two separate cooking experiments are giving the same useful power output, there is no guarantee that the solid fuel briquettes are being consumed at the same rate. The fuel consumption rate depends on many factors, such as the combustion temperature, as well as the underlying chemistry of the fuel after torrefaction of different degrees of severity. The useful energy density, as we define below, tells us about how much fuel (in mass) is needed to perform a certain useful purpose (in units of energy):

$$\rho_E \equiv \frac{m_{\text{water}}c_{\text{water}}(T_{\text{end}} - T_{\text{start}})}{m_{\text{fuel,end}} - m_{\text{fuel,start}}}.$$

Figure 55a plots the useful power outputs and Figure 55b plots the useful energy densities of the different fuel types. What is a bit surprising is that in Figure 55a, the useful power output first increases (to 600 watts) and then decreases (to 400 W) as the index of torrefaction is increased. One potential explanation is as follows. Rice husks are known for their high ash content (about 15-20% in raw rice husks). As we increasingly torrefy rice husks, the ash content also increases. A proximate analysis performed on the torrefied rice husks shows that the ash content increases from 22% by mass in the lightly torrefied regime to about 37% by mass in the heavily torrefied regime. Phenomenologically, what we observed happening in the cook stove when we attempted to boil water with the heavily

torrefied rice husk briquettes is that the briquettes quickly became coated in ash, and the red glow of the combustion that was evident on the fuel surface was attenuated significantly. This observation, if true, could then also explain the trend observed in Figure 55b, where after an initial increase in the useful energy density from 3 MJ/kg to 7 MJ/kg upon light torrefaction, this useful energy density did not increase any further upon increasing the torrefaction severity: as the rate of heat release from heavily torrefied fuel became slower in time, the stove needed to expend more energy due to the losses through the side jacket. Therefore, while judging from the index of torrefaction, the heavily torrefied rice husks should have a higher HHV value compared to lightly torrefied rice husks, when these samples were briquetted and combusted, the advantage of the higher HHV value was counteracted by the limited heat release due to the high ash build-up.

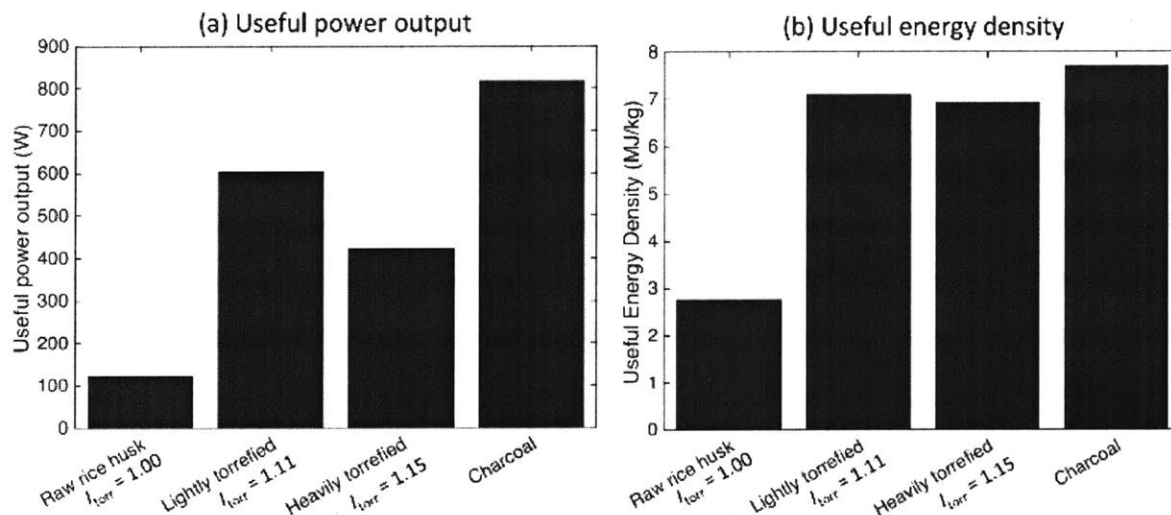


Figure 55 - (a) Useful power outputs and (b) useful energy densities for the following fuel types: raw rice husk briquettes with $I_{torr} = 1.00$, lightly torrefied rice husk briquettes with $I_{torr} = 1.11$, heavily torrefied rice husk briquettes with $I_{torr} = 1.15$, and charcoal briquettes as a positive control.

Therefore, as we see from the exercise above, just because increasing torrefaction severity increases the HHV of the output product, this does not guarantee that the *useful* energy density and power output of the briquetted fuel will increase accordingly. In fact, what our

analysis has revealed is a much more complex landscape between the index of torrefaction and the various “secondary characteristics” of solid fuel cooking.

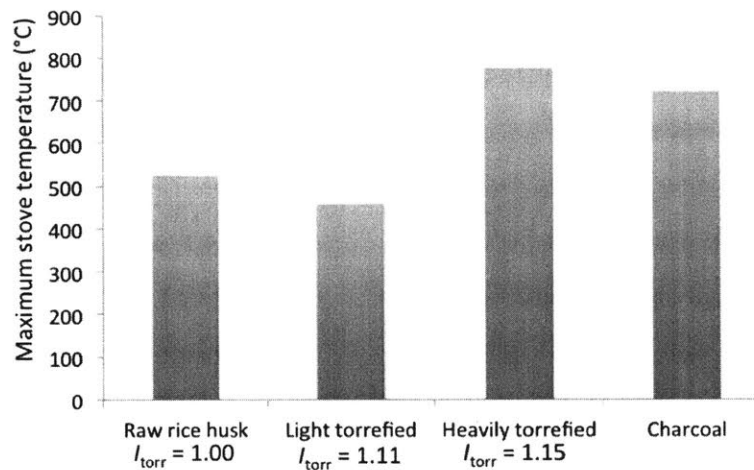


Figure 56 - The maximum stove temperatures reached for cooking on a *jiko* cook stove using different solid fuel types: raw rice husk briquettes with $I_{\text{torr}} = 1.00$, lightly torrefied rice husk briquettes with $I_{\text{torr}} = 1.11$, heavily torrefied rice husk briquettes with $I_{\text{torr}} = 1.15$, and charcoal briquettes as a positive control.

We can do further in analyzing the cooking performance. By tracking the temperature inside the cook stove, we were also able to measure the maximum stove temperature for each type of fuel used. Figure 56 shows the maximum stove temperatures reached during the different cooking experiments. We see that in the case of raw and lightly torrefied rice husk briquettes, the stove temperature remains cold (around 500°C). It is not only until the heavy torrefaction regime do we see an increase in the stove temperature (around 700°C). Therefore, if the torrefied fuel briquettes are used for specific cooking purposes (e.g. baking) where a higher temperature is required, this requirement does impose some constraints on the minimally viable index of torrefaction.

Finally, cooking performance is also dictated by the emissions characteristics, especially if the cooking is done indoors. To evaluate the emission characteristics, a carbon monoxide logger (Bacharach) and a carbon dioxide logger (COZIR-WR) were installed in the exhaust hood above the cook stove experiment. Because the different stoves burn at different rates, we measured the ratio of carbon monoxide to carbon dioxide levels as a relative

quantification of the emission level due to incomplete combustion within the cook stove. Figure 57 plots these ratios for the differently torrefied rice husk solid fuel briquettes.

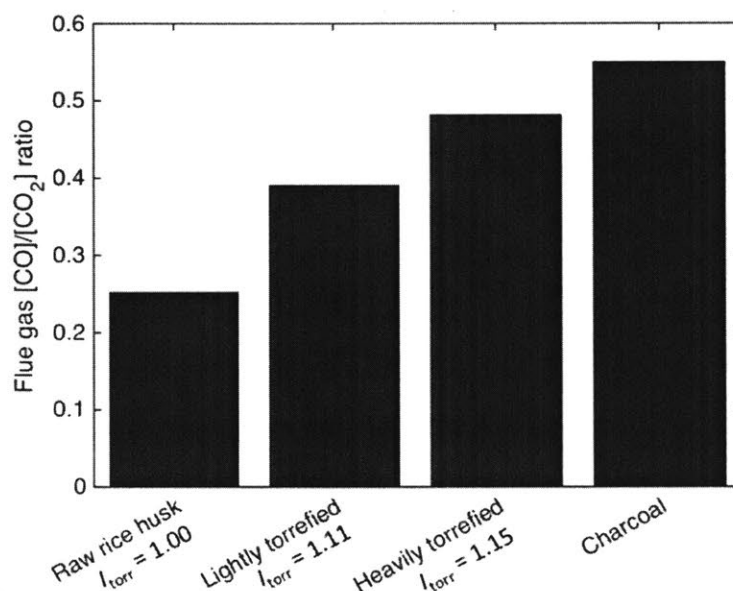


Figure 57 - The carbon monoxide to carbon dioxide ratio under different cooking conditions for the following fuel types: raw rice husk briquettes with $I_{\text{torr}} = 1.00$, lightly torrefied rice husk briquettes with $I_{\text{torr}} = 1.11$, heavily torrefied rice husk briquettes with $I_{\text{torr}} = 1.15$, and charcoal briquettes as a positive control.

As can be observed, the completeness of combustion reduces as the torrefaction severity increases, and the torrefied fuel briquettes increasingly become charcoal-like in their emission profiles (increasing relative carbon monoxide levels). For organizations or end users that rely on indoor cooking, the carbon monoxide level may dictate the maximum possible index of torrefaction, which may very well form a trade-off relationship with the overall energy density of the fuel, for example.

4.5 General Approach for Rapid Reactor Validation and Scaling

In this study, we defined the index of torrefaction as a one-dimensional measure of the severity of torrefaction based on the extent of energy densification in the torrefied biomass, as a result of the combination of normalized air/fuel ratio and the solid residence time.

From this definition, we demonstrated that many “secondary characteristics”—such as fixed carbon content, elemental analysis, grindability, or cooking characteristics—have a functional mapping relationship with the index of torrefaction. As a result of this, we arrived at a much more simplified method of reactor condition selection and design when a “secondary characteristic” is imposed by the end fuel user, without needing to re-run the reactor over a range of operating conditions to map out the constraints. This is the essence and main utility of using the index of torrefaction to guide our design process.

Furthermore, by trying to establish a connection between the index of torrefaction and various cooking characteristics, we demonstrated that even though the higher heating value of the torrefied biomass increases monotonically with the index of torrefaction, it is not guaranteed that when such fuels are briquetted and combusted in a cook stove set-up, there will necessarily be an increase in the useful energy density or useful power output. Rather, our research points to a more complex interplay between the various cooking characteristics and the index of torrefaction. We strongly suspect that most of these characteristics are dependent on the method of briquetting, the cook stove design, and the method of cooking. Therefore, it is recommended that for any new potential application for the torrefied fuel, that the desired performance characteristics of the fuel be carefully mapped using the index of torrefaction as the conduit to guide the design and reactor condition selection.

Chapter 5 Analysis and Mitigation of Energy Loss

Mechanisms in a Torrefaction Reactor

The validation and quantification of a laboratory-scale torrefaction reactor described previously in 0 has the potential to allow us to scale its design for subsequent commercial deployment in order to create economic value from rural agricultural residues. However, this previous study merely describes how the lab reactor performs, and does not propose a science-based method to improve on the existing design in order to make it even more efficient as it scales. This study quantifies the different mechanisms of energy losses throughout the lab reactor system, and therefore proposes concrete steps towards an improved design for scaling up. We identified and characterized three mechanisms of energy losses, and proposed and validated design improvements to counteract against these losses. The first loss is the thermal dissipation through the side wall. By balancing the insulation material cost and the ongoing energy loss, we arrived at a formula that describes the optimal insulation thickness for different reactor operating conditions and scales. The second loss is the thermal dissipation through the char-cooling segment. By modeling an air-preheating channel to recycle the dissipated heat from the char-cooling segment, we concluded that the air channel should be as narrow as practicable, while the length of the char-cooling segment should be as short as possible without causing the torrefied biomass to emerge at an excessive temperature. Finally, the third loss mechanism is in the exhaust stream. We found that most of the energy loss is carried by the chemical enthalpy availability in the escaping unburned volatiles in the exhaust stream, rather in the sensible heat of the exhaust stream. By designing a secondary oxidation zone, we demonstrated that we could harness most of this combustible while minimizing pollution from the reactor. Of the three mechanisms of energy loss, the chemical availability in the exhaust stream by far dominates; therefore, in order to design for scaling up the reactor, a secondary oxidation zone that can stably harness the heat from the unburned volatiles should be of utmost importance.

5.1 Need for an Energy-Based Method for Reactor Improvement

In 0, we described and validated the performance of a laboratory-scale torrefaction reactor. We proposed that our approach and design yield additional scaling insights compared to many other laboratory-scale torrefaction reactors (see Branca *et al.*, 2014, Nhuchhen *et al.*, 2016, and Ren *et al.*, 2012 for different torrefaction reactor design concepts) because ours encapsulate more realistic elements of reactor performance and behavior that are crucial for scaling up the reactor. However, one major weakness of our study, like the previous work in literature, is that our laboratory-scale system merely describes, but does not offer a concrete way forward in improving on the reactor design. In this study, we posit that, given the torrefaction system's primary focus is on energy conversion, we can gain the most insight into how to make the overall scaled-up system more energy-efficient by studying the overall energy balance and losses through the current laboratory-scale torrefaction reactor, and understanding how these losses will scale as the reactor design is scaled up. This will then allow us to propose various improvements and optimizations that we can undertake to improve the reactor's overall energy performance.

We begin our analysis by quantifying the total biomass that flows through the reactor under different solid residence time and normalized air/fuel ratio conditions. Then we characterize the various losses as a fraction of this total quantity. In particular, we focus our attention on three types of energy loss mechanisms: (1) thermal dissipation from the reactor side walls, (2) thermal dissipation from the char-cooling segment, and (3) potential energy loss due to unburned volatiles mixed in the reactor exhaust stream. These mechanisms are illustrated in Figure 58. In each of the sections in this chapter, we measure and quantify each of these loss mechanisms, and then through a mixture of analysis and experimentation, propose and validate design improvements that will minimize the effects of these loss mechanisms.

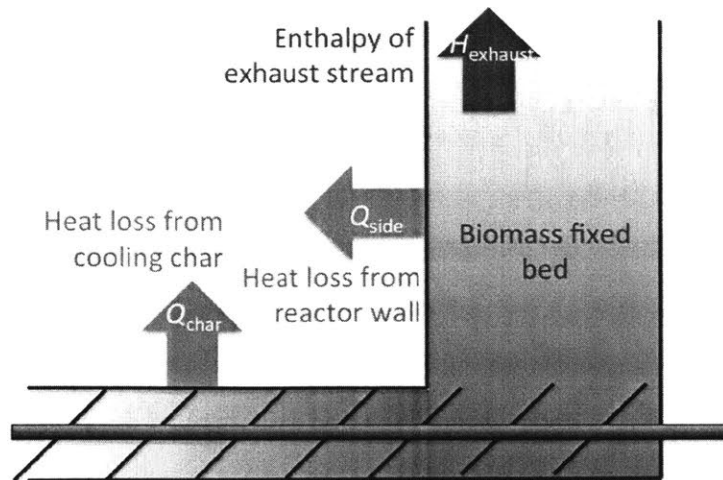


Figure 58 - Illustration of the three types of energy loss mechanisms from the reactor assembly analyzed in detail in this study.

5.2 Total Biomass Energy Fluxes from the Reactor System

By changing the residence time of the reactor and even the type of biomass (which affects the bulk bed density), we alter the mass flow rate of biomass through the system, and necessarily, the total energy flow rate through the system. This will then also affect the absolute magnitudes of the various losses. Therefore, in order to discuss the losses under various operating conditions and for different types of biomass in a meaningful way, we need a basis against which to compare these losses. Given a reactor of cross-sectional area πR_r^2 , we define this basis as the total biomass energy flux from the system, φ_{BM} , as follows:

$$\varphi_{BM} \equiv \frac{\dot{m}_{char} HHV_{char}}{\pi R_r^2}.$$

This quantity is related to the biomass energy that flows through the reactor, normalized by the reactor cross-sectional area. Therefore, a larger reactor processing more biomass operating at the same reaction condition is predicted to still have the same energy flux. Figure 59 plots this total biomass energy flux under different reactor operating conditions for three types of biomass: pine shavings (a), hay (b), and rice husk (c). The overall magnitudes of the energy fluxes are about 0.2-0.7 MW m⁻². This means that for a reactor diameter of 4 inches (10.2 cm), the reactor processes about 2-6 kW's worth of incoming biomass.

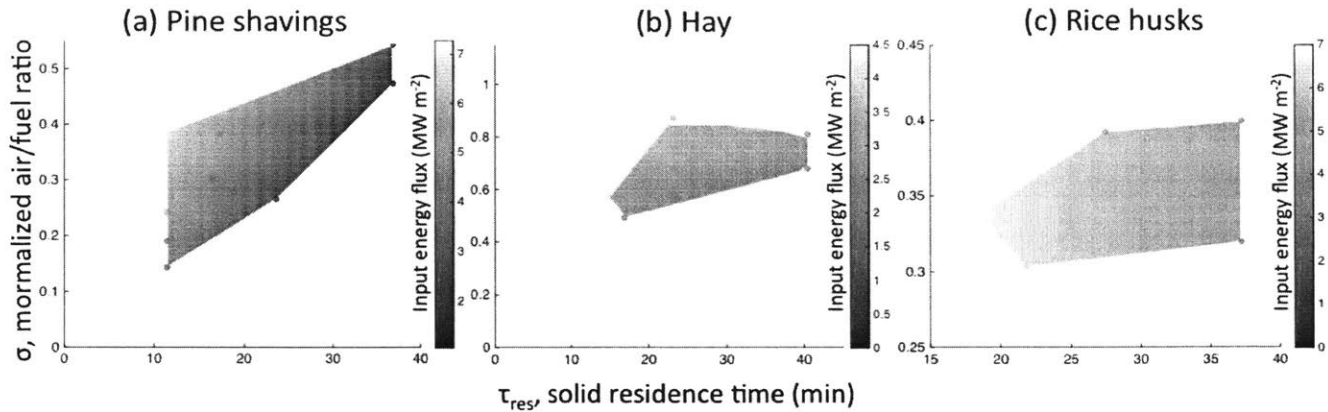


Figure 59 - Total biomass energy flux (ϕ_{BM}) through the reactor system under different reactor operating conditions for pine shavings (a), hay (b), and rice husk (c). There is generally a strong dependency on the solid residence time and a weaker dependency on the normalized air/fuel ratio.

We first note that there is a strong dependency of the total energy flux on the solid residence time: the shorter the solid residence time is, the higher the solid mass flow rate is through the reactor, and therefore the higher the total energy flux is. However, there is also some dependency on the normalized air/fuel ratio, and the reason is perhaps more subtle: a more severe torrefaction condition typically results in a higher volumetric reduction (and hence greater downward axial velocity) in the biomass fixed bed and therefore a higher effective solid mass flow rate. This quantity then gives us a basis for evaluating the magnitudes of the subsequent energy losses: all these losses will be expressed as a fraction of the total biomass energy flow through the reactor.

5.3 Characterizing and Mitigation Losses from Reactor Side Walls

The fixed bed reactor is surrounded by insulation in order to minimize heat loss from the hot central core. Even so, we believe that heat dissipation from the reactor side walls is non-trivial and set out to quantify it.

5.3.1 Measurement Methodology

We first installed a series of thermocouples, spaced about 1.25 inches (3.2 cm) apart, axially on the outer side wall of the reactor (outside the insulation layer). Furthermore, we installed four thermocouples, spaced also about 1.25 inches (3.2 cm) apart, axially on the inner wall of the reactor at the biomass fixed bed interface. As illustrated in Figure 60, this allows us to take the temperature profiles at the inner wall and the outer wall of the reactor.

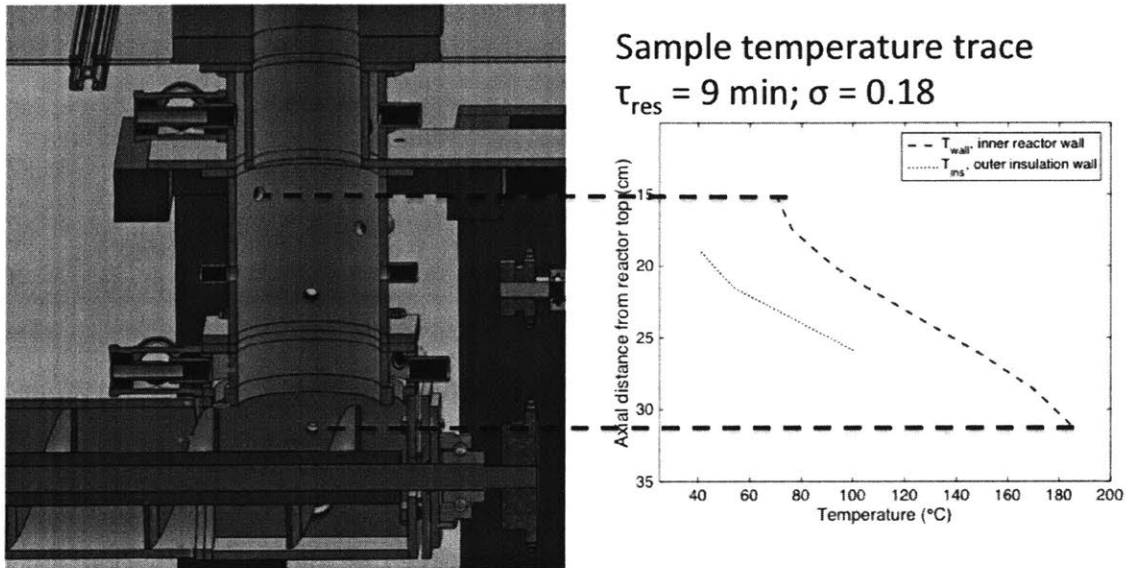


Figure 60 - Thermocouples are placed axially along the outside and inside walls of the reactor assembly in order to measure the heat loss from the reactor side wall. The plot on the right-hand side shows the steady-state sample temperature profiles at the inner reactor wall (T_{wall} , blue dashed line) and at the outer insulation wall (T_{ins} , red solid line). The difference between the two profiles can be used to compute the overall heat loss.

In Figure 60, having obtained the steady-state temperature profiles both at the inner reactor wall $T_{wall}(z)$ (blue dashed line) as well as at the outer insulation surface of the wall $T_{ins}(z)$ (red solid line), we note that the inner reactor wall at steady state is maintained at a consistently higher temperature compared to the outer reactor wall. This signifies a net heat flow from the inside of the reactor to the outside. To quantify this heat flow, we need to construct a heat loss model (Figure 61).

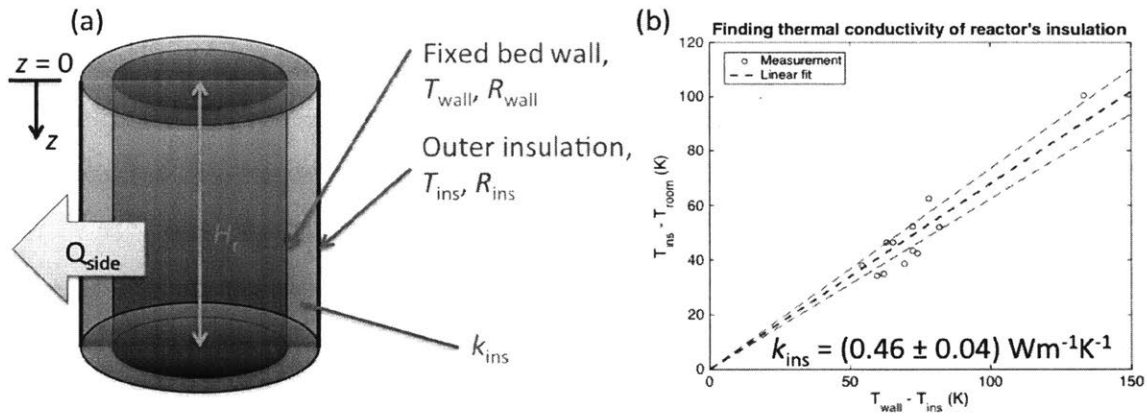


Figure 61 - (a) Schematic of a heat loss model through the reactor side wall. The reactor is approximated as a cylinder of height H_r . The insulated side wall is approximated to have an effective thermal conductivity of k_{ins} [$\text{W m}^{-1} \text{K}^{-1}$]. (b) A plot of temperature differences inside and outside the reactor that is used to infer the effective thermal conductivity k_{ins} .

As Figure 61 indicates, we approximated the reactor as a cylinder with a radius at the inner wall of R_{wall} and the radius at the outer insulation surface of R_{ins} . The height of the reactor cylinder is H_r . Therefore, the thickness of the stainless steel wall plus the insulation layer is $R_{\text{ins}} - R_{\text{wall}}$, and this layer is assumed to have a uniform effective thermal conductivity of k_{ins} [$\text{W m}^{-1} \text{K}^{-1}$].

With these assumptions in place, we can consider a small axial slice dz of the reactor and write the radial heat flow dQ_{side} [J s^{-1}] through this slice as:

$$dQ_{\text{side}}(z) = \frac{2\pi k_{\text{ins}} dz}{\ln(R_{\text{ins}}/R_{\text{wall}})} (T_{\text{wall}} - T_{\text{ins}}) = 2\pi h_{\text{air}} R_{\text{ins}} dz (T_{\text{ins}} - T_{\text{amb}}),$$

where $h_{\text{air}} \approx 10 \text{ W m}^{-2} \text{K}^{-1}$ is the convective heat transfer coefficient of ambient (still) air at the outer insulation surface, and where T_{amb} is the temperature of the ambient air. Based on the equation above, we see that we can infer k_{ins} by linear-fitting the following relationship (Figure 61b):

$$(T_{\text{wall}} - T_{\text{ins}}) = \frac{h_{\text{air}} R_{\text{ins}} \ln(R_{\text{ins}}/R_{\text{wall}})}{k_{\text{ins}}} (T_{\text{ins}} - T_{\text{amb}}).$$

From the composite steady-state data points involving multiple experiments, we estimated that $k_{\text{ins}} \approx (0.46 \pm 0.04) \text{ W m}^{-1} \text{ K}^{-1}$ for the case of our laboratory-scale reactor. Then, we can integrate the differential heat losses over the side wall over the entire axial length of the reactor to obtain:

$$Q_{\text{side}} = \int_0^{H_r} dQ_{\text{side}}(z) dz = \frac{2\pi k_{\text{ins}}}{\ln(R_{\text{ins}}/R_{\text{wall}})} \int_0^{H_r} (T_{\text{wall}}(z) - T_{\text{ins}}(z)) dz.$$

In this case, in order to obtain a continuous integrant, we interpolated and extrapolated the temperature profiles $T_{\text{wall}}(z)$ and $T_{\text{ins}}(z)$ beyond the few axial points sampled by the thermocouples.

5.3.2 Results and Discussion

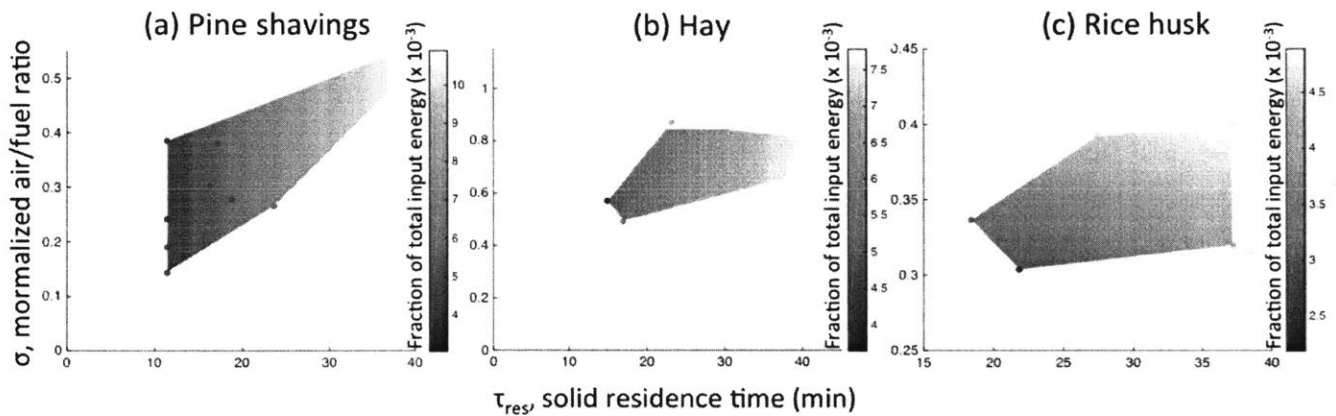


Figure 62 - Total thermal dissipation from the reactor side wall, as a fraction of the total biomass energy flow, under different reactor operating conditions for pine shavings (a), hay (b), and rice husk (c). There is generally a strong dependence on the solid residence time.

We can observe in Figure 62 that generally, with a small reactor at the laboratory scale, about 1% of the total biomass energy is lost due to thermal dissipation from the reactor side wall. For all three types of biomass, this loss is most significant for long solid residence time, and this trend makes sense: a hot reactor at a given temperature dissipates the same power as thermal loss, but increasing the solid residence time means reducing the total

biomass energy flow through the reactor. Therefore, we can see that from the perspective of minimizing energy loss, one important mitigation strategy is to minimize the solid residence time, which maximizes the mass flow rate of solid fuel that can be processed through a reactor of a given size.

5.3.3 Scaling the Side Wall Thermal Loss

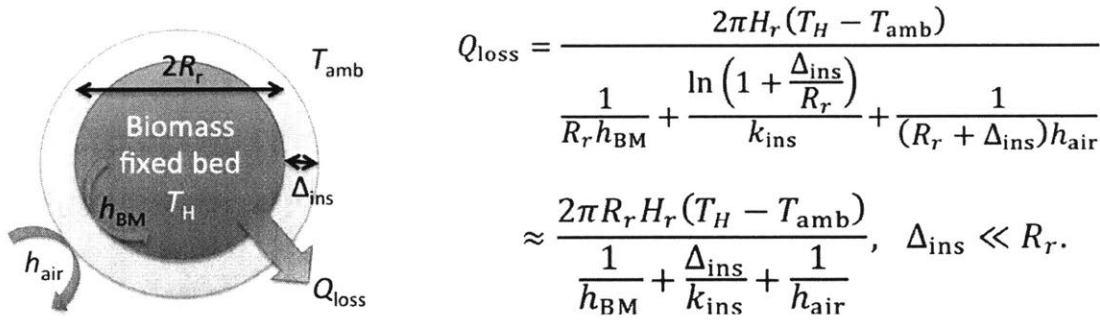


Figure 63 - A simplified analysis of how the thermal dissipation from the reactor side wall depends on reactor scale.

In addressing thermal dissipation from the reactor side wall, the first point to note is that because our reactor is small, it has a high surface area-to-volume ratio and therefore tends to dissipate heat significantly through its surfaces. How differently will a scaled-up reactor behave? To get a coarse-grained approximation, we first assume that the reactor is a cylinder of height H_r and radius R_r and operates uniformly at some elevated temperature T_H compared to the ambient temperature T_{amb} (Figure 63).

As we scale the reactor, as long as the biomass mass flux Φ_{BM} through the reactor remains constant, then the reactor radius R_r will scale as $\sqrt{\dot{m}_{\text{BM}}/\Phi_{\text{BM}}}$. Let us denote the relative heat loss R_{loss} with respect to the total biomass energy flow through the reactor as $\epsilon_{\text{loss}} = Q_{\text{loss}}/(\dot{m}_{\text{BM}} \text{HHV}_{\text{BM}})$. Then assuming that the heat transfer characteristics ($h_{\text{BM}}, k_{\text{ins}}, h_{\text{air}}$), the biomass characteristics (HHV_{BM}), and the thickness Δ_{ins} of the reactor wall and insulating material does not change as the reactor scales up in the feeding rate, we see that in the limit that $\Delta_{\text{ins}} \ll R_r$,

$$\frac{\mathcal{E}_{\text{loss}}^*}{\mathcal{E}_{\text{loss}}} = \sqrt{\frac{\dot{m}_{\text{BM}}}{\dot{m}_{\text{BM}}^*}}$$

where the asterisk superscripts denote a new loss and mass flow rate in a scaled-up reactor. Therefore, as the reactor scales, its relative heat loss from the side wall decreases as $1/\sqrt{\dot{m}_{\text{BM}}}$. For our laboratory-scale reactor, we started with 0.4% and 0.3% side wall heat loss in the mild and severe torrefaction cases, respectively. Table 22 predicts the same side wall heat losses as the reactor scales up. We can therefore see that as the reactor radius increases, the thermal dissipation from the side wall quickly becomes unimportant compared to losses.

Table 22 - Predicted relative magnitude thermal dissipation from the reactor side wall as the reactor is scaled up.

Biomass feed rate	Reactor radius	$\mathcal{E}_{\text{side}}$, mild torrefaction	$\mathcal{E}_{\text{side}}$, severe torrefaction
~ 1 kg/h	5.1 cm	0.4%	0.3%
~ 20 kg/h	22.9 cm	0.09%	0.07%
~200 kg/h	73.2 cm	0.03%	0.02%

5.3.4 Optimization of Thermal Insulation

While we can, if we wish, reduce the side wall heat dissipation by a few percentage points by insulating the walls more or selecting a material with a lower thermal conductivity k_{ins} . In general, there is a trade-off between the cost of the insulation material and the overall thermal resistance. That is, while more thermally resistant insulation may reduce the heat loss from the side walls and therefore the recurrent cost C_0 in terms of lost biomass calorific value, the total installation cost C_1 of the thermal also becomes more expensive. Therefore, there is a trade-off between the upfront installation cost C_1 and the constant recurrent cost C_0 , which is discounted into the future with an interest rate of $r = 5\%$ per annum, assuming a reactor lifetime operation of $\tau_{\text{life}} = 5$ years. Therefore, we can define an objective function $O(\Delta_{\text{ins}})$ of the form

$$O(\Delta_{\text{ins}}) \equiv C_I(\Delta_{\text{ins}}) + C_O(\Delta_{\text{ins}}) \int_0^{\tau_{\text{life}}} e^{rt} dt = C_I(\Delta_{\text{ins}}) + \frac{C_O(\Delta_{\text{ins}})}{r} (e^{r\tau_{\text{life}}} - 1).$$

Eq. 1

Now, how do C_I and C_O relate to design parameters such as the thickness of the thermal insulation? For a common insulation material such as fiberglass, the cost is about \$26.50 per 15 in. (38.1 cm) by 25 ft. (7.62 m) for a R-30 (in U.S. customary unit) roll (Home Depot, 2017). This is equivalent to a thermal conductivity coefficient of $k = 0.04 \text{ W K}^{-1} \text{ m}^{-1}$, and a cost per surface area of $c_V = \$43.68 \text{ m}^{-3}$. Therefore, for a reactor of height H_r and radius R_r and an outer insulation thickness of Δ_{ins} , the total installation cost C_I of the fiberglass insulation needed around the side wall is

$$C_I = \pi H_r \Delta_{\text{ins}} (2R_r + \Delta_{\text{ins}}) c_V.$$

So far we have calculated the installation cost of the thermal insulation material. On the other hand, we need to consider the recurrent cost due to equivalent biomass energy loss from the side wall. For common types of agricultural residues in the rural area being earmarked for thermal co-firing, the average price paid is around $c_{\text{BM}} = \$40/\text{wet ton}$ (Shantilal, 2015). Assuming that the common agricultural residue has an average moisture content of $Y_M = 40\%$, then the calorific value on a wet basis is $\text{HHV}_{\text{Dry}} / (1 + Y_M)$. This means that the average price of biomass energy can be expressed as $c_{\text{BM}} (1 + Y_M) / \text{HHV}_{\text{Dry}} [\$ \text{J}^{-1}]$. For typical biomass of a higher heating value of around $\text{HHV}_{\text{Dry}} = 18 \text{ MJ kg}^{-1}$ on a dry basis, the average price turns out to be about $\$0.03 \text{ MJ}^{-1}$.

As illustrated in Figure 63, we already have the expression of reactor's energy loss $Q_{\text{loss,side}}$ from the side wall. This means that the equivalent recurrent cost C_O is given by

$$C_O = \frac{P_O Q_{\text{loss,side}} c_{\text{BM}} (1 + Y_M)}{\text{HHV}_{\text{Dry}}},$$

where the proportionality factor P_O is related to the fraction of time that the machine will actually be processing biomass. Assuming two harvest seasons in a year, each lasting about 2 months, and a daily operation of 12 hours, then $P_O = 0.083$. Plugging in both C_I and C_O into Eq. 1, we obtain:

$$O(\Delta_{\text{ins}}) = \pi H_r \Delta_{\text{ins}} (2R_r + \Delta_{\text{ins}}) c_V + \frac{2\pi R_r H_r (T_H - T_{\text{amb}}) P_0 (1 + Y_M) (e^{r\tau_{\text{life}}} - 1) c_{\text{BM}}}{\text{HHV}_{\text{Dry}} \left(\frac{1}{h_{\text{BM}}} + \frac{\Delta_{\text{ins}}}{k_{\text{ins}}} + \frac{1}{h_{\text{air}}} \right) r}$$

This massive equation encapsulates many of the design parameters, and it is worthwhile to discuss them one by one. The first term on the right-hand side essentially states that as the insulation thickness and the cost per volume of insulation increases, the overall cost will also increase. As the reactor scales (increasing R_r), this installation cost also increases. Under these conditions, a reactor with lighter outer insulation is preferred. The second term on the right-hand side, which describes the present value of all future recurrent cost arising from the biomass equivalent of thermal loss from the reactor side wall, is more involved. The recurrent cost goes up, and thus a heavier insulation outer layer is preferred, as the reactor scales up (increasing R_r , H_r), as the torrefaction reaction becomes more severe (increasing T_H), as the input biomass is wetter (increasing Y_M), as the life span of the reactor increases (increasing τ_{life}), as the price of biomass increases (increasing c_{BM}), as the reactor use frequency increases (increasing P_0), as the intrinsic calorific value of the biomass decreases (decreasing HHV_{Dry}), as the prevalent discount rate decreases (decreasing r), and finally, as the various thermal resistance terms against side wall heat loss become larger (such as increasing the ratio $\Delta_{\text{ins}}/k_{\text{ins}}$).

We can see that the objective function is of the form $a\Delta_{\text{ins}} + b\Delta_{\text{ins}}^2 + \frac{c}{d+e\Delta_{\text{ins}}}$. To understand which terms are more important, we plot the total cost (discounted into present value) as a function of the different insulation thicknesses, for (a) light torrefaction and (b) severe torrefaction in Figure 64 using the laboratory-scale reactor.

We can see that the installation cost (blue dashed lines) increases over thickness, as more material is used. However, the recurrent thermal loss cost (red dotted lines) decreases very rapidly as the insulation thickness increases. This gives rise to the overall cost (solid black lines) which has minima at around $\Delta_{\text{ins}} = 13.5$ cm for mild torrefaction, and $\Delta_{\text{ins}} = 16.6$ cm for severe torrefaction. This makes sense: as the temperature within the reactor becomes higher, there is more heat loss from the side wall, and therefore both a greater total cost as well as a thickness insulation layer necessary. Note that these costs are independent of the

overall biomass flow rate: that is, at a given reactor temperature and dimension, it is in our interest to maximize the solid flow rate (minimize solid residence time) if our design goal is to minimize thermal losses such as from the side wall.

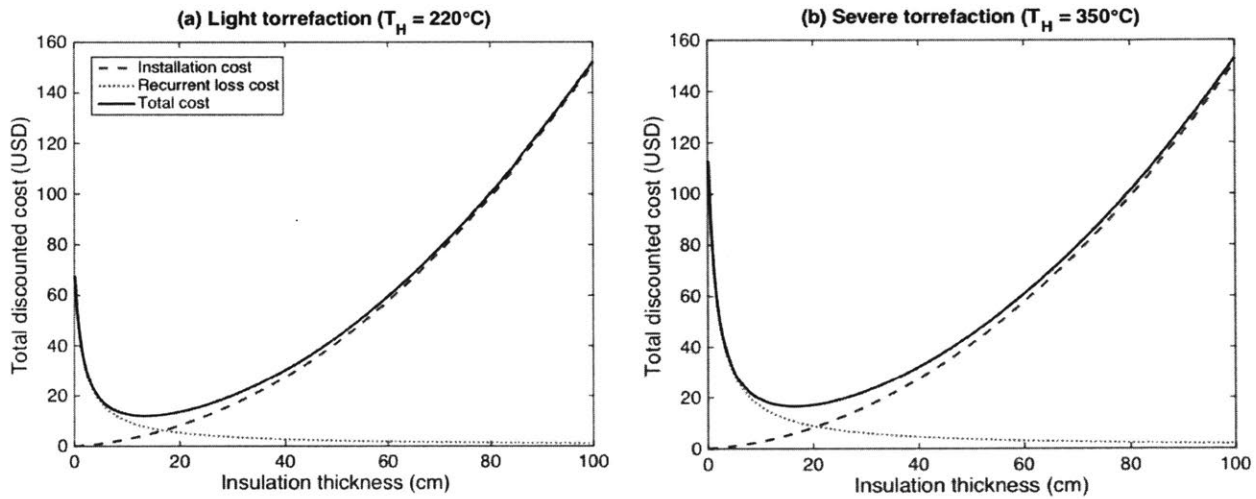


Figure 64 - Total present value of all costs associated with side wall thermal loss as a function of insulation thickness, for (a) light torrefaction and (b) severe torrefaction using the laboratory-scale reactor.

Table 23 - Predicted optimal insulation layer thickness.

Biomass feed rate	Reactor radius	Δ_{ins} , mild torrefaction	Δ_{ins} , severe torrefaction
~ 1 kg/h	5.1 cm	13.5 cm	16.6 cm
~ 20 kg/h	22.9 cm	19.5 cm	24.3 cm
~200 kg/h	73.2 cm	23.4 cm	29.7 cm

In Table 23, we summarize the results of the optimization study on the insulation layer thickness at different reactor scales and under different torrefaction conditions. We demonstrate that, in general, as the reactor scales up, the thickness of the insulation also increases, but only mildly, and therefore remain within the regime of feasibility.

5.4 Characterizing and Mitigating Losses from the Char-Cooling Segment

The fixed bed reactor is surrounded by insulation in order to minimize heat loss from the hot central core. Even so, we believe that heat dissipation from the reactor side walls is non-trivial and set out to quantify it.

5.4.1 Measurement Methodology

After the torrefied biomass emerges from the fixed bed, it is carried in the screw auger through a 2-foot-long (61 cm) char-cooling segment. The design of this cooling segment is to prevent hot torrefied product from seeing significant of air prematurely, which could cause spontaneous combustion. Therefore, the cooling segment is designed to lower the temperature of the torrefied product effectively, and has no insulation beyond a stainless steel outer surface. Therefore, we imagine that significant amount of heat may be lost through this char-cooling segment.

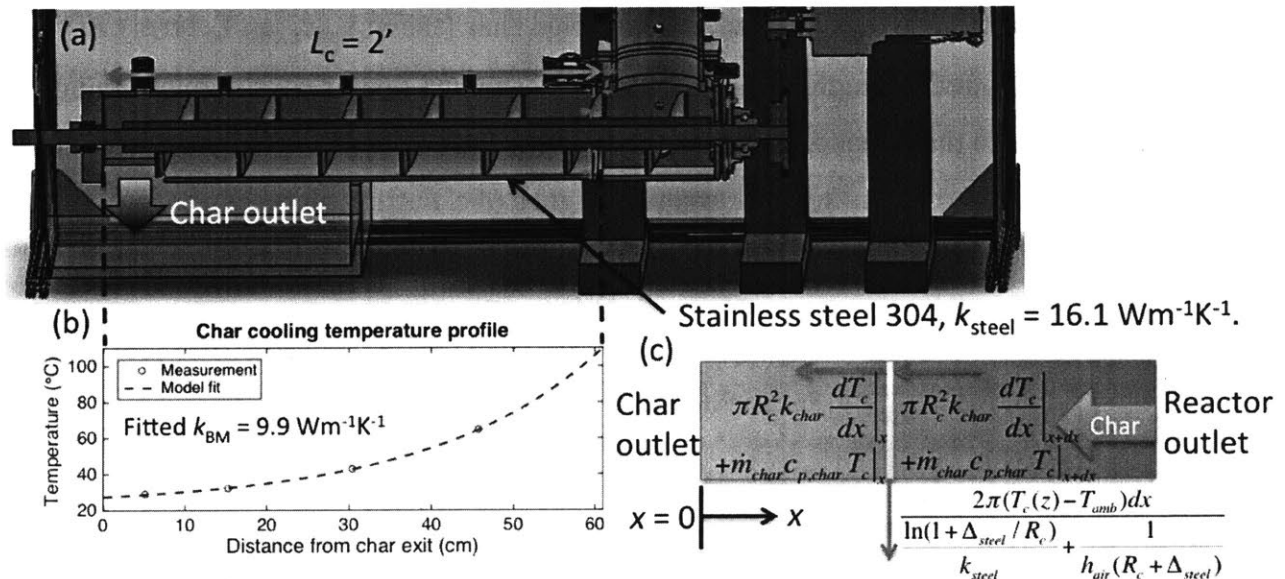


Figure 65 - (a) Schematic of the char-cooling segment. Hot torrefied product is carried by the turning screw auger through this cooling segment before it emerges into the ambient atmosphere from the outlet. (b) A sample steady-state temperature profile along the char-cooling segment, for pine shavings with $\tau_{\text{res}} = 9$ min and $\sigma = 0.18$, with a model fit in dashed line. (c) A schematic of the heat transfer model utilized to generate the model fit in (b). The differential heat transfers into and out of the thin orange slice dx are shown in blue arrows.

In order to quantify the extent of heat loss, we installed thermocouples lengthwise, spaced about 15 cm apart, axially throughout the char-cooling segment (Figure 65a) located at the inner wall at the interface with the cooling biomass. This gives us temperature readouts at four points (Figure 65b), to which an extrapolated model is fitted (blue dashed line).

Because the axial temperature readouts here are much sparser compared to the previous case of measuring the heat loss from the reactor side wall, in this case, we need to consider more carefully how we can use a science-based approach to construct a thermal model that can interpolate and extrapolate the temperature profile along the char-cooling segment (as shown in the blue dashes in Figure 65b). In Figure 65c, we sketch out the schematic of a simplified heat transfer model. Here we assume that there is no radial inhomogeneity, and that the axial heat transfer occurs, as shown in the two horizontal blue arrows, via (a) axial conduction (the $\pi R_c k_{\text{char}} dT_c/dx$ term) through a combination of the torrefied char, gases, and the outer stainless steel lining (with a bulk effective thermal conductivity k_{char} to be determined by fitting, which we assume to the first order is temperature-independent), and (b) axial convection by the slow-moving torrefied char (the $\dot{m}_{\text{char}} c_{p,\text{char}} T_c$ term). At the same time, throughout the length of the char-cooling segment, heat is continuously being lost via the surface to the outside, as represented by the $2\pi R_c k_{\text{steel}}(T_c - T_{\text{amb}})dx$ term and shown by the downward-pointing blue arrow in Figure 65c. Putting all these energy balance terms together, we arrive at the following model to describe the axial temperature profile:

$$k_{\text{char}} \frac{d^2 T_c}{dx^2} + c_{p,\text{char}} \rho_{\text{char}} v_{\text{char}} \frac{dT_c}{dx} = \frac{2}{R_c^2 \Omega} (T_c - T_{\text{amb}}),$$

Eq. 2

where the thermal resistance term Ω is defined as:

$$\Omega \equiv \frac{\ln(1 + \Delta_{\text{steel}}/R_c)}{k_{\text{steel}}} + \frac{1}{h_{\text{air}}(R_c + \Delta_{\text{steel}})}.$$

Here, $\Delta_{\text{steel}} = 0.64$ cm is the thickness of the type 304 stainless steel we used to build the char-cooling segment, and $k_{\text{steel}} = 16.2$ W m⁻¹ K⁻¹ is the thermal conductivity of the same steel. Normally, the heat capacity ($c_{p,\text{char}}$) and bulk density (ρ_{char}) of the torrefied char may be a function of temperature, and therefore may exhibit spatial dependence as the torrefied

char cools axially in the segment. Nonetheless, here for simplicity we ignore this second-order effect, and evaluated ρ_{char} by weighing the product. As for $c_{p,\text{char}}$, we do not have a simple way to experimentally determine it; however, knowing the elemental (ultimate) analysis of the torrefied product, we can approximate it by Merrick's correlation (1983):

$$c_{p,\text{char}} = \frac{R}{\langle \text{MW} \rangle_{\text{char}}} \left(e^{\frac{380}{T}} \left(\frac{e^{\frac{380}{T}} - 1}{380/T} \right)^{-2} + 2e^{\frac{1800}{T}} \left(\frac{e^{\frac{1800}{T}} - 1}{1800/T} \right)^{-2} \right),$$

where the effective molecular weight $\langle \text{MW} \rangle_{\text{char}}$ of the torrefied char is defined as:

$$\langle \text{MW} \rangle_{\text{char}} \equiv \left(\sum_{i \in \{\text{C,H,O,N,S}\}} \frac{Y_{i(\text{DAF})}}{\text{MW}_i} \right)^{-1}.$$

In Eq. 2, we have a second-order differential equation of the type $aT_c'' + bT_c' + c(T_c - T_{\text{amb}}) = 0$ that can be solved analytically, with the general solution:

$$T_c(x) = r_1 e^{r_1 x} + r_2 e^{r_2 x} + T_{\text{amb}}, \quad r_1, r_2 = \frac{-b \pm \sqrt{b^2 - 4ac}}{2a}.$$

For each operating condition, this model was utilized to fit $T_c(x)$ to the thermocouple readouts using the `cftool` fitting function in MATLAB. Once we obtain the interpolated and extrapolated profile $T_c(x)$, we can then compute the total heat flow from the char-cooling segment as:

$$Q_{\text{char}} = \frac{2\pi}{\Omega} \int_0^{L_c} (T_c(x) - T_{\text{amb}}) dx.$$

5.4.2 Results and Discussion

The thermal dissipation from the char-cooling segment in Figure 66 under different reactor operating conditions for different biomass types. We observe that in contrast to the dissipation from the side wall, the relative magnitude of the dissipation from the char-cooling segment is also minor (around 1% of the total biomass energy flow through the reactor). However, the same strong dependence on the solid residence time, as rationalized previously, persists.

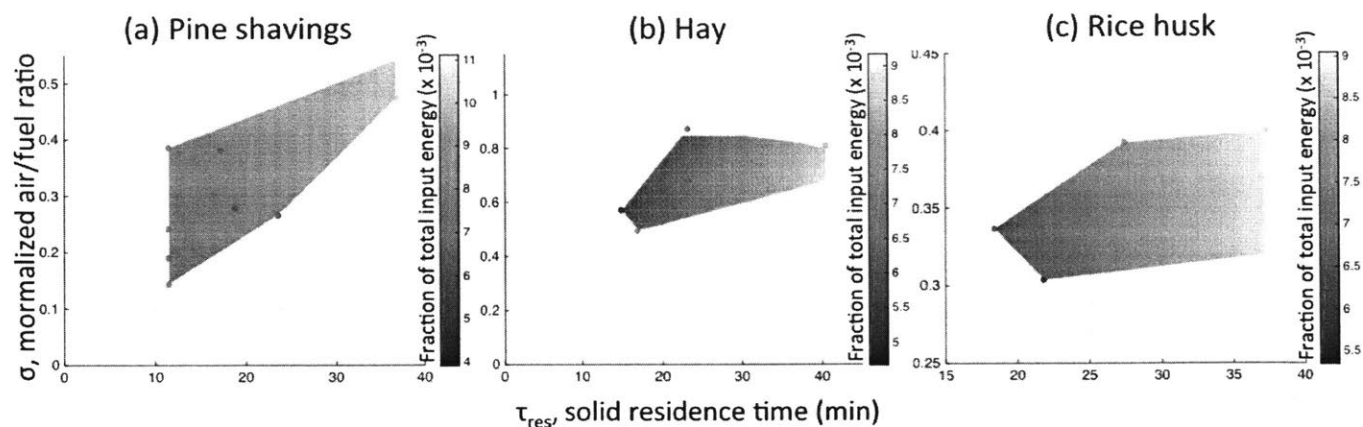


Figure 66 - Total thermal dissipation from the char-cooling segment, as a fraction of the total biomass energy flow, under different reactor operating conditions for pine shavings (a), hay (b), and rice husk (c). There is generally a strong dependence on the solid residence time.

5.4.3 Proposed Air-Preheating Mechanism and Validation Strategy

In a sense, it is desirable to lose heat as quickly as possible in the char-cooling segment. Nonetheless, this heat is not necessarily irrevocably “lost” to the environment: a scaled-up reactor design with improvement in overall energy performance may utilize this dissipated heat to pre-heat the incoming air that will ultimately enter into the reactor. This pre-heating is beneficial as it stabilizes the torrefaction reaction and reduces product inhomogeneity. While it is beyond the scope of this thesis to build and validate this air-preheating mechanism, in this section we use modeling tools to pursue an initial validation and design selection of such a mechanism.

Figure 67 illustrates our general modeling approach by viewing the char-cooling segment and air-preheating channel in a transverse (axial) cross section (a) as well as in a longitudinal cross section (b).

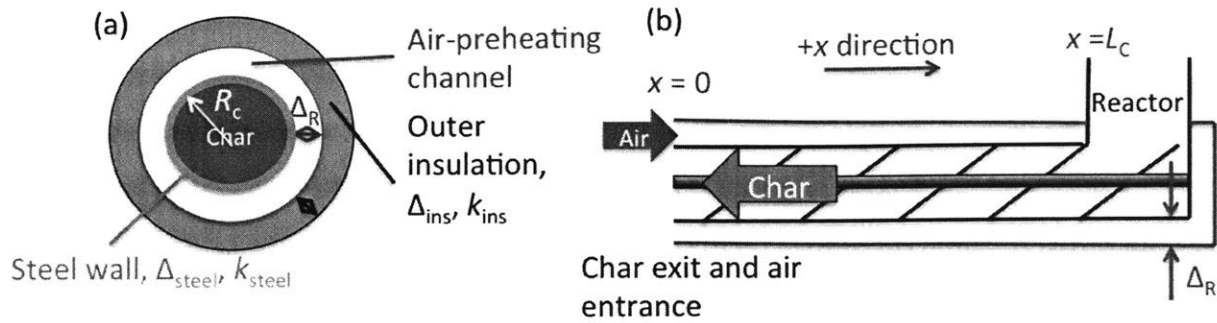


Figure 67 - (a) Schematic of a transverse (axial) cross section of the char-cooling segment with a proposed outer surrounding air-preheating channel. (b) Schematic of a longitudinal cross section of the same char-cooling segment and air-preheating channel.

Let us examine the transverse cross section view first (Figure 67a). We see that the central core consists of the cooling char of radius R_c , which is then surrounded by steel of thickness Δ_{steel} and thermal conductivity k_{steel} (shown in light gray), followed by the air-preheating channel of width Δ_R (shown in white). Finally, outside of the air-preheating channel there is an outer insulation of thickness Δ_{ins} and thermal conductivity k_{ins} (shown in dark gray). Then from the longitudinal cross section view (Figure 67b), we can define an axial distance variable x , where $x = 0$ represents the solid (torrefied product) outlet at temperature $T_c(z = 0)$ as well as the pre-heated air inlet at temperature $T_p(z = 0)$, and where $x = L_c$ indicates the beginning of the char-cooling segment, where the temperature $T_c(z = L_c)$ of the torrefied biomass is maximum and the temperature $T_p(z = L_c)$ of the pre-heated air is also maximum. The torrefied biomass is conveyed by the auger axially from right to left (decreasing x), while the pre-heated air travels from left to right (increasing x).

With the modeling set-up defined, we proceed to make a few assumptions. Firstly, we assume that the temperature profile in the solid (cooling torrefied biomass) phase and the gaseous (pre-heating air) phase is most interesting in the axial direction (as air is heated up and char cools), and that any radial temperature profile is both less significant and less interesting. We therefore ignore any radial temperature profiles, and assume that at a given z position, the entire solid phase is at a homogeneous temperature, and the entire incoming air is also at a different homogeneous temperature. Based on these assumptions,

we can modify Eq. 2, our earlier attempt at describing the char-cooling temperature profile (illustrated in Figure 65), as follows:

$$k_{\text{char}} \frac{d^2 T_c}{dx^2} + c_{p,\text{char}} \rho_{\text{char}} v_{\text{char}} \frac{dT_c}{dx} = \frac{2}{R_c^2 \Omega} (T_c - T_p),$$

where the radial thermal resistance term Ω is defined, assuming that $R_c \ll L_c$, as:

$$\Omega \equiv \frac{\ln(1 + \Delta_{\text{steel}}/R_c)}{k_{\text{steel}}} + \frac{1}{h_{\text{air}}(v_{\text{air}})(R_c + \Delta_{\text{steel}})}.$$

Here, on the end of the torrefaction reactor ($x = L_c$), the temperature of the torrefied solid is given by

$$T_c(x = L_c) = T_{\text{torr,out}},$$

Eq. 3

while on the end of the solid outlet ($x = 0$), the boundary condition is governed by the thermal conductivity across the air-facing stainless steel cap (SS 304, thickness of $\Delta_{\text{cap}} = 2.5$ cm, of thermal conductivity coefficient k_{cap}) from the cooling char to the outside air at an ambient room temperature of T_{amb} :

$$-k_{\text{cap}} \left. \frac{dT_c}{dx} \right|_{x=0} = \frac{T_c(z = 0) - T_{\text{amb}}}{\frac{1}{h_{\text{air}}} + \frac{\Delta_{\text{cap}}}{k_{\text{cap}}}}.$$

Thus we have a second-order differential equation with two boundary conditions.

Here, we have written the convective thermal coefficient of the pre-heating air h_{air} as a function of the air velocity v_{air} , which is in turn related to the design parameter Δ_R (width of the air-preheating channel) as well as the torrefaction reactor operating conditions as follows:

$$v_{\text{air}} = (\text{AF})_{\text{stoic}} H_r \frac{\rho_{\text{BM}}}{\rho_{\text{air}}} \left(\frac{R_r^2}{2(R_c + \Delta_{\text{steel}})\Delta_R + \Delta_R^2} \right) \frac{\sigma}{\tau_{\text{res}}},$$

where H_r is the height of the torrefaction reactor region. There are various estimations for the convective heat transfer coefficient of air as a function of its velocity. For simplicity we implemented the following empirically determined in the literature (ETB, 2017):

$$h_{\text{air}}(v_{\text{air}}) \approx 10.45 - v_{\text{air}} + 10\sqrt{v_{\text{air}}}.$$

Next, we turn our attention to describe the air-preheating phase. Because the air flows into the reactor at a much faster timescale compared to that of the solid being transported in the char-cooling segment, we made the assumption that the axial convection of air dominates over axial conduction (supported by that the Biot number is around 500 in our design regime of interest). Hence the pre-heated air can be approximated in a plug-flow fashion, reducing the steady-state heat transfer equation in the gas phase into a first-order differential equation:

$$\frac{dT_p}{dz} = \frac{2\pi(R_c + \Delta_{\text{steel}})}{\dot{m}_{\text{air}}c_{\text{air}}\Theta_{\text{char}\rightarrow\text{air}}}(T_c - T_p) - \frac{2\pi(R_c + \Delta_{\text{steel}} + \Delta_R + \Delta_{\text{ins}})}{\dot{m}_{\text{air}}c_{\text{air}}\Theta_{\text{air}\rightarrow\text{amb}}}(T_p - T_{\text{amb}}),$$

where the thermal resistance term $\Theta_{\text{char}\rightarrow\text{air}}$ describes the heat transfer between the cooling char at location z and the pre-heating air across the steel wall:

$$\Theta_{\text{char}\rightarrow\text{air}} \equiv \frac{\ln(1 + \Delta_{\text{steel}}/R_c)}{k_{\text{steel}}} + \frac{1}{h_{\text{air}}(R_c + \Delta_{\text{steel}})},$$

and where the thermal resistance term $\Theta_{\text{air}\rightarrow\text{amb}}$ describes the heat transfer between the pre-heating air at location z and the outside ambient air (room temperature) across the outer insulation:

$$\Theta_{\text{air}\rightarrow\text{amb}} \equiv \frac{1}{h_{\text{air}}(R_c + \Delta_{\text{steel}} + \Delta_R)} + \frac{\ln\left(\frac{R_c + \Delta_{\text{steel}} + \Delta_R + \Delta_{\text{ins}}}{R_c + \Delta_{\text{steel}} + \Delta_R}\right)}{k_{\text{ins}}} + \frac{1}{h_{\text{amb}}(R_c + \Delta_{\text{steel}} + \Delta_R + \Delta_{\text{ins}})}.$$

Furthermore, the mass flow rate of air (\dot{m}_{air}) as noted in the differential equation above can also be re-expressed in terms of the key reactor operating parameters:

$$\dot{m}_{\text{air}} = \rho_{\text{BM}}\pi R_r^2 H_r (\text{AF})_{\text{stoic}} \sigma / \tau_{\text{res}}.$$

In order to solve this first-order differential equation, we note that the initial condition is

$$T_p(z = 0) = T_{\text{amb}}.$$

Therefore, in summary, we have two coupled differential equations: a second-order equation describing the cooling solid phase, and a first-order equation describing the heating gaseous phase. The solution was implemented in MATLAB using the method of lines.

5.4.4 Air-Preheating Validation Results

Figure 68 indicates some temperature profiles of the air (blue, panels b and d) and torrefied biomass (red, panels a and c) phases under different design conditions. Panels a-b indicate the different results when the width of the air pre-heating channel is varied. Panels c-d indicate the different results when the length of the char-cooling segment is varied. Let us focus on the case of varying the width of the air-preheating channel first. Panel (b) shows that as the channel width decreases from 5 cm to 1 cm, the final pre-heating temperature of air also increases from about 80°C to about 90°C. The reasoning is that at a given air mass flow rate, a narrower channel forces the air to flow through at a higher velocity. This means that the convective heat transfer coefficient h_{air} of air, as described in Eq. 4, also increases. We therefore see the pre-heated air equilibrate to a higher temperature. In the meanwhile, the temperature profile in the torrefied output does not have a significant change.

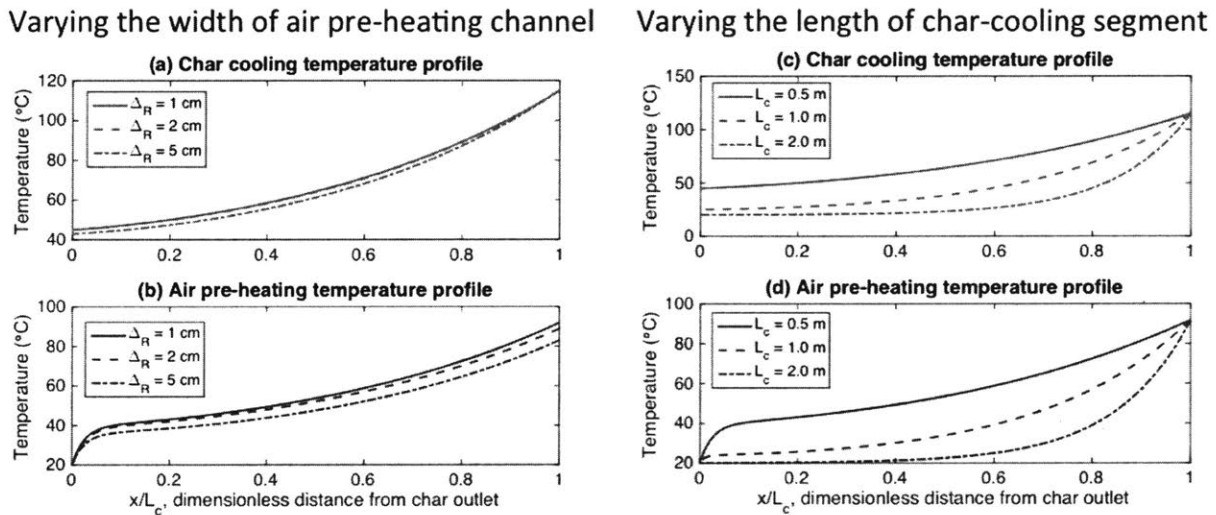


Figure 68- Modeled air pre-heating (blue, panels b and d) and char cooling (red, panels a and c) temperature profiles under different pre-heating and char-cooling design configuration. (a-b) As we narrow the width of the air-preheating channel, the air pre-heating becomes less effective. (c-d) As we decrease the length of the char-cooling segment, the residual temperature of the torrefied biomass at the outlet also increases.

On the other hand, if we consider Panel (c), we observe that as we increase the char-cooling length, the temperature of the torrefied biomass at outlet ($z = 0$) also decreases. This makes sense, as a longer char-cooling segment also allows the torrefied biomass more time to cool down. However, what is remarkable is in Panel (d), varying the char-cooling segment length has no effect on the final air-preheating temperature. If we examine all the air pre-heating temperature profiles in Panels (b) and (d), we can start to see why. As seen in the rapid rise of the air temperature near $z = 0$ (air inlet), we realize that air is actually pre-heated very rapidly within a short length (in the initial 5-10%) of the char-cooling segment. For the remaining part of the char cooling segment, the main limitation in air pre-heating is not due to the specific heat capacity of air nor the thermal conductivity from the hot torrefied biomass into cold air, but rather, due to the gentle temperature rise in the char-cooling segment. This is also evident if we compare the shapes of the temperature profiles of torrefied biomass (in red) to the respective temperature profiles of pre-heating air, and notice that except for the initial segment, the shapes are nearly replica of each other.

This observation yields a significant insight: the length of the char-cooling segment is not dictated by the need to adequately pre-heat air, but rather, the need to drop the temperature of the cooling torrefied biomass down sufficiently such that it is not dangerous to handle (e.g. causing a spontaneous combustion) as it emerges out of the char-cooling segment. Therefore, in designing a good air-preheating and char-cooling segment, we should aim to reduce the width of the air channel as much as possible (to provide for a greater extent of pre-heating) as well as to reduce the length of the char-cooling segment as much as practicable (to minimize the size of the reactor, and as we will see in later analysis, the “fin effect” for increased thermal dissipation over a large surface area).

In order to understand better the combination of char-cooling segment length and the air-preheating channel width to select for our design, we swept across different combinations of char-cooling segment length and air channel width and plotted in Figure 69 the exit temperature of cooled torrefied biomass (Panel a) as well as the final temperature of the pre-heated air (Panel b) under different design configurations. We note that the final torrefied biomass temperature at exit is almost exclusively a function of the char-cooling

segment length. On the other hand, the final air-preheating temperature is almost exclusively a function of the air channel width only. This “uncoupled” relationship should not be surprising given our prior discussion and insights.

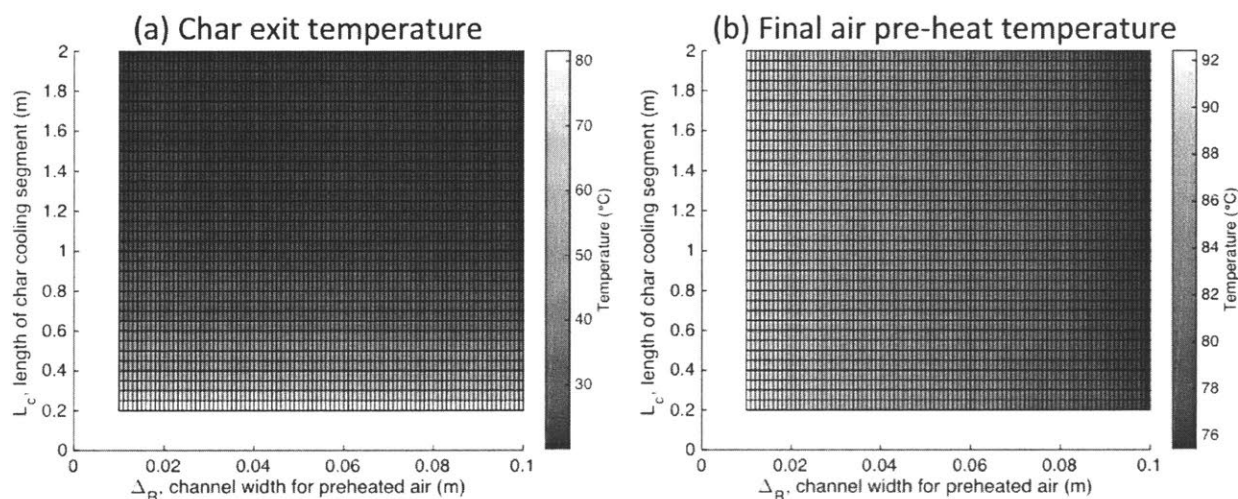


Figure 69 - (a) Temperature of cooling torrefied biomass upon exit and (b) final air pre-heating temperature under different air channel width (x -axis) and char-cooling segment length (y -axis). The char exit temperature is almost exclusively a function of the char-cooling length, while the air-preheating temperature is almost exclusively a function of the air channel width.

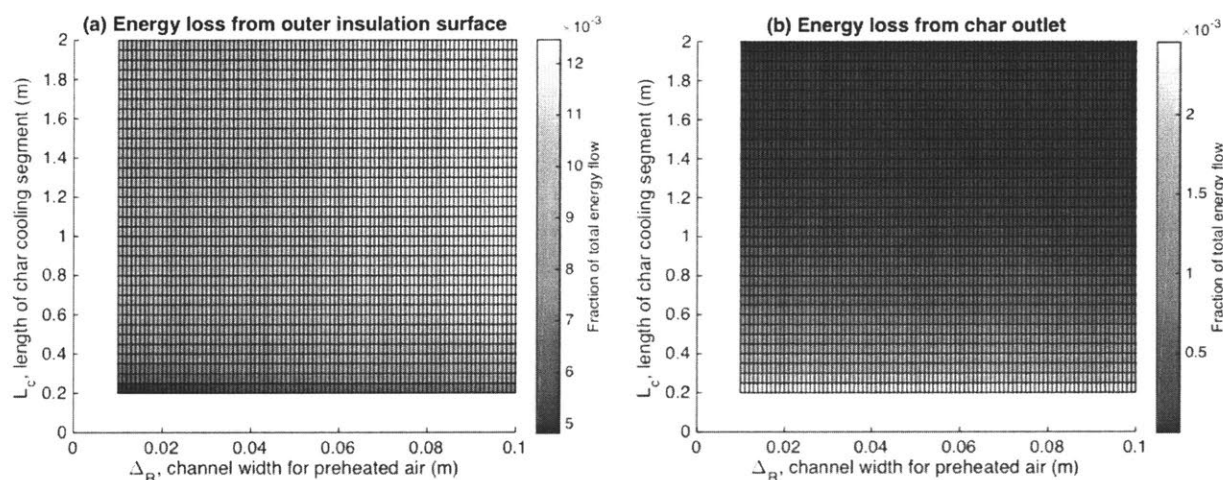


Figure 70 - Two types of energy losses consisting of thermal dissipation from the outer insulation surface (a) and sensible heat loss from the cooling char at the reactor outlet (b) under different air-preheating channel widths and char-cooling segment lengths.

Next, we consider the different forms of energy losses that can arise in this char-cooling, air-preheating segment. Firstly, despite using the residual heat from the char cooling for preheating air, we still expect heat to be lost through the outer insulation surface to the ambient. Secondly, at the reactor outlet, the cooling char may not have stabilized to room temperature, and therefore still carry some sensible heat that will also be lost to the reactor system. Figure 70 summarizes these two types of losses. We first look at Panel (b), which quantifies the energy loss from the char outlet as a fraction of the total solid energy passing through the torrefaction system. Not surprisingly, this value is directly proportional to the temperature of the exiting char, and increases sharply as the char-cooling segment length decreases. On the other hand, Panel (a), which quantifies the fraction of energy loss from the outer insulation surface, tells a more complicated story. There are two dependencies here, both due to the same underlying cause which is related to the total surface area for heat loss. The first dependency is that this loss increases as the length of the char-cooling segment increases. This is due to the “fin effect”, as explained below. In order to keep everything else constant in this study, the boundary condition of Eq. 3 imposes a fixed solid-phase temperature at the torrefaction reactor outlet (we assume that we can adjust the solid residence time and the normalized air/fuel ratio to achieve this temperature as discussed in 0). As the total char-cooling length (and therefore surface area) increases, the total thermal dissipation from the entire length also increases. This means in order to maintain the boundary condition, the torrefaction reactor must now work harder to compensate for this additional heat loss. We can therefore see that increasing the char-cooling segment length is analogous to adding a cooling fin to the torrefaction system: while it aids the cooling and safe exit of torrefied biomass, it conversely also imposes an energy penalty on the overall system. The second dependency is that the energy loss increases as the air-preheating channel width increases. To understand why, we undertake a sensitivity analysis of the different variables as we double the air channel width and summarize the results in Table 24.

Table 24 - Sensitivity analysis of various values as the air channel width is doubled.

Variable	Nominal value for $\Delta_R = 1$ cm	% change as Δ_R is doubled
Air velocity (v_{air})	7.3 cm s ⁻¹	-52%
Air convective heat transfer coefficient (h_{air})	13.1 W m ⁻¹ K ⁻¹	-10%
Char-to-air thermal resistance ($\theta_{\text{char} \rightarrow \text{air}}$)	0.71 m K W ⁻¹	+11%
Air-to-ambient thermal resistance ($\theta_{\text{air} \rightarrow \text{amb}}$)	2.5 m K W ⁻¹	-4%
Outer surface area	0.55 m ²	+7%

From Table 24, we can see that as the air channel width doubles, the air velocity almost halves. This results in a 10% decline in the convective heat transfer coefficient, such that it becomes more difficult both for heat to get from the cooling char to the pre-heated air, which increases the char-to-air thermal resistance. However, somewhat counter-intuitively, the air-to-ambient thermal resistance actually decreases, making it easier for heat to be lost from the pre-heated air to the ambient surrounding. This is because increasing the air channel width will necessarily increase the outer radius and thus surface area of the insulation, making it easier for heat to escape. The overall result is an increase in the energy loss as we increase the air channel width. In fact, by making the char-cooling segment very long (2 m) while maximizing the air channel width (0.1 m), we can lose as much as 30% of the overall total solid energy through the exterior surface of the char-cooling segment!

The summation of Panels (a) and (b) in Figure 70 gives us the total energy loss through both the exterior insulation as well as the char outlet. Comparing this quantity with the original energy lost in the char-cooling segment without air-preheating, we can compute the fraction of energy saved from the original loss. This quantity is plotted in Figure 71. We see that across the board, there is significant energy saving (from 68-82% of the original energy loss without pre-heating) due to implementing air pre-heating. This saving is most

significant when the air channel width is small, and the char-cooling segment length is short. However, due to physical dimensions, we cannot make either dimension arbitrarily small. Furthermore, the requirement that the cooling char emerges from the reactor in a manner that is safe to handle will impose additional lower bounds on the char-cooling segment length. From Figure 69 above, we see that if we wish the torrefied biomass to emerge at a temperature of no more than 50°C, then the minimum viable char-cooling length will be around 0.5 m. This length, combined with an air channel width of 1 cm, gives a 75% saving in energy loss compared to the default design case without air pre-heating in place.

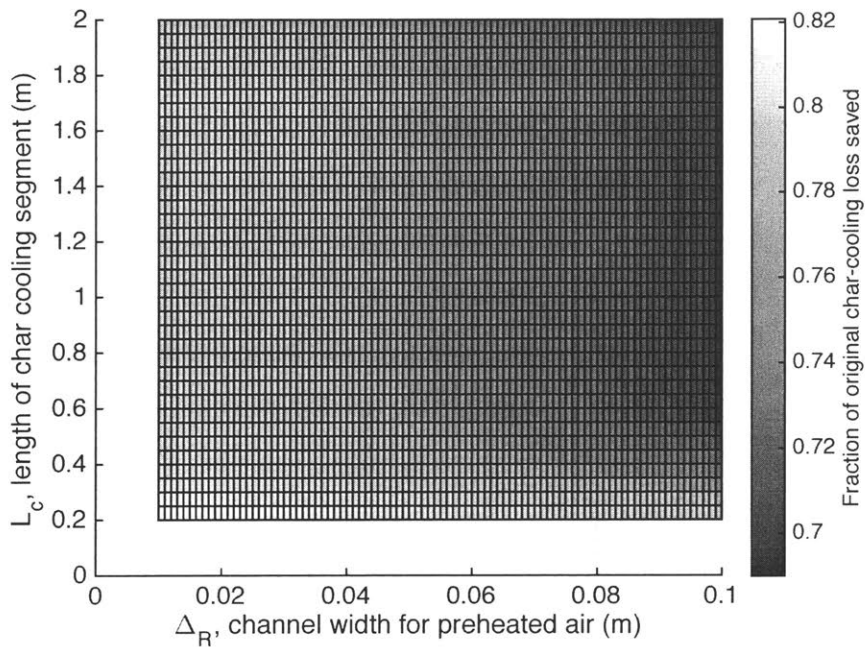


Figure 71 - Fraction of the original char-cooling energy loss (without air pre-heating in place) saved as a result of implementing air pre-heating under different air channel width and char-cooling length configurations.

5.5 Characterizing and Mitigation Losses and Emissions from the Exhaust

Finally, we consider the energy losses from the escaping exhaust gases (CO_2 , H_2O , other post-combustion products, as well as unburned volatiles). These losses come in the form of (a) sensible enthalpy loss (residual heat from the reactor being carried away by the exhaust

gases at a higher-than-room temperature, and (b) chemical enthalpy loss (unreacted escaped volatile gases that have a positive higher heating value).

5.5.1 Measuring the Sensible Enthalpy Loss

In order to quantify the sensible enthalpy loss from the exhaust stream, a thermocouple was placed at the exit of the reactor assembly and monitored the exit temperature of the exhaust stream under different reactor operating conditions. Figure 72 plots the calculated energy losses due to the sensible heat from the exhaust stream. The temperature of the exhaust stream increases as the torrefaction becomes more severe, and thus the overall sensible energy loss also increases. However, this energy loss generally occupies a very small fraction of the total solid energy flow through the reactor system, typically no more than 1%. As we will show in the next section, it is much more interesting quantifying and harnessing the energy losses present in the unburned volatiles in the exhaust stream.

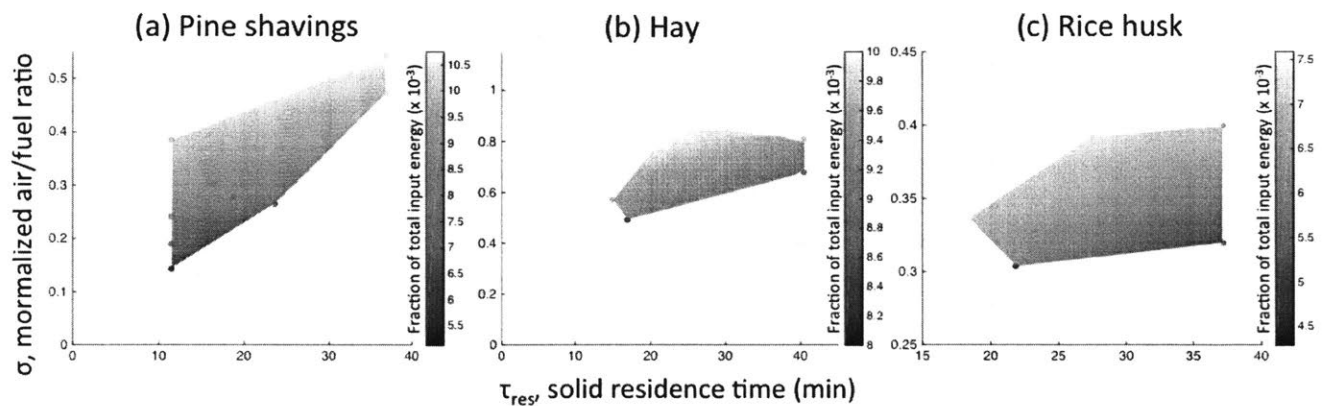


Figure 72 - Energy losses due to the sensible heat from the hot flue gases escaping the reactor, as a fraction of the total biomass energy flow, under different reactor operating conditions for pine shavings (a), hay (b), and rice husk (c).

5.5.2 Measuring the Chemical Enthalpy Availability

As illustrated in Figure 73, on top of the reactor outlet, we propose to build an additional column with a profile thermocouple to monitor the temperature at different axial positions. First, as the warm exhaust gas mixture exits from the reactor at temperature T_A . Then, there is a port where a certain amount of preheated air is injected into the column at a

specified flow rate. The amount of preheating is adjusted until there is flammability of the exhaust mixture, and the air flow rate is adjusted until a maximum reaction zone temperature T_B is achieved. From the flame temperature, the chemical enthalpy of the unburned volatile gas mixture can be estimated.

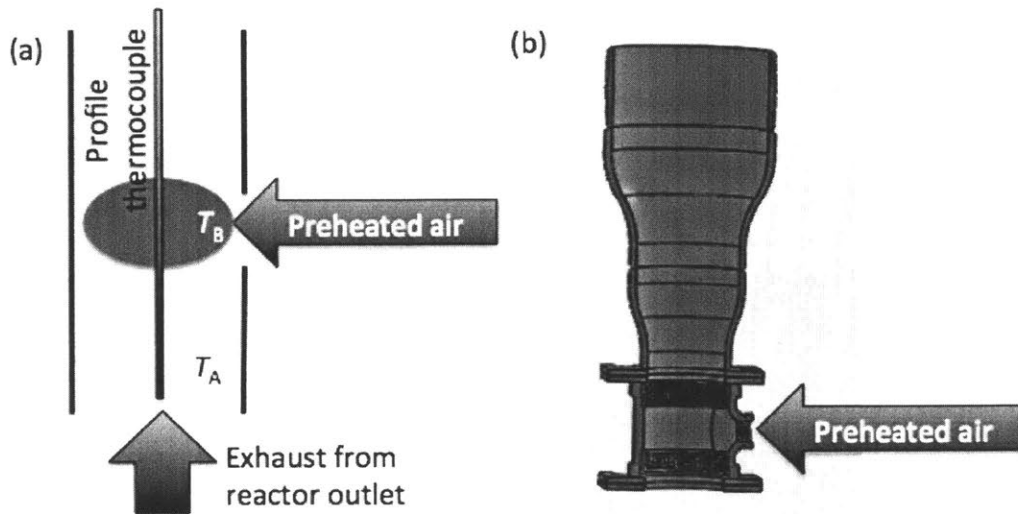


Figure 73 - Experimental set-up to characterize the chemical enthalpy availability in the reactor exhaust stream. The exhaust from the reactor outlet is mixed with preheated secondary air stream and undergoes oxidation. A profile thermocouple measures the temperature of the oxidation zone. (a) A conceptual schematic, and (b) a SolidWorks rendering of this set-up.

Figure 74 illustrates the experimental set-up by showing the reactor outlet (a) without secondary oxidation, and (b) with secondary oxidation in the zone below. As can be seen in the reactor's native state (a) without secondary oxidation, there is significant amount of particulate matter emerging from the outlet. After the secondary oxidation zone was implemented in (b), we see that the post-combustion flue gas is devoid of visible particles. This is an initial visual proof that secondary oxidation not only able to harness the unburned energy in the exhaust stream, but also to significantly clean up the emission profiles of the exhaust stream. While in this section, we will focus primarily on the energy harnessed from secondary oxidation, in a following section, we will also explore how we

can quantify the completeness of combustion and the reduction in the emission profiles from the reactor exhaust stream.

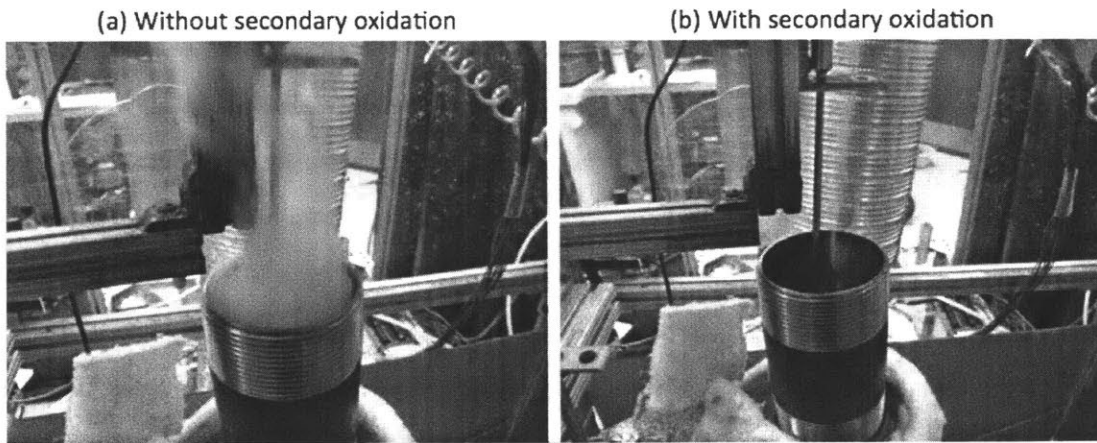


Figure 74 - Implementation of the reactor outlet (a) without the secondary oxidation zone and (b) with the secondary oxidation zone. Contrast the amount of visible particulates emerging from the reactor in the two cases.

In order to understand how this secondary oxidation, we repeated the experiment over various reactor conditions for pine shavings and rice husks. Experiments on hay were not performed, as our hay straws have similar dimensions as the reactor radius, and the current experimental set-up caused excessive clogging of biomass particles in the secondary oxidation zone, leading to significant safety hazard.

The first question we asked is: How much secondary air pre-heating is needed to sustain an oxidation flame that lasts at least one minute in duration? For each type of biomass and reactor condition, we adjusted the power output of the inline heater element for the secondary air, and noted the minimum viable pre-heating temperature where such a flame can be sustained. In the case of pine shavings, in the severe torrefaction regime, no pre-heating was needed. As the torrefaction reaction became less severe, we needed to increase the air pre-heating temperature, to the point where this pre-heating was so intensive (above 300°C) such that it could not be feasibly achieved using any natural heat exchange mechanism in our torrefaction setup without external energy input. This boundary of feasibility is delineated by the dashed black line in Figure 75. In the case of rice husks

(Panel b), we generally observed that it was much more difficult than pine shavings to sustain a stable flame: in all conditions in Panel b, a significant amount of pre-heating (at least 200°C) was required.

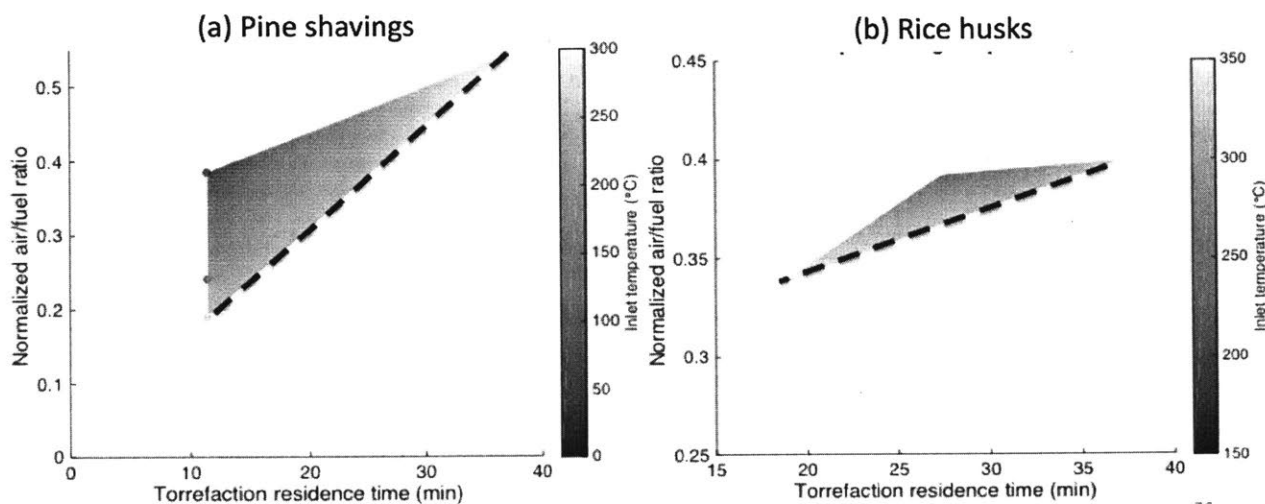


Figure 75 - Minimum secondary air pre-heating temperature required to oxidize the unburned volatiles in the exhaust stream under different reactor conditions for (a) pine shavings and (b) rice husks. In general, as the torrefaction condition becomes less severe, the amount of secondary air pre-heating also increased significantly, to the point that no amount of realistic air pre-heating sufficed to start an oxidation flame (delineated by the black dashed line in both plots).

The next question that we pursue is: Given a certain amount of minimum required secondary air pre-heating in order to maintain a stable flame, what is this flame (oxidation) temperature in each case? Figure 76 summarizes the answer for different reaction conditions and biomass types. We see that for pine shavings (Panel a), an oxidation of around 600°C was achievable under the severe torrefaction conditions. As the torrefaction severity reduces, the flame temperature also decreases to around 450°C whilst the air pre-heating temperature increases. This signals decreasing chemical enthalpy availability as torrefaction severity decreases. We observe a similar in the case of rice husks (Panel b), but in this case, the flame temperature is significantly lower, at around 400-450°C.

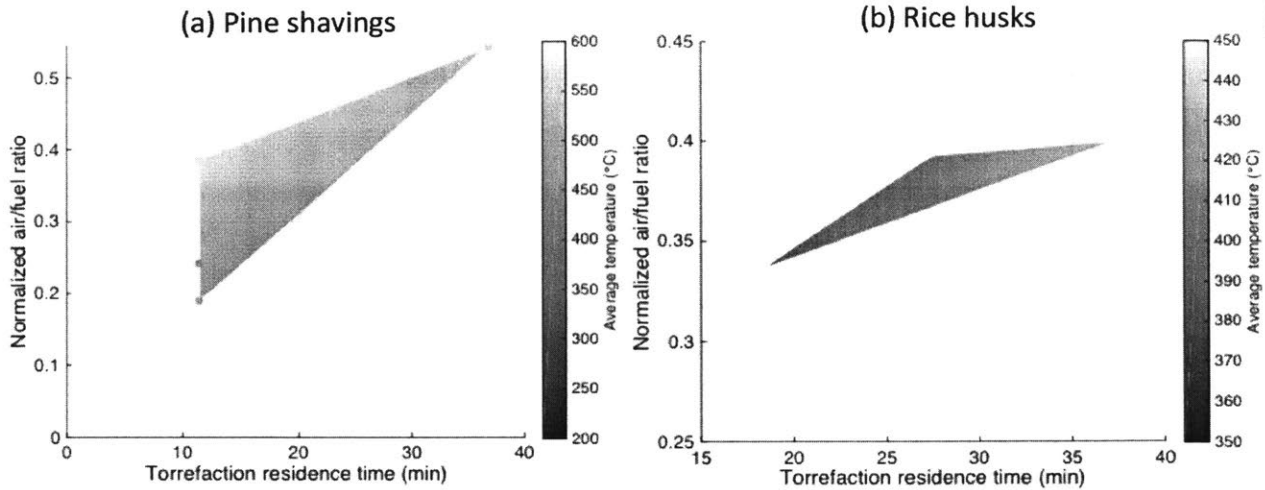


Figure 76 - Temperature in the secondary oxidation zone for (a) pine shavings and (b) rice husks under different torrefaction conditions. This oxidation temperature was observed to decrease as torrefaction becomes less severe.

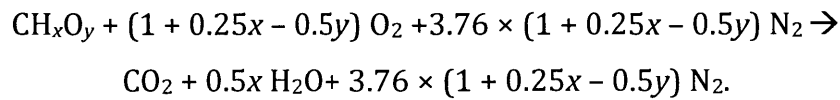
Now, knowing (a) the temperature and mass flow rate of the unburned exhaust stream emerging from the reactor, (b) the pre-heating temperature and mass flow rate of secondary air stream, and (c) the temperature in the secondary oxidation zone, we can estimate the chemical enthalpy availability \dot{H}_{chem} from the original (native) exhaust stream that can be harnessed by the method of secondary oxidation as follows:

$$\dot{m}_{exh}c_{p,exh}(T_{exh} - T_0) + \dot{m}_{air2}c_{p,air}(T_{air2} - T_0) + \dot{H}_{chem} - (\dot{m}_{air2} + \dot{m}_{exh})c_{p,flue}(T_{flame} - T_0) - \dot{m}_{H_2O}\Delta H_{vap} - Q_{loss} = 0,$$

where the first term with the subscript “exh” refers to the incoming enthalpy carried by the unburned exhaust emerging from the reactor unit, the second term with the subscript “air2” refers to the incoming pre-heated air, the fifth term refers to the heat of condensation of steam, and the sixth term Q_{loss} refers to the energy loss through the side wall of the secondary oxidation zone, which is a function of the difference between the oxidation temperature and the ambient air temperature. The third term \dot{H}_{chem} [W] in this case reflects the difference in chemical availability between the incoming mixture (exhaust and some portion of unreacted volatiles) and the outgoing mixture (exhaust and a much smaller portion of unreacted volatiles), or in other words, the chemical availability that can

be harnessed in the secondary oxidation mechanism for useful purpose such as pre-drying biomass.

The mass flow rates of the unburned exhaust, secondary air, and flue gas are all provided from actual measurement and mass balance. In the fifth term, the mass flow rate of steam is more difficult to access. To quantify this, we first obtained the ultimate (elemental) analysis of the raw biomass and the torrefied biomass. This helps us deduce the elemental composition of the volatile gases and exhaust mixture, of the form CH_xO_y . By chemical balance, we have the following equation:



This gives us an estimate of the final composition of the flue gas, and we can therefore deduce the amount of steam in the mixture that would release the enthalpy of condensation in the fifth term.

The sixth term, which describes the energy loss from the side wall of the secondary oxidation zone, can be formulated in the same manner as done previously for the case of thermal dissipation through an insulated surface:

$$Q_{\text{loss}} = \frac{2\pi H_{\text{ox}}(T_{\text{flame}} - T_{\text{amb}})}{\frac{1}{h_{\text{flue}}R_{\text{ox}}} + \frac{\ln(1 + \Delta_{\text{steel}}/R_{\text{ox}})}{k_{\text{steel}}} + \frac{\ln(R_{\text{out,ox}}/(R_{\text{ox}} + \Delta_{\text{steel}}))}{k_{\text{ins}}} + \frac{1}{h_{\text{flue}}R_{\text{out,ox}}}},$$

where H_{ox} and R_{ox} are respectively the height and radius of the secondary oxidation zone, and $R_{\text{out,ox}} = R_{\text{ox}} + \Delta_{\text{steel}} + \Delta_{\text{ins}}$ is the radius of the outer insulated surface surrounding the secondary oxidation zone.

Figure 77 plots this chemical availability term \dot{H}_{chem} as a fraction of the total solid energy flow through the torrefaction reactor under different reaction conditions and biomass types. In regions of flammability delineated in Figure 75, this value was experimentally determined. Outside of this region of flammability, this value was deduced through linear interpolation in MATLAB.

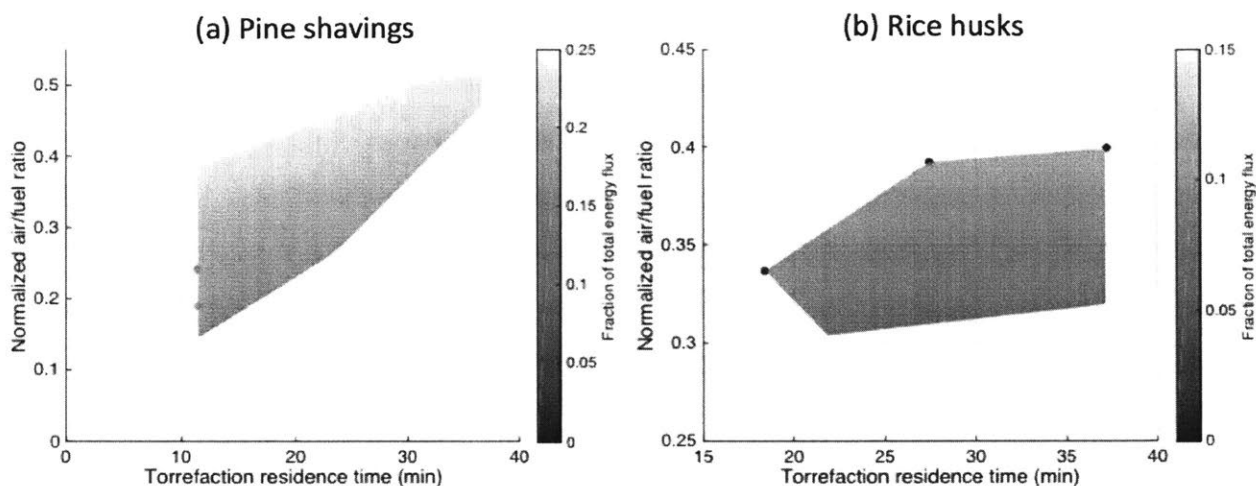


Figure 77 - Total chemical enthalpy availability harnessed by the secondary oxidation mechanism under different reactor conditions for (a) pine shavings and (b) rice husks, as a fraction of the total solid energy flow through the reactor system. In general the amount of chemical enthalpy availability increases as the torrefaction reaction becomes more severe.

We see that in general, the total chemical enthalpy availability that can be harnessed by the secondary oxidation mechanism represents a significant portion of all the losses characterized so far. This chemical availability is in the range of 10-25% of the total solid energy flow, and generally increases as the torrefaction severity increases. In the case of rice husks, we should be mindful that we are sweeping over a much more restricted area of normalized air/fuel ratio (torrefaction severity), and therefore we observe a lower chemical availability (~10-15%) and a gentler trend of increase compared to the case of pine shavings.

5.5.3 Emission Profiles and Completeness of Secondary Combustion

In the discussion above, we assumed that the secondary oxidation mechanism reacts any unburned fractions in the exhaust stream virtually to completion. In order to evaluate the completeness of this secondary combustion process, and to characterize the changes in the emission profiles of the post-combustion flue gas, we selected two quantities to keep track: carbon monoxide level, and particulate-2.5 μm (PM-2.5) level. For monitoring the carbon monoxide level, we installed a commercial CO datalogger (Lascar EL-USB-CO) inside the

exhaust duct approximately 0.5 m above the reactor outlet. Likewise, for monitoring the PM-2.5 level, we installed, at the same position, a UCB particle sensor capable of detecting PM-2.5 down to 25 mg m^{-3} . This sensor was specifically designed for characterizing the emissions from burning biomass-based fuel in the kitchen, and has been scientifically validated elsewhere (Lifton *et al.*, 2004; Edwards *et al.*, 2006, and Chowdhury *et al.*, 2007). A pressure transducer (Omega Engineering PX278-30D5V) was tapped into the exhaust duct to constantly monitor the total gas flow rate. This gives us the dilution ratio needed to back out the actual emission levels emerging from the reactor outlet. The emission levels in the post-combustion flue gas (after secondary oxidation) are compared against those in the reactor's native state (without secondary oxidation) in order to provide some measure for the completeness of combustion as well as the environmental emission profiles.

We first give the measured values of the native (without secondary oxidation) emission profiles of carbon monoxide and particulates emerging from the reactor under different reaction conditions. As shown in Figure 78, which summarizes these values, we observe that the emission levels increase as the torrefaction reaction becomes more severe, which makes sense as more energy is contained in the unburned volatiles in the exhaust stream under this regime. For carbon monoxide (Panels a and b), under severe torrefaction conditions, the CO level is about tripled than under the moderate conditions. For particulates, in the case of pine shavings, the level is almost doubled. However, for rice husks, the increase is more gentle, from about $1,800\text{-}2,500 \text{ }\mu\text{g m}^{-3}$. These differing trends may reflect the intrinsic chemical differences and combustion characteristics of bulk pine shavings and rice husks, which were qualitatively noted previously in Chapter 3.

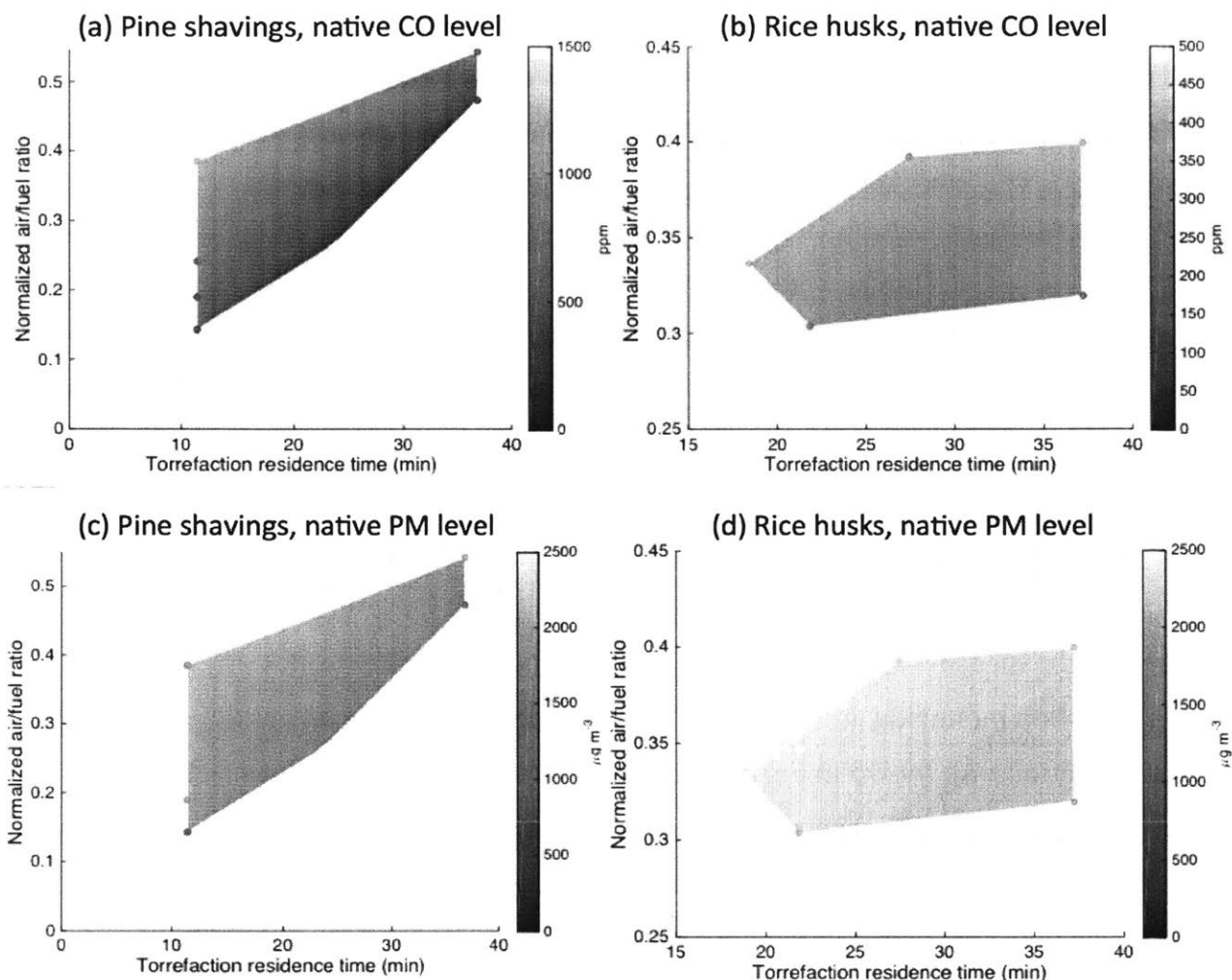


Figure 78 - Native emission profiles of carbon monoxide from the reactor outlet (without secondary oxidation) for (a) pine shavings and (b) rice husks under various torrefaction reaction conditions, as well as particulate levels for (c) pine shavings and (d) rice husks.

We then took the emission measurements with the secondary oxidation mechanism in place, and compared the two emission results. In Figure 79, we plot a sample trace of the measured CO level under a representative torrefaction reactor operation (pine shavings, $\tau_{\text{res}} = 12$ min, $\sigma = 0.37$). In the first part of the time trace ($t < 60$ min), the reactor was warming up to a steady-state level, and no secondary oxidation was implemented. As we can see, the CO level was consistently high, and increased to above 1000 ppm as the reactor approached the steady-state condition. After the start of the secondary oxidation mechanism, we observed a dramatic drop of CO levels generally to less than 100 ppm. Even

during this period, they were a few spikes in the CO level. These spikes correspond to the temporary flame-outs in the secondary oxidation flame as we had to periodically feed raw biomass into the reactor through the secondary oxidation zone. Therefore, these spikes can be considered as artifacts that can be removed with an improved biomass input feed design that is not within the scope of our study. During our analysis later, we removed these spikes from consideration by including the stabilized CO levels only 30 seconds after we visually observed a stable secondary oxidation flame. However, in short, from Figure 79, it is clear there is a reduction in the CO emission after the onset of secondary oxidation.

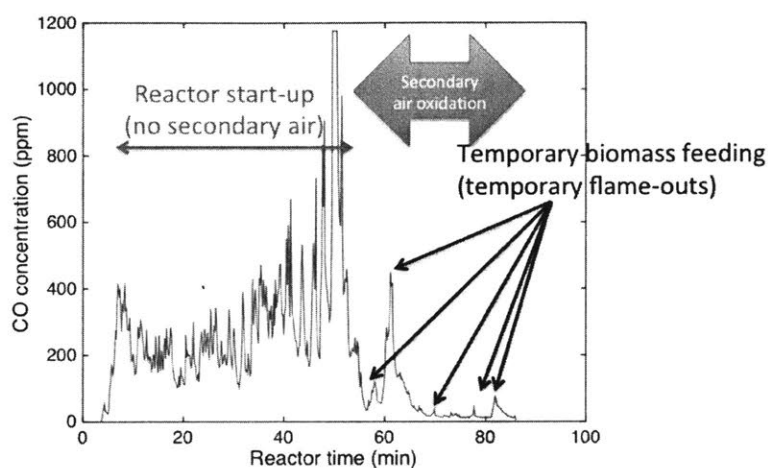


Figure 79 - Sample time trace of the carbon monoxide level under a representative torrefaction reactor operation condition (pine shavings, $\tau_{res} = 12$ min, $\sigma = 0.37$). In the first part of the reactor warm-up (up to $t = 60$ min), there was no secondary air oxidation. Afterwards, secondary oxidation was implemented, with temporary flame-outs due to biomass feeding.

In order to quantify this reduction over a larger range of reactor operating conditions, we took the ratio of the mean emission level (CO and particulates) with secondary oxidation to the mean emission level (CO and particulates) in the reactor's native state without secondary oxidation, at the same time accounting for the differences in the air dilution factor in the exhaust hood. In Figure 80, we report the percentage reduction in the emissions (CO and particulates) from the native reactor operation without secondary oxidation. These figures can also be used, on the first-order approximation, as proxy for

quantifying the completeness of combustion in the secondary oxidation mechanism (as well as the percentage of chemical availability that can be harnessed by the secondary oxidation). We generally observe a significant reduction of 95-98% in carbon monoxide emission and of 97-99% in the particulate emission with the onset of secondary oxidation. As the torrefaction becomes less severe, the emission reduction (and by proxy, the completeness of reduction) also reduces slightly. This is not surprising, as at a lower oxidation temperature under the mild torrefaction regime, oxidation kinetics proceed at a slower rate, and within a certain gas residence time, the combustion will be less complete.

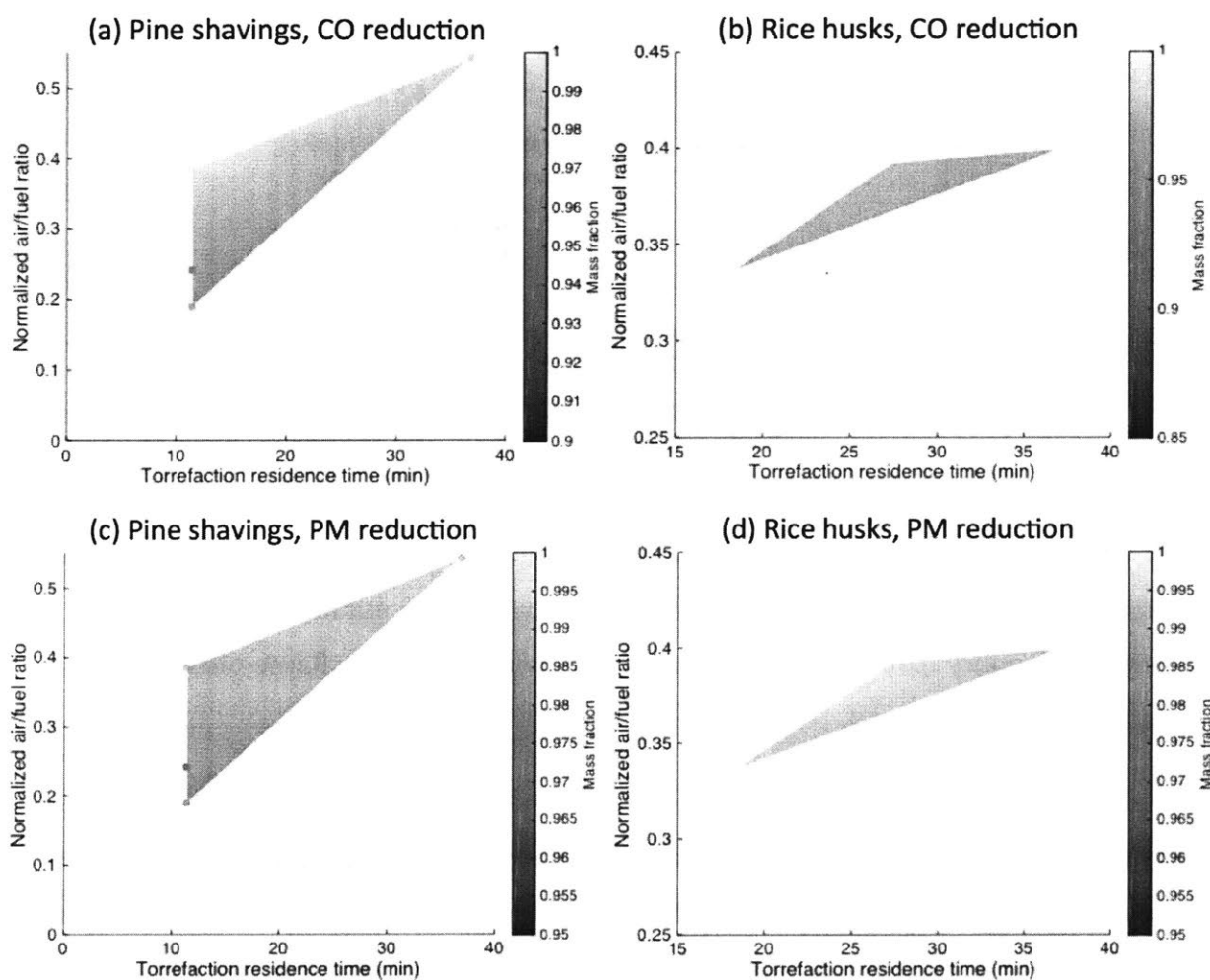


Figure 80 - Percentage reduction of carbon monoxide from the reactor outlet with the secondary oxidation mechanism compared to the native case (without secondary oxidation) for (a) pine shavings and (b) rice husks under various torrefaction reaction conditions, as well as the percentage reduction of particulate levels for (c) pine shavings and (d) rice husks.

5.5.4 Characterization of Uncertainty Ranges

In order to be confident about the results discussed above and the apparent improvements brought about by the implementation of secondary oxidation, it is important to consider the uncertainty ranges of the various quantities that we measured or calculated. In this section, we characterize the effects of various uncertainties on the measurement of volatile chemical availability as well as the emission characteristics using the same method as we carried out in Section 3.6 for the reactor performance metrics.

First we examined intrinsic uncertainties. These govern input quantities such as the mass flow rates of the primary and secondary air into the reactor, as well as output quantities such as the temperature and emission readouts. These uncertainties are listed in Table 25 below; some of these ranges have been replicated from Table 13 for convenience of reference.

Table 25 - Summary of various instruments used in the experiment and their intrinsic uncertainty ranges in the readout signals.

Quantity	Instrument	Uncertainty range
Mass flow, primary air	Omega FMA5528A	Max of $\pm 1.5\%$ and ± 0.1 L/m
Mass flow, secondary air	Dwyer RMC series	Max of $\pm 2\%$ and ± 10 scfh
Temperature	Omega	Max of $\pm 0.4\%$ and ± 1.1 K
Particulate levels	UCB	$\pm 32\%$
Carbon monoxide levels	Lasca EL-USB-CO	Max of $\pm 6\%$ and ± 7 ppm
Dilution factor calculation	Omega PX278-30D5V	$\pm 1.0\%$
Solid mass (in/out)	Dr. Meter ES-PS01	Max of $\pm 1\%$ and ± 5 g

Likewise, we summarize the extrinsic uncertainties in Table 26. Once again, these extrinsic uncertainties—which reflect the variation in the reactor operation and process, are computed by taking replica measurements of the same quantities and tabulating their means and standard deviations in order to compute the standard errors of the mean.

Table 26 - Summary of the uncertainty ranges associated with reactor operation with respect to various relevant variables, for the sample case of pine shavings, $\tau_{res} = 12$ min, $\sigma = 0.23$.

Quantity	Uncertainty range (% of the mean)
Solid residence time	$\pm 14\%$
Temperature of native exhaust stream	$\pm 4\%$
Temperature of secondary oxidation	$\pm 4\%$
Thermal conductivity of outer insulation	$\pm 9\%$
Particulate levels, native	$\pm 10\%$
Particulate levels, secondary oxidation	$\pm 50\%$
CO levels, native	$\pm 28\%$
CO levels, secondary oxidation	$\pm 26\%$

Note that in Table 26, the variables listed are only associated with reactor operations (and the measured outputs). For any directly measurable inputs that are not affected by the reactor operations (such as the temperature and mass flow rate of the pre-heated air entering into the secondary oxidation zone), then the uncertainty range is limited to that described in Table 25 by the measurement instrument.

From Table 26, what may seem a little surprising is that some emission levels, such as the particulate measurement under secondary oxidation conditions, have a disproportionately large uncertainty range (as large as $\pm 50\%$). One main reason why this is so is that these sensors are mostly designed to measure high-emission conditions. The UCB particulate sensor, for example, is designed specifically for indoor biomass cooking experiments. While these sensors are simple and low-cost to use, under low-emission conditions, their accuracy tends to fare worse compared to high-end emission characterization sensors. The UCB particulate sensor, for instance, has a lower detection limit of $30 \mu\text{g m}^{-3}$ for PM-2.5 levels. During secondary oxidation conditions, the measured particulate levels are often as

low as $40\text{-}60 \mu\text{g m}^{-3}$, and under this regime, it is no longer surprising that there is a large measurement uncertainty.

However, we argue that these large uncertainty ranges in the emission level measurement do not significantly affect the interpretation of our results of the performance of secondary oxidation. As shown in Figure 80, we generally expect a 97-99% in reduction in the particulate emissions with secondary oxidation. This means that for the hypothetical case of a native particulate emission of $2000 \mu\text{g m}^{-3}$ (with an uncertainty range of $\pm 200 \mu\text{g m}^{-3}$), the post-secondary-oxidation particulate emission level is on average $40 \mu\text{g m}^{-3}$. A $\pm 50\%$ uncertainty means that this post-secondary-oxidation value could be anywhere between 20 to $60 \mu\text{g m}^{-3}$. However, regardless of the large uncertainty range, what is certain is that it is still a dramatic improvement compared to the native emission level of $(2000 \pm 200) \mu\text{g m}^{-3}$ by two orders of magnitude. In other words, this uncertainty range translates to an ultimate uncertainty of $\pm 1\%$ in the 98% emission reduction.

5.5.5 Discussion on Energy Losses in the Exhaust Stream

In this section, we focused our attention on quantifying the energy losses in the exhaust stream. We first found that this loss predominantly occurs through the chemical enthalpy availability in the unburned volatiles in the exhaust stream, rather than the sensible enthalpy in the exhaust stream. We then built an experimental set-up to quantify the chemical enthalpy availability that can be harnessed by creating a secondary oxidation zone. We demonstrated that we can capture between 10-25% of the total solid energy flow from the uncombusted volatiles, and that secondary oxidation reduces the emission (in terms of carbon monoxide and particulates) by above 95%. We can therefore also use this emission reduction as a proxy for quantifying the completeness of combustion, and conclude that the secondary oxidation is able to harness the majority of the combustibles in the native reactor exhaust stream.

More importantly, the experimental set-up in this section is also an indirect validation of a design improvement that we can implement to the reactor in order to introduce an actual

secondary oxidation zone. The excess heat can then be redirected for other purposes such as pre-drying the incoming biomass. Pre-drying the biomass before it enters into the reactor proper also serves the purpose of reducing the amount of dilution of the combustible fraction in the exhaust stream, thereby improving the secondary oxidation zone stability and completeness of combustion. To demonstrate how this could work with pre-drying the biomass, we constructed a simplified process model for pre-drying biomass before it enters into the reactor, as shown in Figure 81. For each reactor operation condition, we obtain a certain flow rate and temperature of the exhaust as well as secondary air. Given a certain flow rate of wet biomass into the dryer (and subsequently into the reactor), we ask ourselves the following question: what is the maximum permissible moisture content Y_M that the initial biomass can have and be adequately dried by the sensible heat carried in the flue gas from the secondary oxidation zone, assuming no other heat loss mechanisms?

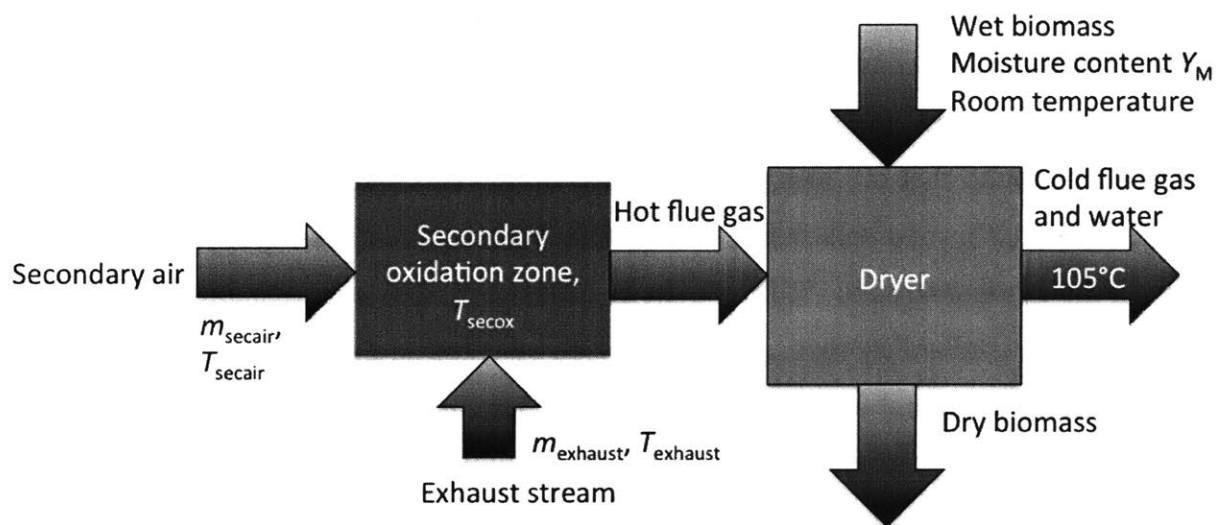


Figure 81 – A simplified process flow-sheet model for incorporating pre-drying of biomass utilizing the heat harnessed in the secondary oxidation zone. We assumed that the dryer is continuously operated at 105°C.

We implemented the overall system energy balance calculation in MATLAB, and display the results in Figure 82. We see that by harnessing the sensible heat from the flue gas emerging

from the secondary oxidation zone, we can pre-dry incoming biomass with a moisture content of up to 60% for pine shavings, and up to 32% for rice husks. As we increase torrefaction severity, we can see that the system can support pre-drying of feedstock with increased moisture content. Therefore, we can imagine that part of the reactor condition selection may depend on the original moisture content of the native biomass.

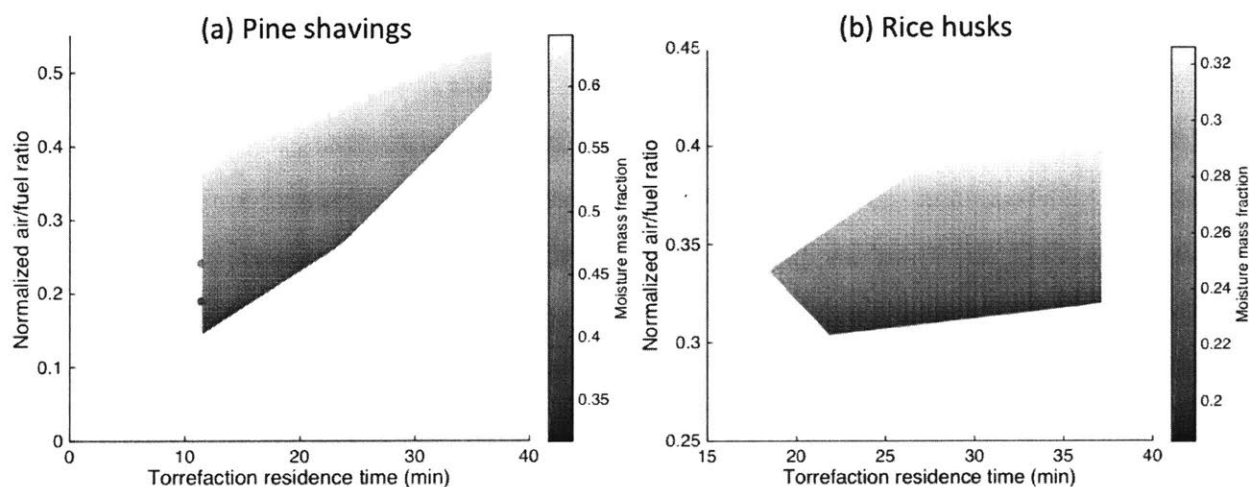


Figure 82 – Maximum possible moisture content in the incoming biomass while still allowing for adequate pre-drying by utilizing the sensible heat from the secondary oxidation zone prior to entering into the torrefaction reactor, for (a) pine shavings and (b) rice husks under various torrefaction reaction conditions.

5.6 Summary and Perspectives for Improvement

Based on the insights we gained in the previous sections, we now have a more refined view of how the reactor operates, and what we should do to arrive at a more energy-efficient design. We identified three mechanisms of energy losses—loss from the side wall, loss from the char-cooling segment, and loss from the exhaust stream—and experimentally quantified their relative magnitudes. We found that in general, the loss from the exhaust stream is one order of magnitude greater than either the loss from the side wall or the loss from the char-cooling segment. Of the loss from the exhaust stream, we also concluded that

the chemical availability from the unoxidized volatile species dominate over the sensible heat loss. While in a scaled-up reactor, it is important to optimally insulate the reactor side walls and to recycle the char-cooling heat by pre-heating incoming air, how to design an effective secondary oxidation zone that can stably harness the chemical availability should command our utmost attention, not only to improve energy efficiency, but also to reduce potential pollution from the volatile emissions into the atmosphere.

Chapter 6 Bulk Hydrodynamic Characteristics in a Biomass Moving Bed and Their Effects on Scaling

A moving bed is a very common design for a continuous biomass-processing reactor in a wide range of applications, such as torrefaction, gasification, and incineration. In order to ensure effective heat and mass transfer through the fixed bed, a good understanding of the bulk hydrodynamic characteristics in the fixed bed is of critical importance. Nonetheless, so far there lacks sufficient data in the literature documenting these characteristics with respect to different types of biomass of various particle sizes. In this paper, we describe an experimental framework to determine and quantify the bulk fixed-bed hydrodynamic characteristics. We assumed—and verified—that the gas flow inside a biomass fixed bed can be roughly approximated via Darcy's law. We obtained the bulk porosities of a range of biomass types and demonstrated that they often diverge from predictions derived from common empirical correlations. We then used our newfound data for a specific application of designing a torrefaction reactor for scale-up, and showed that under certain conditions, the reactor can be powered entirely by the stack effect generated by a hot column of rising gas without any external pressure drive. Therefore, we showed that our methodology can be useful in informing some fundamental scaling questions regarding biomass reactor operation and performance.

6.1 Importance of Hydrodynamic Data in Biomass Moving Bed

A moving bed is a common reactor designed to allow two heterogeneous materials (commonly a solid and a gas, for example) to react with each other. In a moving bed reactor, a solid phase in a packed bed typically migrates downwards by gravity, and is continuously fed from the top and removed from the bottom. A fluid (gas or liquid) phase passes through the packed bed and reacts with the solid phase. Moving bed reactors is not a new concept by any means, but has recently received renewed attention in many chemical engineering design situations, such as wastewater treatment (Rakovitsky *et al.*,

2016; Mazioti *et al.*, 2017), chemical synthesis (Constantino *et al.*, 2016; Tie *et al.*, 2016), and biofuel production (Ray and Ray, 2016; Regufe *et al.*, 2016). In the realm of biomass processing and conversion, which this paper is focused on, moving bed reactors are also a common choice for various processes such as combustion (Mahmoudi *et al.*, 2016; Razmjoo *et al.*, 2016), gasification (Adnan *et al.*, 2017; Tursun *et al.*, 2016), pyrolysis (Branca *et al.*, 2016; Cai and Liu, 2016), and torrefaction (Kuzmina *et al.*, 2016; Park *et al.*, 2015).

For moving bed reactors to work, a crucial element to consider is the hydrodynamic property of the solid packed bed material. To wit, different particle sizes and different bulk porosities can imply that different pressure drives are required to deliver a specified flow of gases past the solid packed bed. For applications with a well-defined solid component or catalyst that does not readily change, this may not be of much interest or relevance beyond an initial bed optimization selection. However, in the case of biomass processing, one common functional requirement is that the moving bed reactor should be adaptable to different types of biomass of different physical characteristics. In this case, we may find that the ability to quickly characterize the bulk hydrodynamic characteristics of the packed bed and relate these to the overall reactor operating requirements to be highly useful in scaling the reactor. As a motivating illustration, in the case of a moving bed torrefaction reactor design (described previously in Section 2.5), one important scaling consideration is how to supply air in the correct ratio with respect to biomass into the base of the reactor in order to achieve a desired torrefaction severity. A dense biomass packed bed, for example, may require an externally powered pressure drive (e.g. a fan) to maintain the flow. On the other hand, a loose biomass packed bed may be able to rely on the natural stack effect from the hot rising column of air within the reactor to continuously draw air in from the base and expel exhaust from the top of the reactor, without an external pressure drive. The ability to measure the hydrodynamic characteristics and to predict in which regime we operate, and if needed, to size the appropriate pressure drive requires a good quantification of the effective bulk bed permeability and the extent to which the biomass bed impedes fluid flow.

Typically, for a porous packed biomass bed, a good first-order relationship between pressure drive/drop (ΔP [Pa]) and the fluid flow (Q [$\text{m}^3 \text{s}^{-1}$]) is Darcy's law, and we assume—and later verify—that this law is indeed applicable to a biomass bed in our regime of interest:

$$Q = -\frac{\kappa A_r \Delta P}{\mu H_r},$$

where $A_r = \pi R_r^2$ is the cross-sectional area of the moving bed reactor (with a radius R_r), H_r is the height of the solid packed bed portion within the moving bed reactor, μ is the viscosity [Pa s] of the flowing fluid (which we can look up in the literature), and κ is effective bulk permeability [m^2] of the biomass moving bed (which we must determine experimentally).

Currently, there is surprisingly little quantification in the literature on the effective bulk permeability for the purpose of biomass moving bed reactor design. The only study we are aware characterizing this value comes from Di Blasi *et al.* (2004), which in their biomass gasifier model assumes that a straw bed has a bulk permeability of $1 \times 10^{-6} \text{ m}^2$, and char has a bulk permeability of $5 \times 10^{-6} \text{ m}^2$. Beyond these two materials, data from other types of biomass, to our best knowledge, remain unquantified.

In this study, we describe an experimental setup to help us obtain the data for the relevant types of biomass of interest to us, and compare the results with the predictions from existing correlations. Finally, we discuss how we can use the data to inform reactor-scaling strategy in the particular case of biomass torrefaction.

6.2 Experimental Set-Up

To verify the applicability of Darcy's law in a biomass moving bed and then to quantify the bulk moving bed permeability, one strategy is to control the gas flow rate Q and then measure the pressure drop ΔP across the moving bed for different reactor heights H_r . Then we can fit for the bulk permeability knowing the gas viscosity as well as the cross-sectional area of the moving bed. In setting up the experiment, we assumed that because typically,

the biomass migrates downwards in the reactor at a very slow rate (around 4 cm/min)¹ compared to the typical velocity of the upward-flowing gas (around 2 cm/s)², we can approximate the moving bed biomass as quasi-static in the timescale of gas flow. This stationary solid approximation hugely simplifies our experimental design and data collection set-up. Figure 83 illustrates this experimental set-up, where the biomass moving bed is approximated as a stationary batch reactor (represented by a 4" NPT threaded pipe, McMaster-Carr 4549K814) open at the upper end and capped at the lower end by a modified NPT cap (McMaster-Carr 4880K811) that has a 1" hole drilled at the center for gas inlet. The gas is connected on the other end to a compressed nitrogen cylinder (NI 300) and the flow rate (Q) in the line is regulated by a mass flow controller (Omega Engineering FMA-5528A) within a range of between 0.1 to 50.0 standard L/min. Immediately before the entrance at the bottom of the biomass packed bed, a differential pressure transducer (Omega Engineering PX278-30D5V) measures the pressure difference (δP_{exp}) between this point and the top of the biomass packed bed.

For each type of biomass, we varied the height (H_r) of the packed bed to be 8, 15, 23, and 30 cm, and measured the pressure difference under various incoming flow rates. In order to subtract the effect of any major and minor losses within the reactor that are unrelated to the porous flow through biomass, we also conducted a control experiment where the same pressure-flow rate relationship was obtained by flowing gases through an empty reactor column ($H_r = 0$), yielding the reference pressure differential δP_0 . This gave us the baseline major and minor loss approximation that we need to subtract from the measured pressure differences in the actual biomass experiments. In general, we found the baseline major and

¹ For rice husk with a bulk density of 100 kg/m³ and maximum mass flow rate of 2 kg/h in a 4-inch-diameter reactor, the downward migration velocity is about 4 cm/min; for pine shavings with a bulk density of 30 kg/m³ and maximum mass flow rate of 0.5 kg/h in a reactor of the same diameter, the downward migration velocity is about 3 cm/min.

² For a torrefaction experiment with pine shavings where room-temperature air is injected at a normalized air/fuel ratio of 0.37 into the biomass moving bed, it travels upwards at a superficial velocity of 2 cm/s if the bed were unreactive (at room temperature). In a hot, reactive bed such as under torrefaction conditions, the density of air drops by a factor of 2-3, which means that the superficial velocity also increases by a factor of 2-3.

minor losses to comprise no more than 5-25% of the total measured pressure drop. Therefore, the final pressure drop ΔP_{porous} attributable to the porous flow is given by:

$$\Delta P_{\text{porous}} = -(\delta P_{\text{exp}} - \delta P_0).$$

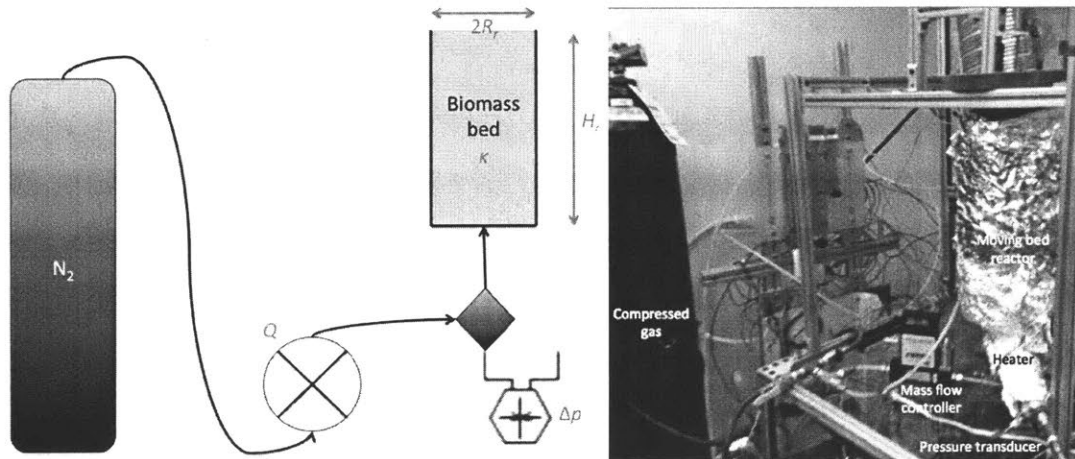


Figure 83 - Experimental set-up showing a biomass packed bed connected with a compressed gas source with adjustable flow rate control, and a pressure transducer to measure the pressure difference across the biomass packed bed.

Furthermore, in order to conduct the experiment over a wide range of physical characteristics, we selected four types of biomass: pine shavings, hay, rice husk, and sawdust. Three of these types (pine shavings, hay, and rice husk) were also used in our laboratory-scale torrefaction reactor tests described in 0. For pine shavings, hay, and rice husk, we were also able to physically measure the dimensions (major and minor axis lengths) of 100 randomly selected particles each, in order to understand how similar or dissimilar in physical characteristics these different types of biomass are from each other.

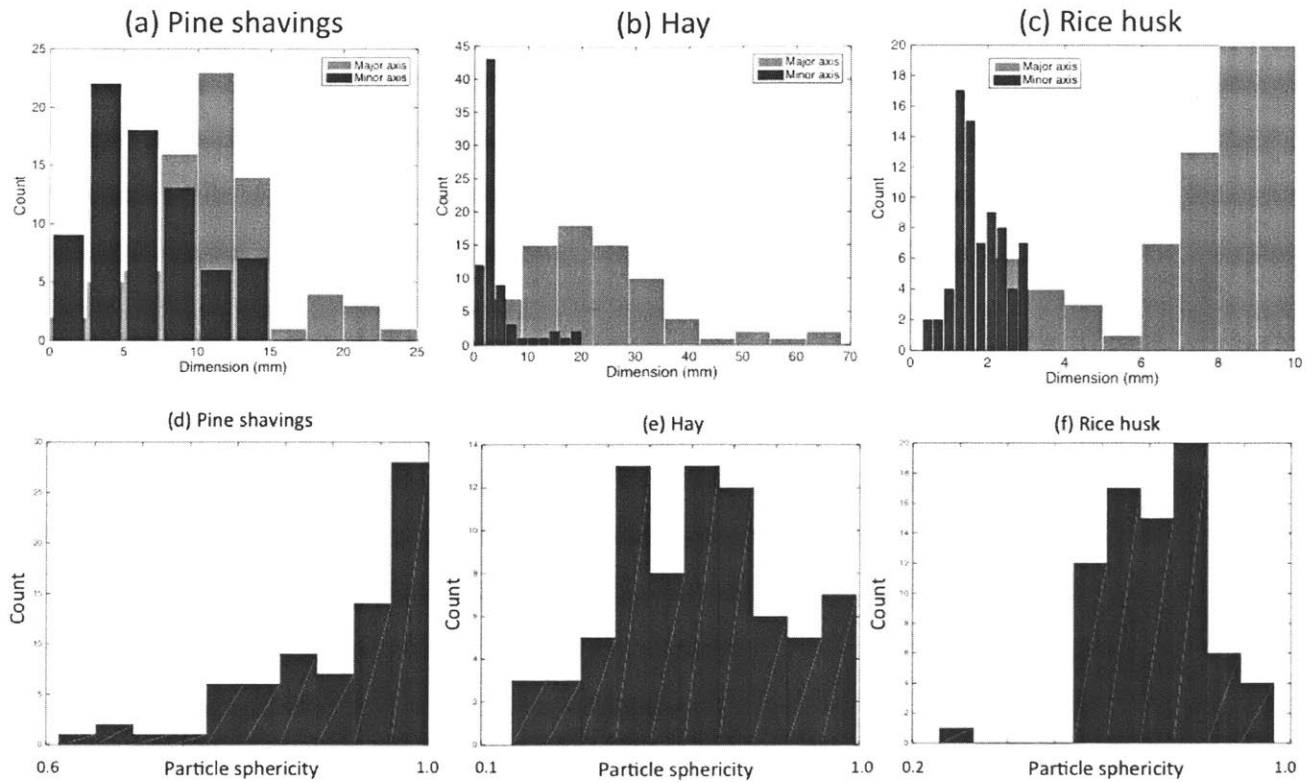


Figure 84 – Single-particle characteristics for different types of biomass. Top row, (a-c): Distribution of particle sizes (major axis lengths: red; minor axis lengths: blue) of 100 representative biomass particles for pine shavings (a), hay (b), and rice husk (c). Bottom row, (d-f): Distribution of particle sphericities of 100 representative biomass particles for pine shavings (d), hay (e), and rice husk (f).

Figure 84(a-c) shows the distributions of the particle sizes of these representative particles. Because most biomass particles are not isotropic in all dimensions, for each particle, we measured the lengths of the longest axis (major axis) and the shortest axis (minor axis). We see that all three types of biomass have distinct distributions for the major axis lengths compared to minor axis lengths, but for some types of biomass (such as hay), these two distributions are more distinct from each other. This means that hay particles have a much more elongated shape. In order to quantify this biomass particle disparity further, we draw upon a mathematical concept called sphericity S , which measures how close to a spherical shape an object is, and can be defined in 2D (major and minor axes are assumed to be perpendicular to each other) as

$$S \equiv \frac{2\sqrt{ab}}{C(a,b)}$$

where a, b are the major and minor axes, respectively, and $C(a,b)$ is the circumference length of an ellipse with a major axis a and minor axis b . For a perfectly spherical biomass particle, we would expect the sphericity to be 1. In the limiting case of a one-dimensional line, the sphericity would be 0. Figure 84(d-f) plots the distributions of sphericities of the same 100 representative particles of each of the three biomass types. We can more clearly see from these plots that pine shaving particles most closely resemble spheres, while hay particles most closely resemble needles, which intuitively makes sense. Table 27 summarizes the average statistics derived from these representative biomass particles.

Table 27 - Characteristic dimensions of 100 representative particles from 3 types of biomass.

Biomass type	Mean major axis length	Mean minor axis length	Characteristic particle size	Mean sphericity
Pine shavings	11.09 mm	6.35 mm	8.39 mm	0.91
Hay	22.89 mm	4.35 mm	9.98 mm	0.61
Rice husks	7.59 mm	1.76 mm	3.65 mm	0.71

From the exercise above, we can therefore see that we have selected biomass types that are quite distinct from each other not only in terms of particle sizes, but also in terms of their geometrical shapes. We believe that all these differences will factor into the bulk permeability of the moving bed, and our next task is to quantify this permeability.

6.3 Validation of Darcy's Law in Biomass Moving Bed

Having selected and characterized a few dissimilar types of biomass, we now proceed to verify whether or not we can describe the hydrodynamic characteristics of the biomass moving bed using Darcy's law. Figure 85 plots the response curves of measured pressure drop ΔP across the biomass packed bed *attributable* to the porous flow (i.e. major and

minor losses within the reactor length have been subtracted) as a function of variable nitrogen gas flow rates Q . For both hay (a) and rice husk (b), we observe a roughly linear increase in the pressure drop as a function of flow rate, and the slope ($\Delta P_{\text{porous}}/Q$) increases with increasing biomass packed bed depth H_r . Both of these observations are consistent with Darcy's law description for porous medium flow.

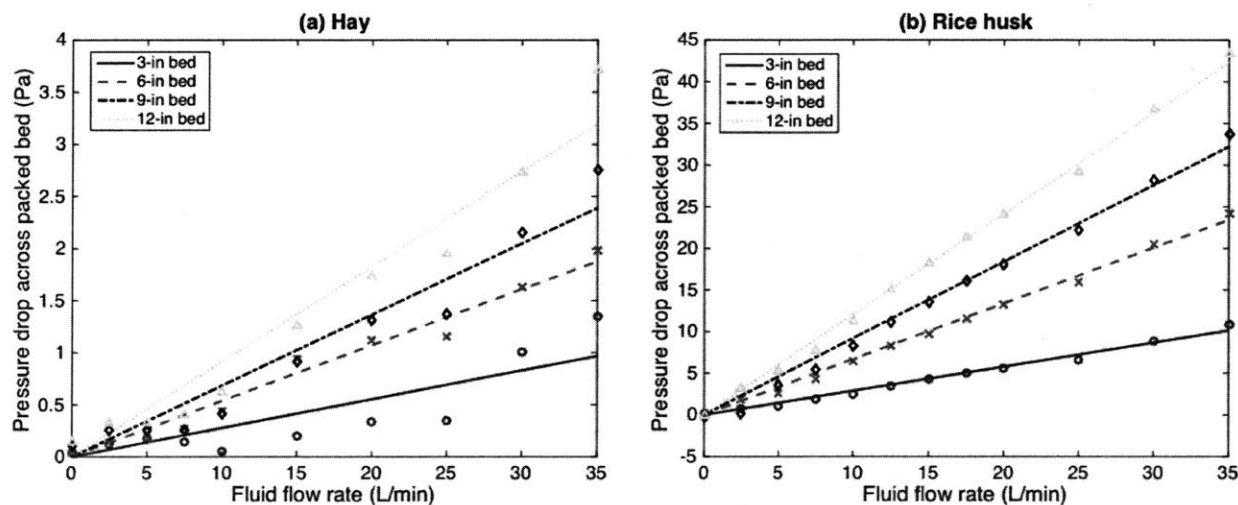


Figure 85 - Response curves of measured pressure drop across the biomass packed bed (ΔP , y-axis) versus gas flow rate (Q , x-axis) generally show a behavior consistent with Darcy's law, for different biomass bed depths, for hay (a) and rice husk (b). The different colors show biomass packed beds of different depths; the dots are experimentally measured data points; and the lines are linear fits to these dots.

In the case of the looser biomass (hay), we notice that the linear fit for $\Delta P_{\text{porous}}-Q$ is not as tight as the denser biomass (rice husk), and there are larger relative deviations of the data points from the linear fit line. We attribute these deviations to the limitation of a small-scale laboratory set-up to fully emulate a relatively homogeneous biomass bulk, as for our reactor size (4 inches), this dimension approaches the characteristic size of the larger biomass particles such as hay (which is on the order of an inch along its major axis).

Based on a given linear fit for $\Delta P_{\text{porous}}-Q$ data of slope $(\Delta P_{\text{porous}}/Q)_{\text{fit}}$, we are able to deduce the bulk packed bed permeability as follows:

$$\kappa_{\text{measured}} = -\frac{\mu H_r}{\pi R_r^2 (\Delta P_{\text{porous}}/Q)_{\text{fit}}}$$

These deduced permeability values for the four types of biomass measured in this study are listed in Table 28.

Table 28 - Deduced bulk permeability values of packed biomass bed consisting of different types of biomass.

Biomass type	Measured permeability
Pine shavings	$(1.5 \pm 0.2) \times 10^{-7} \text{ m}^2$
Hay	$(1.0 \pm 0.1) \times 10^{-7} \text{ m}^2$
Rice husk	$(8.6 \pm 0.2) \times 10^{-9} \text{ m}^2$
Sawdust	$(2.4 \pm 0.3) \times 10^{-10} \text{ m}^2$

It makes sense to observe that loose biomass such as pine shavings and hay typically have a higher measured permeability (around 10^{-6} m^2) compared to dense biomass such as sawdust (10^{-10} m^2), which is akin to that of typical sand. Furthermore, for loose biomass types such as pine shavings and hay, the values we measured are about an order of magnitude smaller compared to the value for similarly loose straw assumed by Di Blasi *et al.* (2004).

In brief, in this section, we demonstrated that the four types of biomass, in packed bed, behave hydrodynamically consistent with Darcy's law, and that we are able to experimentally calculate their bulk permeability values.

6.4 Comparison with Existing Permeability Correlations

Once we obtain the permeability values above, the next question to ask is: How do they compare with existing correlations? Could we save the trouble of setting up the experiment

for multitude of biomass types if we could just calculate and predict their values from a handful of physical parameters. To address this question, we begin by citing a commonly used empirical model for calculating the permeability coefficient described by the Carmen-Kozeny equation (1937):

$$\kappa_{CK} = \frac{\langle S \rangle^2 \varepsilon^3 \langle d_p \rangle^2}{\alpha (1 - \varepsilon)^2 \psi^2}, \quad \psi \equiv 1 + \frac{2}{3(1 - \varepsilon)} \frac{d_p}{2R_r'}$$

where $\langle S \rangle$ is the mean sphericity of the particles, $\langle d_p \rangle$ the mean characteristic size of the particles (both were measured earlier in Figure 84), $\alpha = 180$ is a proportionality constant, and ε is the bulk porosity of the bed, which can be approximated as:

$$\varepsilon = 1 - \frac{\rho_{\text{bulk}}}{\rho_{\text{solid}}},$$

where ρ_{bulk} is the measured mass density [kg m^{-3}] of the uncompacted biomass in a packed bed, and ρ_{solid} is the intra-particle mass density. As an example, pine shavings that we obtained in our study has a bulk density of about 30 kg m^{-3} , but its actual intra-particle density is around 400 kg m^{-3} . Therefore, the packed bed porosity is $\varepsilon = 0.93$ in the uncompacted form. Given these parameters, we can calculate the theoretically predicted bulk permeability values for these same four types of biomass, and the outcome is given in Table 29.

Table 29 - Bulk permeability of biomass packed beds predicted by the Carmen-Kozeny relation and its overestimation factor in comparison with experimental values.

Type of biomass	Predicted permeability	Overestimation factor
Pine shavings	$1.5 \times 10^{-5} \text{ m}^2$	100
Cut hay	$4.1 \times 10^{-6} \text{ m}^2$	40
Rice husk	$1.0 \times 10^{-7} \text{ m}^2$	12

Somewhat surprisingly, we note that theoretical correlations consistently overestimate the biomass fixed bed permeability. We define the “overestimation factor” as the ratio between the bulk permeability predicted by the Carmen-Kozeny relation to the actual measured bulk permeability for each type of biomass. We see that the overestimation is consistently

by over an order of magnitude. We also note that the theoretical estimation tends to improve as the particle sizes are reduced (i.e. in the case of rice husks).

We can think of two possible explanations for this consistent overestimation: (a) irregular biomass particle geometry, and (b) distribution of different particle sizes. Firstly, we note that Carmen-Kozeny relation was built upon the idealized assumption that the packed bed consists of perfect spheres of identical radii. In the case of actual biomass particles, these are often irregular in sizes. Some of these geometrical irregularities may create additional losses as a fluid flows past them, thereby creating additional pressure losses, which partially account for the perceived reduction in the bulk permeability values. Secondly, biomass particles do not come in one size, but consist of a distribution of sizes. Therefore, packed amongst the larger particles are smaller particles, and so forth. This tends to create further blockage for the fluid channels, reducing their effective hydraulic diameter while at the same time increasing the contours. All these changes contribute towards a larger pressure loss and therefore further perceived reduction in bulk permeability.

From the comparison between our measured permeability and the theoretical gold standard, we conclude that currently there lacks good datasets as well as useful tools to predict the bulk hydrodynamic characteristics of a biomass packed bed. As many biomass reactor (e.g. gasifier, pyrolysis) modeling studies have been based on these theoretical permeability values, it is important to note that the accuracy of these studies may have been negatively affected without a more accurate permeability value. Therefore, the methodology developed in this study presents a novel contribution towards a more accurate understanding and quantification of the same.

6.5 Scaling Pressure Requirements in Torrefaction Reactor

Finally, we present an application of why our hydrodynamic studies in biomass packed beds is important and relevant for biomass reactor design, by considering how such data can be used to scale a moving bed biomass torrefaction reactor, described previously in

Section 2.5. In this prototype, the amount of air entering into the reactor was controlled by a compressed source. However, in a scaled-up version of the reactor, a compressed gas source is not a realistic set-up; rather, the air must either be forced into the reactor through a fan (ΔP_{forced}), or be drawn in by the natural stack effect (ΔP_{stack}) due to a hot rising column of air inside the reactor. It is important for us to quantify this further, in order to know the design requirements for scale-up. We assume that in this study, the design of the reactor does not incorporate the improved secondary air oxidation mechanism (as described earlier in 0).

In a simple sense, the pressure that is supplied to push/pull the air upwards through the reactor ($\Delta P_{\text{forced}} + \Delta P_{\text{stack}}$) must be enough to counteract against the pressure loss through the porous medium ($\Delta P_{\text{loss,bed}}$) as well as the major and minor losses through the rest of the non-biomass-filled stack ($\Delta P_{\text{loss,stack}}$):

$$\Delta P_{\text{loss,bed}} + \Delta P_{\text{loss,stack}} = \Delta P_{\text{forced}} + \Delta P_{\text{stack}}.$$

Here, based on ΔP_{stack} and two ΔP_{loss} terms, we calculate the design requirement for ΔP_{forced} .

Let us first start with $\Delta P_{\text{loss,bed}}$. We first make the assumption that the bulk moving bed permeability is approximately constant as a function of temperature. While in principle our prior experimental setup can be modified to measure the effective permeability coefficients at different temperatures in a large furnace, we will reserve this potential characterization as future work, and in this Chapter, simply assume that any variations in the permeability occur within the same order of magnitude in the temperature range of interest. With this assumption in place, we already know how to estimate a differential porous pressure drop $d(\Delta P_{\text{loss,bed}})$ across a thin axial slice of the reactor dz via Darcy's law:

With these assumptions in place, we can re-write Darcy's law as:

$$d(\Delta P_{\text{loss,bed}}) = -d(\Delta P_{\text{porous}}) = \frac{\mu(T)Q(T)}{\kappa\pi R_f^2} dz = \frac{\mu(T)Q_0}{\kappa\pi R_f^2} \frac{T}{T_0} dz,$$

where we have related the volumetric flow rate $Q(T)$ of the gas at temperature T to that (Q_0) at the reference temperature T_0 by applying the ideal gas law:

$$Q(T) = \left(\frac{T}{T_0}\right) Q_0.$$

Furthermore, the viscosity term μ is also temperature-dependent. However, for pure gases such as nitrogen and carbon dioxide, its temperature-dependence is well characterized. For example, one common correlation is given by the Sutherland equation,

$$\mu(T) = \frac{kT^n}{T + C}$$

where the constants k , C , and n are given in the literature such as Bonilla *et al.* (1951). For the calculation below, for simplicity, we used the coefficients for air, where $k = 1.458 \times 10^{-6} \text{ kg m}^{-1} \text{ s}^{-1} \text{ K}^{-1/2}$, $C = 110.4 \text{ K}$, and $n = 1.5$.

Integrating both sides, and rewriting the air flow rate in terms of the desired solid (biomass) flux and the normalized air/fuel ratio, and hence, in terms of the solid residence time, we obtain:

$$\begin{aligned} \Delta P_{\text{loss,bed}} &= \frac{\dot{Q}_{\text{air},0}}{\kappa \pi R_r^2 T_0} \int_0^{H_r} T(z) \mu(T(z)) dz \\ &= \frac{H_r (\text{AF})_{\text{stoic}}}{T_0} \left(\frac{\rho_{\text{BM}}}{\rho_{\text{air}}} \right) \frac{\sigma}{\tau_{\text{res}}} \int_0^{H_r} T(z) \mu(T(z)) dz, \end{aligned}$$

where $(\text{AF})_{\text{stoic}}$ is the mass ratio of air to biomass at stoichiometric combustion of the latter. Therefore, we see when we have a way to establish the validity of Darcy's law and quantify the bulk bed permeability κ , then it is possible to relate the pressure loss term within the biomass moving bed to the original reactor design parameters defined previously in 0, as well as the biomass type (which affects $(\text{AF})_{\text{stoic}}$ and native ρ_{BM}). In particular, the $(\sigma/\tau_{\text{res}})$ dependency makes intuitive sense: as we increase the normalized air/fuel ratio, then we are dictating more air to go through the reactor system; likewise, as we reduce the solid residence time, the air flow rate must also increase in order to keep up with the increase in the overall biomass flow rate. In both cases, we are driving more air through the biomass moving bed, leading to a greater pressure loss. We have assumed a nominal biomass moving bed height $H_r = 1 \text{ m}$. Given that the viscosity of the volatile and exhaust gas mixture is difficult to experimentally measure online at a wide range of temperature and reaction conditions, we estimated this quantity using the kinetic mechanism and transport model proposed by Anca-Couce *et al.* (2014) for different types of biomass under the torrefaction regime. In general, the viscosities are much more strongly a function of temperature rather

than gas composition.³ Therefore, even if our simplifying assumption introduces errors into the estimation for the viscosity, we do not expect that this will significantly affect the results.

In Figure 86, we plot the projected pressure loss incurred across the biomass moving bed under different torrefaction reaction conditions for (a) pine shavings, (b) hay, and (c) rice husks. We note that in general, the pressure loss is heavily modulated by the bulk bed permeability: it is around 1-5 Pa for loose biomass such as pine shavings and hay, and around 100-300 Pa for dense biomass such as rice husks. Therefore, we can see that more than any other variable, the bulk permeability is probably still the most important factor in determining the absolute scale of the pressure requirement. Then, for each given type of biomass, we observe that the pressure loss increases as the normalized air/fuel ratio increases (increasing torrefaction severity) and as the solid residence time decreases. This makes sense because the pressure loss/requirement is directly related to the amount of gas flow through the biomass moving bed. As the torrefaction severity increases, there is more air inflow for a given biomass flow rate. Furthermore, as the solid residence time decreases, the biomass is flowing through the reactor at a higher rate, and therefore, in order to keep the normalized air/fuel ratio the same, we must also increase the flow rate of air through the moving bed.

³ To support this claim, we list in the table below the kinematic viscosities for typical flue gas and air at different temperatures (Chu, 2017).

Temperature (°C)	Kinematic viscosity ($\text{m}^2 \text{s}^{-1} \times 10^{-6}$)	
	Flue gas	Air
50	17	18
100	22	23
150	27	27
200	33	32
250	40	36
300	46	41

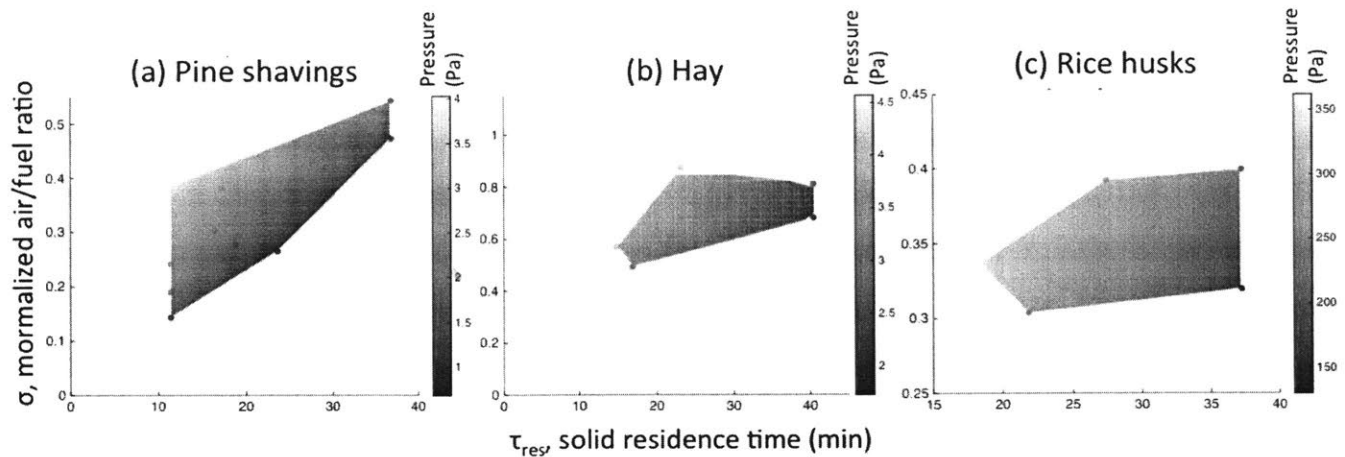


Figure 86 - Projected pressure loss across the biomass moving bed under different torrefaction reaction conditions for (a) pine shavings, (b) hay, and (c) rice husks. The pressure requirements increase as a function of increasing torrefaction severity as well as reducing solid residence time. The ranges of pressure differences are 1-4 Pa for pine shavings, 1-5 Pa for hay, and 130-360 Pa for rice husks.

Next, let us consider $\Delta P_{\text{loss,stack}}$. This term describes the major and minor losses that occur in the non-biomass-filled portion of the stack, assuming that the chimney height H_c is greater than the biomass bed height H_r , and assuming a laminar flow regime⁴:

$$\Delta P_{\text{loss,stack}} = \left(\frac{f(H_c - H_r)}{4R_r} + \frac{1}{2} \right) \rho v_{\text{exhaust}}^2 = \frac{16\mu v_{\text{exhaust}}}{R_r} + \frac{\rho v_{\text{exhaust}}^2}{2},$$

where the friction factor $f = 64/\text{Re}$ is approximated by applying Poiseuille's law. Here, the first term on the right-hand side is the major loss in the chimney length, while the second term is the exit loss at the top of the chimney. It can be shown that the velocity of the exhaust mixture can be rewritten as a combination of the reactor design parameters as well as the performance factor (e.g. solid mass yield, Y_M):

$$v_{\text{exhaust}} = \frac{(\sigma(\text{AF})_{\text{stoic}} + 1 - Y_M)H_r}{\tau_{\text{res}}} \frac{\rho_{\text{BM}}}{\rho_{\text{exhaust}}} \left(\frac{R_r}{R_c} \right)^2.$$

⁴ For a laboratory-scale reactor with a diameter of 4 inches (10 cm) and a typical exhaust flow rate, the axial flow velocity is about 0.02 m/s. This translates to a Reynolds number of 30. For scaling up, increasing the reactor diameter by a factor of 20 while keeping all other variables constant results in a Reynolds number of 600. Both of these numbers are well within the laminar flow regime.

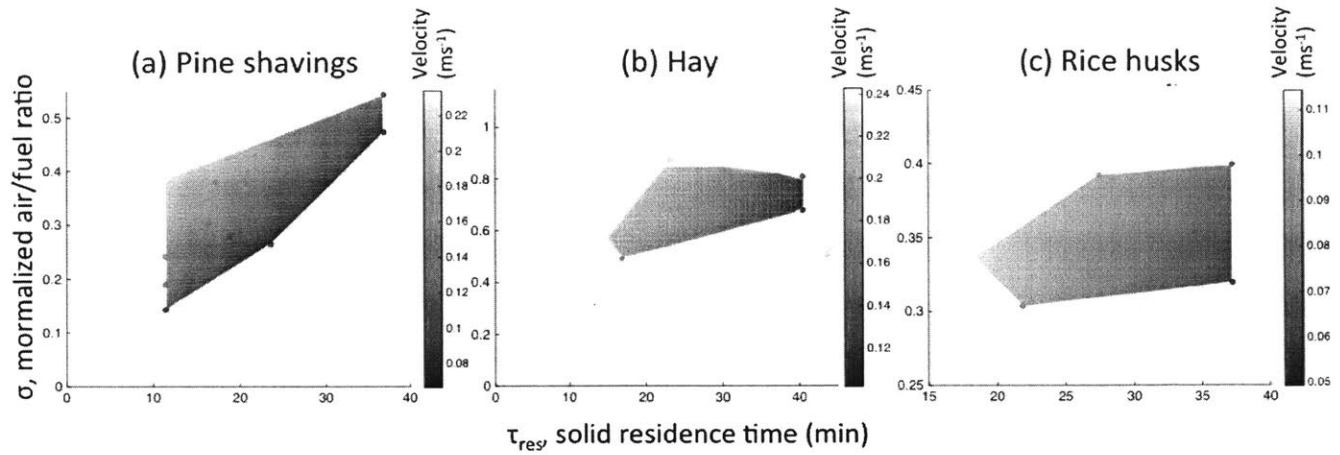


Figure 87 - Estimated exhaust stream velocity from the reactor outlet under different torrefaction reaction conditions for (a) pine shavings, (b) hay, and (c) rice husks. The pressure requirements increase as a function of increasing torrefaction severity as well as reducing solid residence time. The ranges of velocities are 0.07-0.22 m s^{-1} for pine shavings, 0.10-0.24 m s^{-1} for hay, and 0.05-0.12 m s^{-1} for rice husks.

The exhaust velocities under different reaction conditions for different types of biomass are plotted in Figure 87. Irrespective of the type of biomass, the general velocities are between 0.03 to 0.22 m s^{-1} . The velocity tends to increase as the solid residence time decreases and as the normalized air/fuel ratio increases, for the same reason as the pressure drop across the moving bed increases (due to increased flow). Then, knowing the estimated exhaust velocities, we can then compute the $\Delta P_{loss,stack}$ term under different reaction conditions, as we have done in Figure 88. Once again, the pressure losses in the chimney segment and the exit pressure losses increase as a function of reducing solid residence time and increasing normalized air/fuel ratio. The general range of values is between 0.002 to 0.017 Pa, which is miniscule compared to the pressure drops across the moving bed characterized earlier in Figure 86, and as we will see, the magnitude of the natural stack effect. Therefore, for the purpose of estimation, we can safely ignore the $\Delta P_{loss,stack}$ term, and simply compare the natural stack effect against the pressure drop to drive gases through the moving bed to determine whether or not forced air mechanism is needed.

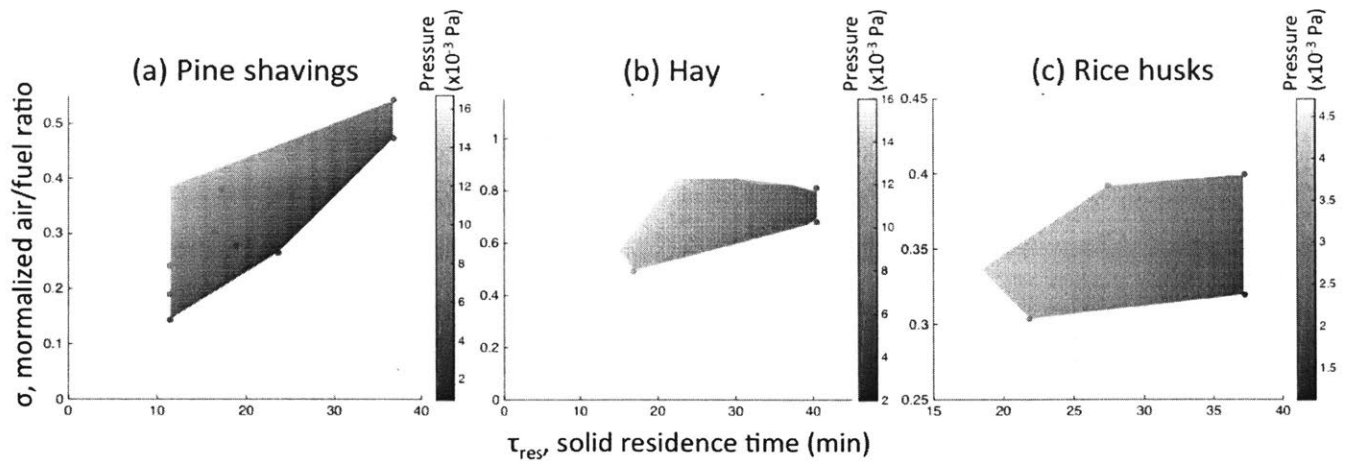


Figure 88 - Estimated pressure loss in the chimney segment and the exit pressure loss under different torrefaction reaction conditions for (a) pine shavings, (b) hay, and (c) rice husks. The pressure requirements increase as a function of increasing torrefaction severity as well as reducing solid residence time. The ranges of pressure losses are 0.001-0.015 Pa for pine shavings, 0.002-0.016 Pa for hay, and 0.001-0.05 Pa for rice husks. These pressure losses are almost negligible compared to those across the moving bed, or as we will see later, compared to the natural stack effect.

Next, we need to find a way to infer ΔP_{stack} , which measures the pressure drive due to the natural stack effect of a hot column of rising gas. With the current laboratory-scale reactor, we do not have a good means of measuring the natural stack effect. However, we can derive this stack effect from first principles, and then express it in terms of the reactor design parameters. First we assume a simplified reactor model where the inside of the reactor is at an elevated temperature T_H with a lower gas density of ρ_H , and the ambient air is at a colder temperature T_C with a higher gas density of ρ_C . We know that the net stack effect arises due to the hot column of air (dictated by the overall height of the hot air column $H_r + H_c$) at a lighter density:

$$\Delta P_{stack} = (\rho_C - \rho_H)gH_c = \frac{p_{atm}}{R} \left(\frac{MW_C}{T_C} - \frac{MW_H}{T_H} \right) g(H_r + H_c),$$

where R is the gas constant, and MW_C and MW_H are the mean molecular weights [kg mol^{-1}] of the cold and hot gases, respectively. In this case, the molecular weight of the cold gas (ambient air) is well known. On the other hand, the molecular weight of the hot gas

(reactor exhaust) can be calculated by knowing the (a) mass flow rate of the gas, (b) volumetric flow rate of the gas, and (c) temperature profile of the gas. Most studies evaluating the stack effect make the approximation that $MW_H \approx MW_C = 0.029 \text{ kg mol}^{-1}$ (Klote, 1991; Chu, 2017).

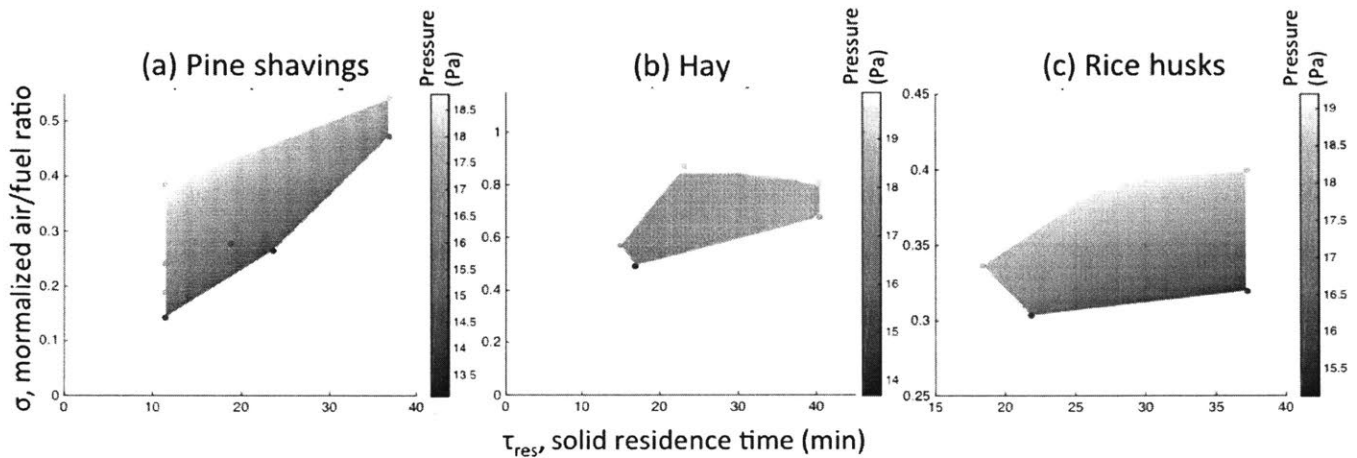


Figure 89 - Estimated natural stack effect in the reactor assembly (moving bed and chimney, which is assumed to be 1 m tall) under different torrefaction reaction conditions for (a) pine shavings, (b) hay, and (c) rice husks. The stack effect increases mostly as a function of increasing torrefaction. The ranges of values are 13-19 Pa for pine shavings, 14-20 Pa for hay, and 15-20 Pa for rice husks.

In Figure 89, we plot the estimated natural stack effect in terms of the pressure drive [Pa]. We note that the general range of values is between 13 to 22 Pa, irrespective of the type of biomass. This should not be surprising, as the natural stack effect has less to do with the physical properties of biomass, and rather with the elevated temperature inside the reactor. As the normalized air/fuel ratio increases, the reactor temperature is also expected to increase, which leads to a larger natural stack effect, as observed.

Now, we have all the quantities that we need to answer the question: Is the natural stack effect sufficient to supply enough air to the reactor to sustain the torrefaction reaction, without an external source of pressure drive? To do this assessment, we compare the values in Figure 86 (pressure losses across the moving bed) to those in Figure 89

(magnitudes of the natural stack effect). As discussed earlier, we neglect the major and minor losses in the chimney stack as these losses are at least one order of magnitude smaller than the other terms above. Table 30 summarizes the typical ranges of values that we estimate. As we can see, the answer depends largely on the type of biomass. Namely, because the magnitude of the stack effect does not vary greatly, what dictates the answer is the bulk permeability of the moving bed, which then determines the pressure loss in the moving bed. We see that for pine shavings and hay—which have comparable bulk permeability coefficients as determined in Table 29—the natural stack effect provides sufficient drive. On the other hand, because rice husks have a bulk permeability that is 2 orders of magnitude lower, the pressure loss across a moving bed constituted of rice husks is also two orders of magnitude higher. As a result, the natural stack effect is insufficient to provide sufficient flow to overcome this resistance to flow. For rice husks, as well as for other types of biomass with smaller particle sizes and bulk permeability constants, it is important that an external forced air mechanism provide the majority of the pressure drive needed to guarantee sufficient flow through the moving bed.

Table 30 - Can the natural stack effect provide enough air into the reactor to sustain the torrefaction reaction?

Biomass type	Pressure loss in moving bed	Pressure drive due to stack effect	Is the natural stack effect sufficient?
Pine shavings	1-4 Pa	13-19 Pa	Yes
Hay	1-5 Pa	14-20 Pa	Yes
Rice husks	130-360 Pa	15-20 Pa	No

6.6 Discussion

In this study, we began with the premise that the existing literature has done insufficient work in characterizing the bulk permeability of different types of biomass in a moving bed setting and instead has been reliant on idealized correlations, and we set out to

characterize the same with greater care. We verified that generally, in our operating regime of interest, the biomass moving bed obeys a Darcy's law behavior where the pressure drop scales roughly linearly with the flow through the reactor. From this, we also determined the bulk permeability constants of pine shavings, hay, rice husks, and sawdust. We found significant deviations—in particular for loose biomass—compared with the idealized models, and therefore concluded that it is important to reconsider the way that the existing literature modeled the hydrodynamic characteristics across a biomass moving bed.

By estimating the pressure losses across the moving bed and comparing it with the magnitude natural stack effect, we also concluded that for loose biomass such as pine shavings and hay, the stack effect should be able to provide sufficient flow of air to the reactor. On the other hand, in the case of dense biomass such as rice husks, an external pressure drive is necessary.

In principle, the pressure losses across the moving bed are directly proportional to the height of the moving bed. Therefore, we can reduce the pressure losses by simply making the bed shorter. Another consideration is that the natural stack effect can be increased simply by increasing the height of the chimney. We also naturally expect that if we implement the secondary air oxidation improvement to the reactor assembly, the secondary combustion occurring at a higher temperature will provide a further boost to the natural stack effect in the upper section of the reactor. However, there are also limits to these design changes. For example, we cannot make the chimney arbitrarily tall; for the scale of our reactor, a height of several meters probably is the maximum. In the cases where the natural stack effect is at least one order of magnitude smaller than the pressure losses through the moving bed, simply increasing the chimney height is not enough, as the stack effect only scales linearly with increasing chimney height.

Finally, while this Chapter provides an initial quantification for the pressure drives necessary to provide sufficient air to drive torrefaction, beyond simply using a compressed air source, the calculations done in this Chapter are largely estimated, likely accurate only to the order of magnitude. While this study provides guidelines and preliminary insights

regarding the reactor system performance, it should not be used to make specific design decisions. It is important in the scale-up step to experimentally verify the magnitudes of the stack effect and how it compares with the pressure losses across the moving bed, and to incorporate the experimental features needed to quantify these pressure losses and drives.

Chapter 7 Characterization of Transition Timescales in Scaling Biomass Reactor Operations (How to Design a Reactor Operation to Start/Stop Effectively)

Most laboratory-scale studies in biomass reactors have focused on the steady-state operation of the reactor, and so far paid little attention to the practicalities such as what it takes to start the reactor from a cold state, to stop a reaction quickly, or to adjust the reaction conditions. Such discussions are invariably important when it comes to scaling the reactor in real life. In this study, we analyze experimental time series temperature data and infer the transient behaviors of the test reactor, as well as how it changes with reactor scaling. We show that the thermal mass of the reactor has a significant part to play in the reactor's temporal response to changes, and demonstrate that in our design, it is possible to achieve a reasonable temporal response time at scale. Based on our analysis, we devise a series of start-up and cooling operation strategies that seek to optimize the time and feedstock consumption requirements. Finally, we apply the learning to consider the case of transitioning between two reactor operating conditions, and show, rather counterintuitively, that the default transition method—which continuously feeds biomass into the reactor—is probably the least efficient of all possible methods. The insights learned in this study provide a basis for a more comprehensive study of the reactor transitional operations that can be encapsulated into an automated control system to minimize human intervention.

7.1 Transient Response of the Reactor System

In a continuous-flow reactor design in biomass processing, the primary question of interest is often the steady-state operation conditions of the reactor, which we have addressed previous in 0 through Chapter 6. However, in order to arrive at the steady state, the reactor must have originated from a cold state. In practical scale-up operation, it matters how long the reactor takes to reach this steady state: an unacceptably long start-up time may mean that the output product, for a long while, may not be subject to the correct reaction

condition. In this study, we set out to characterize the response time of our laboratory-scale reactor in different modes of operation, such as (a) starting from a cold state, (b) shutting down quickly or slowly, and (c) transitioning from one reaction condition to the next. We also derive the scaling laws for this reactor response time, thereby deriving insight into how the response time varies as the reactor size changes. Therefore, we create an analytical framework for characterizing the response time that has applications not only in our laboratory-scale torrefaction reactor, but also more generally to other biomass reactors (e.g. gasifiers, incinerators) as well as beyond.

7.2 Analysis of Reactor Thermal Mass

In order to understand the response time of the reactor, the first important question to ask is how much thermal inertia the reactor has. Our test reactor has an inner radius $R_r = 2$ inches (5.1 cm) and is comprised of $\frac{1}{4}$ -inch-thick (0.64 cm) stainless steel 304. Then outside of the stainless steel wall, the reactor is surrounded by a formable ceramic insulation sheet that is about 1 inch (2.5 cm) thick. We assume that the reactor is completely filled with biomass (pine shavings, which has a bulk moving bed density of 30 kg m^{-3}). Given these data, we can break down the thermal mass of the reactor into three components: biomass, metal wall, and insulation. Table 31 illustrates calculation of the heat capacity (thermal mass) [J K^{-1}] from these data. As we observe, the volumes of the three components in our laboratory-scale reactor are comparable (on the order of $10\text{-}100 \text{ cm}^3$), but the density of the stainless steel is almost two orders of magnitude higher than either the biomass or the insulation material. Even though as a counteracting factor, stainless steel also has a lower specific heat capacity compared to the other two materials, ultimately, it contributes to about 84% of the system's thermal inertia at the laboratory scale.

Table 31 - Calculation of the various components of the thermal mass comprising the laboratory-scale reactor assembly.

Components	Biomass (pine shavings)	Metal (stainless steel 304)	Insulation (AlSi ceramic)
Volume	49 cm ³	13 cm ³	68 cm ³
Density	30 kg/m ³	8,050 kg/m ³	96 kg/m ³
Mass	0.15 kg	11 kg	0.65 kg
Specific heat capacity	1,300 J K ⁻¹ kg ⁻¹	452 J K ⁻¹ kg ⁻¹	1,130 J K ⁻¹ kg ⁻¹
Heat capacity	190 J K ⁻¹	4,800 J K ⁻¹	740 J K ⁻¹

One may wonder how the relative contributions to the thermal inertia change as the reactor scales. This is approximated in Table 32 for three different dimensions of the reactor. As the reactor scales up, the amount of biomass that resides within the reactor volume at a given time is proportional to R_r^2 . On the other hand, for both metal and insulation, assuming that their respective thicknesses Δ_i are small compared to the overall reactor dimension R_r (thin cylindrical shell approximation where $\Delta_i \ll R_r$), then we see that their masses scale linearly with the reactor radius as $\sim 2\pi R_r \Delta_i$. This explains why, as the reactor scales, the relative contribution of biomass to the overall thermal mass goes up to 43% while that of metal and insulation decreases. However, at operational scale (200 kg h⁻¹), we see that the thin metal wall still contributes to more than half of the system's overall thermal inertia. A high thermal inertia is undesirable from the point of view of long lags in starting up, cooling down, or making general adjustments to the reactor. The next question, then, is whether we can improve the system's response time by directly targeting the metal component.

Table 32 - Relative contributions of the different components to the total thermal inertia of the reactor, as a function of the reactor scale.

Reactor dimension	Mass flow rate	Biomass contribution	Metal contribution	Insulation contribution
10 cm (dia) × 60 cm (L)	0.5 kg h ⁻¹	3%	84%	13%
50 cm (dia) × 90 cm (L)	13 kg h ⁻¹	16%	75%	9%
2 m (dia) × 120 cm (L)	200 kg h ⁻¹	43%	51%	6%

The thermal mass comprises the products of the following material characteristics: density, volume, and specific heat capacity. We can somewhat change the density and specific heat capacity by changing the selection of the wall material, but we cannot get too creative here, as we want a commonly manufacturable metal that can also withstand high temperatures and abrasive conditions. Let us assume that we stay with stainless steel; then, the only variable we can change is the overall volume, or namely, the metal wall thickness. We therefore define a “*lightweight design scenario*” where instead of the original quarter-inch-thick stainless steel, we assume that it is feasible to manufacture the wall at one-sixteenth of an inch. This then effectively cuts down the relative contribution of metal to the overall thermal inertia by a factor of four. Table 33 shows the updated relative contributions from the different materials to the total thermal mass in this lightweight design scenario.

Table 33 - Relative contributions of the different components to the total thermal inertia of the reactor, as a function of the reactor scale, in the lightweight design scenario.

Reactor dimension	Mass flow rate	Biomass contribution	Metal contribution	Insulation contribution
10 cm (dia) × 60 cm (L)	0.5 kg h ⁻¹	10%	56%	34%
50 cm (dia) × 90 cm (L)	13 kg h ⁻¹	36%	42%	21%
2 m (dia) × 120 cm (L)	200 kg h ⁻¹	70%	20%	10%

Naturally, ultimately, the useful measure of reactor performance is the response time; therefore, in the next sections, we will explore how this thermal mass translates in terms of the overall response time for different operating conditions

7.3 Starting a Reactor from Cold State

We first consider the case of starting the reactor from a cold state. Our goal is to identify a start-up strategy that minimizes both the start-up response time and the amount of biomass consumed during the start-up phase. We further assume that we have a specified target temperature T_{target} that the reactor must reach by the end of the start-up phase.

First, we remark that during the start-up transition phase, if we are continuously flowing biomass through the system under a small normalized air/fuel ratio $\sigma < 1$ —as we would do during the steady-state torrefaction process—then we are simply wasting much of the biomass as they come out unusable due to incomplete torrefaction. Therefore, for the purpose of minimizing wasting biomass, the start-up procedure we have decided to take is to bring the normalized air/fuel ratio all the way to stoichiometric combustion ($\sigma \sim 1$). This serves two purposes. Firstly, it completely combusts the unusable biomass and harnesses all the energy for starting the reactor up; secondly, this method maximizes the flame temperature, thereby heating up the reactor thermal mass more aggressively.

To better understand and quantify the reactor start-up process, we utilized a simplified heat transfer model shown in Figure 90a. Here, at the bottom, the reactor wall is hottest, assuming a temperature T_H . We further estimate that there is some bulk convective transfer coefficient h between the reactor wall and the upflowing post-combustion flue gas, such that when the flue gas escapes from the reactor, it has been cooled to a temperature T_C . Figure 90b shows the corresponding experimental setup. We tested the start-up procedure under two different biomass mass fluxes (which signifies different power outputs for heating up the reactor): $4 \text{ g s}^{-1} \text{ m}^{-2}$, and $6 \text{ g s}^{-1} \text{ m}^{-2}$. Note that once the biomass

flux was specified, the air flow rate was adjusted to provide an approximately stoichiometric combustion ($\sigma \sim 1$).

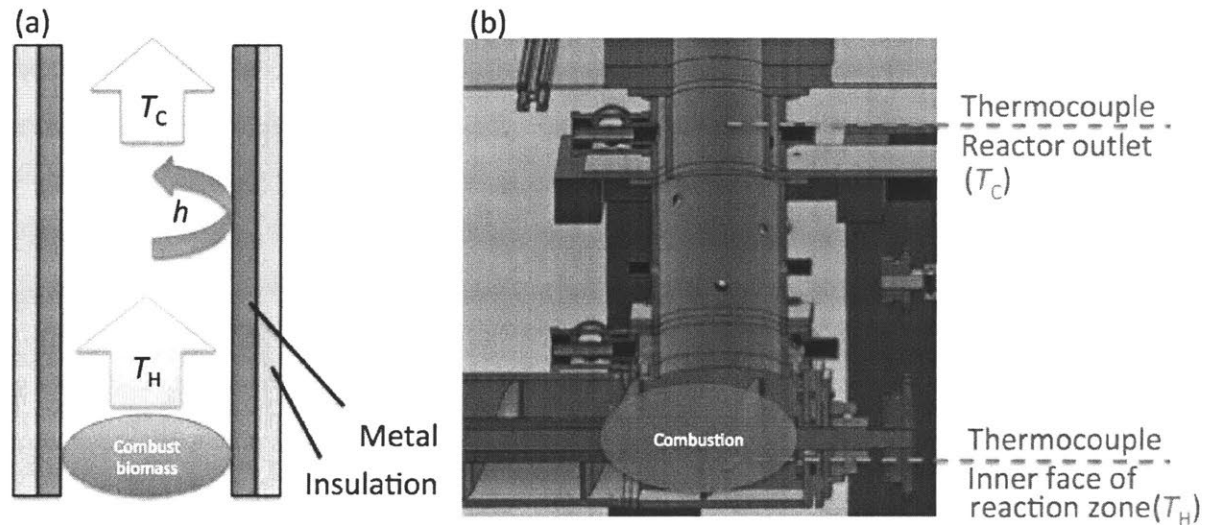


Figure 90 - (a) Conceptual model used for evaluating reactor start-up timescale. (b) The corresponding experimental setup, showing the locations of the thermocouples.

Figure 91 shows the temperature traces (in time, where $t = 0$ represents starting from the cold state) for the lower biomass flux ($4 \text{ g s}^{-1} \text{ m}^{-2}$, Figure 91a) and for the higher biomass flux ($6 \text{ g s}^{-1} \text{ m}^{-2}$, Figure 91b). In both plots, the red line traces the inner surface temperature of the reaction zone (proxy for T_H), and the blue line traces the temperature at the reactor outlet (proxy for T_C). In both cases, the reactor heats up on the order of 2 hours, though depending on the biomass flux (power output), the final steady-state temperature is different: it is around 225°C for a biomass flux of $4 \text{ g s}^{-1} \text{ m}^{-2}$, and about 290°C for a biomass flux of $6 \text{ g s}^{-1} \text{ m}^{-2}$.

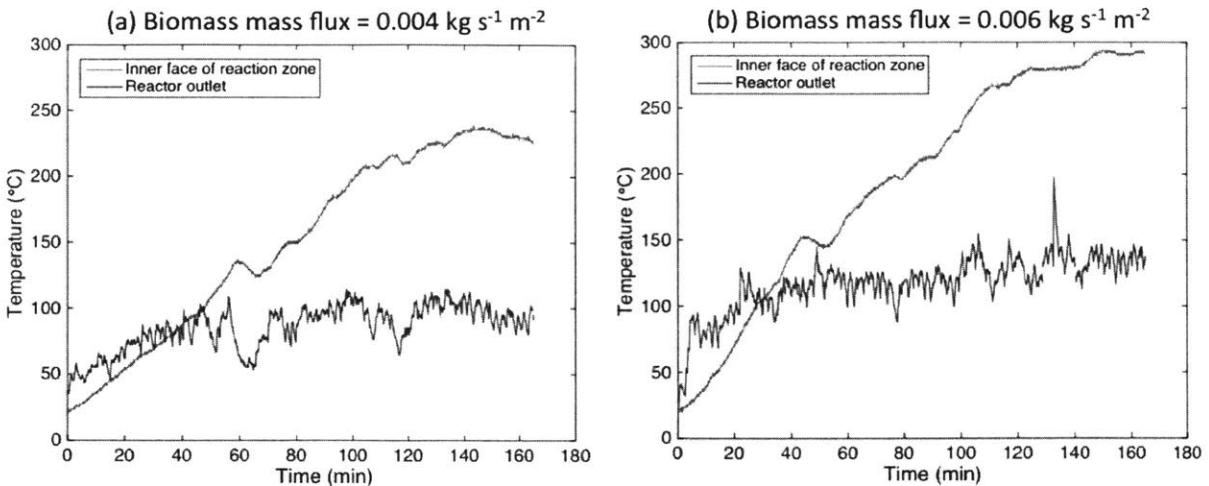


Figure 91 - Temperature traces in time at the inner face of the reaction zone (red lines) and at the reactor outlet (blue lines) for starting up the reactor by the stoichiometric biomass combustion at two biomass mass fluxes: $4 \text{ g s}^{-1} \text{ m}^{-2}$, and $6 \text{ g s}^{-1} \text{ m}^{-2}$.

What does this mean in terms of designing the optimal procedure for starting up the reactor? Given that we know a specific target torrefaction temperature T_{target} to reach, then, firstly, T_{target} sets a constraint on the minimally viable biomass mass flux: as an example, if we want the target torrefaction temperature to be at 260°C , then it makes little sense to try to warm up the reactor using a biomass mass flux of $4 \text{ g s}^{-1} \text{ m}^{-2}$, as we know from the experiment above that under this low flux, the steady-state reactor temperature will never reach 260°C . Rather, a higher biomass mass flux is needed. However, as Figure 92 illustrates, we have various choices for the biomass mass flux: should we (a) find a biomass mass flux where the final steady-state temperature is just barely above T_{target} , or should (b) we aim for a higher mass flux with a final steady-state temperature way above T_{target} , and then transition to the continuous steady-state reactor operation as soon as the reactor temperature reaches the vicinity of the target temperature? We see that these two approaches have a trade-off between the total start-up time required (shorter for scenario b) and the total amount of biomass consumed/wasted for starting the reactor up (lesser for scenario a). We put forth the concept here only, and will work through a more quantitative approach to this design choice/trade-off later in the section.

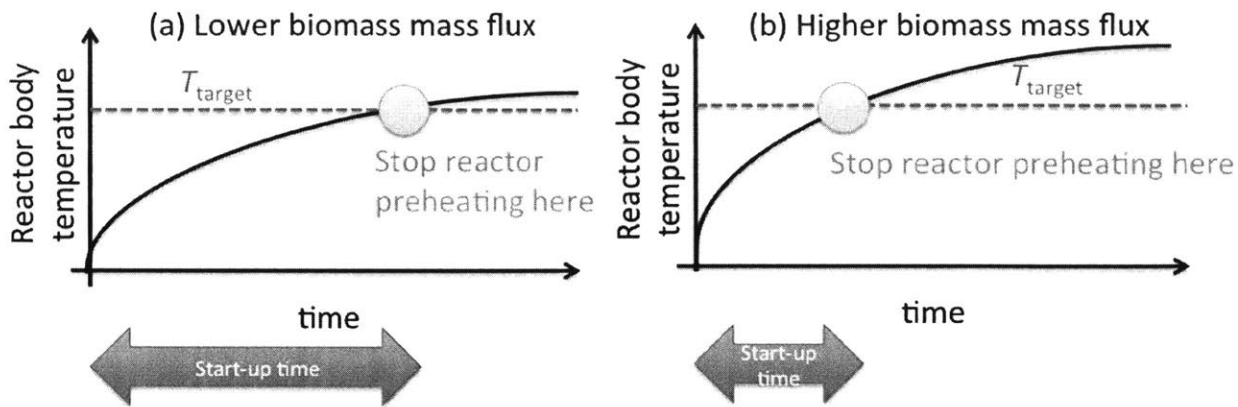


Figure 92 - Trade-off between (a) starting a reactor with a lower biomass mass flux which takes longer start-up time, and (b) starting a reactor with a higher biomass mass flux which may consume more biomass for the start-up procedure.

In order to quantify this trade-off in greater detail, we first need to put some theoretical framework behind the observations above. We first assume that heat transfer from the post-combustion flue gas to the reactor can be approximated as a lump sum. This is true when the Biot number of the reactor assembly is much less than 0.1. We verified that, given the inner metal wall lining with rapid heat conduction, this condition is satisfied. This implies that heating the metal from the post-combustion flue gas—rather than the heat conduction through the metal—is the rate-limiting step in starting up the reactor. The equation below describes that the energy balance of the post-combustion flue gas:

$$\varepsilon_{\text{comb}} \dot{m}_{\text{BM}} \text{HHV}_{\text{BM}} = 2\pi R_r L_r h (T_H - T_{\text{metal}}) + \dot{m}_{\text{flue}} c_{p,\text{flue}} (T_C - T_{\text{air}}).$$

Eq. 5

Here, the left-hand side represents the heat of biomass combustion (adjusted by a lump-sum efficiency factor $\varepsilon_{\text{comb}} < 1$); the first term on the right-hand side represents the heat transferred from the post-combustion flue gas to the metal body through the convective heat transfer coefficient h , and this process cools the upflowing flue gas from the original T_H at the reactor core to T_C at the reactor outlet; and finally, the second term on the right-hand side represents the sensible heat loss from the warm flue gas at the reactor exit. Here, we do not know many terms, such as the combustion efficiency factor $\varepsilon_{\text{comb}}$, and the specific

heat capacity of the flue gas $c_{p,\text{flue}}$. But as we will show later, it is not necessary to know the values of these terms in order to approximate the reactor's start-up response time.

Next, we can write the energy balance of the metal as:

$$m_{\text{metal}}c_{\text{metal}}\frac{dT_{\text{metal}}}{dt} = 2\pi R_r L_r h(T_H - T_{\text{metal}}) - \frac{2\pi L_r}{\Omega}(T_{\text{metal}} - T_{\text{air}}),$$

where we have the initial condition $T_{\text{metal}}(t = 0) = T_{\text{air}}$ in the cold state. Here, the first term on the right-hand side represents the heat transfer from the post-combustion flue gas to the metal body, and the second term on the right-hand side represents the heat loss from the metal body through the insulation material to the ambient air, and this loss is governed by the thermal transfer resistance factor Ω , defined as:

$$\Omega \equiv \frac{\ln(1 + \Delta_{\text{metal}}/R_r)}{k_{\text{metal}}} + \frac{\ln(1 + \Delta_{\text{ins}}/(R_r + \Delta_{\text{metal}}))}{k_{\text{ins}}} + \frac{1}{h(R_r + \Delta_{\text{metal}} + \Delta_{\text{ins}})}.$$

By observing the blue lines in Figure 91, we made the observation that the temperature at the reactor outlet—while fluctuating widely throughout—rapidly assumes its steady-state temperature in comparison with the much slower rise in the reactor core (red lines). Therefore, in Eq. 5 above, we can assume that T_C is independent of time, and can be represented by some time-independent average value $\langle T_C \rangle$.

By combining the two equations above, and rearranging the terms, we obtain:

$$\frac{dT_{\text{metal}}}{dt} = \frac{\dot{m}_{\text{BM}}}{m_{\text{metal}}c_{p,\text{metal}}}(\mathcal{E}_{\text{comb}}\text{HHV}_{\text{BM}} - \sigma\text{AF}_{\text{stoic}}(\langle T_C \rangle - T_{\text{air}})) - \frac{2\pi L_r}{m_{\text{metal}}c_{p,\text{metal}}\Omega}(T_{\text{metal}} - T_{\text{air}}). \quad \text{Eq. 6}$$

Here, if we assume that the heat capacity of the metal does not vary greatly with temperature in our regime of interest,⁵ and we assume that $\langle T_C \rangle$ can be approximated as a time-independent constant, then we see that the first term on the right-hand side is approximately a constant term (time-independent), while the second term on the right-

⁵ For stainless steel 304, the specific heat capacity can be estimated by $c_{p,\text{metal}} = 443 + 0.2T - (8 \times 10^{-7})T^2$ [J K⁻¹ kg⁻¹] (Valencia and Qusted, 2008), valid for the temperature range of between 298 and 1727 Kelvins. At room temperature ($T = 298.15$ K), $c_{p,\text{metal}} = 503$ J K⁻¹ kg⁻¹. At the high end of the torrefaction regime ($T = 598.15$ K), $c_{p,\text{metal}} = 562$ J K⁻¹ kg⁻¹. The difference between the two values is less than 10%.

hand side has a time-dependent T_{metal} term. For the purpose of curve-fitting from our experimental data, this equation can be simplified into the linear equation $Y = A - X / \tau_s$, where

$$Y \equiv \frac{dT_{\text{metal}}}{dt}, \quad X \equiv T_{\text{metal}} - T_{\text{air}}, \quad \text{and} \quad \tau_s \equiv \frac{m_{\text{metal}} c_{p,\text{metal}} \Omega}{2\pi L_r}.$$

Here, the time constant τ_s in fact represents the response time of the reactor in starting up based on biomass combustion. Table 34 gives the fitting parameters for the two different biomass mass fluxes measured previously.

Table 34 - Fitted parameters to calculate the reactor start-up response time.

Biomass mass flux	Fitted value for A	Fitted value for τ_s
4 g s ⁻¹ m ⁻²	2.10 ± 0.11 [K s ⁻¹]	147 ± 1 [min]
6 g s ⁻¹ m ⁻²	3.15 ± 0.12 [K s ⁻¹]	114 ± 1 [min]

Indeed, as remarked earlier, the representative time constant is around 2 hours, which is consistent with our earlier observations in Figure 91. We also see that the fitted constants change as we change the biomass mass fluxes; this should not surprise us, as different temperatures and combustion conditions can affect various factors in Eq. 6.

The next question that we wish to ask is: How does the reactor response time scale as we scale up the reactor for real-life operation? We note that Eq. 6 contains various reactor's geometrical factors R_r and L_r , and we can therefore make an educated guess for the new reactor start-up response timescale τ_s^* given new dimensions L_r^* and R_r^* of the scaled-up reactor:

$$\frac{\tau_s^*}{\tau_s} = \frac{L_r^* \Omega}{L_r \Omega^*}$$

Eq. 7

assuming all other factors (such as choice of insulation material) are held constant. By the same logic, we can also make an educated guess for the new reactor start-up response timescale in the lightweight design scenario (where the metal thickness, Δ_{metal} , is 1/16

inches (16 mm) rather than 1/4 inches (64 mm), which also affects the heat transfer resistance term Ω). The results are summarized in Table 35.

Table 35 - Predicted reactor start-up timescales under various reactor dimensions and metal thicknesses (shaded versus non-shaded).

Reactor dimensions (diameter × height)				
Metal thickness	BM mass flux	10 cm × 60 cm	50 cm × 90 cm	2 m × 1.2 m
64 mm (traditional)	4 g s ⁻¹ m ⁻²	147 min	179 min	188 min
	6 g s ⁻¹ m ⁻²	114 min	139 min	146 min
16 mm (lightweight)	4 g s ⁻¹ m ⁻²	52 min	68 min	62 min
	6 g s ⁻¹ m ⁻²	40 min	52 min	48 min

We therefore make two observations. Firstly, as we make the reactor lightweight (use less metal), we can drastically reduce the reactor's start-up response time by a factor of 2-3. Secondly, as we scale up the reactor using the current metal thickness (1/4-inch stainless steel), the reactor's response time increases only mildly, and therefore, manageably: while the biomass flow rate is increased by a factor of 400 (with a 80" reactor diameter compared to a 4" reactor diameter), for both biomass fluxes, the reactor's start-up response timescale increases only by a factor of 1.3. However, in the case of the lightweight design scenario, as the reactor scales up, the response timescale initially increases mildly, and then decreases at the largest scale (80" compared to 20" in reactor diameter) mildly.

To intuitively understand this mild dependence as the reactor scales up, we note that in the limit that R_r becomes very large in comparison with Δ_{metal} and Δ_{ins} , we can approximate the response timescale as

$$\tau_s = \frac{\pi L_r ((R_r + \Delta_{\text{metal}})^2 - R_r^2) c_{p,\text{metal}} \Omega}{2\pi L_r} \rightarrow \frac{c_{p,\text{metal}} \Delta_{\text{ins}}}{k_{\text{ins}}} \Delta_{\text{metal}} (1 + \Delta_{\text{metal}}).$$

The strong dependency on Δ_{metal} explains the drastic improvement in the reactor's response time in the lightweight design scenario, and the fact that this expression has no dependence on the reactor's dimensions explains why the response timescale changes only

mildly as the reactor scales up: the timescale is asymptotically approaching a constant value that depends only on the insulation and the metal thickness.

Finally, we revisit the earlier concept and trade-off captured in Figure 92, which outlines different biomass mass flux rates we can undertake to reach the same target reactor temperature, some faster than others, and some consume less biomass than others. Now, with the reactor's start-up response timescale quantified, we can proceed to capture this trade-off also in a more quantitative manner. For the ease of analysis, we will assume that the target reactor temperature is $T_{\text{target}} = 225^\circ\text{C}$, and carry out the analysis using the two biomass mass fluxes that we experimentally carried out to measure the temperatures in Figure 91. This process below is used as an example to illustrate an experimental and design framework that can be generalized (for other biomass mass fluxes) to optimize the reactor start-up operations for other target temperatures and types of biomass.

If we want to reach $T_{\text{target}} = 225^\circ\text{C}$ with a biomass mass flux of $\Phi_{\text{BM}} = 4 \text{ g s}^{-1} \text{ m}^{-2}$, then we see that from Figure 91a, the red curve takes about $\tau_t = 130$ minutes to cross the 225°C line. This means that for our laboratory-scale reactor with a radius $R_r = 2$ inches, the total amount of biomass consumed is $m_{\text{BM}} = \pi R_r^2 \Phi_{\text{BM}} \tau_t = 252 \text{ g}$. On the other hand, for the biomass mass flux of $\Phi_{\text{BM}} = 6 \text{ g s}^{-1} \text{ m}^{-2}$, the red curve takes only about $\tau_t = 95$ minutes. In this case, the total amount of biomass consumed is 295 kg. Therefore, we see that in this case, if we put in a higher biomass mass flux, we get a 30% decrease in the overall start-up time, but only a 17% increase in the total amount of biomass consumed/wasted for starting the reactor up. Which mass flux to select depends on the operation needs: if we are in a hurry to process a massive amount of biomass for a long time period, then the time it saves during the start-up phase may very well justify the extra consumption of biomass to start. However, on the other hand, if we are only processing a small batch of biomass, or if the biomass is very expensive, then every gram of it counts, and in this case we may select to have a slower start-up time that also consumes a smaller quantity biomass.

The next question we ask is: How does this biomass consumption scale as the reactor scales? Because as the reactor scales, we will be processing biomass at a significantly

higher flow rate, in order to make the figures comparable between different scales, we define a quantity for the reactor start-up phase called the *specific residence time* τ_r :

$$\tau_r \equiv \frac{\pi R_r^2 \Phi_{BM} \tau_t}{\dot{m}_{BM}},$$

where \dot{m}_{BM} is the steady-state biomass mass flow rate of the reactor. This quantity has the unit of time. Therefore, in essence, we are normalizing the total biomass consumed/wasted during the start-up period by the nominal steady-state biomass mass flow rate, and this quantity reflects the time's worth of the amount of biomass consumed/wasted during the start-up period. As an example, for the calculations done above for the base case of our laboratory-scale reactor ($\dot{m}_{BM} \sim 0.5 \text{ kg h}^{-1}$). For the case of the lower biomass mass flux, $\tau_r = 252 \text{ g} / (500 \text{ g h}^{-1}) \sim 30 \text{ min}$. For the case of the higher biomass mass flux, $\tau_r \sim 35 \text{ min}$. Therefore, in terms of the amount of biomass consumed/wasted to warm up the reactor, it represents, respectively, 30 and 35 minutes' worth of continuous reactor processing.

Table 36 - The amount of biomass consumed/wasted to warm up the reactor—expressed in terms of the *specific residence time*—for different reactor scales for the target temperature of $T_{\text{target}} = 225^\circ\text{C}$ for pine shavings.

Reactor dimensions (diameter × height)				
Metal thickness	BM mass flux	10 cm × 60 cm	50 cm × 90 cm	2 m × 1.2 m
64 mm (traditional)	4 g s ⁻¹ m ⁻²	30 min	35 min	37 min
	6 g s ⁻¹ m ⁻²	35 min	42 min	48 min
16 mm (lightweight)	4 g s ⁻¹ m ⁻²	11 min	13 min	13 min
	6 g s ⁻¹ m ⁻²	12 min	16 min	15 min

We see from Table 36 that, as already observed previously in the reactor response timescale, even as we massively scale up the reactor, the specific residence time is not predicted to change drastically. We assume that for a real-life reactor operation at scale, it will visit a 1-acre farm over a period of one day, processing about 2 dry tons/acre of biomass residues. At a scale of 200 kg h⁻¹ (reactor diameter = 80 inches), this requires about 10 hours of continuous operation. Therefore, wasting approximately 40 minutes'

worth of biomass to start up the reactor represents no more than 7% of the overall feedstock assuming that the wall is ¼-inch stainless steel. In the lightweight design scenario, the waste represents no more than 3% of the overall feedstock, which is an improvement by more than a factor of 2. This is encouraging, as it suggests that we do not need to implement additional strategies to facilitate the start-up timescale as the reactor scales up.

Therefore, in conclusion, for the reactor start-up procedure, we showed that it generally takes about 2 hours for the standard reactor design, and about 1 hour for the lightweight reactor design (with 1/16" or 16 mm steel), and the amount of biomass consumed is about 40 and 20 minutes' worth of the steady-state operating time for the two respective scenarios above. These numbers only scales weakly as the reactor scales up. Furthermore, there is generally a trade-off between warming the reactor up with a higher biomass mass flux (reducing the start-up time) and with a lower mass flux (reducing the amount of biomass wasted for starting up). The actual operation selection will depend on the use scenario, considering whether a faster processing time or overall conversion efficiency is the higher priority.

7.4 Two Methods for Shutting Down the Reactor

In the previous section, we discussed at length the design considerations in selecting an operating condition to warm the reactor up. In this section, we consider the opposite topic: How do we shut down the reactor effectively? We note that, unlike the case of starting up the reactor, where we tend to want the system response time to be as fast as possible, in the case of shutting down the reactor, the desired system response time depends on the specific use case. For example, in the case of a reactor malfunction, and we want the repair done quickly and safely without affecting the production, then the functional requirement is that the reactor should be cooled down as soon as possible. On the other hand, in the case of finishing the torrefaction reaction at one farm and immediately moving to a different farm, then the functional requirement is that the reactor should stay warm for as long as

possible, so that when the unit is moved to the new farm, we do not expend extra energy to try to warm up the reactor assembly again. In this section, we consider both cases.

7.4.1 Keeping the Reactor Warm

In the case of keeping the reactor warm, then we want to fill the reactor core completely with biomass, so that the hot metal wall is not exposed to the outside ambient air. In addition, we will also cap the top of the reactor, so that it does not promote an updraft stack effect (Figure 93a). In this case, the biomass bulk is still going to admit heat loss from the hot metal wall, but the amount of air flow—and the extent of convective cooling—through the inner metal wall will be very limited, and instead, heat loss will mostly be happening through the outer insulation with the ambient air (with a convective heat transfer coefficient of h), which will be slower.

Figure 93b shows a sample experimental temperature trace of the temperature from a thermocouple probe located at the center of the biomass bed at the lower part of the reactor, for a sample pine shavings experiment. Here, we see that the heat loss is indeed very slow, and after more than 2 hours, the inner reactor still retains about 50% of the original heat. In order to understand the timescale and how it scales more quantitatively, we assume that the reactor can be modeled as a simplified lump sum block with a total mass m_r and specific heat capacity $c_{p,r}$, and write the overall heat loss equation as follows:

$$m_r c_{p,r} \frac{dT}{dt} = - \left(\frac{2\pi L_r}{\Omega_{ds}} + \frac{2\pi R_r^2}{\Omega_{cap}} \right) (T - T_{air}).$$

Eq. 8

Here, Ω_{cap} represents the bulk heat transfer resistance offered in the axial direction by the reactor caps. The Ω_{dr} term in the denominator on the right-hand side depicts the radial heat loss through the biomass bulk, the metal and the insulation layers:

$$\Omega_{ds} \equiv \frac{\ln\left(\frac{R_r}{R_{in}}\right)}{k_{BM}} + \frac{\ln\left(1 + \frac{\Delta_{metal}}{R_r}\right)}{k_{metal}} + \frac{\ln\left(1 + \frac{\Delta_{ins}}{R_r + \Delta_{metal}}\right)}{k_{ins}} + \frac{1}{h(R_r + \Delta_{metal} + \Delta_{ins})}.$$

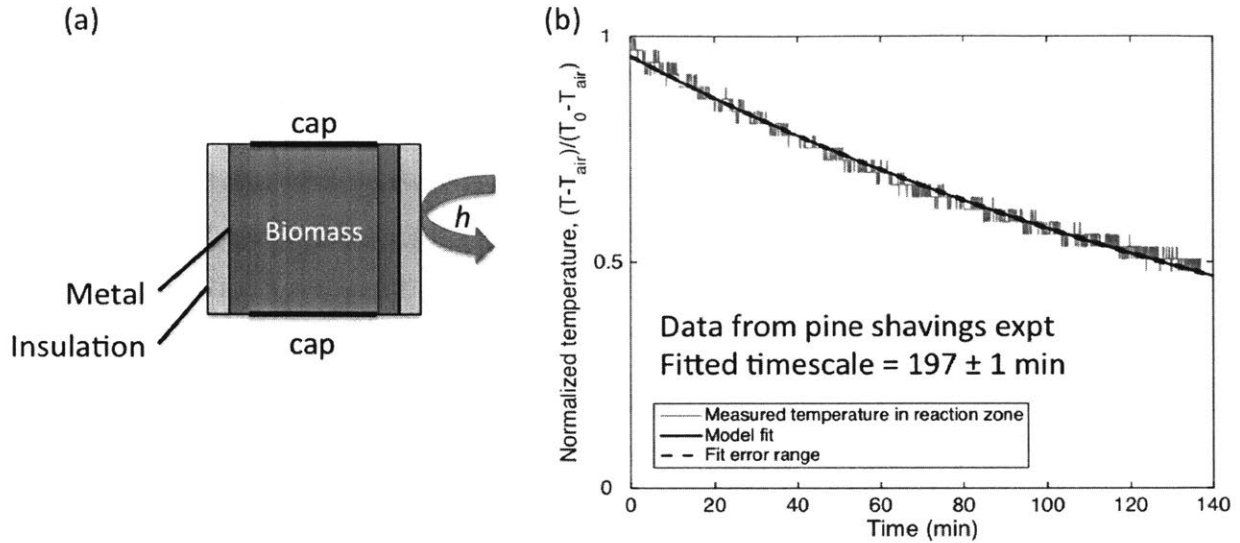


Figure 93 - Strategy for keeping the reactor warm as long as possible, by filling the inner volume with biomass and capping the reactor outlets (a), together with a sample temperature trace in time showing the cooling profile for an experiment with pine shavings (b).

From Eq. 8, we can see that the heat loss timescale τ_{ds} in this case can be defined as:

$$\tau_{ds} \equiv \frac{m_r c_{p,r}}{\frac{2\pi L_r}{\Omega_{ds}} + \frac{2\pi R_r^2}{\Omega_{cap}}}$$

and Eq. 8 can simply be solved analytically as a decaying exponential, assuming that the different terms in the equation are temperature-independent. When this exponential is fitted to the experimental data in Figure 93b, we obtain an approximate timescale of 197 ± 1 min.

Now, we proceed to investigate how this cooling timescale changes as the reactor is scaled up, using the same logic of proportionality as done earlier in Eq. 7. Then, Table 37 reports the outcome.

Table 37 - Reactor cooling timescale at different reactor scales and metal thicknesses, in the scenario of keeping the inner core of the reactor warm as long as possible.

	Reactor dimensions (diameter × height)		
Metal thickness	10 cm × 60 cm	50 cm × 90 cm	2 m × 1.2 m
1/4 inches (64 mm)	3.3 hours	6.0 hours	8.4 hours
1/16 inches (16 mm)	1.2 hours	2.0 hours	2.8 hours

From Table 37, we can see that as the reactor scales up by factor of 400 (in terms of the biomass mass flow capacity), the cooling timescale also increases by a factor of 2.3 to 2.5. At scale, the reactor design made from thicker metal has a cooling timescale that is 3 times greater than the lightweight design, due to the massive thermal inertia in the metal. Therefore, we can immediately see a design trade-off here: while in the previous case, having a lightweight reactor design (with thinner metal walls) may make the reactor more agile in terms of start-up response time, here, this agility actually works against the reactor’s ability in retaining heat over a long period of time. However, the more practical question to ask is: If the reactor is moved from one farm to another and need to stay warm as long as possible, how long is this transit time? If the transit time is shorter than 3 hours, then even in the lightweight reactor design at scale, there is sufficient thermal mass to keep the reactor reasonably warm over that time period. However, if the transit time will be longer than 3 hours, then perhaps a solution is to look for an intermediate metal thickness between the two investigated in this study to find the optimal trade-off between reactor thermal agility in heating up and thermal inertia in cooling down.

One final note is that during the cooling down process, if we are filling the reactor in full with biomass, then by necessity we are consuming/wasting the amount of biomass equivalent to the reactor’s solid residence time in order to keep the reactor warm.

7.4.2 Cooling the Reactor Quickly

In the previous case, we considered in how to keep the reactor warm as long as possible during the cooling process. In this section, we consider the opposite scenario: Suppose that the reactor has a fault during operation, and repair needs to be performed quickly and safely in order to minimize reactor downtime. In this case, our interest is in cooling the reactor down as quickly as possible. Instead of filling the reactor with biomass and capping both ends to avoid the natural stack effect, in this case, we want to remove the biomass completely from the inner reactor, and keep the inner metal exposed to the cooling air, such that the reactor body can be cooled both on the inside and the outside (through the outer insulation).

Figure 94a shows the conceptual illustration of this cooling strategy, and Figure 94b shows the experimental cooling data. While on the outside, the air is relatively still (with convective heat transfer coefficient h_s). Inside the reactor, depending on the amount of stack effect (which we quantified earlier in Section 6.5) and the pressure drive we apply, we can achieve forced cooling to various extents (given by a convective heat transfer coefficient h_f). Here, in our experiment, we let air flow through the reactor at three velocities: 0 cm/s (black), 1.9 cm/s (blue), and 2.8 cm/s (red). The discrete points are real experimental data, while the dashed lines are the exponential curve fits (strategy to be described next) and their error bars.

To develop a quantitative method to curve-fit and extract the quantitative timescale in different cooling scenarios and to infer reactor scaling, we again build a heat loss model based on Figure 94a by assuming that the reactor body (metal and insulation layers) can be approximated as a simplified lump sum with total mass m_r and specific heat capacity $c_{p,r}$. We can then write the heat loss equation as:

$$m_r c_{p,r} \frac{dT}{dt} = -2\pi L_r \left(h_f R_r + \frac{1}{\Omega_{dr}} \right) (T - T_{air}).$$

Eq. 9

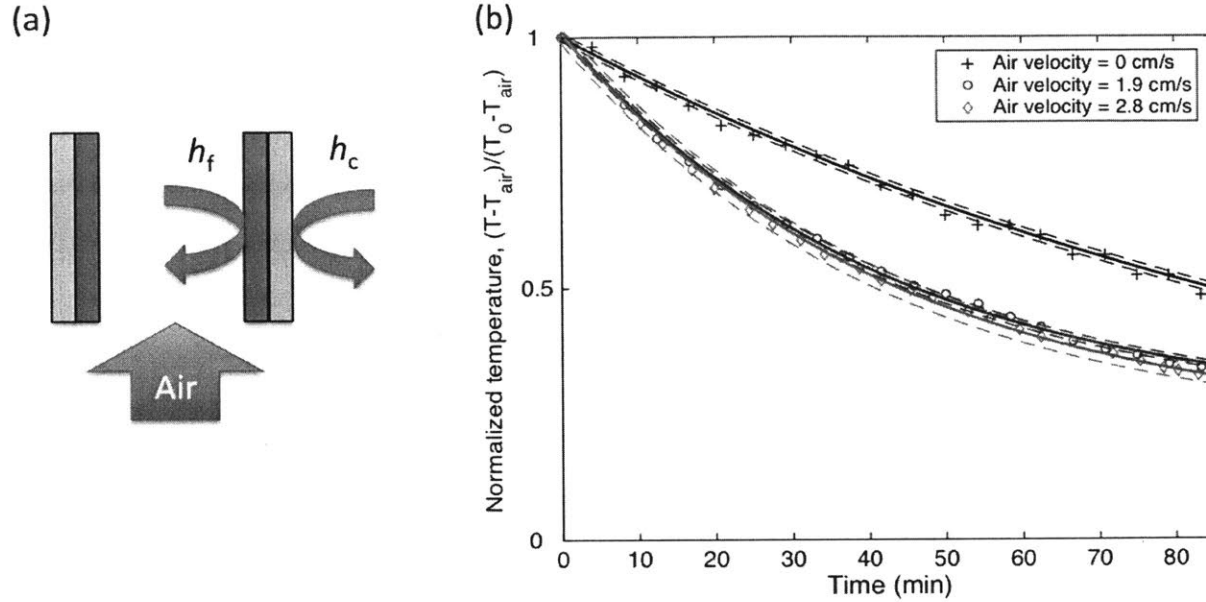


Figure 94 - Strategy for cooling the reactor down as quickly as possible, by letting cooling air flow inside the reactor, together with a sample temperature trace in time showing the cooling profile for an experiment with pine shavings (b) under different inner air flow velocities of 0 cm/s (black), 1.9 cm/s (blue), and 2.8 cm/s (red).

Here, the h_f term on the right-hand side represents heat loss due to forced convection inside the reactor, and the Ω_{dr} term on the right-hand side represents heat loss through the reactor's outer insulation:

$$\Omega_{dr} \equiv \frac{\ln\left(1 + \frac{\Delta_{metal}}{R_r}\right)}{k_{metal}} + \frac{\ln\left(1 + \frac{\Delta_{ins}}{R_r + \Delta_{metal}}\right)}{k_{ins}} + \frac{1}{h(R_r + \Delta_{metal} + \Delta_{ins})}$$

By assuming that only the temperature T is the time-dependent term in Eq. 9, we can then define the rapid cooling reactor response time τ_{dr} as:

$$\tau_{dr} \equiv \frac{m_r c_{p,r}}{2\pi L_r \left(h_f R_r + \frac{1}{\Omega_{dr}} \right)}$$

Eq. 10

By fitting the various experimental data in Figure 94b with decaying exponentials and then extracting the time constant, we obtained the following time constants: at an air velocity of

0 cm/s, $\tau_{dr} = (124.1 \pm 0.6)$ min; at 1.9 cm/s, $\tau_{dr} = (78.1 \pm 3.7)$ min; and at 2.8 cm/s, $\tau_{dr} = (76.7 \pm 9.2)$ min. We can therefore see that forced convection does result in faster cooling timescales. However, how does the timescale depend on the air velocity?

To answer this question, we assume that the forced convective heat transfer coefficient, h_f , is a *linear* function of the air velocity:

$$h_f(v_{air}) \approx h_f^0 + \left(\frac{dh_f}{dv_{air}} \right) v_{air}.$$

Then, we can rewrite the rapid cooling timescale equation (Eq. 10) as:

$$\left(\frac{1}{\tau_{dr}} \right) = \frac{2\pi L_r R_r}{m_r c_{p,r}} \left(\frac{dh_f}{dv_{air}} \right) v_{air} + \frac{2\pi L_r}{m_r c_{p,r}} \left(h_f^0 R_r + \frac{1}{\Omega_{dr}} \right).$$

We can see that this equation is of the linear form $Y = aX + b$, where $Y = 1/\tau_{dr}$, and $X = v_{air}$.

Figure 95 shows this linear fitting for the three experimental data points we carried out for pine shavings.

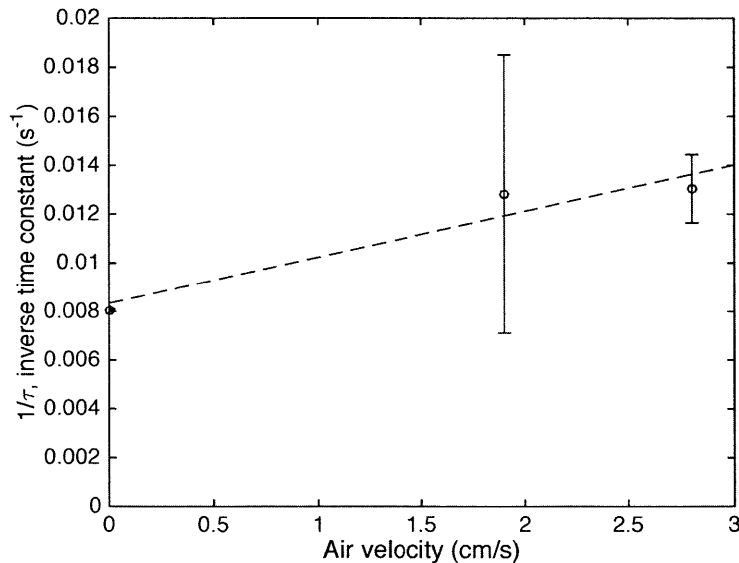


Figure 95 - Linear fitting for the inverse time constant as a function of the air velocity inside the reactor.

Once we have an idea of the main dependencies of the rapid cooling timescale, including the dependency on forced air cooling velocity, the next question we explore is: How does this timescale change in response to scaling the reactor up? We use the same logic of

proportionality as described in the previous section, and Table 38 reports the outcomes from scaling the reactor up.

Table 38 - The reactor's rapid cooling timescale, for different reactor scales for pine shavings under different forced air flow velocities inside the reactor.

Metal thickness	Air velocity	Reactor dimensions (diameter × height)		
		10 cm × 60 cm	10 cm × 60 cm	10 cm × 60 cm
1/4 inches or 16 mm (traditional)	0 cm s ⁻¹	124 min	115 min	114 min
	1.9 cm s ⁻¹	78 min	73 min	72 min
	2.8 cm s ⁻¹	77 min	71 min	70 min
1/16 inches or 16 mm (lightweight)	0 cm s ⁻¹	41 min	38 min	38 min
	1.9 cm s ⁻¹	26 min	24 min	24 min
	2.8 cm s ⁻¹	25 min	24 min	23 min

From Table 38, we observe that as we increase the forced cooling air velocity inside the reactor from 0 to 1.9 cm/s, there is a reduction in rapid cooling time by almost 40%. However, additional velocity increase to 2.8 cm/s only sees a very marginal further reduction. Therefore, we conclude that forced air cooling is effective in moderate velocities. Furthermore, as the reactor scales up, we generally see a weak dependency in the rapid cooling timescale. Finally, as we reduce the metal thickness to 1/16 inches (16 mm), the rapid cooling timescale decreases by a factor of about 3. Therefore, in consideration of rapid cooling, the reactor should be as thermally light as possible.

Another alternative strategy for enhancing the rapid cooling of the reactor is to design the outer insulation to be removable. In the case of warming up the reactor as quickly as possible and/or preserving heat within the reactor as long as possible, it is in our interest to put the thermal insulation on the exterior of the reactor. However, in the case of rapidly cooling the reactor, if we are able to remove this external insulation jacket, then this will drastically cut down the Ω_{dr} term, which is also expected to decrease the rapid cooling time even further.

7.4.3 Perspectives in Cooling the Reactor

Table 39 - A summary of the two cooling modes explored in this study.

	Slow cooling mode	Fast cooling mode
Purpose	Retain heat as long as possible	Lose heat as quickly as possible
Use case	Reactor is being moved from one farm to the next for ongoing conversion.	Reactor breaks down and needs quick and safe service.
Strategy	Fill interior with biomass; cap top and bottom to eliminate stack effect.	Empty biomass, drive forced cooling air through the reactor interior.
Scaling performance	2-3 times improvement in storage time as reactor scales by 400 times	Weak reduction in rapid cooling time as reactor scales by 400 times
Reducing metal use	Adverse affects performance	Improves performance

In this section, we explored the strategies for cooling the reactor. In the first application, we want to retain as much of the heat for as long as possible. In the second application, we want to cool as rapidly as possible. We showed that with the current reactor design, all these processes happen in the timescale of an hour to hours, which is not unreasonable for the scaled-up reactor operation. However, the two applications have design requirements that are diametrically opposite from each other: the former (slow cooling) requires as much thermal mass and insulation as possible, while the latter (rapid cooling) requires the reactor to be as thermally agile as possible. In each single design, it is not possible to accomplish both optimally. Therefore, the final design will depend on the actual operation requirements, in order to prioritize the design requirements. Another alternative, as discussed earlier, is to design the outer insulation jacket to be removable on demand. While this may increase the complexity and overall capital cost of the reactor, the benefit is a higher performance in both cooling applications. A cost-benefit analysis is needed to

determine the warrant of this additional design feature. Table 39 summarizes these two different cooling modes.

7.5 Transitioning Between Two Reaction Conditions

In the previous sections, we discussed the design strategies for heating and cooling the reactor. Finally, in this section, we explore what it takes for the reactor to transition between two steady-state operating conditions. As explained later, due to the higher degree of quantifying and generalizing the reactor transition timescale, we do not seek to predict its scaled-up performance, but rather just verify that within the laboratory-scale reactor unit, the transition between two steady-state conditions can occur within a reasonable timeframe. This transition timescale is applicable in use cases where we make adjustments to the reaction condition, and where we start feeding a different type of biomass, for example, that has different physical and chemical properties.

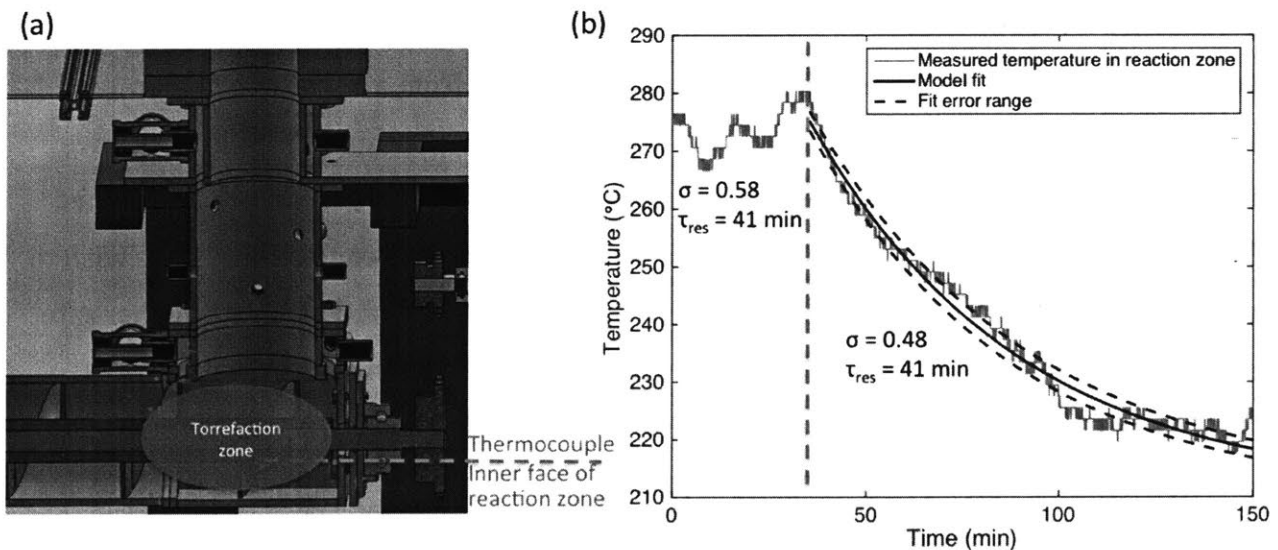


Figure 96 - Illustration of the transition timescale between two reactor operating conditions. (a) Placement of the thermocouple for experimental measurement; (b) an example trace of temperature in time, for pine shavings, as the reactor's normalized air/fuel ratio is reduced from $\sigma = 0.58$ to $\sigma = 0.48$. This results in a decrease in the steady-state reactor temperature from about 280°C to 210°C.

Figure 96a shows the placement of the thermocouple probe within the reactor to take the temperature measurement, and Figure 96b shows the result of this temperature profile as a time series. At $t = 40$ min, the pine shavings reactor, which has been previously operating at a normalized air/fuel ratio of $\sigma = 0.58$, transitions to a new ratio of $\sigma = 0.48$. During the transition time, the reactor is still being continuously fed as in the original steady state. We see a gradual decrease of the reactor core temperature from about 280 to 210°C in a period of about 2.5 hours. We note that this timescale is very long, and during the transition, we will be wasting 2.5 hours' worth of biomass if we feed the reactor continuously.

In comparison, for the laboratory-scale reactor, we would achieve a faster transition timescale if we first vacate the reactor of biomass and then proceed to cool the interior via forced convection, and then when the reactor approaches the desired final temperature, refill the reactor with biomass. According to Table 38 above, using rapid cooling, we could achieve this transition in less than 78 minutes.

On the other hand, what if we are transitioning the reactor from a lower to a higher temperature (more severe torrefaction)? In this case, our earlier analysis tells us that we should also first vacate the reactor of the biomass, and then feed a certain predetermined flow of biomass mass and air into the reactor to ensure complete combustion. If we wish to accomplish the transition more quickly, we should flow biomass and air in at a higher rate (thus wasting more of the biomass in the process). If we are not in a hurry, we can flow biomass and air in at a lower rate. In either case, as Table 35 shows, the transition can be accomplished at an equal or less time compared to 2.5 hours above, but we will be wasting much less biomass compared to simply continuously feeding biomass into the reactor during the transition process.

Unlike in previous sections, it is much more difficult to generalize the transition timescale because this timescale will change with the specific biomass mass flux (residence time) at each operating condition. However, by showing one example case study in Figure 96, we make a case that there are better strategies to accomplish the transition using either rapid

cooling or rapid warm methods described earlier. No doubt further work can be done on other operating conditions to verify whether or not this is true.

7.6 Discussion

In this study, we consider the transient timescales of the laboratory-scale reactor assembly. This may seem like a peripheral study as it does not delve into the underlying thermochemistry of torrefaction, but nonetheless it is important from the perspective of understanding how we can most effectively start a reactor from a cold state, and then after a fruitful steady-state production of torrefied output, shut it down effectively or move it elsewhere to operate at a different reaction condition. We first quantified the thermal mass (and hence inertia) in the reactor system, and showed that in most cases, this resides in the high-density metal. We identified that for rapid warming up and cooling, thermal agility is a desired property of the reactor, and this can be effectively achieved by reducing the amount of metal we use in designing the reactor (such as reducing the wall thickness to the extend feasible). We further showed that, in cases where we may want to retain the heat within the reactor for as long as possible (such as when moving the reactor from one farm to the next), we can devise an alternative strategy by capping the reactor and filling it completely with biomass. Thermal agility can be further improved by designing a removable exterior insulation jacket in the case of the need for rapid cooling. By building thermal transfer descriptions of the different processes, we also have the ability to predict how these timescales change as the reactor is scaled up. We showed that scaling the reactor does not generally scale these timescales: they only weakly respond to scaling. This is a desirable characteristic, as it assures us that as we scale up the reactor from the current laboratory-scale prototype, all the start-up and cooling timescales will still remain physically realistic.

A non-obvious insight that came out from this analysis is that, when we make an adjustment in the reactor condition, instead of continuously flowing biomass through whilst the transition occurs, it is often more time-efficient and feedstock-efficient utilize the

rapid start-up or rapid cooling procedure. No doubt, this prediction should be verified experimentally in greater detail, under different reactor operating conditions, for both the laboratory-scale reactor as well as for subsequent scale-up.

Finally, the insights learned in this study will also be helpful towards the design of an automated control system that can achieve these transition goals efficiently. With the few experimental conditions carried out, this study only serves as an initial proof of concept based on which a more extensive set of tests can be carried out for all the imaginable reactor operation and transition conditions. Ultimately, while it is not always possible for the reactor's operator in the field to know precisely, for example, the amount of air to feed into the reactor during start-up or cooling down, our laboratory-scale reactor and subsequent scale-up prototypes present a low-cost and rapid way to experimentally test and encapsulate these data empirically into the control system, so that the reactor runs with minimum need for human intervention.

Chapter 8 Perspectives and Future Work

In this thesis, we began with the premise that the majority of the biomass in the form of agricultural residue does not present itself in a form suitable for energy conversion and processing, because it is often inherently wet, bulky, and loose, which makes the collection and long-distance logistics expensive. We identified decentralized biomass torrefaction as a promising preprocessing method to improve the quality of biomass *in situ*, notably, leading to better long-term storage and transportability. An overview of the existing torrefaction reactor designs found that they have often been designed for large-scale, centralized biomass processing; scaling down such technologies to a decentralized application would cause challenges due to the high degree of complexity and cost built into such large-scale systems.

Instead, we explored the possibility torrefaction under a low-oxygen environment, and showed that this could lead to a much more simplified moving bed reactor design. An initial coarse-grained model was implemented to determine that the dominant form of heat transfer was in the gaseous phase. A subsequent fine-grained model was implemented that coupled chemical kinetics, thermodynamics, and heat transfer within the moving bed, and we verified that a moving bed reactor concept would indeed satisfy the requirements of torrefaction within physical length scales.

This informed a more detailed design and implementation of a laboratory-scale test reactor, which was validated in its performance metrics (mass yield, energy yield, and energy densification) over various operating conditions and over three types of biomass feedstock: pine shavings, hay, and rice husks. Therefore, our first main contribution is in developing and validating a laboratory-scale biomass torrefaction reactor that more accurately captures the realities of scaling up, in contrast to the many existing reactors which tend to impose artificially controlled conditions such as external heating, a completely inert condition, and arbitrarily large insulation. We further demonstrated the differences in the performance metrics between our reactor and those quoted in the

literature under similar conditions. These differences—generally an increased torrefaction severity and decreased solid mass and energy yields—are likely a result of a combination of (a) the penalty in low-oxygen torrefaction, and of (b) other real-life reactor design conditions that we imposed that may lead to a greater extent of product inhomogeneity and imperfect mixing compared to the idealized inert reactor case.

Having mapped out the performance of our reactor under various operating conditions, our second contribution is to establish a design-oriented approach to connect a diverse range of external performance requirements—such as fixed carbon content, grindability, and cooking characteristics—back to the reactor operating conditions, by linking the two with an index of torrefaction, which was defined based on the energy densification ratio and which is one way to quantify the torrefaction severity. We proceeded to show that the index of torrefaction has a functional (one-to-one) mapping against many of these external fuel characteristics/requirements. This then implies that our design selection process can be simplified into a one-dimensional space. Furthermore, we revealed that while increasing the torrefaction severity typically leads to a monotonic increase in the energy densification, this does not always lead to a monotonic increase in the useful energy output and density in a real-life cooking performance testing setting. This implies that many of these external performance requirements may have a much more complex relationship with torrefaction severity, and therefore, it is recommended that the effect of torrefaction be explored beyond a laboratory setting in a real-life setting.

Having understood how to operate the reactor and then select for specific operating conditions, our third major contribution is in characterizing the various energy loss mechanisms from the current reactor design, and then proposing and validating design improvements for subsequent scale-up. By characterizing thermal dissipation from the reactor side wall, we developed a method to calculate the optimal insulation thickness under different operating conditions and reactor scales. By characterizing the thermal dissipation in the char-cooling segment, we proposed and modeled a mechanism for recycling this dissipated heat back to the reactor in the form of air pre-heating, and estimated that we can save 65-80% of the energy loss from the char-cooling segment in

this way. Finally, in attempting to quantify any energy losses—both thermal and chemical—occurring through the escaping exhaust stream, we proposed and implemented a secondary oxidation zone above the reactor assembly in order to harness the remaining chemical energy in the combustible portion of the exhaust stream. We demonstrated that the majority of the energy loss from the exhaust stream occurs through the unreacted chemical availability, and that by introducing a secondary oxidation zone, under moderate to severe torrefaction conditions, we can harness above 95% of the chemical availability in the exhaust stream, and reduce the associated particulate and carbon monoxide emissions by as much. This therefore is also a laboratory-scale proof-of-concept of the secondary oxidation mechanism that can be improved in the scale-up stage of the reactor.

Next, we explored other design decisions required to effectively scale up the reactor. One of these centers around how to provide the pressure drive to ensure a continuous flow of air can flow into the reactor to maintain a low-oxygen torrefaction environment. In an attempt to answer this question, we made careful measurements of the hydrodynamic characteristics through a biomass moving bed, which has not been done before in the existing literature. Our fourth contribution lies in showing that the biomass moving bed roughly follows Darcy's law in our operating regime of interest, and that the current models often used for biomass moving bed are actually a poor description of the actual measured bulk bed permeability. Using these data, we were able to compare the pressure drive required to move air across different types of biomass moving bed to the pressure drive provided by the natural stack effect due to a hot column of rising air. We calculated that for loose biomass such as pine shavings and hay, the natural stack effect sufficiently provides enough pressure differential to drive the air through the biomass moving bed without necessitating an external pressure drive. On the other hand, for dense biomass such as rice husks, an external pressure drive is needed.

Finally, we made the fifth contribution by proposing and validating strategies for starting the reactor from a cold state, to shut down the reactor effectively, and to transition the reactor from one operating condition to another. By deriving scaling laws from the transient measurements of our current laboratory-scale reactor, we are able to predict and

recommend how the different transition timescales change as the reactor scales. Furthermore, we showed that in the current design, the metal component of the reactor constitutes the largest thermal inertia to the system; by redesigning a scaled-up version using thinner metal, we calculated that we can greatly improve the agility of our reactor performance.

While we have accomplished much in validating a scalable biomass torrefaction unit for decentralized deployment, this is only the first step in the long journey to scale this reactor up and bring it to commercialization. In the remaining Chapter, we discuss some of the next steps that should be done.

Firstly, the original goal of the torrefaction reactor design is that it should not only be deployable in the decentralized, rural setting, but also it should be sufficiently robust to be compatible with different types of biomass. So far, in the limited scope of the laboratory setting, we have validated the reactor's operation on three different types of biomass—namely, pine shavings, hay, and rice husks—however, these only represent a small selection of the much more diverse biomass types. Furthermore, in the laboratory condition, these biomass samples are relatively homogeneous and dry—about 5-10% moisture maximum by way of proximate analysis on our TGA equipment. In order to scale the reactor in the real-life setting, not only is it necessary to validate its performance against a wide selection (at least 10) types of biomass of different particle sizes, but also at a much more realistic moisture content. While we do not doubt that a slight increase in the moisture content will not affect the performance much, a doubling or tripling of the moisture content may influence the operations in a significant way (for example, by preventing the secondary oxidation zone from sustaining a stable flame), that it becomes necessary to pre-dry the biomass in a separate step.

This brings us to the second area of investigation: the implementation of a pre-drying mechanism in tandem with a hopper that automatically feeds the pre-dried biomass into the torrefaction reactor without human intervention. While there are many existing dryers already, there still lies the challenge of selecting the appropriate type that will meet the

requirements of our system: for example, given a flow rate of biomass, at what temperature and what moisture content should the biomass enter into the torrefaction reactor in order to achieve an optimal result, both in terms of the solid conversion process as well as the stability of the secondary oxidation reaction? How does this pre-drying mechanism adapt to different types of biomass, with different particle sizes of different thermal thickness?

Thirdly, while the auger system has been serviceable for the duration of the laboratory experiments associated with this thesis, there are many aspects of solid conveyance that can be improved. Firstly, the auger, with its very tight clearance with the inner wall of the char-cooling segment, is prone to clogging—even with torrefaction—for fibrous biomass types such as hay and even rice husks. Furthermore, in a small-scale test operation, we have also found that the auger movement could impart a certain undesirable discreteness into the continuous reactor—for example, when a lump of biomass suddenly falls into a new opening between the auger flights. While part of this problem may be resolved and the reactor approaches continuous operation when it is scaled-up, there still remains much work that can be done to strengthen the design of the solid conveyance system. A concept, for example, involving two augers working in parallel can be explored that allows the torrefied biomass greater flexibility to move around, thereby reducing the risk of clogging, lowering the torque and therefore power required to turn the auger, while at the same time potentially improving mixing and homogeneity within the moving bed reactor.

Fourthly, a large part of this thesis is concerned about the overall performance of the reactor. Many of these performance metrics that we care about—such as mass yield, energy yield, and energy densification ratio—are rather phenomenological. There underlies a complex interplay between chemistry and heat exchange that affects these characteristics that are still not well understood in a low-oxygen torrefaction setting like ours. Ironically, while low-oxygen torrefaction allows the reactor design to be greatly simplified, because of the presence of reactive oxygen, the underlying torrefaction chemistry and thermodynamics become much more complex to understand at a fundamental level. How does the biomass devolatilize under a low-oxygen torrefaction environment? How does the devolatilization kinetics and thermodynamics change? What volatile species are produced?

How do they react with oxygen? And how is the heat of reaction generated and transferred throughout the moving bed? Phenomenologically, we observe that pine shavings burn with a much more fiery flame, while hay and rice husks smother. What explains these differences, and how can they be understood and used to better design the torrefaction process and the reactor system? These fundamental questions, if addressed, will provide a much more powerful tool in scaling the torrefaction reactor not only under different conditions, but also across different types of biomass.

Fifthly, in Chapter 6, we made an effort at exploring the hydrodynamic properties of the biomass moving bed in order to understand the pressure requirements necessary to supply a certain flow rate of air through the moving bed. We also attempted to predict the natural stack effect that can be provided by a hot rising column of air. However, the current laboratory reactor setting prevents us from making actual measurements on these pressure differences. As the reactor is scaled up, one critical piece of investigation will be around the selection of a pressure drive. That is to say, every effort will be made to see whether, given a particular type of biomass, the pressure difference required to flow a certain amount of air through the moving bed can be supplied and regulated by natural means. If that proves insufficient—as we predict for dense biomass such as rice husks and sawdust—then it will be necessary to source an external pressure pump or fan to accomplish this. What kind of pressure drive will satisfy the specific requirements of torrefaction? How will it be realistically powered in a rural, decentralized setting?

Finally, this thesis focuses mostly on the technical aspects of scaling a torrefaction reactor. However, as the author learned through his education in the MIT Tata Center, technology by itself is hardly sufficient to address a problem as complex as underutilized biomass resources. As the author learned through his visits (generously sponsored by the MIT Tata Center) in India and elsewhere, biomass utilization is highly context-dependent. Different regions and different stakeholders result in different use cases, unit economics, and even government policies and subsidies. Therefore, beyond technology, the economics, local culture, and policies must be considered, in the style of Helmer (2015). The author has had some exposure in the non-technical aspects of biomass utilization from his experience co-

founding and running a biochar company in Kenya that utilizes rice husk waste, and can therefore speak to the immense difficulty of trying to get all the non-technical pieces to work. While a thorough examination of the techno-economics of decentralized biomass torrefaction, as well as a survey of the related policy framework—both in India and elsewhere—is beyond the scope of this thesis, they are equally if not more important to understand as the technical components, so that the torrefaction reactor proposed in this work, rather than collecting dust in a windowless, nondescript laboratory in Cambridge, MA, actually has a fighting chance to see the light of the day, whether in a chicken and alpaca farm in New Hampshire, in the Gangetic Plains, in the Rift Valley Highlands, or in other yet unimaginable places in this world.

Bibliography

Acharya, B., and Dutta, A. 2015. Fuel property enhancement of lignocellulosic and nonlignocellulosic biomass through torrefaction. *Biomass Conversion and Biorefinery* 6(2): 139-149.

Adnan, M.A., Susanto, H., Binous, H., Muraza, O., and Hossain, M.M. 2017. Enhancement of hydrogen production in a modified moving bed downdraft gasifier – a thermodynamic study by including tar. *International Journal of Hydrogen Energy*: 1-15.

Anca-Couce, A. 2012. Multi-scale approach to describe fixed-bed thermo-chemical processes of biomass. PhD thesis, Technical University of Berlin, Berlin, Germany.

Anca-Couce, A., Mehrabian, R., Scharler, R., and Obernberger, I. 2014. Kinetic scheme to predict product composition of biomass torrefaction. *Chemical Engineering Transactions* 37: 43-48.

Anca-Couce, A., Zobel, N., and Jakobsen, H.A. 2013. Multi-scale modeling of fixed-bed thermo-chemical processes of biomass with the representative particle model: application to pyrolysis. *Fuel* 103: 773-782.

Andreae, M.O., and Merlet, P. 2001. Emission of trace gases and aerosols from biomass burning. *Global Biogeochemical Cycles* 15: 955-966.

Arena, U., Di Gregorio, F., and Santonastasi, M. 2010. A techno-economic comparison between two design configurations for a small scale, biomass-to-energy gasification based system. *Chemical Engineering Journal* 162(2): 580-590.

Arias, B., Pevida, C., Feroso, J., Plaza, M.G., Rubiera, F., and Pis, J.J. 2008. Influence of torrefaction on the grindability and reactivity of woody biomass. *Fuel Processing Technology* 89(2): 169-175.

Armendáriz-Amez, C., Edwards, R.D., Johnson, M., Rosas, I.A., Espinosa, F., and Maser, O.R. 2010. Indoor particle size distributions in homes with open fires and improved Patsari cook stoves. *Atmospheric Environment* 44(24): 2881-2886.

Bain, K.L., and Overend, R.P. 2002. Biomass for heat and power. *Forest Products Journal* 52: 12-19.

Banzaert, A. 2013. Viability of waste-based cooking fuel for developing countries: combustion emissions and field feasibility. PhD thesis, Massachusetts Institute of Technology, Cambridge, MA, USA.

Barr, P.V., Brimacombe, J.K., and Watkinson, A.P. 1989. A heat-transfer model for the rotary kiln—I. Pilot kiln trials. *Met. Trans B*. 20B: 391-402.

Basu, P., Kulshreshtha, A., and Acharya, B. 2017. An index for quantifying the degree of torrefaction. *BioResources* 12(1): 1749-1766.

Basu, P., Rao, S., Acharya, B., and Dhungana, A. 2013. Effect of torrefaction on the density and volume changes of coarse biomass particles. *The Canadian Journal of Chemical Engineering* 91(6): 1040-1044.

Bates, R.B., and Ghoniem, A.F. 2012. Biomass torrefaction: modeling of volatile and solid product evolution kinetics. *Bioresource Technology* 124: 460-469.

Bates, R.B., and Ghoniem, A.F. 2013. Biomass torrefaction: modeling of reaction thermochemistry. *Bioresource Technology* 134: 331-340.

Bates, R.B., and Ghoniem, A.F. 2014. Modeling kinetics-transport interactions during biomass torrefaction: the effects of temperature, particle size, and moisture content. *Fuel* 137: 216-229.

Bellais, M., Davidsson, K.O., Liliedahl, T., Sjostrom, H., and Pettersson, J.B.C. 2003. Pyrolysis of large wood particles: a study of shrinkage importance in simulations. *Fuel* 82(12): 1541-1548.

Benanti, E., Freda, C., Loreface, V., Braccio, G., and Sharma, V.K. 2011. Simulation of olive pits pyrolysis in a rotary kiln plant. *Thermal Science* 15(1): 145-158.

Benk, A., and Coban, A. 2011. Molasses and air blown coal tar pitch binders for the production of metallurgical quality formed coke from anthracite fines or coke breeze. *Fuel Processing Technology* 92(5): 1078-1086.

Bergman, P.C.A. 2005. Combined torrefaction and pelletisation. Technical report, ECN Biomass.

Bergman, P.C.A., Boersma, A.R., and Kiel, J.H.A. 2004. Torrefaction for entrained-flow gasification of biomass. In *Contributions ECN Biomass to the 2nd World Conference and Technology Exhibition on Biomass for Energy, Industry, and Climate Protection*. Rome, Italy: 77-82.

Biesa, M.J., Miranda, J.L., Izquierdo, M.T., and Moliner, R. 2003. Curing temperature effect on mechanical strength of smokeless fuel briquettes prepared with molasses. *Fuel* 82(8): 943-947.

Biomass Technology Group (BTG). 2017. Torrefaction.
<<http://www.btgworld.com/en/rtd/technologies/torrefaction>>.

- Boateng, A.A., and Barr, P.V. 1996. A thermal model for the rotary kiln including heat transfer within the bed. *Int. J. Heat Mass Transfer* 39(10): 2131-2147.
- Bonilla, C.F., Brooks, R.D., and Walker, P.L. 1951. Viscosity of steam and of nitrogen at atmospheric pressure and high temperatures. *General Discussions on Heat Transfer*, London, England.
- Branca, C., Di Blasi, C., and Galgano, A. 2016. Chemical characterization of volatile products of biomass pyrolysis under significant reaction-induced overheating. *Journal of Analytical and Applied Pyrolysis* 119: 8-17.
- Branca, C., Di Blasi, C., Galgano, A., and Broström, M. 2014. Effects of the torrefaction conditions on the fixed-bed pyrolysis of Norway spruce. *Energy Fuels* 28(9): 5582-5591.
- Bridgeman, T.G., Gones, J.M., Williams, A., and Waldron, D. 2010. An investigation of the grindability of two torrefied energy crops. *Fuel* 89(12): 3911-3918.
- Cai, W., and Liu, R. 2016. Performance of a commercial-scale biomass fast pyrolysis plant for bio-oil production. *Fuel* 182: 677-686.
- Carmen, P.C. 1937. Fluid flow through granular beds. *Transactions, Institution of Chemical Engineers, London* 15: 150-166.
- Chattopadhyay, S., Kumar, N., Fine, C., and Olivetti, E. 2016. Industrial symbiosis among small and medium scale enterprises: case of Muzaffarnagar, India. *REWAS* 173-177.
- Chen, W.-H., Lu, K.-M., Liu, S.-H., Tsai, C.-M., Lee, W.-J., and Lin, T.-C. 2013. Biomass torrefaction characteristics in inert and oxidative atmospheres at various superficial velocities.
- Cheng, F., Lu, G., Yang, F., and Zhang, N. 2008. Study on using the denatured biomass as briquette binder. *Coal Chemical Industry*.
- Chilton, T.H., and Colburn, A.P. 1934. *Ind. Eng. Chem.* 26: 1183.
- Chin, O.C., and Siddiqui, K.M. 2000. Characteristics of some biomass briquettes prepared under modest die pressures. *Biomass and Bioenergy* 18(3): 223-228.
- Cho, Y.S., and Joseph, B. 1981. Heterogeneous model for moving-bed coal gasification reactors. *Ind. Eng. Chem. Process Des. Dev.* 20: 314.
- Chowdhury, Z., Edwards, R., Johnson, M., Shields, K.N., Allen, T., Canuz, E., and Smith, K.R. 2007. An inexpensive light-scattering particle monitor: chamber and field validations with wood smoke. *Journal of Environmental Monitoring*, 9(10): 1099-1106.

- Chu, H. 2017. Flues and chimneys. Lecture at the National Cheng Kung University. <myweb.ncku.edu.tw/~chuhsin/ppt/.../11-Flues%20and%20Chimneys.ppt>.
- Cleaves, R., Mazuroski, N., and Annad, C. Personal interview. November 5, 2015 and November 18, 2015.
- Cooper, J., and Hallett, W.L.H. 2000. A numerical model for packed-bed combustion of char. *Chemical Engineering Science* 55: 4451-4460.
- Constantino, D.S.M., Faria, R.P.V., Pereira, C.S.M., Loureiro, J.M., and Rodrigues, A.E. 2016. Enhanced simulated moving bed reactor process for butyl acrylate synthesis: process analysis and optimization. *Industrial and Engineering Chemistry Research* 55(40): 10735-10743.
- Couhert, C., Salvador, S., and Commandré, J.-M. 2009. Impact of torrefaction on syngas production from wood. *Fuel* 88(11): 2286-2290.
- Crombie, K., Mašek, O., Sohi, S.P., Brownsort, P., and Cross, A. 2013. The effect of pyrolysis conditions on biochar stability as determined by three methods. *GCB Bioenergy* 5: 122-131.
- Davidsson, K.O., and Pettersson, J.B.C. 2002. Birch wood particle shrinkage during rapid pyrolysis. *Fuel* 81: 263-270.
- De Acetis, J., and Thodos, G. 1960. *Ind. Eng. Chem.* 52:1003.
- Demirbaş, A, and Şahin, A. 1998. Evaluation of biomass residue: 1. Briquetting waste paper and wheat straw mixtures. *Fuel Processing Technology* 55(2): 175-183.
- Dhungana, A., Basu, P., and Dutta, A. 2012. Effects of reactor design on the torrefaction of biomass. *Journal of Energy Resources Technology* 134.
- Di Blasi, C. 2000. Dynamic behavior of stratified downdraft gasifiers. *Chemical Engineering Science* 55: 2931-2944.
- Di Blasi, C. 2004. Modeling wood gasification in a countercurrent fixed-bed reactor. *AIChE* 50(9): 2306-2319.
- Di Blasi, C., and Branca, C. 2013. Modeling a stratified downdraft wood gasifier with primary and secondary air entry. *Fuel* 104: 847-860.
- Di Blasi, C., Branca, C., Teislev, B. 2004. Development of a novel reactor for the oxidative degradation. *Bioresource Technology* 91: 263-271.
- Dong, L., Liu, H., and Riffat, S. 2009. Development of small-scale and micro-scale biomass-fuelled CHP systems – a literature review. *Applied Thermal Engineering* 29(11-12): 2119-2126.

- Dzhaphyev, K., Miropol'skii, A.L., and Mal'Kovskii, V.J. 1986. *Thermal Engineering* 33: 70.
- Edwards, R., Smith, K.R., Kirby, B., Allen, T., Litton, C.D., and Hering, S. 2006. An Inexpensive Dual-Chamber Particle Monitor: Laboratory Characterization. *Journal of the Air and Waste Management Association*, 56: 789-799.
- Emerhi, E.A. 2011. Physical and combustion properties of briquettes produced from sawdust of three hardwood species and different organic binders. *Pelagia Research Library, Advances in Applied Science Research* 2(6): 236-246.
- Engineering Tool Box (ETB). 2017. Convective heat transfer. <http://www.engineeringtoolbox.com/convective-heat-transfer-d_430.html>.
- Eranki, P.L., Bals, B.D., and Dale, B.E. 2011. Advanced regional biomass processing depots: a key to the logistical challenges of the cellulosic biofuel industry. *Biofuels, Bioproducts, and Biorefining* 5: 621-630.
- Eseyin, A.E., Steele, P.H., and Pittman, Jr., C.U. 2015. Current trends in the production and applications of torrefied wood/biomass – a review. *BioResources* 10(4): 8812-8858.
- Flynn, P.C., Kumar, A., and Cameron, J.B. 2003. Biomass power cost and optimum plant size in western Canada. *Biomass and Bioenergy* 24: 445-464.
- Flynn, P., and Searcy, E. 2009. The impact of biomass availability and processing cost on optimum size and processing technology selection. *Applied Biochemistry and Biotechnology* 154: 271-286.
- Froment, G.F., and Bischoff, K.B. 1979. *Chemical Reactor Design*. Wiley, New York.
- Gamson, B.W., Thodos, G., and Hougen, O.A. 1943. *Trans. Am. Inst. Chem. Engrs.* 39:1.
- Ghani, M.U., Radulovic, P.T., and Smoot, L.D. 1996. An improved model for fixed-bed coal combustion and gasification: sensitivity analysis and applications. *Fuel* 75: 1213-1226.
- Goh, Y.R., Yang, Y.B., Zakaria, R., Siddall, R.G., Nasserzadeh, V., and Swithenbank, J. 2001. Development of an incinerator bed model for municipal solid waste incineration. *Combustion Science and Technology* 162(1): 37-58.
- Govin, A., Repellin, V., Rolland, M., and Duplan, J.-L. 2009. Effect of torrefaction on grinding energy requirement for thin wood particle production. Nicolas Roche. XII Congrès de la Société Française de Génie des Procédés Pour relever les défis industriels du XXI siècle A la croisée des Sciences et des Cultures, Marseille, France. Société Française de Génie des Procédés, 98, 2009, *Récents Progrès en Génie des Procédés*. <hal-00462339>.

Grigante, M., and Antolini, D. 2014. Experimental results of mass and energy yield referred to different torrefaction pathways. *Waste and Biomass Valorization* 5(1): 11-17.

Gronnow, M.J., Budarin, V.L., Mašek, O., Crombie, K.N., Brownsort, P.A., Shuttleworth, P.S., Hurst, P.R., and Clark, J.H. 2012. Torrefaction/biochar production by microwave and conventional slow pyrolysis – comparison of energy properties. *Bioenergy* 5(2): 144-152.

Gupta, A.S., and Thodos, G. 1963. Direct analogy between mass and heat transfer to beds of spheres. *AIChE* 9(6): 751.

Helmer, R.M. 2015. Light Coal: Development of a torrefaction reactor and business system for Himalayan India. Master's thesis, Delft University, the Netherlands.

Hess, J.R., Wright, C.T., and Kenney, K.L. 2007. Cellulosic biomass feedstock and logistics for ethanol production. *Biofuels, Bioproducts and Biorefining* 1: 181-190.

Hiloidhari, M., Das, D., and Baruah, D.C. 2014. Bioenergy potential from crop residue biomass in India. *Renewable and Sustainable Energy Reviews* 32: 504-512.

Hobbs, M.L., Radulovic, P.T., and Smoot, L.D. 1990. Chemical and physical processes in counter-current fixed-bed coal gasification. In 23rd Symposium of the Combustion Institute, 1990.

Hobbs, M.L., Radulovic, P.T., and Smoot, L.D. 1992. Modeling fixed-bed coal gasifiers. *AIChE* 38(5): 681-702.

Hobbs, M.L., Radulovic, P.T., and Smoot, L.D. 1993. Combustion and gasification of coal in fixed-beds. *Prof. Energy Combust. Sci.*, 19: 505.

Huang, Y.F., Chen, W.R., Chiueh, P.T., Kuan, W.H., and Lo, S.L. 2012. Microwave torrefaction of rice straw and Pennisetum. *Bioresource Technology* 123: 1-7.

Jacobson, M.Z. 2014. Effects of biomass burning on climate, accounting for heat and moisture fluxes, black and brown carbon, and cloud absorption effects. *J. Geophys. Res. Atmos.* 119: 8980-9002.

Jain, H., Vijayalakshmi, Y., and Neeraja, T. 2015. Preparation of briquettes using biomass combinations and estimation of its calorific value. *International Journal of Science and Research* 4(3): 322-324.

Jenkins, B.M. 1997. A comment on the optimal sizing of a biomass utilization facility under constant and variable cost scaling. *Biomass and Bioenergy* 13: 1-9.

Jetter, J.J., and Kariher, P. 2009. Solid-fuel household cook stoves: characterization of performance and emissions. *Biomass and Bioenergy* 33(2): 294-305.

Jones, J.M., Saddawi, A., Dooley, B., Mitchell, E.J.S., Werner, J., Waldron, D.J., Weatherstone, S., and Williams, A. 2015. Low temperature ignition of biomass. *Fuel Processing Technology* 134: 372-377.

Kaliyan, N., and Morey, R.V. 2010. Natural binders and solid bridge type binding mechanisms in briquettes and pellets made from corn stover and switchgrass. *Bioresource Technology* 101(3): 1082-1090.

Kennedy, E.I. 1965. Strength and related properties of wood grown in Canada. Technical Report 1104, Canadian Department of Forestry, Ottawa, Canada.

Khalsa, J.H.A., Leistner, D., Weller, N., Darvell, L.I., and Dooley, B. 2016. Torrefied biomass pellets—comparing grindability in different laboratory mills. *Energies* 9(10): 794.

Klote, J.H. 1991. A general routine for analysis of stack effect. *NISTIR* 4588.

Koppejan, J. 2012. Status overview of torrefaction technologies. IEA Bioenergy Task 32 report. <http://www.ieabcc.nl/publications/IEA_Bioenergy_T32_Torrefaction_review.pdf>.

Kunii, D., and Smith, J.M. 1960. Heat transfer characteristics of porous rocks. *AIChE* 6(1): 71.

Kuzmina, J.S., Director, L.B., Shevchenko, A.L., and Zaichenko, V.M. 2016. Energy efficiency analysis of reactor for torrefaction of biomass with direct heating. *Journal of Physics* 774(1).

Lal, R. 2005. World crop residues production and implications of its use as a biofuel. *Environment International* 31: 575-584.

Lamers, P., Roni, M.S., Tumuluru, J.S., Jacobson, J.J., Cafferty, K.G., Hansen, J.K., Kenney, K., Teymouri, F., and Bals, B. 2015. Techno-economic analysis of decentralized biomass processing depots. *Bioresource Technology* 194: 205-213.

Larfeldt, J., Leckner, B., and Melaaen, M.C. 2000. Modelling and measurements of the pyrolysis of large wood particles. *Fuel* 79: 1637-1643.

Laurin, M., and Chamberland, A. 1981. Gasification of agricultural residues for energy production. *Energy Sources* 5(4): 361-380.

Li, D. 2015. Impact of torrefaction on grindability, hydrophobicity, and fuel characteristics of biomass relevant to Hawai'i. M.S. Thesis, University of Hawai'i at Manoa.

Li, H., Liu, X., Legros, R., Bi, X.T., Lim, C.J., and Sokhansanj, S. 2012. Torrefaction of sawdust in a fluidized bed reactor. *Bioresource Technology* 103: 453-458.

Li, S.-Q., Chi, Y., Li, R.-D., Yan, J.-H., and Cen, K.-F. 2002. Axial transport and residence time of MSW in rotary kilns: Part II. Theoretical and optimal analyses. *Powder Technology* 126: 228-240.

Lin, T., Rodriguez, L.F., Davis, S., Khanna, M., Shastri, Y., Grift, T., Long, S., and Ting, K.C. 2016. Biomass feedstock preprocessing and long-distance transportation logistics. *Bioenergy* 8(1): 160-170.

Litton, C.D., Smith, K.R., Edwards, R., and Allen, T. 2004. Combined optical and ionization measurement techniques for inexpensive characterization of micrometer and submicrometer aerosols. *Aerosol Science and Technology*, 38: 1054-1062.

Lowder, S.K., Scoet, J., and Raney, T. 2016. The number, size, and distribution of farms, smallholder farms, and family farms worldwide. *World Development* 87: 16-29.

Lowry, H.H. 1963. *Chemistry of Coal Utilization*. Wiley, New York.

Mahmoudi, A.H., Besseron, X., Hoffmann, F., Markovic, M., and Peters, B. 2016. Modeling of the biomass combustion on a forward acting grate using XDEM. *Chemical Engineering Science* 142: 32-41.

Martin, G. 2014. Stanford study shows effects of biomass burning on climate, health. *Stanford Report*. <<http://news.stanford.edu/news/2014/july/biomass-burning-climate-073114.html>>.

Mazioti, A.A., Stasinakis, A.S., Psoma, A.K., Thomaidis, N.S., and Andersen, H.R. 2017. Hybrid moving bed biofilm reactor for the biodegradation of benzotriazoles and hydroxyl-benzothiazole in wastewater. *Journal of Hazardous Materials* 322(A): 299-310.

McCracken, P., and Smith, K.R. 1998. Emissions and efficiency of improved woodburning cookstoves in Highland Guatemala. *Environment International* 24(7): 739-747.

McNamee, P., Adams, P.W.R., McManus, M.C., Dooley, B., Darvell, L.I., Williams, A., and Jones, J.M. 2016. An assessment of the torrefaction of North American pine and life cycle greenhouse gas emissions. *Energy Conversion and Management* 113(1): 177-188.

Mercado, U.R., Masera, O., Zamora, H., and Smith, K.R. 2011. Adoption and sustained use of improved cookstoves. *Energy Policy* 39(12): 7557-7566.

Milham, N., Kumar, P., Crean, J., and Singh, R.P. 2014. Policy instruments to address air pollution issues in agriculture: implications for Happy Seeder technology adoption in India. *ACIAR Final Report* FR2014-17.

Miller, B. 2016. Biomass torrefaction: tapping the hidden value of farm waste. <<http://energy.mit.edu/news/biomass-torrefaction-tapping-hidden-value-farm-waste/>>.

Ministry of New and Renewable Energy (MNRE). 2016. Overview of biomass power sector in India. <<http://biomasspower.gov.in/About-us-3-Biomass%20Energy%20scenario-4.php>>.

NASA. 2015. Stubble burning in Punjab, India. *Visible Earth* <<https://visibleearth.nasa.gov/view.php?id=86982> >.

Nhuchhen, D.R., Basu, P., and Acharya, B. 2014. A comprehensive review on biomass torrefaction. *International Journal of Renewable Energy and Biofuels* 2014: 1-56.

Nhuchhen, D.R., Basu, P., and Acharya, B. 2016. Torrefaction of poplar in a continuous two-stage, indirectly heated rotary torrefier. *Energy Fuels* 30(2): 1027-1038.

O'Brien, M.L. 2016. Design of a mobile torrefaction reactor for *in-situ* conversion of agricultural waste to solid fuel. M.Sc. thesis, Massachusetts Institute of Technology.

Pandey, J.S., Kumar, R., and Devotta, S. 2005. Health risks of NO₂, SPM and SO₂ in Delhi. *Atmos. Environ.* 39(36): 6868-6874.

Parikh, S. 2017. Personal communication.

Park, C., Zahid, U., Lee, S., and Han, C. 2015. Effect of process operating conditions in the biomass torrefaction: a simulation study using one-dimensional reactor and process model. *Energy* 79: 127-139.

Pérez, J., Muñoz-Dorado, J., de la Rubia, T., and Martinez, J. 2002. Biodegradation and biological treatments of cellulose, hemicellulose, and lignin: an overview. *International Microbiology* 5(2): 53-63.

Peters, B., and Bruch, C. 2003. Drying and pyrolysis of wood particles: experiments and simulation. *J. Analy. Appl. Pyrolysis* 70: 233-250.

Phanphanich, M., and Mani, S. 2011. Impact of torrefaction on the grindability and fuel characteristics of forest biomass. *Bioresource Technology* 102(2): 1246-1253.

Pirraglia, A., Gonzalez, R., Saloni, D., and Denig, J. 2013. Technical and economic assessment for the production of torrefied ligno-cellulosic biomass pellets in the US. *Energy Conversion and Management* 66: 153-164.

Radulovic, P.T., Ghani, M.U., and Smoot, L.D. 1995. An improved model for fixed bed coal combustion and gasification.

Rajaseenivasan, T., Srinivasan, V., Syed Mohamed Qadir, G., and Srithar, K. 2016. An investigation on the performance of sawdust briquette blending with neem powder. *Alexandria Engineering Journal* 55(3): 2833-2838.

- Rakovitsky, N., Brook, I., Van Rijn, J., Ryskin, M., Mkhweli, Z., Etkin, H., and Nir, S. 2016. Purification of greywater by a moving bed reactor followed by a filter including a granulated micelle-clay composite. *Applied Clay Science* 132-133: 267-272.
- Ramanathan, V., Ramana, M.V., Roberts, G., Kim, D., Corrigan, C., Chung, C., and Winker, D. 2007. Warming trends in Asia amplified by brown cloud solar absorption. *Nature* 448: 575-578.
- Ratte, J., Fardet, E., Mateos, D., and Hery, J.S. 2011. Mathematical modeling of a continuous biomass torrefaction reactor: TORSPYD™ column. *Biomass Bioenergy* 35(8): 3481-3495.
- Ray, N.M., and Ray, A.K. 2016. Modelling, simulation, and experimental study of a simulated moving bed reactor for the synthesis of biodiesel. *The Canadian Journal of Chemical Engineering* 94(5): 913-923.
- Razmjoo, N., Sefidari, H., and Strand, M. 2016. Measurements of temperature and gas composition within the burning bed of wet woody residues in a 4 MW moving grate boiler. *Fuel Processing Technology* 152: 438-445.
- Regufe, M.J., Faria, R.P.V., Ribeiro, A.M., Loureiro, J.M., and Rodrigues, A.E. 2016. Synthesis of the biofuel additive 1,1-diethoxybutane in a fixed-bed column with amberlyst-15 wet. *Chemical Engineering and Technology* 39(8): 1509-1518.
- Ren, S., Lei, H., Wang, L., Bu, Q., Wei, Y., Liang, J., Liu, Y., *et al.* 2012. Microwave torrefaction of Douglas fir sawdust pellets. *Energy Fuels* 26: 5936-5943.
- Repellin, V., Govin, A., Rolland, M., and Guyonnet, R. 2010. Energy requirement for fine grinding of torrefied wood. *Biomass and Bioenergy* 34(7): 923-930.
- Repellin, V., Govin, A., Rolland, M., and Guyonnet, R. 2010. Modelling anhydrous weight loss of wood chips during torrefaction in a pilot kiln. *Biomass and Bioenergy* 34(5): 602-609.
- Richards, S.R. 1990. Physical testing of fuel briquettes. *Fuel Processing Technology* 25(2): 89-100.
- Riechel, D., Boblenz, K., Krzack, S., and Meyer, B. 2010. Coal/biomass pyrolysis as initial step in gasification. In *4th International Freiberg Conference on IGCC & XtL Technologies* 09-3, Dresden, Germany.
- Roden, C.A., Bond, T.C., Conway, S., and Pinel, A.B.O. 2006. Emission factors and real-time optical properties of particles emitted from traditional wood burning cookstoves. *Environment Science and Technology* 40: 6750-6757.
- Rubio, B., Izquierdo, M.T., and Segura, E. 1999. Effect of binder addition on the mechanical and physicochemical properties of low rank coal char briquettes. *Carbon* 37(11): 1833-1841.

Satpathy, S.K., Tabil, L.G., Meda, V., Naik, S.N., and Prasad, R. 2014. Torrefaction of wheat and barley straw after microwave heating. *Fuel* 124: 269-278.

Shang, L. 2012. Upgrading fuel properties of biomass by torrefaction. PhD thesis, Technical University of Denmark.

Sharma, A.R., Kharol, S.K., Badarinath, K.V.S., and Singh, D. 2010. Impact of agriculture crop residue burning on atmospheric aerosol loading – a study over Punjab State, India. *Ann. Geophys.* 28: 367-379.

Shyamalee, D., Amarasinghe, A.D.U.S., and Senanayaka, N.S. 2015. Evaluation of different binding materials in forming biomass briquettes with saw dust. *International Journal of Scientific and Research Publications* 5(3): 1-8.

Singh, A., Chakraborty, S., and Roy, T.K. 2006. Village size and development in India. <<http://epc2006.princeton.edu/papers/60018>>.

Singh, A., Tuladhar, B., Bajracharya, K., and Pillarisetti, A. 2012. Assessment of effectiveness of improved cook stoves in reducing indoor air pollution and improving health in Nepal. *Energy for Sustainable Development* 16(4): 406-414.

Sivakumar, K., Mohan, N.K., and Sivaraman, B. 2012. Performance analysis on briquetting biomass with different size in 10 kW down draft gasifier. *Precedia Engineering* 38: 3824-3832.

Survilo, J., and Beryozkina, S. 2016. Optimal territory of renewable fuel collection for cogeneration plant. In 57th International Scientific Conference on Power and Electrical Engineering of Riga Technical University (RTU CON), Riga, Latvia.

Subramanian, M. 2016. Delhi's deadly air. *Nature* 534: 166-168.

Svanberg, M., Olofsson, I., Floden, J., and Nordin, A. 2013. Analysing biomass torrefaction supply chain costs. *Bioresource Technology* 142: 287-296.

Taulbee, D., Patil, D.P., Honaker, R.Q., and Parekh, B.K. 2009. Briquetting of coal fines and sawdust part I: binder and briquetting-parameters evaluations. *International Journal of Coal Preparation and Utilization* 1.

Thamer, D. 2013. New challenges in torrefaction of biomass. *ACB Torrefaction* <www.syncoal.com>.

Thrän, D., Witt, J., Schaubach, K., Kiel, J., Carbo, M., Maier, J., Ndibe, C., Koppejan, J., Alakangas, E., Majer, S., and Schipfer, F. 2016. Moving torrefaction towards market introduction – Technical improvements and economic-environmental assessment along the

overall torrefaction supply chain through the SECTOR project. *Biomass and Bioenergy* 89: 184-200.

Tie, S., Sreedhar, B., Agrawal, G., Oh, J., Donaldson, M., Frank, T., Schultz, A., Bommarius, A., and Kawajiri, Y. 2016. Model-based design and experimental validation of simulated moving bed reactor for production of glycol ether ester. *Chemical Engineering Journal* 301: 188-199.

Times of India. 2016. Big gap in per capita income in urban and rural areas. <<http://timesofindia.indiatimes.com/city/delhi/Big-gap-in-per-capita-income-in-urban-and-rural-areas/articleshow/52207415.cms>>.

TorfTech. 2017. TORBED expanded bed reactor. <http://www.torftech.com/technologies/expanded_bed_reactor.html>.

Tursun, Y., Xu, S., Wang, C., Xiao, Y., and Wang, G. 2016. Steam co-gasification of biomass and coal in decoupled reactors. *Fuel Processing Technology* 141(1): 61-67.

Valencia, J.J., and Quested, P.N. 2008. Thermophysical properties. *ASM Handbook* 15: 468-481.

van der Werf, G.R., Randerson, J.T., Giglio, L., Collatz, G.J., Kashbhatla, P.S., and Arellano, Jr., A.F. 2006. Interannual variability in global biomass burning emissions from 1997 to 2004. *Atmos. Chem. Phys.* 6: 3423-3441.

Villiermaux, J., Antoine, B., Lede, J., and Soullignac, F. 1986. A new model for thermal volatilization of solid particles undergoing fast pyrolysis. *Chem Engineering Science* 40(1): 151-157.

Wang, C., Peng, J., Li, H., Bi, X.T., Legros, R., Lim, C.J., and Sokjansanj, S. 2013. Oxidative torrefaction of biomass residues and densification of torrefied sawdust to pellets. *Bioresource Technology* 127: 318-325.

Wang, M.J., Huang, Y.F., Chiueh, P.T., Kuan, W.H., and Lo, S.L. 2012. Microwave-induced torrefaction of rice husk and sugarcane residues. *Energy* 37: 177-184.

Yang, H., Yan, R., Chen, H., Zheng, C., Lee, D.H., and Liang, D.T. 2006. In-depth investigation of biomass pyrolysis based on three major components: hemicellulose, cellulose, and lignin. *Energy and Fuels* 20: 388-393.

Zhang, X., Xu, D., Xu, Z., and Cheng, Q. 2001. The effect of different treatment conditions on biomass binder preparation for lignite briquette. *Fuel Processing Technology* 73(3): 185-196.

Zhao, Z., Chen, T., and Ghoniem, A.F. 2012. Rotary bed reactor for chemical-looping combustion with carbon capture. Part 1: reactor design and model development. *Energy and Fuels* 27(1): 327-343.

Zhao, Z., Iloeje, C.O., Chen, T., and Ghoniem, A.F. 2014. Design of a rotary reactor for chemical-looping combustion. Part 1: Fundamentals and design methodology. *Fuel* 121: 327-343.

Appendix A: Table of Common Symbols

Symbol	SI dimension	Description
$(AF)_{\text{stoic}}$	[]	Mass ratio of air to biomass (as received) to support stoichiometric oxidation
$c_{p,s}, c_{p,BM}$	[J kg ⁻¹ K ⁻¹]	Specific heat capacity of the solid (biomass) phase
$c_{p,i}$	[J kg ⁻¹ K ⁻¹]	Specific heat capacity of the <i>i</i> th component
d_p	[m]	Characteristic dimension of a biomass particle
HHV_i	[J kg ⁻¹]	Higher heating value of the <i>i</i> th component
\dot{H}_{chem}	[W]	Measured enthalpy flow in uncombusted volatiles in the native reactor exhaust
H_c	[m]	Height of the reactor chimney
H_i	[J kg ⁻¹]	Enthalpy of the <i>i</i> th component
H_r	[m]	Height of the moving bed reactor
h_{air}	[W m ⁻² K ⁻¹]	Convective heat transfer coefficient of air
I_{torr}	[]	Index of torefaction, solid energy densification ratio
k_r	[W m ⁻¹ K ⁻¹]	Bulk axial thermal conductivity coefficient in biomass moving bed
k_{steel}	[W m ⁻¹ K ⁻¹]	Thermal conductivity coefficient of 304 stainless steel
L_c	[m]	Length of the char-cooling segment
\dot{m}_{air}	[kg s ⁻¹]	Mass flow rate of input primary air to the reactor
\dot{m}_{BM}	[kg s ⁻¹]	Mass flow rate of input biomass through the reactor
\dot{m}_{char}	[kg s ⁻¹]	Mass flow rate of output torrefied biomass (char)
MW_i	[kg mol ⁻¹]	Molecular mass of the <i>i</i> th component
P_u	[W]	Useful power output in a cook stove experiment
p_{atm}	[Pa]	Standard atmospheric pressure
Q	[m ³ s ⁻¹]	Volumetric fluid flow rate
Q_i	[W]	Energy (thermal) loss due to the <i>i</i> th mechanism
R	[J mol ⁻¹ K ⁻¹]	Gas constant
R_c	[m]	Internal radius of the char-cooling segment
R_r	[m]	Internal radius of the moving bed reactor
S	[]	Sphericity of a biomass particle
T_{amb}	[K]	Ambient temperature
T_c	[K]	Native exhaust gas temperature at reactor exit
T_H	[K]	Temperature in torrefaction "hot zone"
T_{ins}	[K]	Temperature measured at outer insulation surface
T_{wall}	[K]	Temperature measured at inner reactor wall
v_{air}	[m s ⁻¹]	Axial velocity of pre-heating air
v_{BM}	[m s ⁻¹]	Downward velocity of input biomass in moving bed
v_{exhaust}	[m s ⁻¹]	Upward velocity of the exhaust gas from the reactor
v_g	[m s ⁻¹]	Upward velocity of gas in biomass moving bed
x	[m]	Longitudinal distance from the torrefied biomass exit
Y_j	[]	Mass fraction of the <i>j</i> th component
z	[m]	Axial distance in the reactor from the top

Δ_{ins}	[m]	Thickness of reactor's outer insulation layer
Δ_R	[m]	Radial width of the air-preheating channel
Δ_{steel}	[m]	Thickness of the reactor steel wall
$\delta P_i, \Delta P_i$	[Pa]	Pressure difference/drop associated the i th event
δ_H	[m]	Axial thickness of the torrefaction "hot zone"
ε	[]	Bulk porosity of the biomass moving bed
κ	[m ²]	Bulk permeability of the biomass moving bed
μ	[kg m ⁻¹ s ⁻¹]	Fluid viscosity
Φ_{BM}	[kg m ⁻² s ⁻¹]	Input mass flux of solid through the reactor
φ_{BM}	[W m ⁻²]	Input energy flux of solid through the reactor
Ω_i	[m K W ⁻¹]	Thermal resistance through the i th component
$\Theta_{i \rightarrow j}$	[m K W ⁻¹]	Thermal resistance from the i th to the j th component
ρ_{BM}	[kg m ⁻³]	Mass density of input biomass
ρ_E	[kg m ⁻³]	Useful fuel energy density in a cook stove experiment
σ	[]	Normalized air/fuel ratio
τ_{res}	[s]	Torrefaction solid residence time
τ_s	[s]	Transient timescale for starting up the reactor